THE UNIVERSITY
of EDINBURGH

Wireless Power and Communication System for Medical Implants

Liyu Huang

A thesis submitted for the degree of Doctor of Philosophy

The University of Edinburgh

2020

Acknowledgement

I would like to thank my supervisors, Prof. Alan Murray and Dr Brian Flynn, for their guidance and support during my study. Alan has always been the greatest guider during my research and study. He is always here to keep me in the right direction when I got lost and solve my concerns when I am stuck. Brian is one of the smartest people I have ever seen. He is always ready to support me with his knowledge and experience in RF engineering. I am grateful for their trust and patience, which have encouraged me to carry on during the hard times and explore the unknown.

I would also like to thank Dr Martin Reekie for his help and support during my study. His rigour in research and passion for acquiring knowledge are the most precious things I have learned in the university. I am especially grateful for his advice in the design of rectifiers in this thesis and in the field of analogue circuits.

I would also like to thank Prof. Ian Underwood for his encouragement and trust as my former personal tutor and as the chair of Scottish Microelectronic Centre.

I would also like to thank Iain Gold, Mark Mason and the other technical staff in the School of Engineering for their generous support in the construction of experiment apparatus and their patient assistance in building and testing the circuits.

I would also like to thank Chandrasekaran Gunasekaran and Rui Song, who gave me enormous support in the design, layout and testing of rectifier chips. It is fun and enjoyable to work with them.

I would also like to thank the IMPACT team that gave me significant support in my research.

I would also like to thank EPSRC for the funding of the research.

I am truly grateful to my family during my time in Edinburgh; My parents Shiwen Huang and Jianxin She, and my sister Liyan Huang for their love and motivations.

I would also like to express my gratitude to my girlfriend, Olivia Yuan, and all my other friends in Edinburgh who accompany me and support me in my everyday life.

Thank you all.

Abstract

This thesis aims to examine the hypothesis that "**Power of more than 1 mW can be received by the microsystem inside a human body through a wireless magnetic coupling link with a receiver of a diameter less than 2mm from a transfer distance as much as 20 cm**" and "**Data can be transmitted wirelessly from the microsystem to an external reader using the same magnetic coupling link as the wireless power system**". A 3-coil weakly coupled magnetic resonance wireless power transfer system has been built based on solenoid coils. The design of the transmitter of the system includes the designs of a single-turn coupling coil and a multi-turn primary coil. To maximise the magnetic field generated by the transmitter, the relative position of the two coils is optimised to match the impedances of the coils. Design flow is reported for the optimum dimensional parameters (coil diameter, gap interval, number of turns) of the primary coil after a detailed analysis of the co-dependencies of the parameters. The design of the receiver of the system includes the designs of the receiver coil and the rectifier. Two kinds of solenoid receiver coils have been analysed, the air-core coil and the ferrite-core coil. Due to the size limitation (2 mm-diameter) of the receiver, only the ferrite-core solenoid coil is able to meet the power demand. Design flow of the ferrite-core coil is reported. In terms of the rectifier, a novel static gate-control bootstrapping rectifier (static BSR) and a novel opto-coupled dynamic gate-control (OCDGC) bootstrapping rectifier are reported, which have low power consumption and high power conversion efficiency compared with junction-diode rectifiers and comparator-based rectifiers. The power delivered to load (PDL) of the whole WPT system is tested in air and human conductive tissue at transfer distances within 20 cm with consideration of rectifier power conversion efficiencies and different load conditions (500 Ω and 5 kΩ). Results show that, at 20 cm transfer distance, the system will be able to meet the 1 mW power demand for light load condition (5 kΩ) both in air and in human conductive tissue; But in heavy load condition (500 Ω), a high number of receiver coil turns will be needed to meet the power demand. The sensitivity of the data transfer of the whole WPT system is also analysed based on load shift keying (LSK) modulation. The S-parameter S_{11} ratio is the Figure of Merit (FOM) of the data transfer analysis. It can be concluded that the hypotheses of the thesis are feasible, which is an inspiration of multiple deep-tissue micro-implants for medical purposes.

To my parents

And my sister

Contents

List of figures

List of tables

Acronyms and abbreviations

3-D	3-Dimentional
AC	Alternating Current
BR	Basic Restriction
BSR	Bootstrapping Rectifier
DC	Direct Current
DUT	Device Under Test
EM	Electromagnetic
EMI	Electromagnetic Interference
FEA	Finite Element Analysis
FOM	Figure of Merit
FSK	Frequency Shift Keying
IMD	Implantable Medical Device
IMPACT	Implantable Microsystems for Personalised Anti-Cancer Therapy
LED	Light Emission Diode
LSK	Load Shift Keying
MCU	Micro-Controlled Unit
MOSFET	Metal-Oxide-Semiconductor Field-Effect Transistor
MPE	Maximum Permissible Exposure
OCDGC	Opto-Coupled Dynamic Gate-Control
PDL	Power Delivered to Load
PMOS	P-type Metal-Oxide-Semiconductor
PSK	Phase Shift Keying
PTE	Power Transfer Efficiency
PWM	Pulse Width Modulation
PZT	Piezoelectric Transducer
RF	Radio Frequency
RFID	Radio Frequency IDentification
RMS	Root Mean Square
RMSE	Root-Mean-Square Error
SAR	Specific Absorption Rate
SNR	Signal to Noise Ratio
SRF	Self-Resonant Frequency
SRMSE	Standard Root-Mean-Square Error
TDE	Time-Delay Induced Electric-Field

VCR	Voltage Conversion Ratio
WPDT	Wireless Power and Data Transfer
WPT	Wireless Power Transfer

Nomenclature

Latin letter

A_{eff}	Effective area of a single turn of coil
$\mathbf{B}$	Magnetic flux density
$B_{\mathbf{z}}$	Magnetic flux density in z direction
C	Capacitance
c	Speed of light in free space ($299{,}792{,}458\ m/s$)
C_{AF}	Axial field capacitance at a solenoid coil
C_{ext}	External variable capacitor to connect to a coil to resonate
C_{FF}	Fringe field capacitance at a solenoid coil
C_{Load}	Load capacitor
C_M	Capacitor at impedance matching circuit at coupling coil circuit
C_{MR}	Capacitor at impedance matching circuit at receiver circuit
$C_{pr\text{-}eq}$	Equivalent parasitic capacitance
$C_{Primary}$	Tuning capacitor at primary coil circuit
$C_{Resonant}$	Capacitor connected to a coil for resonance
C_{Rx}	Receiver coil self-capacitance
D_{fc}	Demagnetising factor of a cylindrical ferrite core
D_{fe}	Demagnetising factor of an ellipsoid ferrite core
$d\mathbf{l}$	Infinitesimal length
D_{loop}	Diameter of coil
D_{pri}	Diameter of primary coil
D_{Rx}	Diameter of receiver coil
D_{Tx}	Diameter of transmitter coil
d_{wire}	Diameter of wire of a coil
$\mathbf{E}$	Electric field strength
E_C	Energy stored in a capacitor
E_{CON}	Control energy loss of a rectifier
E_{FOR}	Forward energy from input to output of a rectifier
E_{heat}	Heat loss of a rectifier
E_{IN}	Input energy of a rectifier
E_L	Energy stored in an inductor
E_{leak}	Leakage loss of a rectifier
E_{other}	Other energy loss of a rectifier
E_{OUT}	Output energy of a rectifier
E_{REV}	Reverse energy from output to input of a rectifier
f	frequency
G	Ratio between source output power with off-state receiver and power with on-state receiver
G_1	Ratio between powers with no impedance matching circuit at coupling coil circuit
G_2	Ratio between powers with an impedance matching circuit at coupling coil circuit
GND	Ground
h	Transfer distance between transmitter coil and receiver coil
$\mathbf{H}$	Magnetic field strength
h_{NPri}	Transfer distance between N_{Pri} turn of primary coil and receiver coil
H_z	Magnetic field strength in z-direction
I	Current
$i(t)$	Instantaneous current
i'_{Couple}	Current at coupling coil
$I'_{Primary}$	Current at primary coil with an impedance matching circuit at coupling coil circuit

$I'_{Primary(max)}$	Maximum primary coil current with an impedance matching circuit at coupling coil circuit
I_0	Current amplitude
$I_0(x)$	Modified Bessel's function of first kind
$I_1(x)$	Modified Bessel's function of second kind
$i_{CTL}(t)$	Instantaneous current flowing to control circuit of a rectifier
i_{Couple}	Current at coupling coil circuit
$i_{ds}(t)$	Instantaneous current flowing from drain to source of a MOSFET
$i_{FOR}(t)$	Forward current flowing from input to output of a rectifier
$i_{IN}(t)$	Instantaneous input current to a rectifier
IN-	Negative input port
IN+	Positive input port
$i_{OUT}(t)$	Instantaneous output current to a rectifier
$I_{Primary}$	Current at primary coil
$I_{Primary}(max)$	Maximum primary coil current
$i_{REV}(t)$	Reverse current flowing from output to input of a rectifier
$\boldsymbol{J}$	Current density
$K_0(x)$	Modified Bessel's function of first kind
$K_1(x)$	Modified Bessel's function of second kind
k_L	Nagaoka's coefficient
k_{loop}	Coil coefficient
L	Self-Inductance of coil
L_{Couple}	Inductor of coupling coil
l_{loop}	Length of coil
L_M	Inductor at impedance matching circuit at coupling coil circuit
L_{MR}	Inductor at impedance matching circuit at receiver coil circuit
$L_{Resonance}$	Resonant inductor
l_{wire}	Length of wire of a coil
M	Mutual-inductance
m_0	Product of loop current and loop area
N	Number of turns
N_{pri}	Primary coil number of turns
N_{Rx}	Receiver coil number of turns
P	Real power
p	Coil gap interval
$p(t)$	Instantaneous real power
$p_{IN}(t)$	Instantaneous input real power of a rectifier
P_{Load}	Load power
P_{OUT}	Output real power
$p_{OUT}(t)$	Instantaneous output real power of a rectifier
Q	Quality factor
$\boldsymbol{r}$	Vector distance
R	Resistor
R'_{Couple}	Reflected coupling coil resistance
R'_{Pri}	Reflected primary coil resistance
$R'_{Receiver}$	Reflected receiver circuit resistance
R'_{Source}	Equivalent source impedance at output of impedance matching circuit
R_0	Characteristic resistance of a solenoid coil
R_{AC_couple}	AC resistance of coupling coil
$R_{AC\_primary}$	AC resistance of primary coil
$R_{AC\text{-}coil}$	AC resistance of coil itself
R_{core}	AC resistance caused by core of coil
R_{Couple}	Total resistance of coupling coil
R_{Load}	Load resistor
R_{Loss}	Equivalent heat-loss resistor
$R_{pr\text{-}eq}$	Equivalent parasitic resistance

$R_{Primary}$	Total resistance of primary coil
R_{Rad}	Equivalent radiation resistor
R_{RX}	Receiver coil resistance
RX	Receiver
S_{11}	Reflection coefficient at port 1 at a network
S_{eff}	Total effective area of surface
TX	Transmitter
u_{hx}	Nominal velocity
u_{hx}/c	Nominal velocity factor
$v(t)$	Instantaneous voltage
V_0	Voltage amplitude
V_{AC_IN}	AC input voltage of rectifier
V_{CAP}	Voltage at Bootstrapping capacitor at BSR rectifier
V_{DC}	DC voltage
V_{DC_OUT}	DC output voltage of rectifier
VDD	DC voltage of power source or output voltage of a rectifier
$v_{ds}(t)$	Instantaneous voltage between drain and source of a MOSFET
V_{FWD}	Forward voltage drop across a diode or a switch MOSFET of a rectifier
V_g	Gate voltage of switch MOSFET of a rectifier
VIN	Input voltage
V_{IN}	Input voltage of a rectifier
$v_{IN}(t)$	Instantaneous input voltage to a rectifier
VIN'	Input voltage at coupling coil after impedance matching circuit
V_{IND}	Induced voltage on coil
V_{Load}	Load voltage
V_{OUT}	Output voltage
$V_{OUT}(avg)$	Average value of output voltage of a rectifier
$V_{OUT}(max)$	Maximum value of output voltage of a rectifier
$V_{OUT}(min)$	Minimum value of output voltage of a rectifier
$V_{OUT}(rms)$	Root-mean-square value of output voltage of a rectifier
$v_{OUT}(t)$	Instantaneous output voltage to a rectifier
V_{peak}	Peak voltage
$V_{primary}$	Voltage at primary coil
V_{rms}	Root-mean-square voltage
V_{sg}	Voltage between source and gate of switch MOSFET of a rectifier
V_{Source}	Voltage of power source
V_{th}	Threshold voltage of MOSFET
$W(x)$	Ollendorff's function
$\vec{x}$	Unit vector in the x-direction
X_{tot}	Total reactance
$\vec{y}$	Unit vector in the y-direction
$\vec{z}$	Unit vector in the z-direction
Z	Impedance
$Z*$	Complex conjugate of impedance
Z_{Couple}	Impedance at coupling coil
$Z_{Primary}$	Impedance at primary coil
Z_{Rec}	Rectifier input impedance

Greek letter

α	Attenuation constant
β	Phase constant
δ	Skin depth
λ	Wavelength

λ_0	Wavelength in free space
λ_g	Wavelength in media
Ξ	Skin effect factor
ρ	Resistivity of a material
Ψ	Pitch angle between wire and cross-section of coil
ε	Dielectric permittivity of a material
ε_0	Dielectric permittivity of free space ($8.854\times 10^{-12}\ F/m$)
ε_i	Relative dielectric permittivity of internal material
ε_r	Relative dielectric permittivity of a material
ε_{rad}	Relative dielectric permittivity of radial propagation
ε_x	Relative electric permittivity of external material
σ	Electric conductivity
φ	Phase of instantaneous voltage or instantaneous current
ψ	Magnetic flux
ϕ	Angular displacement
η	Efficiency
η_{CTL}	Efficiency of loss caused by control loss
η_{diode}	Efficiency loss caused by diode of a junction-diode rectifier
η_{FWD}	Forward efficiency of a rectifier
η_{heat}	Efficiency of loss caused by heat loss
η_{other}	Efficiency loss caused by other energy loss
η_{OUT}	Efficiency between output and input of a rectifier
η_{REV}	Efficiency loss caused by reverse energy loss
η_{tot}	Total efficiency
μ	Magnetic permeability of core of a coil
μ_0	Magnetic permeability of free space ($4\pi \times 10^{-7}\ H/m$)
μ_r	Relative permeability of core of a coil
$\mu_r{}'$	Real component of complex magnetic permeability of ferrite
$\mu_r{}''$	Imaginary component of complex magnetic permeability of ferrite
μ_{r-eff}	Effective relative permeability of a ferrite core
ω	Angular frequency
ω_r	Resonance angular frequency

Introduction

Implanted electronic devices are increasingly being used in medical treatment and diagnostics. Wireless power transfer (WPT) is a desirable option for powering such devices as it removes the requirement for batteries or subcutaneous wiring, avoiding the risk of infection or chemical battery leakage. This has distinct advantages for the safety and convenience of patients, potentially extending the life of the implanted device and reducing the need for further surgical intervention. WPT also allows, in principle, larger numbers of sensors to be implanted, which is crucial to provide rich 3D information for the clinicians involved in therapy. Multiple sensors become very inconvenient (and generally impossible) with wiring.

In recent decades, WPT has been used in a wide range of implantable medical devices (IMDs), for cochlear [1][2][3], cardiac [4]-[7], retinal [8]-[23], spinal [24][25], cortical [26]-[33], and peripheral implants [34]-[46]. Meanwhile, many wireless power capsule-dedicated implants have been developed for biopsy [47]-[52], therapy [53], locomotion [54]-[57] and visual prostheses [58]-[63] applications.

Implants are becoming smaller, and the implanted positions are becoming deeper within the patient's body, while the required power remains largely unchanged. Increasingly, there is a requirement for data transmission alongside the wireless power transfer, for real-time medical diagnostics and monitoring in neural implants and biopsy implants [33][53]-[56][64][65].

With the development of WPT technologies, different techniques have been used to power medical implants. These include power transfer using electromagnetic (EM) energy, such as magnetic coupling (also called inductive coupling or near field coupling) and EM wave transfer (far-field transfer), as well as power transfer using mechanical energy methods, such as ultrasonic. These technologies each have their own advantages and disadvantages and are best suited to different situations. A detailed discussion of these WPT technologies is carried out in Section 1.2.

1.1 Motivations

In the “Implantable Microsystems for Personalised Anti-Cancer Therapy” (IMPACT) project at Edinburgh University [66], an implantable integrated chip has been developed for real-time sensing of tumour hypoxia. With these implantable chips inside the patient’s body, a real-time 3-dimensional (3-D) image model for hypoxic tumour cells can be built, which allows radiotherapy-resistant cells, largely those in a hypoxic (oxygen-starved) state to be given a greater dose than “normal” cancer cells [66].

While the microsystem could be powered with wire connections, wireless powering is a preferable option because of the reduced infection risk, the reduced impact on patients’ everyday life and the ultimate aim of multiple sensors.

The operation of the IMPACT microsystem has the following limitations and requirements:

Requirement	Limitations	Reasons
Cross-section diameter	No more than 2 mm	Needle diameter restriction
Length	no more than 5 cm	Chip physical robustness
Maximum implantation depth	20 cm from skin	For average size people
Power requirement	1 mW	For operation of active sensors
Data transmission	Up-flow data with at least 1 byte/s	Adequate for sensor data collection and for minimal power consumption

Table 1.1-1 Limitations and requirements of the implanted microsystem

Unlike other wireless power implants, whose sizes are from a few centimetres (e.g. capsule) to a few decimetres (e.g. pacemaker), the IMPACT microsystem has a cross-section diameter of no more than 2 mm. Moreover, as introduced in Section 1.2, most of the WPT systems are designed for a transfer distance less than 10 cm. The IMPACT system, however, needs to have a transfer distance up to 20 cm.

To meet the requirements of the IMPACT microsystem, this thesis aims to examine the hypotheses that:

- *Power of more than 1 mW can be received by the microsystem inside a human body through a wireless magnetic coupling link with a receiver of a diameter less than 2 mm from a transfer distance as much as 20 cm.*
- *Data can be transmitted wirelessly from the microsystem to an external reader using the same magnetic coupling link as the wireless power system.*

To explore the different possibilities to meet the above requirements, a literature review and a discussion of different options for wireless power and data transfer for medical implants are carried out in Section 1.2.

1.2 Literature review and options for wireless power and data transfer for medical implants

1.2.1 Introduction

Wireless power and data transfer (WPDT) for medical implants can be achieved in many different ways.

In terms of power transfer, the most commonly used ways are

- Magnetic coupling resonance
- Ultrasonic wave
- EM mid field and far field radiation

There are also other, less common, approaches. They are

- Capacitive coupling
- Environmental power harvesting
- Near-infrared light

In terms of data transfer, there are two different methods

- Single carrier frequency, which applies the principle of radio frequency identification (RFID)
- Multiple carrier frequencies, which applies the principle of radio frequency (RF) antennas

In the following section, the two methods of wireless data transfer for medical implants are discussed in Section 1.2.2. The different methods for wireless power transfer are then discussed.

1.2.2 Wireless data transfer with wireless power transfer

1.2.2.1 Wireless power and data transfer with single carrier

(1) What is single carrier frequency?

In a wireless power and data transfer system, “single carrier” means that the data transfer system shares the same frequency as the wireless power transfer system. The data are sent by adjusting the electrical power, which is the “carrier” that links the transmitter and the receiver. In this way, the data transfer and the power transfer are interfering with each other. A single carrier wireless power and data transfer system works on the same principle of passive radio-frequency identification (RFID) systems,

which is a method for out-of-sight identification, where a reader activates a mobile data carrier (e.g. a tag or a transponder) by transmitting RF power to it and receive the data stored in it by backscattering method [67][68]. An RFID system modulates signals with frequency shift keying (FSK) or load shift keying (LSK).

(2) How does a single-carrier wireless power and data transfer system work?

A near-field passive RFID system is shown in Figure 1.2-1. In the system, the inductive RFID reader generates power and data, which are transferred to the receiver (RFID tag) through the Transmitting (TX) and Receiving (RX) coupling coils. The tag receives the power and sends data back to the reader by switching a MOSFET (Metal-Oxide-Semiconductor Field-Effect Transistor) (the load modulator) 'on' and 'off' to achieve LSK. The MOSFET can also connect to a capacitor, which changes the receiver resonance frequency when switched 'on' and 'off' to achieve FSK. When the load impedance or the resonance frequency of the RX coil is changed, the power delivered from the TX coil changes accordingly. The reader detects this change of power and reads out the data from the tag.

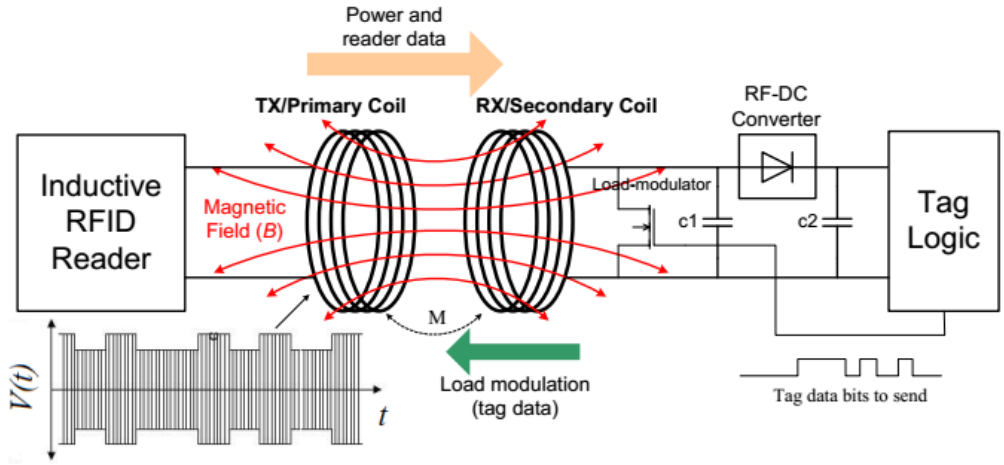

Figure 1.2-1 Block diagram of a passive near-field magnetic coupling RFID system [69]

(3) Advantages and Disadvantages

Similar to a passive RFID system, the wireless power and data transfer with a single carrier has the following advantages:

- Simple system complexity
- Low power requirement in data modulation

However, it also has the following disadvantages:

- Interference between data transfer and power transfer reduces energy transfer efficiency in a unit period
- Low data rate

As discussed, the wireless power and data transfer system with a single carrier shares the same pair of coupling coils as the wireless power transfer system. Besides the data coding logic (in the tag logic), which is needed in every system that requires data transfer, the only required component for the data transfer with a single carrier is the load modulator MOSFET (and a capacitor for FSK). Therefore, the system complexity is very low, and the power consumption is minimal compared with other methods.

However, for LSK, the data transfer in the system is achieved by adjusting the working state of receiver, which changes the transferred power at the receiver. The data transfer will, therefore, inevitably reduce the total transferred energy in a period of time. This effect can be minimised by proper coding of data to limit the time when the load modulator MOSFET is switched on. For FSK, this problem is less troublesome, because the reader can generate power of the same frequency as the RX coil resonance frequency when the receive coil load modulator is in the on-state. However, this will add complexity to the reader.

The other disadvantage related to a single-carrier wireless power and data transfer system is the low data rate, which is constrained by the operational frequency of the wireless power transfer system. This is because the symbol rate of a signal cannot be more than half of the carrier frequency, according to the Nyquist–Shannon sampling theorem [70]. Because the operational frequency is determined by the design of the wireless power transfer system, the data rate will inevitably be limited. However, this is not a major issue in the application that motivates this thesis, as is discussed in Section 1.1.

(4) Application range

From the discussion above, the wireless data transfer with a single carrier is most suitable to use in near-field wireless power transfer systems where the power budget is limited, and a low data rate can be accepted. The IMPACT microsystem is within this application range, as the requirements shown in Table 1.1-1.

(5) Examples

Much research has been conducted on wireless data transfer with a single carrier.

A data rate ranging from 1 kbps to 1 Mbps is normally achieved with such a wireless power transfer system. In [71], the wireless power and data transfer system is tested at a transfer distance up to 5 cm. LSK is applied in the uplink data transfer, and a 4 Mbps data rate is achieved with a centre frequency of 25 MHz. In [72], with the application of LSK, the system achieves 1 Mbit/s data rate in a 1 cm transfer distance with a power frequency of 8.4 MHz. In [73], the wireless power and data system works

in a range between 7 mm to 15 mm. A pseudo pulse width modulation is applied with LSK, and 3.3 kbps data rate is achieved with power transfer frequency being 1 MHz. In [74], with a power transfer frequency of 13.56 MHz, 500 kbps data rate is achieved based on LSK. The LSK is also used in systems with higher frequencies. With a power transfer frequency of 1.32 GHz, [75] achieves a higher data rate of 2 Mbps with low-depth LSK modulation. In recent years, developments have been made to improve the data rate of single-carrier data transfer, in [76], both the data rate issue and energy efficiency reduction issue are solved with a modulation scheme called Cyclic On–Off Keying, where the load modulator MOSFET switches once per cycle when the receiver inductor current reaches maximum. With this modulation scheme, 89.2% of power transfer efficiency (PTE) is achieved in the wireless power transfer system, and 6.78 Mb/s data rate is achieved with 13.56 MHz operational frequency. Another way to improve data rate is to apply phase shift keying (PSK), which shifts the phase of the power wave instead of the amplitude to minimise the effect on power transfer. In [77], a new modulation scheme called Passive Phase-Shift Keying is proposed based on LSK. This scheme improves the data rate by switching the load modulator only when the receiver voltage cross zero. At an operational frequency of 13.56 MHz, 1.35 Mb/s is achieved with a bit error rate less than 10^{-5} at a transfer distance between 5 mm to 15 mm. The energy transfer efficiency, however, drops 6% with the application of this technique. Another phase shift keying scheme is the binary phase shift keying [78][79]. At a transfer distance of 15 mm, [80] obtains a data rate of 1.2 Mbps at 10 MHz power frequency with an integrated binary phase shift keying demodulator based in a hard-limited Costas loop topology.

1.2.2.2 Wireless power and data transfer with multiple carriers

(1) What is a multiple-carrier wireless power and data transfer system?

A multiple-carrier data transfer system has more than one carrier frequency, with each carrier frequency dedicated either to transfer power or to communicate data. Normally, each carrier has its own wireless link to avoid interference, but with careful design, they can also share the same link to reduce the size of implants.

(2) How does it work?

Typical block diagrams of wireless power and data transfer systems with multiple carriers are shown in Figure 1.2-2 [81][82].

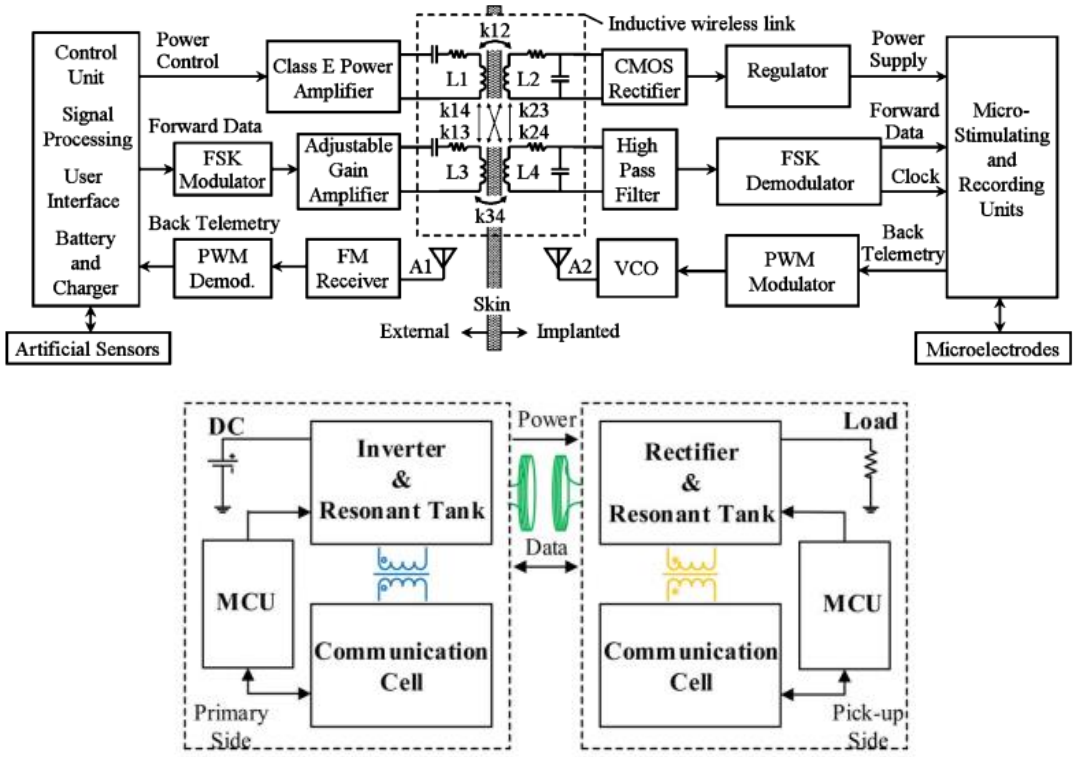

Figure 1.2-2 (Upper) block diagram of a magnetic coupling wireless power transfer system with multiple-links for data tranfser, where the upper link is for power transfer, the middle link is for forward data and the bottom link is for back telemetry [81]; (bottom) block diagram of a single-link magnetic coupling wireless power transfer system with multiple carriers [82]

In the upper diagram, the power transfer link, the forward data transfer link and the backward data transfer link each has its own dedicated pair of transceivers. While electrical power is transferred wirelessly through the magnetic coupling link L1-L2, the forward data is transmitted with FSK modulation through the magnetic coupling link L3-L4. The forward data (downlink) is then demodulated and processed in the receiver. For backward data telemetry (uplink), the data are sent through RF antennas A1-A2 after pulse width modulation (PWM). The signals will then be demodulated at the external transmitter [81]. In some other wireless power and data transfer systems with multiple links, only a downlink or an uplink exists, and the modulation scheme may vary. Still, the system structure is similar to the block diagram.

In the bottom diagram in Figure 1.2-2, the power transfer and the data transfer share the same pair of coils but operate in different frequencies [82]. The power wave and the data wave then overlap with each other at the primary coil and receiver coil. During backward data transfer (from the receiver to the transmitter), the communication cell in the receiver modulates the data and couples the data wave with the power wave. The backward wave will then be filtered out at the transmitter and demodulated by the micro-control unit (MCU). In some other wireless power and data transfer system with multiple carriers in a single link, the approaches to coupling and separating the data

and power waves may be different, but the process of coupling and separation cannot be excluded.

(3) Advantages and disadvantages

A wireless power and data transfer system with multiple carriers and multiple links has the following advantages:

- High data rate
- Flexible for optimisation

Its disadvantages are:

- Large receiver size
- High power consumption on data transfer
- Magnetic interference between links (for magnetic coupling coils)

Because the data transfer does not need to share the same carrier as the power transfer, the data transfer frequency is independent of the power transfer frequency. Therefore, a high data rate can be achieved with a high data transfer frequency. Because the data transceivers (antennas) are physically independent of the power transceivers (coils), they can be optimised separately to achieve a high quality factor in the power transceivers and a wide bandwidth at the data transceivers [63]. This is, however, not an essential issue in the application of IMPACT.

Because of the separate links, the receiver size will inevitably be larger than the receiver size with a single link, which may exceed the size limitation of implants. For example, the maximum diameter of the implant needle is 2 mm for IMPACT. Also, extra power will be consumed to generate the data signals for transmission from the receiver in backward telemetry. Moreover, the power carrier will interfere with the data signal and lower the signal to noise ratio (SNR) in the communication channel [82].

A single-link wireless power and data transfer system with multiple carriers shares some features with the multiple-link ones, but it has its own advantages and disadvantages.

Advantages:

- Moderate data rate

Disadvantages:

- High power consumption on data transfer
- A complex circuit in coupling and separating data signal and power wave

The single-link multiple-carrier system also has the advantage of a moderate data rate because of the independent carrier for data transfer. However, extra power will still be consumed to generate the data transfer carrier and amplify the data signals so that it can be coupled with the power wave. This is unfriendly to implants with a low power budget for data transfer. Also, the coupling and separation of data signal and power wave will add complexity in the circuit and increase circuit sizes.

(4) Application range

From the discussion above, a wireless power and data transfer system with multiple carriers is most suitable for applications that require a moderate data rate and have a large power budget with less concern on the receiver size. The IMPACT system is not in this application range.

(5) Examples

Multiple carriers have been reported in several outstanding studies of implanted medical wireless power systems [83]-[91]. It should be noted that in some multiple-link systems, some of the carriers will share the same link, while others have separate links. For example, in [92]-[96], both the power carrier and the uplink carrier operate in the inductive coil link, but a separate RF antenna link has been designed to fulfil downlink data transfer. In other studies [81][97]-[100], each carrier has a dedicated link.

A higher data rate than the power frequency has been achieved using multiple-link multiple-carrier systems. [99] uses the offset quadrature phase-shift keying to obtain a data rate of 4.16 Mbps with 1 MHz power transfer frequency. At 13.56 MHz power transfer frequency, [101] achieves a data rate of 20 Mbps with the application of pulse harmonic modulation. In some applications, RF antennas are also used to achieve even higher data rates. In [87], an impulse-radio ultrawideband transceiver is used, which operates at 2.5-5 GHz. In [89], a data rate of 500 Mbps is achieved uplink with the application of impulse-radio ultrawideband with a power transfer frequency of 13.56 MHz.

As discussed, one of the main problems of a multiple-link system is the strong power interference to the data carrier. Several studies have been attempted to minimise the magnetic interference between the power link and the data link. In [100], mathematical models have been built to analyse the theories behind the magnetic interference. Several methods have been put forward to solve the problem. In [87] and [99], specially designed coil structures have been reported to reduce the crosstalk between two links. Other studies apply special modulation schemes [98]. In [101], pulse harmonic modulation is proposed to replace the data carrier with sharp spike pulses,

which helps to improve the transfer distance and data link selectivity. However, pulse harmonic modulation is proved to lack robustness with interference from the power carrier [98]. Moreover, pulse harmonic modulation is unable to transfer power and data at the same time. In comparison, Pulse Delay Modulation is an alternative scheme, because no power consumption is needed for power interference filtering on the RX side, and the robustness is stronger against power interference. In [102], a non-coherent Differential Phase Shift Keying modulation scheme is used in the transmitter to make the interference cancel each other without filtering when the sample differences are taken.

To avoid large receiver sizes and power carrier interference, single-link wireless power and data transfer systems have also been studied [96]. One of the earliest studies is in [103]. Instead of using a sine-wave power source for the wireless power system, a rectangular wave source is applied, in which 4 switches are turned on and off to generate a rectangular wave from a Direct Current (DC) source. Coupling inductors are used to couple the data carrier with the power carrier. To avoid electromagnetic interference (EMI), the data are transferred only at the non-switching period in sync with the rising edge of the rectangular power wave. With a power transfer frequency of 50 kHz, a 100 Kbps of data rate is achieved with the setup. A similar study is conducted in [82], where ferrite coupling coils are used in filtering out the data carrier from the power carrier. To achieve this, the data carrier frequency is set to be about 50 times higher than the power carrier frequency. With a power carrier frequency of 22.4 kHz, a data rate of 20 kbps is achieved. The drawback of this setup is that the data rate is still limited by the power carrier frequency, even though not as much as the data rates of single-carrier systems [103]. Another kind of multiple-carrier wireless power and transfer system utilises the single-carrier transfer scheme with the multiple-carrier transfer scheme for different carriers. In [104], the uplink data transfer from receiver to transmitter applies the LSK modulation, while the downlink data transfer from transmitter to receiver applies PWM. Because the LSK modulation (which changes amplitude) is orthogonal to the PWM (which changes pulse width), the interference between the data transfers is much reduced.

1.2.3 Magnetic coupling resonance power transfer

The concept of transferring electrical energy without the use of conducting wires is almost as old as our understanding of electricity. Michael Faraday discovered that the flow of current through a coil of wire could generate a magnetic field and transfer an electrical signal [105]. Nikola Tesla developed the use of magnetic resonant coupling between coils using high-frequency Alternating-Current (AC) signals to transfer power

wirelessly [106][107]. The idea of using this to power IMDs was explored for use in artificial hearts in the 1960s [108].

Figure 1.2-3 shows a block diagram of a magnetic coupling resonance power transfer system. A wireless energy transmission system can be divided into two parts: a transmitter and a receiver. The transmitter consists of a coupling coil circuit and a primary coil circuit. An AC signal is applied to a coupling coil, which generates a magnetic field. The coupling coil then couples with the primary coil, which is also coupled with the receiver coil (secondary coil) and transfers power to the receiver circuit. Power transfer is enhanced when all the coils are tuned with the same resonant frequency. This is a non-radiative, near field effect and the maximum transfer range is of the order of a few times of the diameter of the transmitter coil.

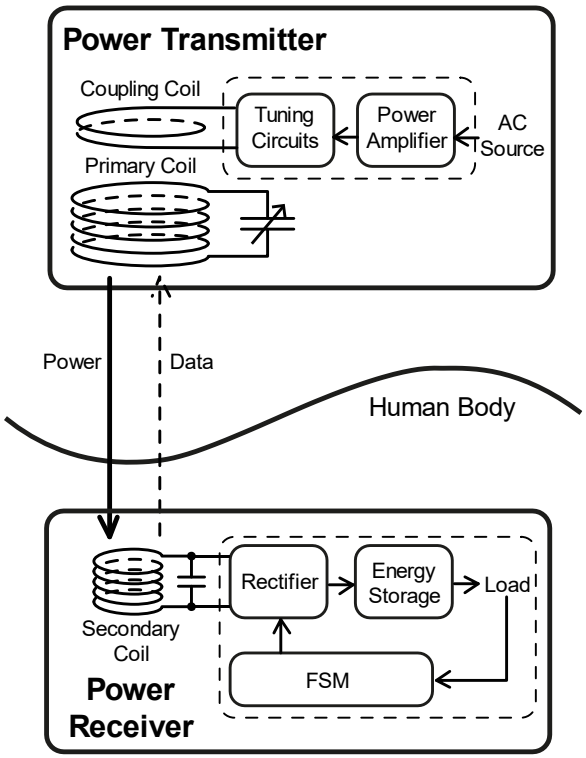

Figure 1.2-3 Block diagram of the wireless power and communication system for medical implants, where FSM is the finite state matchine for control purpose

In previous works of literature, analytical models have been built to gain insight into the performance of the magnetic coupling resonance WPT system [109]-[111]. In [110], complete mathematical models for the magnetic resonance coupling coils have been built based on the electromagnetic theory. Lateral and angular misalignment calculations have been performed for both solenoid coils and printed spiral coils. In [111]-[113], models based on circuit theory have been built. In [112], the coupling coils are treated as the primary and secondary of a transformer. The calculations of the coupling coefficient and mutual inductance become the key to obtain power transfer efficiency. The prediction of power transfer efficiency using the transformer model has shown good agreement with experimental results.

To achieve a high power transfer efficiency (PTE), a careful design of the transmitter coil is vitally important. For power transfer frequencies ranging from 100 kHz to 50 MHz, solenoid coils are normally used as transmitter coils [109][111]-[114][115]. However, when size is an issue, printed spiral coils are also commonly used as transmitter coils [116]-[120]. Because the PTE of a magnetic coupling resonance WPT system is dependent on the physical structure of the transmitter coil, various studies have focused on the optimisation of transmitter coils. In [114], four methods to optimise a solenoid transmitter coil have been proposed, based on mathematical analysis. The methods aim to improve the generated magnetic field strength or the coil quality factor with consideration of coil resistance or receiver movement. Another method for coil optimisation is based on finite element analysis (FEA) [121][122]. In [121], FEA has been applied to design a 200 mm x 300 mm rectangular transmitter coil and a 24 mm-diameter receiver coil. A power transfer efficiency of more than 40% can be achieved at 5cm transfer distance. In [120], a 3D semi-empirical model has been built for the printed spiral coils with consideration of parasitic components. Optimisation of coils based on the model achieves 85.8% power transfer efficiency at 1 cm.

Besides the design of the transmitter, the PTE of a magnetic coupling resonance WPT system is also affected by the number of coils in the system [123]-[125]. In [124], the PTEs and the transmitted power of a system with 2 coils, 3 coils and 4 coils have been analysed, respectively. It shows that the 3-coil system has the highest power transfer efficiency. At a transfer distance of 12 cm, the delivered power of a 3-coil system is 1.5 times of the 2-coil system and 59 times of the 4-coil system. In [123], a comparison of angular misalignment performances was made between a 2-coil system and a 3-coil system. The power transfer efficiency, the voltage gain, and the data bandwidth are assessed. The analysis shows that a 3-coil system has more tolerance against angular misalignment. With a 3-coil system, an average of 40% improvement in PTE and 62.5% in data bandwidth can be obtained. In [111], a 4-coil system has been built based on high-Q multi-layer solenoid coils. The PTE of the 4-coil system is compared with the PTE of a 2-coil system in a transfer distance ranging from 0 to 6 cm. The analysis shows that the 4-coil system outperforms the 2-coil system in PTE at a transfer distance of more than 20 mm, which shows that the 4-coil system has more tolerance than the 2-coil system against the increase of transfer distance. 3-coil and 4-coil systems can achieve a better PTE performance than a 2-coil system with the same transfer distance and coil dimension.

The receiver coil is also of significant importance in the magnetic coupling resonance WPT system. Solenoid coils [111][126]-[128] and planar spiral coils [123]-[125] are

most commonly used as receiver coils because they can be built with small sizes and fit into the medical implants. The diameter of a receiver coil is often related to the power transfer frequency. A higher frequency will result in a smaller receiver coil. In [126], a 9 mm-diameter solenoid RX coil has been built to fit in a medical capsule endoscope, and the power transfer frequency is chosen to be 16.47 MHz. In [128], the operation frequency is 60 MHz with a solenoid RX coil of 4 mm-diameter. A figure of merit (FOM) in the design of a receiver coil is the quality factor, which is affected by the coil resistance. To reduce the coil resistance, the Litz wire has been analysed in [129] in a magnetic coupling resonance WPT system. Using magnetoplated wires, the coil resistance is reduced by 40% at 12 MHz, and the quality factor is correspondingly increased by 66%. In [115], Litz wires have been used in a geometrically orthogonal-3D RX coil to reduce skin effect and proximity effect losses between the adjacent coils. The orthogonal-3D RX coil is built to avoid angular misalignment issues. The size of the actual RX coil is 10mmx12mm, with a maximum received power of 730 mW at 400 kHz operational frequency. In some very small implants, ultra-small coils are needed in the receiver. In this case, integrated on-chip coils are normally used. These RX coils often work in high-frequency systems (100 MHz to 1 GHz) and close transfer distances (<1 cm). In [130] and [131], fully integrated on-chip planar coils with small areas have been used for neural stimulation and interface purposes.

1.2.4 Ultrasonic wave power

Wireless power transfer using ultrasonic waves has also received much attention. The word ultrasonic refers to the sound wave, which has a frequency higher than 20 kHz, which is beyond the range of audio sound. Unlike magnetic power, which is generated by metal wires in the form of a coil, ultrasonic power is generated by piezoelectric transducers (PZT), which are in the form of solid non-metal materials (such as crystals and ceramics) [132]. The theory behind this is called the piezoelectric effect, with which piezoelectric materials have a reversible linear electromechanical interaction between mechanical vibration and alternative electrical change [133].

The ultrasonic wireless power transfer most commonly operates at a frequency range of 2 MHz and 18 MHz. A demonstrative ultrasonic WPT system is shown in Figure 1.2-4. As shown, an ultrasonic WPT system for medical implants contains a transmitter and a receiver, with a PZT on each side. During operation, the piezoelectric transmitter needs to be attached to the skin surface with a matching layer between the skin and the transmitter to reduce wave reflection. The piezoelectric transmitter then converts the electrical energy from the power source into mechanical

waves. The PZT at the receiver then picks up the mechanical waves and converts the energy into electrical form, which is then supplied to the load.

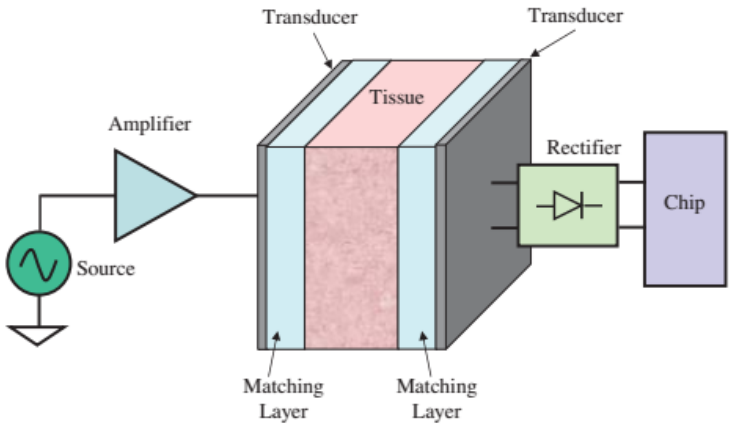

Figure 1.2-4 Demonstrative diagram of ultrasonic WPT system [134]

Compared with the magnetic coupling resonance WPT system, an ultrasonic WPT system has the following advantages:

- The received power is proportional to the area $((D_{Rx}/2)^2)$ of the piezoelectric receiver instead of $(D_{Rx}/2)^4$ in the magnetic coupling resonance WPT system, which means the ultrasonic WPT systems are less sensitive to the change of receiver size, and smaller receiver can thus be implanted under the same power requirement.
- The mechanical wave power has a $(1/r)$ roll-off against transfer distance. In contrast, the electromagnetic field power has a $(1/r^6)$ roll-off in the near-field region, which means the reduction of mechanical wave power is much "slower" than the reduction of an EM field [134]. The roll-off of electromagnetic field against transfer distance is discussed in Section 2.3.4.1.
- The ultrasonic wave becomes omnidirectional at the receiver because of the wave reflection. The ultrasonic WPT system is thus less sensitive to angular misalignment issues [135].

An ultrasonic WPT system also has the following disadvantages:

- The lowest resonance frequency of a PZT is linearly proportional to the decrease of thickness, which causes problems at the choice of operational frequency when a small device is needed [136].
- Prolong exposure of ultrasonic waves and high-density waves may cause damage to human tissues. For example, the high intensity focused ultrasound has been used in tumour treatment [137]. The ultrasonic power has a tight safety regulation instruction to avoid severe heating and cavitation effect.

The discussion above shows that the ultrasonic WPT system can be applied in long-distance wireless power transfer with a relatively low power requirement. It is also suitable for the case where the direction of the receiver is not controllable and has angular misalignment issues. However, the size-frequency relation and the high exposure risk has restricted its use in deep tissue micro-implants. Its suitability for the application of IMPACT is unclear.

Ultrasonic WPT with data transfer has been well studied in recent years. In [138], a bi-directional communication link is proposed with an ultrasonic WPT system. In the system, two pairs of PZTs are used to transmit power and data separately. Unlike the data transfer with magnetic coupling coils, the same frequency is applied for both power transfer and data transfer at two different links. The PZT for data transfer is directly connected to the power transfer circuit in the receiver circuit. An amplitude shift keying modulation scheme is applied, and a FET switch controls the connection between the PZT for data transfer and the power circuit. From a transfer distance between 7 mm to 100 mm, a data rate as much as 9.6 kbps is obtained with a low error rate. In [139] and [140], a downlink data transfer has been built for ultrasonic WPT systems. In [140], a phase shift keying modulation scheme has been applied. A data rate of 25 kbps is obtained with a centre frequency of 1 MHz. Meanwhile, 4.15 mW of power can be received with an acoustic power of 112 mW, which is under the limit of FDA safety limit.

1.2.5 EM mid-field and far-field radiation

The EM wave radiation is commonly used in mobile communication and radar systems. The EM mid-field and far-field radiation WPT systems transfer power in the form of propagating EM wave. For wireless power transfer systems, the operational frequency is mainly from 100 MHz to 2 GHz, and the transfer distance is generally at the same order of the wavelength of the EM wave (for mid-field WPT) or much longer than the wavelength of EM wave (for far-field WPT).

The operation of an EM radiation WPT system is similar to the magnetic coupling resonance power WPT. The difference is that for the EM radiation WPT, the transmitter and receiver are RF antennas instead of coils. The RF antenna theory, instead of Maxwell's equations, are generally used in the analysis of WPT system design and power transfer efficiency.

Compared with the magnetic coupling resonance WPT systems, the advantages of EM radiation WPT systems are as follows:

- Focused EM beam
- A smaller receiver area

- Transferred power proportional to $(1/h^2)$ roll-off
- Control of field distribution to avoid the excessive heating issue (for mid-field)

The disadvantages are:

- Short penetration depth in conductive media
- Lower maximum regulated power for the human body

With proper antenna design, the EM wave power from an RF antenna can focus on a specific direction. With this advantage, most of the EM power from the transmitter antenna of an EM radiation WPT system can be transmitted to the receiver, achieving a high PTE. Because most of the EM power is constrained within a small area, the receiver antenna does not need a large area to improve PTE. Therefore, a high PTE can still be obtained with a small receiver size. According to EM theory, the propagating EM wave in the far-field region has a power roll-off of $(1/r^2)$ against transfer distance, which means the EM mid-field and far-field radiation WPT systems are more suitable for long-range power transfer than EM near-field WPT systems, which have a power roll-off of $(1/r^6)$. For an EM mid-field radiation WPT system, both reactive field components and radiative field components are used to power the receiver antenna [141]. The wave beam from the transmitter antenna can be designed to focus on a small area of the tissues so that the heating of tissue is minimised per unit transferred energy [142][143].

Even with the advantages, the application of EM radiation WPT systems is limited by its disadvantages. In conductive media, propagating EM waves with a high frequency will suffer from a short skin depth (e.g. 10.7 cm for 8 GHz vs 23.8 cm for 8 MHz in conductive human tissue). A detailed discussion of this is written in Section 2.3.4. This means that the power in the high-frequency EM waves will be dissipated as heat rapidly when they enter conductive media. Because some human tissues are conductive, the power receiver location for an EM radiation WPT system may need to be close to the skin surface to maintain the power delivered to load (PDL), which shortens the transfer distance. The power dissipation in conductive media is also the cause of heating problems for human tissues. According to the IEEE Std C95.1™-2005 [144], the maximum regulated power for GHz EM radiation WPT is much lower than near-field EM field WPT. Because the IMPACT sensors' implanted depth can be as much as 20 cm, EM radiation is not suitable for the IMPACT system.

The most outstanding study in the EM radiation WPT in the recent years comes from Poon *et al.* [5][141][142][145]-[149], who basically invented the term "MidField WPT". In [145], a full-wave analysis of EM wave in conductive media has been done with a

consideration of dielectric relaxation loss at high frequencies. It concludes that the optimum frequency for short-range WPT (<1 cm) is at the GHz range, with which the receiver size can be $10^4 \sim 10^6$ smaller and the tissue absorption level is the same at 10 MHz. In [146], a WPT system has been built with an operational frequency of 2 GHz. In the system, the transmitter is optimised based on multi-layer tissue modelling and optimised current distribution on a planar current source. On the receiver side, the power transfer efficiency of a dipole-receiver is compared with the efficiency of a loop-receiver. Poon's analytical result reconfirms that the GHz range is the optimum operational frequency for a short-range transfer distance. It also shows that the optimised transmitter can focus EM power at a small area with greater penetration depth than a circular loop. At the same time, the specific absorption rate (SAR) level is kept under the regulation limit. Moreover, the dipole-receiver outperforms the loop-receiver at an operational frequency beyond 2 GHz. The bi-directional data link has also been developed. In [5], a specially designed pattern metal plate is tested as a transmitter source to power a 2 mm-diameter micro-implant at a transfer distance of around 5 cm. Using a 1.6 GHz optimum frequency, a maximum of 2.1 mW is obtained with the SAR at the regulated limit. With phase adjustment at the input, real-time dynamic focusing can be achieved with the proposed WPT system to address misalignment issues. Because of the deep implantation depth (20 cm) required by the IMPACT system, "MidField WPT" is not suitable for the IMPACT system due to its limited transfer range and transferred power.

With the above discussion, the RF far-field radiation WPT is more suitable for close-to-skin implants, which have a small area limit (<1 cm-diameter) and require a mediate to high amount of power. For mid-field WPT, with the proper design of transmitter antenna, the transfer distance can be extended to a few centimetres. However, the maximum power is still restricted by the lower regulation limit.

1.2.6 Other power supply options

Besides the power supply options discussed in the previous sections, there are other options available for wireless power and data transfer for medical implants. However, all these options have significant drawbacks that make them unsuitable for the application.

(1) Capacitive coupling

Capacitive coupling WPT systems transfer energy using electric fields. In the system, metal plates are normally used as transceivers, like the coils in the magnetic coupling resonance WPT systems. The metal plates in the transmitter and receiver form a capacitor, and electrical energy travels through the gap between the plates in the form

of alternating electric fields or displacement currents [150]. The most crucial drawback of capacitive coupling WPT is its short transfer distance (~1 mm) because of the small absolute value of permittivity of human tissue (an order of 10^{-6} of the absolute value of permeability of human tissue) [151]. Moreover, the human tissue is an unideal lossy dielectric material. According to the displacement current formula ($J = \sigma \mathrm{E}$), the dissipated heat loss is proportional to the electric field strength, which means the PTE is inherently limited by the tissue, and the maximum electric field strength should be kept low to avoid tissue heating problems. Secondly, the transceiver metal plates should have large sizes and be perfectly aligned face-to-face to maintain a high PTE [152][153][154], which is unlikely to achieve for some medical implants. Therefore, the capacitive coupling WPT is unsuitable for WPT for medical implants, especially deep micro-implants.

(2) Environmental power harvesting

Environmental power harvesting for medical implants means that the implanted devices obtain energy without an external specialised power source. Energy mainly comes from the device's environment. Three forms of power harvesting methods are normally used for medical implants: kinetic, thermal effect and fuel cells.

For kinetic energy, the power is obtained mainly from the movement of the body or organs. For kinetic energy from the body movement, the problem is in the unstable power supply. The solution is a large energy storage component in the implants, which is what WPT systems try to avoid. For the movement of organs, the kinetic energy from the heart is the primary choice. In [155], the kinetic energy converter for quartz watches is tested on a dog's heart to supply energy for an implantable cardiac pacemaker. Piezoelectric harvesters are reported in [156] and [157] for the application of medical implants. However, let alone the unmeasured additional burden of energy harvesters on the heart, the heart kinetic energy harvesters are only suitable for implants around the source of kinetic energy (heart). They cannot be used for implants in other parts of the body.

Thermal effect energy is harvested by devices called thermal scavengers, which exploits temperature difference in the body to generate voltage potentials [158]. However, because the temperature in a human body is within a relatively small range ($\pm 1\ ^{\circ}\mathrm{C}$), the power densities of such devices are minimal [159][160].

For fuel cell energy, a similar low power density problem exists. A fuel cell is an electrochemical energy source that converts chemical energy from the reaction of fuels and oxidant into electrical energy with continuous feeding of both fuels and oxidant. For implanted devices, glucose is mostly used as the fuel because of its

constant availability inside the human body. In [161], an implantable fuel cell has been tested in a dog with a 2.2 $\mu W/cm^2$ power density. In [162], a glucose fuel cell is implanted in grapes with a 430 $\mu W/cm^2$ power density. It is obvious that the power density of a glucose fuel cell is directly related to the density of glucose in the fluid. Because of the limited density of fuel reactants in the human body, a low power density can be expected for fuel cells in the human body.

(3) Near-infrared light

Near-infrared light WPT systems transfer energy through optical links. The wavelength of near-infrared light is normally in the range of 600-1300 nm [136]. For implanted devices, light emitter diodes (LEDs) or laser diodes are used as transmitters, and a large area of photodiode arrays are usually used as the receiver to increase the received power [163][164]. The major problem of near-infrared light WPT is the attenuation of optical power at the body tissue. Because of its very short wavelength, the near-infrared light has a minimal skin depth (<1 mm) in conductive media. Therefore, the near-infrared light is only suitable for close-to-skin implants and is inefficient in deep micro-implants.

1.2.7 Options for rectifier in wireless power transfer

In a WPT system, the rectifier (or AC to DC converter) is a vital component because the rectifier's power conversion efficiency (PCE) directly relates to the overall efficiency of the system. It converts the AC power from the receiver coil (for the magnetic coupling resonance WPT) to the DC power for the load.

Conventional rectifiers such as the junction-diode bridge rectifiers (shown in Figure 1.2-5) are not commonly used in a WPT system because of their high forward voltage drop in rectification. To obtain a low dropout voltage, MOSFETs are used to replace junction-diodes because the drain-source voltage drop for on-state MOSFET (0.1 to 0.2 V) is much lower than the voltage-drop at the junction-diode (around 0.7 V). Rectifiers with MOSFETs as rectification components are called switch-mode rectifiers. The basic idea of the operation is that the MOSFET-switches will turn on when the input voltage is higher than the output voltage to allow forward current (from source to load); the MOSFET-switches will turn off when the input voltage is lower than the output voltage to block backward current (from load to source). To achieve this, the design of switch-mode rectifier will focus on the on-off control of MOSFET-switches. The design challenge will be the balance between the precision of on-off control and the power consumption of the control circuit. A higher control precision will require a more complex control circuit, which will consume more power than a low-precision control circuit. In other words, the increase of power consumption due

to higher circuit complexity should be lower than the increase of output power due to more precise control.

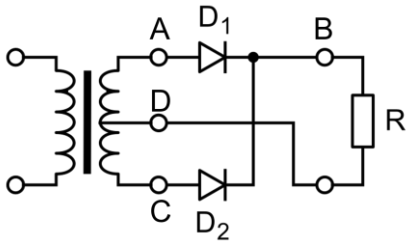

Figure 1.2-5 Conventional junction-diode rectifier

One of the most basic switch-mode rectifiers is the self-synchronous rectifier [165], which utilises a cross-gate structure to avoid latch-up problems. A circuit diagram is shown in Figure 1.2-6. In the circuit, the switches N2 and P1 will turn on when Input-1 is high, VDD will be equal to Input-1 minus voltage drop on P1, and GND will be equal to Input-2 plus voltage drop on N2; when Input-2 is high, N1 and P2 will turn on, and the VDD and GND will equal to the same value as Input-1 is high. The problem of the synchronous circuit is that the on-off time of the switches is controlled by the input voltage, and the on-off time of the switches will not always be at the time when VIN and VOUT cross each other. Therefore, the backward current will be high, which causes a low power efficiency [114]. In fact, in [165], 65% of rectifier efficiency is reported with the load condition unmentioned.

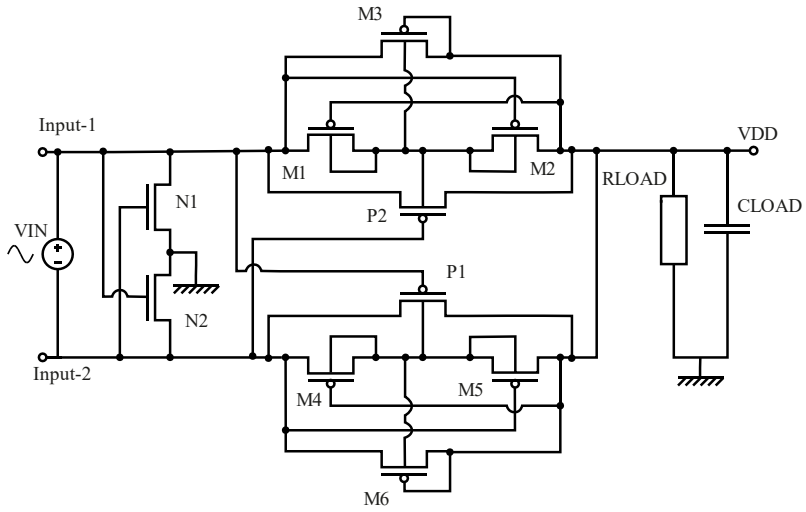

Figure 1.2-6 Circuit diagram of self-synchronous rectifier

Another basic switch-mode rectifier is the bootstrapping rectifier (BSR) [166], which is shown in Figure 1.2-7. Unlike the self-synchronous rectifier, which controls the switch-gate with an AC signal, the BSR controls the gate voltage with DC voltage. A detailed analysis of this circuit will be shown in Section 4.3.

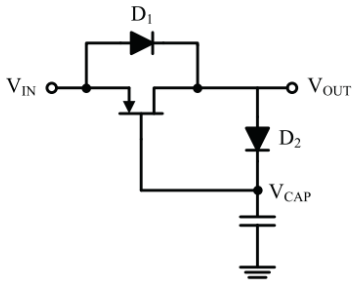

Figure 1.2-7 Circuit diagram of a basic BSR [166]

To improve the precision of switch-gate control in the switch-mode rectifiers, comparator-based rectifiers have been reported [31][167]-[169]. A circuit diagram is shown in Figure 1.2-8. The idea is to directly compare the input voltage and the output voltage using a comparator. When the input voltage is higher than the output voltage, the comparator turns on the switches; when the input voltage is lower than the output voltage, the comparator turns off the switches. In [31], two high-speed comparators are used in a full-wave switch-mode rectifier in a 13.56 MHz wireless power and data transfer system. A rectifier efficiency of 80.2% is achieved with 0.43 V rectifier dropout voltage. In [168], dynamically self-biased comparators are applied, which don't need a constant power supply for operation. A maximum of 79.5% is achieved with a 1.25 V input voltage and a load of 100 Ω to 200 Ω resistor and 20nF capacitor.

There are two problems related to the comparator-based rectifier. The first is the delay between the input and the output of the comparators [114], which will cause the switches to turn on or off slightly (a few μs) later than the cross point of the VIN and VOUT. At high-frequency WPT systems, this delay will become a major limitation of the rectifier efficiency. The second is the power consumption of the comparators. In WPT systems for deep implants, the received power will be very limited (a few mW), which is not enough for the operation of comparators. Therefore, the comparator-based rectifier is only suitable for WPT systems with a high power budget and moderate operational frequency.

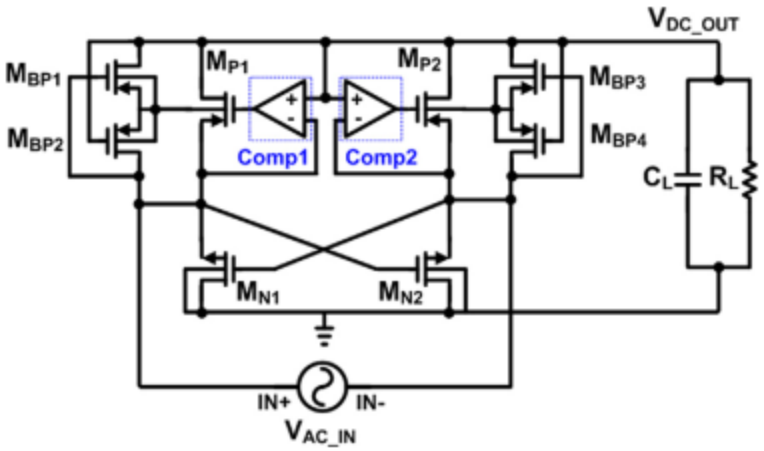

Figure 1.2-8 Comparator-based switch-mode rectifier [168]

In Chapter 4, more analysis is done for the rectifier for implanted WPT systems. A novel dynamic gate-control rectifier for the proposed WPT system is designed based on the BSR.

1.3 Thesis outline

To achieve the aims of the project presented in Section 1.1, wireless power transfer with magnetic coupling resonance was chosen because of its relatively long transfer distance (>10 cm) and low radiation exposure risk compared with EM wave far-field transfer. It also has the advantage over ultrasonic methods of potentially higher power transfer levels. In terms of the data transfer, because the required data rate is much lower than the target operational frequency of the system, the load shift keying (LSK) modulation technique is chosen, so that the power consumption for data transfer can be minimised. Because of the relatively small size of the target receiver (D_{RX}=2 mm) compared with the transfer distance (up to 20 cm), the received power is expected to be very small (a few mW). At these low power levels, the performance of the receiver rectifier, in terms of efficiency, operational power and voltage drop, becomes crucial to the design. To meet this requirement, active switch rectifiers based on the bootstrapping structure are chosen because of their high PCE compared with the junction-diode rectifier and their low power requirements compared with the comparator-based rectifiers.

In this thesis, a system model based on magnetic coupling resonance wireless power transfer (WPT) is built, which directly links the physical parameters of the system to the power delivered to load (PDL). The system model includes a magnetic coupling link model (the transmitter model and the receiver model) and a rectifier model, as shown in Figure 1.2-3. The models are analysed and verified based on calculation results and experimental results. Based on the analysis of the magnetically coupled link between the transmitter and the receiver, an optimum design for the system is reported for a specific operational frequency and transfer distance. The maximum received power in the optimum magnetic link is obtained. Meanwhile, a novel active rectifier with high power conversion efficiency is designed. The optimum magnetic link model is then analysed with the rectifier model to examine the first hypothesis in Section 1.1 that sufficient received power is available to power an implant.

Moreover, with the application of an active rectifier in the receiver, the load shift keying (LSK) modulation scheme is used as an uplink communication method. An analytical model for data transfer sensitivity is built based on the theory of network analyser and reflection coefficient. The application of LSK to the system is analysed to determine whether such a system can give viable communication of information from the implant back to the transmitter to examine the second hypothesis in Section 1.1.

The following chapters are organised as follows:

- In Chapter 2, the theory of the magnetic coupling resonance WPT is discussed and explained. The basic EM laws and related factors and theories that affect the magnetic coupling link from the perspective of the physical structure of the transmitter coil and receiver coil are analysed.
- In Chapter 3, a transmitter model and a receiver model are described and analysed based on the solenoid structure. Optimum designs of transmitter solenoid coils and receiver solenoid coils are presented for a specific operational frequency and transfer distance. Design flows for the optimum transmitter design and receiver design are also reported.
- In Chapter 4, the rectifier for the WPT receiver are discussed. The operation of a bootstrapping rectifier is analysed. Two novel rectifier designs are reported based on the theory of bootstrapping rectifiers. The WPT system performance are discussed and compared with the IMPACT device power requirement based on the optimum magnetic coupling link and the proposed rectifier.
- In Chapter 5, the full WPT system, including the transmitter, the receiver and the rectifier, are discussed. The power delivered to load (PDL) of the full system is calculated at a transfer distance of 20 cm for a 2 mm-diameter receiver coil.
- In Chapter 6, the data uplink based on the proposed WPT system is discussed. The feasibility of an LSK modulation scheme is analysed with the proposed optimum WPT system. The external reader requirement for the data uplink is reported.
- In Chapter 7, a summary of the project is made. The hypotheses mentioned in Section 1.1 are re-examined with a conclusion about the contribution of the project. Future work is discussed.

Chapter 2 Theories for the Magnetic Coupling Resonance Wireless Power Transfer System for deep implanted medical devices

2.1 Introduction

A weakly coupled magnetic resonance wireless power transfer system is a system in which electrical power is transferred wirelessly in the form of a magnetic field; the magnetic field is generated and received by transmitters and receivers which are resonating at the same frequency; the presence of receivers will not affect the resonance of the transmitters and vice versa. A block diagram of the wireless power transfer system is shown in Figure 2.1-1.

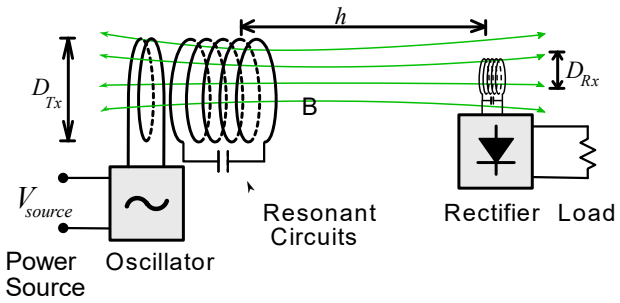

Figure 2.1-1 Block diagram of a basic wireless power transfer system

In the wireless power transfer system for micro-implants, the diameter of implants D_{RX} is within 2 mm while the diameter of transmitter D_{Tx} can be more than 20 cm, with a similar length of separation distance h. Because of the large difference between the size of the transmitter and the size of the receiver as well as the large difference between the transfer distance and the size of the receiver, the coupling coefficient between the transmitter and the receiver is very small. The presence of the receiver will not affect the capacitance and inductance of the transmitter and vice versa. In this case, the system can be treated as a weakly coupled system.

In a weakly coupled system, as the coupling coefficient between the transmitter and the receiver is very low, the presence of the receiver has little effect on the resonance of the transmitter. Therefore, the transmitter and the receiver can be analysed separately, and the overall system efficiency is no longer the figure of merit for analysis. For the transmitter side, the figure of merit (FOM) is the generated magnetic field strength at the surface area where the receiver coil is located. The field strength should be as high as possible under the restriction of the exposure limit of the human

body. As there is no limitation on the sizes and the input power of the devices in the transmitter side, the working efficiency in the transmitter is not a primary consideration. For the receiver side, on the one hand, the receiver coil should have a large effective area for the maximum magnetic flux through the coil in the restricted cross-sectional area; on the other hand, the circuits in the receiver should work with a high efficiency so that the load can receive as much energy as possible.

In the transmitter and the receiver, L-C pairs are used as resonators, of which the resonance frequency is tuned to be the same as the operational frequency. The inductor or a part of the inductor in the L-C pair will be used as the coil that generates the magnetic field for power transfer.

In this section, the basic laws related to wireless power transfer will be discussed, and the resonance of L-C pairs will be analysed using Circuit Theory. The transmitter coil model and receiver coil model will then be analysed separately. Based on the models, the transfer power and system efficiency will be analysed.

2.2 Basic Laws

2.2.1 Biot-Savart Law

Key points of this section

- A loop of current can generate a magnetic field at a distance.
- The strength of the generated magnetic field at a point away from the loop is decided by the value of current I at the loop, the physical structure (shape and size) of the loop and the vector distance between the point and the loop.
- For a circular loop, the direction of magnetic field at the axis of the loop is pointing along the axis.

The following sections 2.2.1 and 2.2.2 refer to the content of *Inductive Wireless Power Transfer for RFID & Embedded Devices: Coil Misalignment Analysis and Design* by Kyriaki Fotopoulou [195], page 40-42, page 80-83.

One of the most fundamental theories behind the magnetic coupling wireless power transfer is that electric currents produce magnetic fields [170]. The relation between the magnetic field and the electric current can be described using the Biot-Savart law, which is expressed as [171]

$$d\boldsymbol{H} = \frac{I}{4\pi}\frac{d\boldsymbol{l} \times \boldsymbol{r}}{r^3} \tag{2.1}$$

It states that for an infinitesimal length of conductor $d\boldsymbol{l}$ with an electric current I, the magnitude of the generated infinitesimal magnetic field at a point $P(x,y,z)$ with a distance r from the infinitesimal conductor is proportional to the magnitude of I and weakens at the 3rd power of the distance r; the direction of the field is perpendicular to the surface where the infinitesimal conductor $d\boldsymbol{l}$ and the displacement vector $\mathbf{r}$ (from the conductor $d\boldsymbol{l}$ and the point $P(x,y,z)$) are located and obeys the right-hand screw rule.

For a finite length closed loop with electric currents, the total magnetic field $\boldsymbol{H}$ can be calculated using the line integral, which can be expressed as [171]

$$\boldsymbol{H} = \frac{I}{4\pi}\oint\frac{d\boldsymbol{l} \times \boldsymbol{r}}{r^3} \tag{2.2}$$

where the path of integration is along the loop.

For a single-turn circular closed loop with a current I, as the loop TX shown in Figure 2.2-1, the magnetic field generated at the point O_{RX} can be calculated as [171]

$$\boldsymbol{H}(\boldsymbol{r}) = \frac{I}{4\pi}\int_0^{2\pi}\frac{d\boldsymbol{l}\times\boldsymbol{r}}{r^3} \tag{2.3}$$

with the origin of the coordinate situated at the centre of the loop TX and the infinitesimal vector $d\boldsymbol{l}$ is on the circumference of the loop.

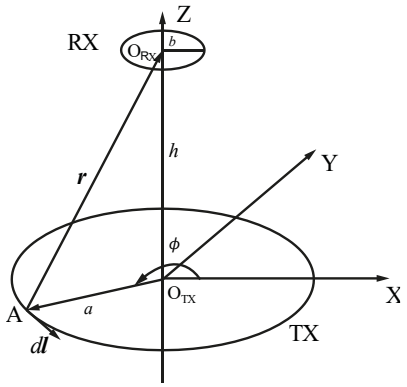

Figure 2.2-1 Coordinate schematic for a single-turn closed loop TX with a radius of a and a current I on it and another loop RX with a radius of b ($b \ll a$) located coaxially with a distance h between them

In order to calculate the magnetic field at O_{RX}, the expression $d\boldsymbol{l}\times\mathbf{r}$ should be calculated first.

From Figure 2.2-1, it shows that

$$\boldsymbol{r} = \boldsymbol{O_{TX}O_{RX}} - \boldsymbol{O_{TX}A} \tag{2.4}$$

where $\boldsymbol{r}$ is the displacement vector from an arbitrary point A on the loop TX to the centre of RX O_{RX}.

As shown in Figure 2.2-1, the vector $\boldsymbol{O_{TX}O_{RX}}$ and $\boldsymbol{O_{TX}A}$ are expressed as

$$\boldsymbol{O_{TX}O_{RX}} = h\vec{\boldsymbol{z}} \tag{2.5}$$

$$\boldsymbol{O_{TX}A} = (a\,cos\phi)\vec{\boldsymbol{x}} + (a\,sin\phi)\vec{\boldsymbol{y}} \tag{2.6}$$

where $\vec{\mathbf{x}}$, $\vec{\mathbf{y}}$ and $\vec{\mathbf{z}}$ are the unit vector in the direction of axis X**,** Y and Z.

Therefore, the vector $\boldsymbol{r}$ can be calculated as

$$\boldsymbol{r} = (-a\,cos\phi)\vec{\boldsymbol{x}} + (-a\,sin\phi)\vec{\boldsymbol{y}} + h\vec{\boldsymbol{z}} \tag{2.7}$$

The magnitude of the vector $\boldsymbol{r}$ is

$$|\boldsymbol{r}| = \sqrt{(a\,cos\phi)^2 + (a\,sin\phi)^2 + h^2} = \sqrt{a^2 + h^2} \tag{2.8}$$

In terms of $d\boldsymbol{l}$, in a cylindrical coordinate, it can be expressed as

$$d\boldsymbol{l} = ad\phi\vec{\boldsymbol{\phi}} \tag{2.9}$$

where $\vec{\boldsymbol{\phi}}$ is the infinitesimal angular vector in the cylindrical coordinate and can be expressed using unit vector $\vec{\mathbf{x}}$ and $\vec{\mathbf{y}}$ as

$$\vec{\boldsymbol{\phi}} = -sin\phi\vec{\boldsymbol{x}} + cos\phi\vec{\boldsymbol{y}} \tag{2.10}$$

Therefore, $d\boldsymbol{l}$ can be expressed as

$$d\boldsymbol{l} = (-a\ sin\phi d\phi)\vec{\boldsymbol{x}} + (a\ cos\phi d\phi)\vec{\boldsymbol{y}} \tag{2.11}$$

The expression $d\boldsymbol{l} \times \mathbf{r}$ thus can be calculated as

$$\begin{aligned} d\boldsymbol{l} \times \boldsymbol{r} &= \begin{vmatrix} \vec{\boldsymbol{x}} & \vec{\boldsymbol{y}} & \vec{\boldsymbol{z}} \\ -a\ sin\phi d\phi & a\ cos\phi d\phi & 0 \\ -a\ cos\phi & -a\ sin\phi & h \end{vmatrix} \\ &= ahcos\phi d\phi\vec{\boldsymbol{x}} + ahsin\phi d\phi\vec{\boldsymbol{y}} + a^2 d\phi\vec{\boldsymbol{z}} \end{aligned} \tag{2.12}$$

By combining (2.3) and (2.12), the magnetic field components at the point O_{RX} in the three directions $\vec{\mathbf{x}}$, $\vec{\mathbf{y}}$, $\vec{\mathbf{z}}$ are

$$H_x = \frac{I}{4\pi}\int_0^{2\pi} \frac{a \cdot h \cdot cos\phi}{(a^2 + h^2)^{\frac{3}{2}}} d\phi \tag{2.13}$$

$$H_y = \frac{I}{4\pi}\int_0^{2\pi} \frac{a \cdot h \cdot sin\phi}{(a^2 + h^2)^{\frac{3}{2}}} d\phi \tag{2.14}$$

$$H_z = \frac{I}{4\pi}\int_0^{2\pi} \frac{a^2}{(a^2 + h^2)^{\frac{3}{2}}} d\phi \tag{2.15}$$

Because the result of integrations $\int_0^{2\pi} \sin\phi d\phi$ and $\int_0^{2\pi} \cos\phi d\phi$ equal to 0, $\mathrm{H_x}$ and $\mathrm{H_y}$ are zero. From (2.15), the magnetic field components in the $\vec{\mathbf{z}}$ direction is

$$H_z = \frac{I}{2\pi}\frac{a^2}{(a^2 + h^2)^{\frac{3}{2}}}\int_0^{\pi} d\phi = \frac{Ia^2}{2(a^2 + h^2)^{\frac{3}{2}}} \tag{2.16}$$

Therefore, the magnetic field generated by a single-turn circular closed loop at a point, which is at the axis of the loop, is

$$\boldsymbol{H} = H_z\vec{\boldsymbol{z}} = \frac{Ia^2}{2(a^2 + h^2)^{\frac{3}{2}}}\vec{\boldsymbol{z}} \tag{2.17}$$

2.2.2 Faraday's Law

Key points of this section

- A changing magnetic field can induce an electric field (and an electric voltage) on a conductive loop.
- The induced voltage on the loop is decided by the strength of the magnetic field at the direction of loop surface, the number of turns, the efficient area of the loop surface and the frequency of the magnetic field.
- In the air, by obtaining the physical structures (shape and size) of the transmitter coil and receiver coil, the interposition between the transmitter coil and receiver coil, as well as the current at the transmitter coil, the open-circuit voltage at the receiver coil can be decided.

Another most fundamental theory behind the magnetic coupling wireless power transfer is the Faraday's law of induction. It describes the relationship between the induced voltage at a conductive loop and the magnetic flux enclosed by the surface of the loop, as shown in Figure 2.2-2, which can be expressed by the Maxwell-Faraday Equation [171],

$$\oint \boldsymbol{E} \cdot d\boldsymbol{l} = -\frac{\partial}{\partial t} \int \boldsymbol{B} \cdot d\boldsymbol{S} \tag{2.18}$$

where $\int \mathbf{B} \cdot \mathrm{d}\mathbf{S}$ is the magnetic flux ψ, and the equation can also be written as [171],

$$\oint \boldsymbol{E} \cdot d\boldsymbol{l} = -\frac{\partial \psi}{\partial t} \tag{2.19}$$

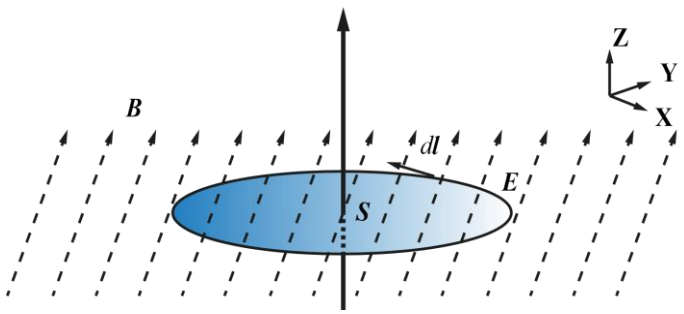

Figure 2.2-2 Closed loop with surface $\boldsymbol{S}$ in a magnetic field with a magnetic flux density $\boldsymbol{B}$, with $\boldsymbol{E}$ being the electromotive force (emf) on the loop and $d\boldsymbol{l}$ being the infinitesimal line component on the loop

The equation states that the line integral of the induced electric field along a closed loop is equal to the change of magnetic flux in time, and the electric field is opposed to the change of the magnetic flux.

The magnetic flux density $\boldsymbol{B}$ can be expressed in the Cartesian coordinate as

$$\boldsymbol{B} = B_x\vec{\boldsymbol{x}} + B_y\vec{\boldsymbol{y}} + B_z\vec{\boldsymbol{z}} \tag{2.20}$$

where B_x, B_y and B_z are the components of the magnetic field in the $\vec{\mathbf{x}}$, $\vec{\mathbf{y}}$, $\vec{\mathbf{z}}$ direction.

If the loop lies on the $\vec{\mathbf{x}}$-$\vec{\mathbf{y}}$ plain, with the surface $\boldsymbol{S}$ facing in the $\vec{\mathbf{z}}$-direction, the infinitesimal surface $d\boldsymbol{S}$ can be expressed as

$$d\boldsymbol{S} = dS\boldsymbol{z} \tag{2.21}$$

Thus, combining (2.20) and (2.21),

$$\boldsymbol{B} \cdot d\boldsymbol{S} = \left(B_x\vec{\boldsymbol{x}} + B_y\vec{\boldsymbol{y}} + B_z\vec{\boldsymbol{z}}\right) \cdot (dS\vec{\boldsymbol{z}}) = B_z dS \tag{2.22}$$

The equation (2.18) thus becomes

$$\oint \boldsymbol{E} \cdot d\boldsymbol{l} = -\frac{\partial}{\partial t}\int B_{\boldsymbol{z}} dS \tag{2.23}$$

In a weakly coupled wireless power transfer system for micro-implants, the receiver coil is much smaller than the transmitter coils. Therefore, the magnetic field generated by the transmitter coil can be approximated as a uniform field on the surface and inside the receiver coil. In this case, the equation (2.23) can be simplified as

$$\oint \boldsymbol{E} \cdot d\boldsymbol{l} = -\frac{d}{dt}B_{\boldsymbol{z}}\int dS = -\frac{d}{dt}B_{\boldsymbol{z}}S_{eff} \tag{2.24}$$

where S_{eff} is the effective area of the receiver coil.

If the receiver coil is a multiturn coil with N turns, and the length of the receiver is effectively small so that the magnetic field flux density B_z can be treated as uniform in all the turns, the total effective area of the receiver coil S_{eff} will thus become

$$S_{eff} = N \cdot A_{eff} \tag{2.25}$$

where A_{eff} is the effective area of each turn of coil.

The equation (2.24) thus becomes

$$\oint \boldsymbol{E} \cdot d\boldsymbol{l} = -N \cdot A_{eff}\frac{dB_{\boldsymbol{z}}}{dt} \tag{2.26}$$

Thus, from (2.26), for a sinusoidal-changing magnetic field, the induced voltage can be written as

$$V_{IND} = -j\omega\mu N H_z A_{eff} \tag{2.27}$$

where

- V_{IND} is the induced voltage on the receiver coil
- N is the number of turns of the receiver coil
- A_{eff} is the effective area of each turn of coil
- H_z is the uniform magnetic field strength component in the $\mathbf{z}$ direction
- ω is the angular frequency of the magnetic field
- μ is the permeability of the core of coil

With this equation, we can calculate the induced voltage on the receiver coil in the weakly coupled wireless power transfer system for micro-implants, when the same-direction magnetic field strength at the receiver coil, the effective area of the coil, the number of turns and the frequency of the field are obtained.

By combining (2.17) and (2.27), the voltage induced at the multiturn receiver coil RX in Figure 2.2-1 can be calculated as

$$V_{IND} = j\omega\mu N A_{eff} \frac{Ia^2}{2(a^2 + h^2)^{\frac{3}{2}}} \tag{2.28}$$

While the shapes and sizes of the primary coil and receiver coil are determined by the design, the current at the primary coil is not yet decided. Moreover, there are other factors affecting the magnetic field during the power transfer. These factors and theories will be discussed in the next section.

2.3 Wireless power transfer theory and important factors

Key points

- To maximise the current through the coil, L-C resonant circuits are used in the transmitter and receiver.
- In an L-C circuit, the AC resistance of the inductor will seriously affect the circuit performance, while the parasitic capacitor of the inductor will limit the operational frequency. The practical model of an inductor is thus analysed.
- The magnetic field will experience attenuation in conduction media, the magnetic field strength will be decreased in human body.

2.3.1 L-C Resonant Circuit Theory

Key points of this section

- An L-C circuit will resonate when the input voltage/current is at a specific frequency, whose value is determined by the values of the inductor and capacitor.
- At resonance, an ideal parallel L-C circuit has infinite impedance and can be regarded as an open circuit; an ideal series L-C circuit has a zero impedance and can be regarded as a short circuit.
- A practical parallel L-C circuit can increase the current through the inductor by a factor of Q. In contrast, a practical series L-C circuit can increase the voltage across the inductor by a factor of Q.

The following section refers to the content of [208], page 21-25.

(1) The voltage and current in a parallel L-C resonant circuit

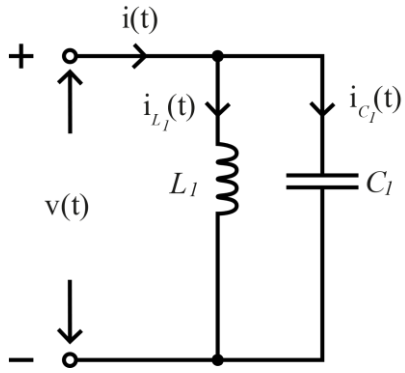

Figure 2.3-1 Parallel L-C circuit

In a parallel L-C circuit, the inductor and the capacitor are connected in parallel, as shown in Figure 2.3-1.

If a sinusoidal voltage $v(t) = V_0 \sin(\omega t + \varphi)$ is input into the circuit, the impedance of inductor L_1 can be noted as $X_{L_1} = j\omega L_1$, and the impedance of capacitor C_1 can be noted as $X_{C_1} = \frac{1}{j\omega C_1}$. The total impedance of the parallel L-C circuit is

$$X_{L\|C} = X_{L_1} \parallel X_{C_1} = \frac{j\omega L_1}{1 - \omega^2 L_1 C_1} \tag{2.29}$$

If $\omega = \omega_R = \frac{1}{\sqrt{L_1 C_1}}$, $X_{L\|C} = \infty$, which means the circuit impedance is infinitely large. The current flowing into the parallel L-C circuit will be 0. Meanwhile, the currents flowing through the inductor and the capacitor are

$$I_{L_1} = \frac{V}{j\omega_R L_1} \tag{2.30}$$

$$i_{L_1}(t) = -\frac{V_0}{\omega_R L_1} cos(\omega_R t + \varphi) = -V_0 \sqrt{\frac{C_1}{L_1}} cos(\omega_R t + \varphi) \tag{2.31}$$

$$I_{C_1} = j\omega_R C_1 V \tag{2.32}$$

$$i_{C_1}(t) = \omega_R C_1 V_0 cos(\omega_R t + \varphi) = V_0 \sqrt{\frac{C_1}{L_1}} cos(\omega_R t + \varphi) \tag{2.33}$$

If $\omega = \omega_R = \frac{1}{\sqrt{L_1 C_1}}$, the currents in the inductor and the capacitor have the same amplitude but opposite phases, which means currents will flow between the inductor and the capacitor, and the energy stored in the inductor or in the capacitor will be exchanged between the two components while the total energy remains constant. The angular frequency ω_R is called the resonance frequency of the parallel L-C circuit.

The instantaneous power of the inductor and the capacitor are

$$p_{L_1}(t) = v(t) i_{L_1}(t) = -\frac{V_0^2}{2} \sqrt{\frac{C_1}{L_1}} sin[2(\omega_R t + \varphi)] \tag{2.34}$$

$$p_{C_1}(t) = v(t) i_{C_1}(t) = \frac{V_0^2}{2} \sqrt{\frac{C_1}{L_1}} sin[2(\omega_R t + \varphi)] \tag{2.35}$$

The total power of the circuit is $p_{L_1}(t) + p_{C_1}(t) = 0$.

The voltage and current responses in the parallel L-C circuit are shown in Figure 2.3-2. The capacitor current and the inductor current are of the same amplitude and in opposite phase, which means electrical power is exchanged between the inductor

and the capacitor. While the capacitor current is 90° ahead of the input voltage in phase, the inductor current is 90° behind the input voltage in phase.

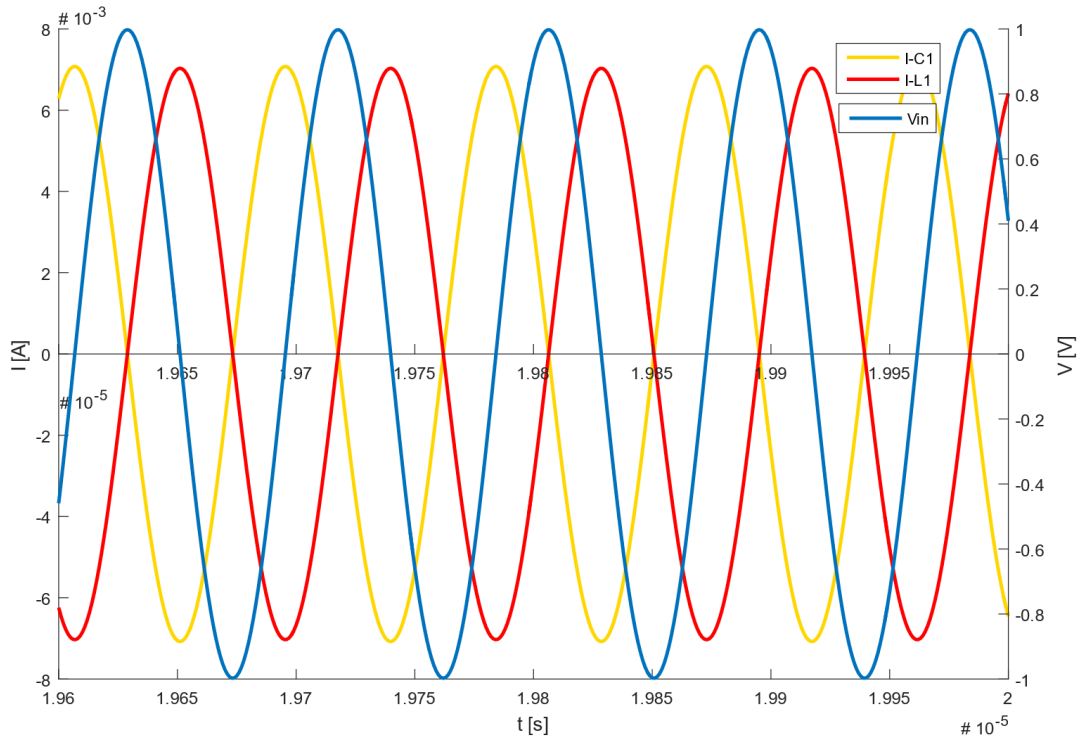

Figure 2.3-2 Voltage, inductor current and capacitor current responses in the parallel L-C circuit for 1 V_{peak} VIN, 100 pF of C_1 and 2 µH of L_1

Instead of a sinusoidal voltage, if a sinusoidal current $i(t) = I_0\sin(\omega_R t + \varphi)$ is input into the circuit, because $X_{L\|C} = \infty$, the amplitude of the voltage $v(t)$ will theoretically be infinity, because $V_0 = I_0 X_{L\|C}$. The amplitude of current flowing between the inductor and the capacitor will theoretically be infinity as well.

In more practical situations, there will be parasitic resistors in parallel with the inductor and the capacitor, as shown in Figure 2.3-3.

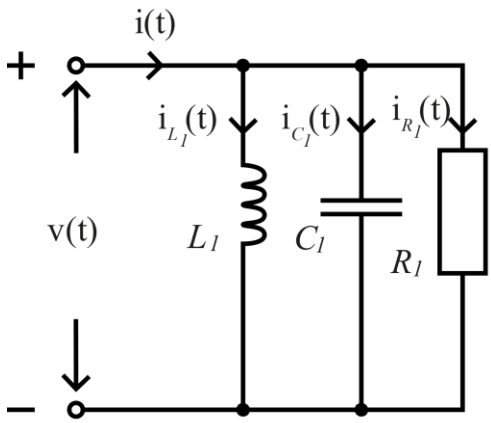

Figure 2.3-3 Parallel L-C circuit with a parallel parasitic resistor

If a sinusoidal voltage $v(t) = V_0 \sin(\omega_R t + \varphi)$ is input into the circuit, because of resonance, the impedance of L_1 and C_1 is still infinite. The total impedance thus becomes

$$X_{L\|C\|R} = X_{L_1} \| X_{C_1} \| R_1 \approx R_1 \tag{2.36}$$

The total current becomes $i(t) = \frac{V_0}{R_1} \sin(\omega_R t + \varphi)$ instead of 0. The instantaneous power of the overall circuit is

$$p(t) = v(t)i(t) = \frac{{V_0}^2}{R_1} sin^2(\omega_R t + \varphi) \tag{2.37}$$

The instantaneous energies stored in the inductor and in the capacitor are the same as the energies in the parallel L-C circuit without the parasitic resistor R_1.

If a sinusoidal current $i(t) = I_0 \sin(\omega_R t + \varphi)$ is input into the circuit, because the total impedance is calculated as

$$X_{L\|C\|R} = X_{L_1} \| X_{C_1} \| R_1 \approx R_1 \tag{2.38}$$

the voltage $v(\mathrm{t})$ becomes $v(t) = I_0 R_1 \sin(\omega_R t + \varphi)$. The currents at the inductor and the capacitor thus becomes

$$i_{L_1}(t) = -\frac{I_0 R_1}{\omega_R L_1} cos(\omega_R t + \varphi) = -I_0 Q cos(\omega_R t + \varphi) \tag{2.39}$$

$$i_{C_1}(t) = I_0 R_1 \omega_R C_1 cos(\omega_R t + \varphi) = I_0 Q cos(\omega_R t + \varphi) \tag{2.40}$$

where Q is the quality factor

$$Q = R_1 \sqrt{\frac{C_1}{L_1}} = \frac{R_1}{\omega_R L_1} = \omega_R R_1 C_1 \tag{2.41}$$

The instantaneous power of the overall circuit is

$$p(t) = v(t)i(t) = \frac{{I_0}^2 R_1}{2} \{1 - cos[2(\omega_R t + \varphi)]\} \tag{2.42}$$

The instantaneous power of the inductor and the capacitor are

$$p_{L_1}(t) = v(t)i_{L_1}(t) = -\frac{{I_0}^2 {R_1}^2}{2} \sqrt{\frac{C_1}{L_1}} sin[2(\omega_R t + \varphi)] \tag{2.43}$$

$$p_{C_1}(t) = v(t)i_{C_1}(t) = \frac{{I_0}^2 {R_1}^2}{2} \sqrt{\frac{C_1}{L_1}} sin[2(\omega_R t + \varphi)] \tag{2.44}$$

The total power of the inductor and the capacitor is $p_{\mathrm{L_1}}(\mathrm{t}) + p_{\mathrm{C_1}}(\mathrm{t}) = 0$.

(2) The voltage and current in a series L-C circuit

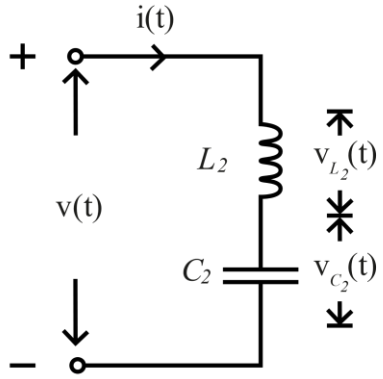

Figure 2.3-4 Series L-C circuit

In a series L-C circuit, the inductor and the capacitor are connected in series, as shown in Figure 2.3-4.

If a sinusoidal current $i(t) = I_0\sin(\omega t + \varphi)$ is input to the circuit, the impedance of the inductor L_2 can be noted as $X_{L_2} = j\omega L_2$, and the impedance of the capacitor C_2 can be noted as $X_{C_2} = \frac{1}{j\omega C_2}$. The total impedance of the parallel L-C circuit is

$$X_{LC} = X_{L_2} + X_{C_2} = j\omega L_2 + \frac{1}{j\omega C_2} = \frac{1-\omega^2 L_2 C_2}{j\omega C_2} \tag{2.45}$$

If $\omega = \omega_R = \frac{1}{\sqrt{L_2 C_2}}$, $X_{LC} = 0$, which means the circuit impedance is 0. The voltage across the series L-C circuit will be 0. Meanwhile, the currents flowing through the inductor and the capacitor are

$$V_{L_2} = j\omega_R L_2 I \tag{2.46}$$

$$v_{L_2}(t) = \omega_R L_2 I_0 cos(\omega_R t + \varphi) = I_0\sqrt{\frac{L_2}{C_2}}cos(\omega_R t + \varphi) \tag{2.47}$$

$$V_{C_2} = \frac{I}{j\omega_R C_2} \tag{2.48}$$

$$v_{C_2}(t) = -\frac{I_0}{\omega_R C_2}cos(\omega_R t + \varphi) = -I_0\sqrt{\frac{L_2}{C_2}}cos(\omega_R t + \varphi) \tag{2.49}$$

If $\omega = \omega_R = \frac{1}{\sqrt{L_2 C_2}}$, the voltages across the inductor and across the capacitor have the same amplitude but opposite phases, and the energy stored in the inductor or in the capacitor will be exchanged between the two components while the total energy remains constant. The angular frequency ω_R is the resonance frequency of the series L-C circuit.

The instantaneous power of the inductor and the capacitor are

$$p_{L_2} = i(t)v_{L_2}(t) = \frac{I_0^2}{2}\sqrt{\frac{L_2}{C_2}}sin[2(\omega_R t + \varphi)] \tag{2.50}$$

$$p_{C_2} = i(t)v_{C_2}(t) = -\frac{I_0^2}{2}\sqrt{\frac{L_2}{C_2}}sin[2(\omega_R t + \varphi)] \tag{2.51}$$

The total power of the circuit is $p_{L_2} + p_{C_2} = 0$.

The voltage and current responses in the series L-C circuit are shown in Figure 2.3-5. The capacitor voltage and the inductor voltage are of the same amplitude and in opposite phase, which means electrical power is exchanged between the inductor and the capacitor. While the inductor voltage is 90° ahead of the input current in phase, the capacitor voltage is 90° behind the input current in phase.

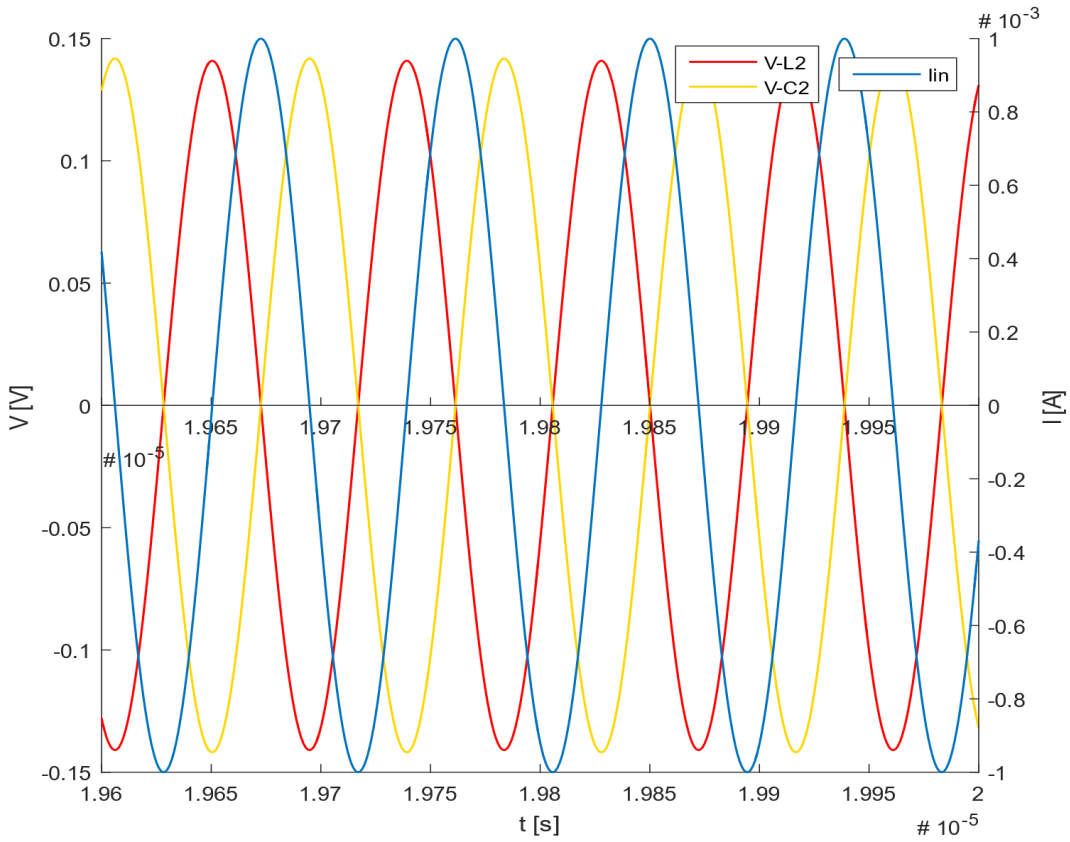

Figure 2.3-5 Voltage, inductor current and capacitor current responses in the series L-C *circuit for 1 mA$_{peak}$ of I_{IN}, 100 pF of C_1 and 2 µH of L_1*

In more practical situations, there will be parasitic resistors in series with the inductor and the capacitor, as shown in Figure 2.3-6.

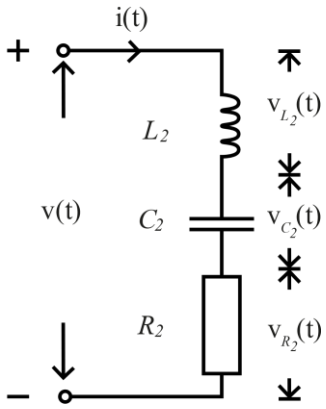

*Figure 2.3-6 S*eries L-C *circuit with a series parasitic resistor*

If a sinusoidal current $i(t) = I_0 \sin(\omega_R t + \varphi)$ is input into the circuit, because of resonance, the impedance of L_2 and C_2 is still 0. The total impedance thus becomes

$$X_{RLC} = X_{LC} + R_2 \approx R_2 \tag{2.52}$$

The total voltage becomes $v(t) = I_0 R_2 \sin(\omega_R t + \varphi)$ instead of 0. The instantaneous power of the overall circuit is

$$p(t) = v(t)i(t) = {I_0}^2 R_2 sin^2(\omega_R t + \varphi) \tag{2.53}$$

The instantaneous energies stored in the inductor and in the capacitor are the same as the energies in the parallel L-C circuit without the parasitic resistor R_1.

If a sinusoidal voltage $v(t) = V_0 \sin(\omega_R t + \varphi)$ is input into the circuit, because the total impedance is calculated as

$$X_{RLC} = X_{LC} + R_2 \approx R_2 \tag{2.54}$$

the current $i(t)$ becomes $i(t) = \frac{V_0}{R_2} \sin(\omega_R t + \varphi)$. The voltages across the inductor and across the capacitor thus becomes

$$v_{L_2}(t) = \frac{\omega_R L_2 V_0}{R_2} cos(\omega_R t + \varphi) = V_0 Q cos(\omega_R t + \varphi) \tag{2.55}$$

$$v_{C_2}(t) = -\frac{V_0}{\omega_R C_2 R_2} cos(\omega_R t + \varphi) = -V_0 Q cos(\omega_R t + \varphi) \tag{2.56}$$

where Q is the quality factor

$$Q = \frac{1}{R_2}\sqrt{\frac{L_2}{C_2}} = \frac{\omega_R L_2}{R_2} = \frac{1}{\omega_R R_2 C_2} \tag{2.57}$$

The instantaneous power of the overall circuit is

$$p(t) = v(t)i(t) = \frac{{V_0}^2}{2R_2}\{1 - cos[2(\omega_R t + \varphi)]\} \quad (2.58)$$

The instantaneous power of the inductor and the capacitor are

$$p_{L_2}(t) = i(t)v_{L_2}(t) = \frac{{V_0}^2}{2R_2^2}\sqrt{\frac{L_2}{C_2}}sin[2(\omega_R t + \varphi)] \quad (2.59)$$

$$p_{C_2}(t) = i(t)v_{C_2}(t) = -\frac{{V_0}^2}{2R_2^2}\sqrt{\frac{L_2}{C_2}}sin[2(\omega_R t + \varphi)] \quad (2.60)$$

The total power of the inductor and the capacitor is $p_{L_2}(\mathrm{t}) + p_{C_2}(\mathrm{t}) = 0$.

With the analytical expression of the L-C resonant coil, the condition and performance of the resonant circuit can be determined. However, to have a thorough understanding of the performance of the wireless power system, the parameters of the circuit (L, R, C) need to be known. More importantly, the factors that determines the parameters of the circuit should be analysed.

2.3.2 Impedance matching

In this section

- Introduction of theory behind impedance matching
- Introduction and analysis of two-element L-C impedance matching network
- Introduction and analysis of three-element L-C impedance matching network

In electronics, impedance matching is a method to match two different terminations through a specific passband [172], so that a minimum reflection of electric power occurs when it passes from one termination to the other [172].

Consider the circuit shown in Figure 2.3-7. The AC voltage source VIN has a source impedance Z_S. The load impedance is Z_L.

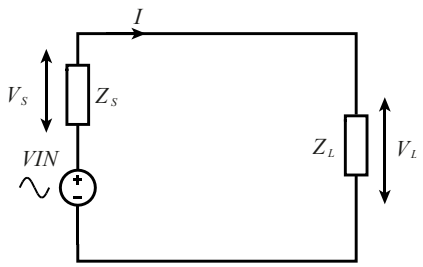

Figure 2.3-7 Simple AC circuit with an AC voltage source VIN, a source impedance Z_S and a load impedance Z_L; the voltage across the source impedance is V_S, and the voltage across the load impedance is Z_L; the current in the circuit is I.

If both the impedances are resistive, which means $Z_S = R_S$ and $Z_L = R_L$,

The real power delivered to the load can be calculated as

$$P_L = \left(\frac{VIN}{R_L + R_S}\right)^2 R_L \tag{2.61}$$

The maximum load power will be obtained when $R_L = R_S$,

$$P_{L-MAX} = \frac{VIN^2}{4R_S} \tag{2.62}$$

If the impedances are complex, when the load impedance is the complex conjugate of the source impedance,

$$Z_L = Z_S^* \tag{2.63}$$

The total impedance in the circuit becomes

$$Z_L + Z_S = Z_S^* + Z_S = 2R_S \tag{2.64}$$

The same maximum load power $P_{L\text{-}MAX}$ will be obtained.

If in practice, the load impedance does not happen to be the complex conjugate of the source impedance (which is always the case), impedance matching circuits will be used.

Because of the operational frequency range (6 to 15 MHz) of the proposed wireless power transfer system, the lumped reactive impedance matching network will be used.

2.3.2.1 Two-element L-section lumped reactive impedance matching network

The lumped reactive impedance matching network is an L-C circuit that converts the load impedance (or the source impedance) to the complex conjugate of the source impedance (or the load impedance).

One of the most commonly used impedance matching networks is the L-section circuit [172][173]. There are two kinds of L-section circuits, the normal L-section circuit (shown in Figure 2.3-8), and the reverse L-section circuit (shown in Figure 2.3-9). The normal L-section circuit is applied when the impedance at the input terminal of the circuit is higher than the impedance at the output terminal of the circuit, while the reverse L-section circuit is applied at the opposite condition.

(1) Normal L-section

In Figure 2.3-8, the impedance $Z_1 = jX_1$ and $Z_2 = jX_2$ forms the normal L-section circuit. The source impedance R_S is assumed to be higher than the load impedance R_L.

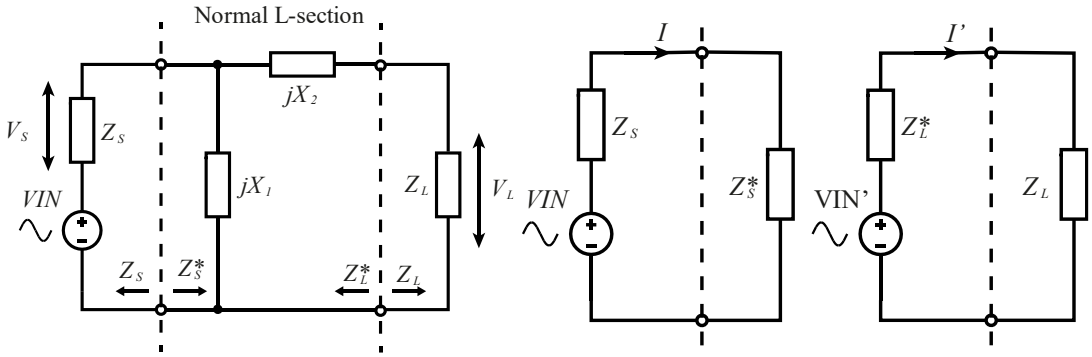

Figure 2.3-8 ($R_S \geq R_L$) normal L-section impedance matching circuit (left), which consists of jX_1 and jX_2. VIN is the voltage source, Z_S is the source impedance (Z_S the complex conjugate), Z_L is the load impedance (Z_L* the complex conjugate). Equivalent circuit from the voltage source side (middle), and the equivalent circuit from the load impedance side (right).*

In order to match the impedances between the source and the load, there are two conditions to meet. Firstly, the total impedance of the impedance matching circuit and the load should be equal to the complex conjugate of the source impedance, which makes the equivalent circuit in the bottom left of Figure 2.3-8; secondly, the total impedance of the impedance matching circuit and the source should be equal to the complex conjugate of the load impedance, which makes the equivalent circuit in the bottom right of Figure 2.3-8.

Therefore,

$$Z_S^* = \frac{Z_1(Z_2 + Z_L)}{Z_1 + Z_2 + Z_L} \tag{2.65}$$

$$Z_L^* = Z_2 + \frac{Z_S Z_1}{Z_1 + Z_S} \tag{2.66}$$

According to Thevenin's theorem, the equivalent voltage source at the bottom right of Figure 2.3-8 can be calculated as

$$VIN' = \frac{Z_1}{Z_1 + Z_S} VIN \tag{2.67}$$

If both the source impedance and the load impedance are complex values,

$$Z_S = R_S + jX_S \tag{2.68}$$

$$Z_L = R_L + jX_L \tag{2.69}$$

As

$$Z_1 = jX_1 \tag{2.70}$$

$$Z_2 = jX_2 \tag{2.71}$$

by combining (2.65) (2.66) (2.70) and (2.71) [172],

$$X_1 = \frac{X_S \pm R_S Q}{\frac{R_S}{R_L} - 1} \tag{2.72}$$

$$X_2 = -(X_L \pm R_L Q) \tag{2.73}$$

$$Q = \sqrt{\frac{R_S}{R_L} - 1 + \frac{X_S^2}{R_S R_L}} \tag{2.74}$$

If both impedances are resistive,

$$X_1 = \frac{\pm R_S}{Q} \tag{2.75}$$

$$X_2 = \mp R_L Q \tag{2.76}$$

$$Q = \sqrt{\frac{R_S}{R_L} - 1} \tag{2.77}$$

(2) Reverse L-section

In Figure 2.3-9, the impedance $Z_1 = jX_1$ and $Z_2 = jX_2$ forms the reverse L-section circuit. The source impedance R_S is assumed to be smaller than the load impedance R_L.

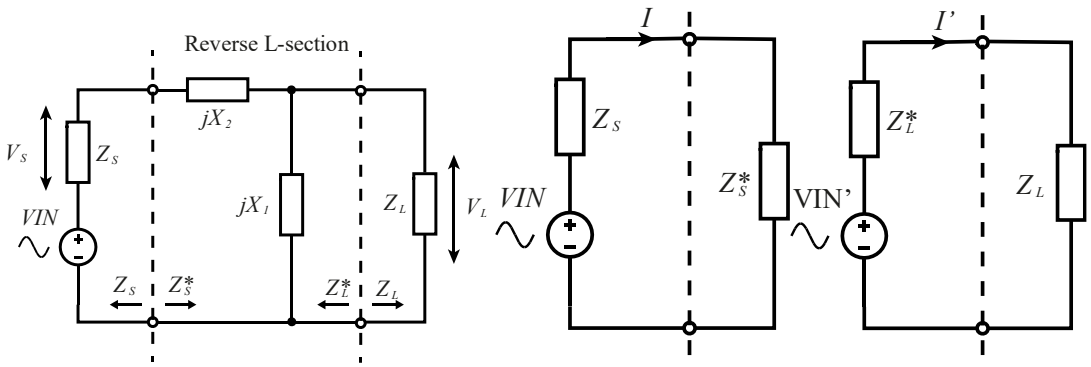

Figure 2.3-9 ($R_L \geq R_S$) reverse L-section impedance matching circuit (left), which consists of jX_1 and jX_2. VIN is the voltage source, Z_S is the source impedance (Z_S the complex conjugate), Z_L is the load impedance (Z_L* the complex conjugate). Equivalent circuit from the voltage source side (middle), and the equivalent circuit from the load impedance size (right).*

The same impedance conditions as the normal L-section are met in the reverse L-section circuit, which gives

$$Z_S^* = Z_2 + \frac{Z_L Z_1}{Z_1 + Z_L} \tag{2.78}$$

$$Z_L^* = \frac{Z_1(Z_2 + Z_S)}{Z_1 + Z_2 + Z_S} \tag{2.79}$$

According to Thevenin's theorem, the equivalent voltage source at the bottom right of Figure 2.3-9 can be calculated as

$$VIN' = \frac{Z_1}{Z_1+Z_2+Z_S} VIN \tag{2.80}$$

If both the source impedance and the load impedance are complex,

$$Z_S = R_S + jX_S \tag{2.81}$$

$$Z_L = R_L + jX_L \tag{2.82}$$

As

$$Z_1 = jX_1 \tag{2.83}$$

$$Z_2 = jX_2 \tag{2.84}$$

by combining (2.78), (2.79), (2.81) and (2.82) [172],

$$X_1 = \frac{X_L \pm R_L Q}{\frac{R_L}{R_S} - 1} \tag{2.85}$$

$$X_2 = -(X_S \pm R_S Q) \tag{2.86}$$

$$Q = \sqrt{\frac{R_L}{R_S} - 1 + \frac{X_L^2}{R_S R_L}} \tag{2.87}$$

If both impedances are resistive,

$$X_1 = \frac{\pm R_L}{Q} \tag{2.88}$$

$$X_2 = \mp R_S Q \tag{2.89}$$

$$Q = \sqrt{\frac{R_L}{R_S} - 1} \tag{2.90}$$

It should be noted that the plus-minus sign in the expressions means that the impedance Z_1 or Z_2 can be either an inductor or capacitor, but if one of them is determined, the other one should be the opposite type [172]. If the series element Z_2 is an inductor, it creates a low-pass topology; when the series element Z_2 is a capacitor, it creates a high-pass topology [173].

The L-section lumped reactive impedance matching network will be able to match any load impedance to any source impedance. However, the disadvantage of this network is that its bandwidth and Q-factor are determined by the source and load impedances, which are already fixed. To improve this, one more impedance element Z_3 are added

into the matching circuit, which makes the π-section and T-section lumped reactive impedance matching network.

2.3.2.2 Three-element lumped reactive impedance matching network

Compared with the two-element matching networks, the three-element circuits can gain extra freedom for bandwidth control and flexibility for component values. The most commonly used three-element circuits are π-section and T-section circuits.

The three-element π-section and T-section circuits will be able to perform impedance matching between two terminals without judging which terminal impedance is higher. They will also be able to control the bandwidth of the matching circuit by freely increasing or decreasing the Q-factor, which is essential in a magnetic resonance wireless power transfer system because a high Q-factor is desired to improve power efficiency at the operational efficiency.

(1) π-section

The π-section circuit is shown in Figure 2.3-10, in which $Z_1 = jX_1$, $Z_2 = jX_2$ and $Z_3 = jX_3$ are the elements of the circuit. It can be seen as two L-section circuits that are "back to back" to each other [172], which is shown in the top of Figure 2.3-11. Here, the impedance Z_3 splits into the impedances Z_4 and Z_5. A virtual impedance level Z is introduced between the two L-section circuits. On the left L-section and the source, the equivalent impedance can be calculated as Z* (an equivalent circuit is shown in the bottom left in Figure 2.3-11), while on the right L-section and the load, the equivalent impedance can be calculated as Z (an equivalent circuit is shown in the bottom right in Figure 2.3-11). Therefore, the two sections are matched together. The value of Z is chosen in consideration of the bandwidth of the matching circuit.

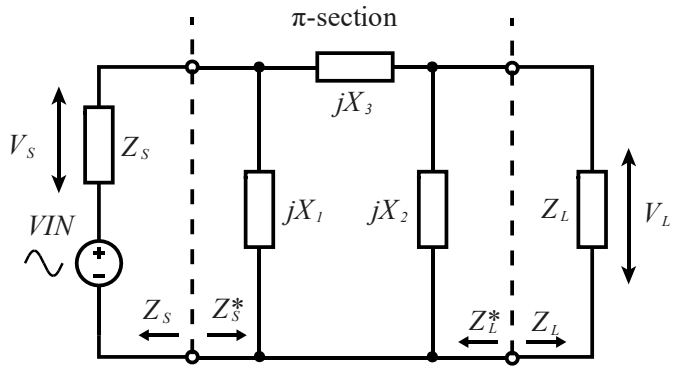

Figure 2.3-10 π-section impedance matching circuit, which consists of jX_1, jX_2 and jX_3. VIN is the voltage source, Z_S is the source impedance (Z_S the complex conjugate), Z_L is the load impedance (Z_L* the complex conjugate).*

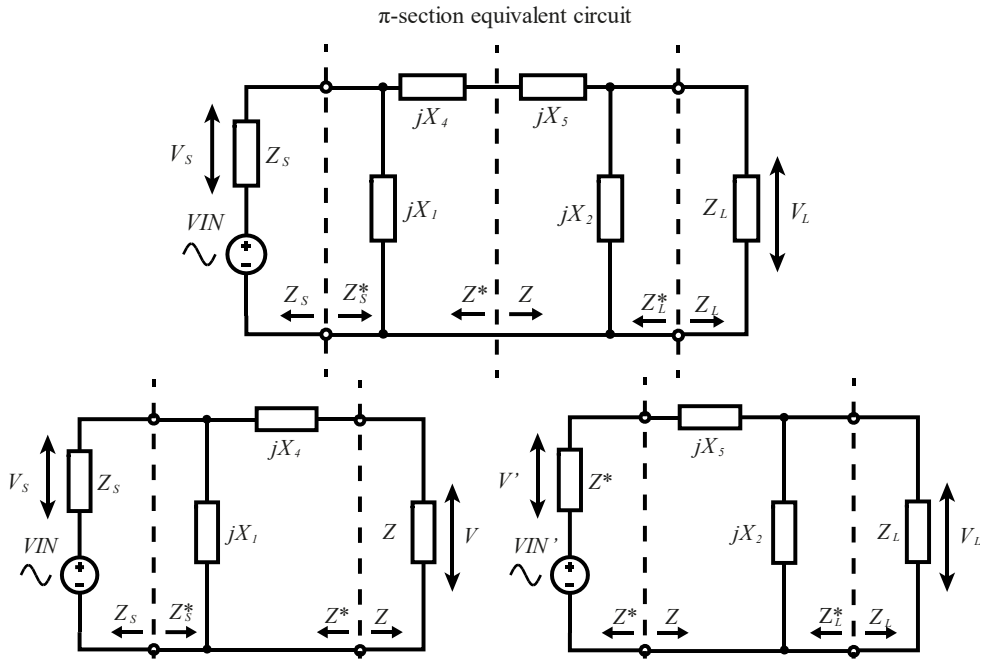

Figure 2.3-11 Equivalent circuits of the π-section impedance matching circuit; in the top one, jX_3 splits into jX_4 and jX_5, and a virtural impedance Z can be assumed to exist between them; in the bottom left, the equivalent circuit is between the voltage source and the virtural impedance Z; in the bottom right, the equivalent is between the virtural impedance Z and the load impedance.

In Figure 2.3-11, the source and the left L-section form a normal L-section circuit, with the impedances having the following relations [172],

$$Z^* = Z_4 + \frac{Z_S Z_1}{Z_1 + Z_S} \tag{2.91}$$

$$Z_S^* = \frac{Z_1(Z_4 + Z)}{Z_1 + Z_4 + Z} \tag{2.92}$$

The right L-section and the load form a reverse L-section circuit, with the impedances having the following relations [172],

$$Z = Z_5 + \frac{Z_L Z_2}{Z_2 + Z_L} \tag{2.93}$$

$$Z_L^* = \frac{Z_2(Z_5 + Z)}{Z_5 + Z_2 + Z_S} \tag{2.94}$$

With these four equations, the value of Z_1, Z_2, Z_4 and Z_5 can be calculated given the value of Z_S, Z_L and Z. It should be noted that the real component of virtual impedance $\mathrm{R} = \mathrm{Re(Z)}$ should be chosen to be smaller than or equal to both R_S and R_L ($R \leq \min(R_S, R_L)$), because the virtual impedance is at the lower impedance side of both split L-sections.

The impedance Z_3 can then be calculated as

$$Z_3 = Z_4 + Z_5 \tag{2.95}$$

The equivalent voltage source in the right L-section can be calculated as

$$VIN' = \frac{Z_1}{Z_1 + Z_S} VIN \tag{2.96}$$

The Q-factor of the π-section will be the higher one of the Q-factors from the left normal L-section and the right reverse L-section.

The equivalent circuit for the right L-section and the load in Figure 2.3-11 can be further simplified and transformed into the circuit in Figure 2.3-12, which is the equivalent circuit from the load impedance side.

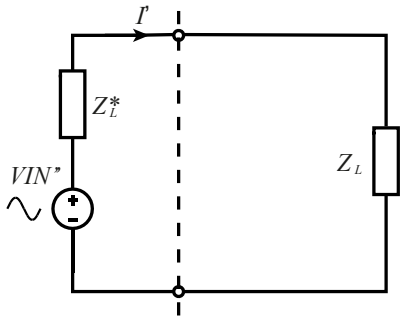

Figure 2.3-12 Equivalent circuit of the π-section impedance matching circuit from the load impedance side

In Figure 2.3-12, the source impedance is the complex conjugate of the load impedance, and the equivalent source voltage can be calculated as

$$VIN' = \frac{Z_2}{Z^* + Z_2 + Z_5} \frac{Z_1}{Z_1 + Z_S} VIN \tag{2.97}$$

(2) T-section

The T-section circuit is shown in Figure 2.3-13, in which $Z_1 = jX_1$, $Z_2 = jX_2$ and $Z_3 = jX_3$ are the elements of the circuit. Similar to the π-section, the T-section circuit can be seen as two reverse L-section circuits that are "back to back" to each other [172], which is shown in the top in Figure 2.3-14. Here, the impedance Z_3 splits into the impedances Z_4 and Z_5. A virtual impedance level Z is introduced between the two L-section circuits. On the left L-section and the source, the equivalent impedance can be calculated as Z^* (an equivalent circuit is shown in the bottom left in Figure 2.3-14), while on the right L-section and the load, the equivalent impedance can be calculated as Z (an equivalent circuit is shown in the bottom right in Figure 2.3-14). Therefore, the two sections are matched together. The value of Z is chosen in the consideration of the bandwidth of the matching circuit.

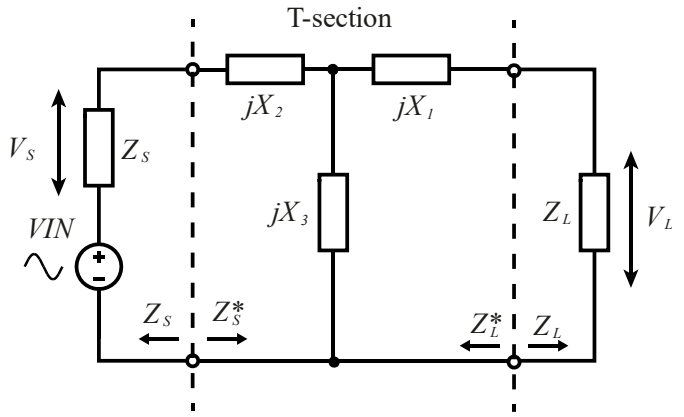

Figure 2.3-13 T-section impedance matching circuit, which consists of jX_1, jX_2 and jX_3. VIN is the voltage source, Z_S is the source impedance (Z_S the complex conjugate), Z_L is the load impedance (Z_L* the complex conjugate).*

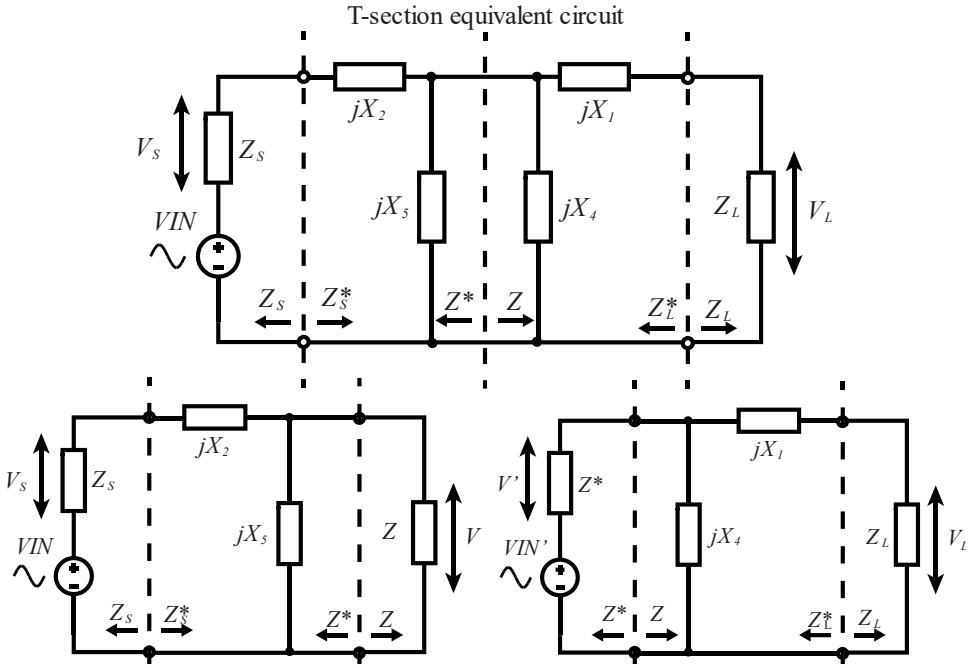

Figure 2.3-14 Equivalent circuits of the T-section impedance matching circuit; in the top one, jX_3 splits into jX_4 and jX_5, and a virtural impedance Z can be assumed to exist between them; in the bottom left, the equivalent circuit is between the voltage source and the virtural impedance Z; in the bottom right, the equivalent is between the virtural impedance Z and the load impedance.

In Figure 2.3-14, the source and the left L-section form a reverse L-section circuit, with the impedances having the following relations [172],

$$Z^* = \frac{Z_5(Z_S + Z_2)}{Z_5 + Z_2 + Z_S} \tag{2.98}$$

$$Z_S^* = Z_2 + \frac{Z_5 Z}{Z_5 + Z} \tag{2.99}$$

The right L-section and the load form a normal L-section circuit, with the impedances having the following relations [172],

$$Z = \frac{Z_4(Z_1 + Z_L)}{Z_4 + Z_1 + Z_L} \tag{2.100}$$

$$Z_L^* = Z_1 + \frac{Z^* Z_4}{Z_4 + Z^*} \tag{2.101}$$

With these four equations, the value of Z_1, Z_2, Z_4 and Z_5 can be calculated given the value of Z_S, Z_L and Z. It should be noted that the real component of virtual impedance $\mathrm{R} = \mathrm{Re(Z)}$ should be chosen to be higher than or equal to both R_S and R_L ($R \geq \max(R_S, R_L)$), because the virtual impedance is at the higher impedance side of both split L-sections.

The impedance Z_3 can then be calculated as

$$Z_3 = Z_4 \parallel Z_5 \tag{2.102}$$

The equivalent voltage source in the right L-section can be calculated as

$$VIN' = \frac{Z_5}{Z_S + Z_2 + Z_5} VIN \tag{2.103}$$

The Q-factor of the T-section will be the higher one of the Q-factors from the left reverse L-section and the right normal L-section.

The equivalent circuit for the right L-section and the load in Figure 2.3-14 can be further simplified and transformed into the circuit in Figure 2.3-15, which is the equivalent circuit from the load impedance side.

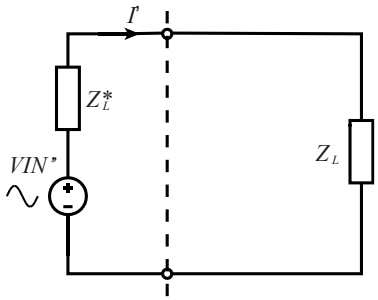

Figure 2.3-15 Equivalent circuit of the T-section impedance matching circuit from the load impedance side

In Figure 2.3-15, the source impedance is the complex conjugate of the load impedance, and the equivalent source voltage can be calculated as

$$VIN'' = \frac{Z_5}{Z_S + Z_2 + Z_5} \frac{Z_4}{Z^* + Z_4} VIN \tag{2.104}$$

(3) Flexible three-element matching circuits

Based on the two-element L-section matching circuit, an extra element (impedance) can be used without obeying the forms of π-section and T-section circuits, especially

at circuits where only one terminal has imaginary parts. An example of load impedance is shown in Figure 2.3-16.

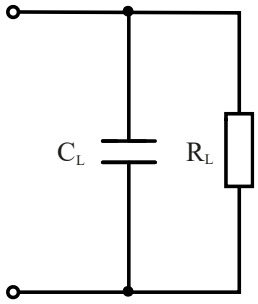

Figure 2.3-16 Load impedance with capacitance C_L

There will be three options [173]:

- Absorb the imaginary parts into the matching network
- Resonate the imaginary parts
- Absorb some of the imaginary parts into the matching network and resonate the remaining imaginary parts

When the imaginary parts of the termination impedance are smaller than the required impedance of the matching network, it can either be absorbed into the matching network with additional impedances (as in the left of Figure 2.3-17) or resonate with an extra element of opposite type (as in the right of Figure 2.3-17).

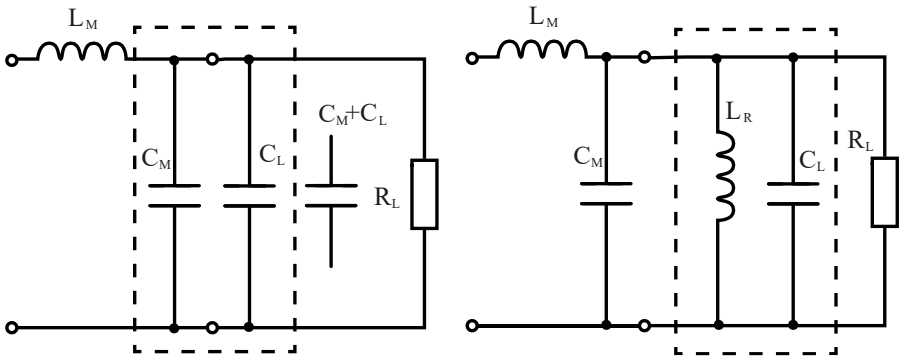

Figure 2.3-17 Reverse L-section matching circuit with a small capacitve load; (left) the load capacitance C_L is absorbed into the matching circuit, and the total capacitance C_M+C_L makes the capacitor of the reverse L-section; (right) the load capacitance C_L resonates with the add-on inductor L_R, the reverse L-section directly matches the leftover load resistance R_L

When the imaginary parts are larger than the required impedance of the matching network, it can either be partly absorbed into the matching network with the remaining parts resonated with an extra element of opposite type (as shown in the left of Figure 2.3-18) or resonate fully with an extra element of opposite type (as shown in the right of Figure 2.3-18).

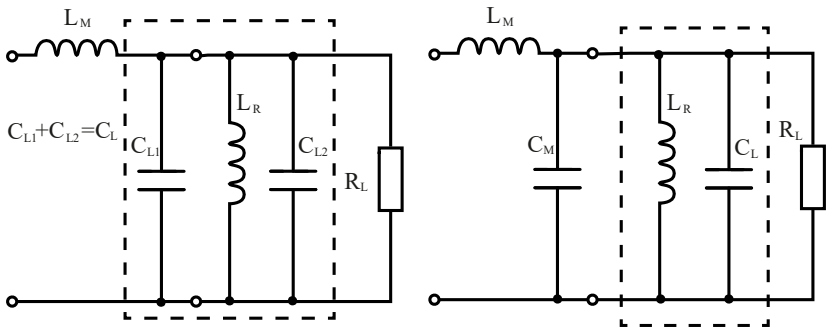

Figure 2.3-18 Reverse L-section matching circuit with a large capacitve load; (left) a part C_{L1} of the load capacitance C_L is absorbed into the matching circuit, and the remaining capacitance C_{L2} resonate with the add-on inductor L_R; (right) the load capacitance C_L resonates with the add-on inductor L_R, the reverse L-section directly matches the leftover load resistance R_L

It should be noted that the options with resonance will reduce the bandwidth, and the more reactance used to resonate, the narrower the frequency response will become [173].

2.3.3 Inductor models and factors

Forward look – next steps

- Formulas to predict solenoid coil capacitance will be introduced, and the relationships between the coil capacitance and the number of turns and the gap interval will be discussed.
- Formulas to predict the free solenoid coil self-resonant frequency (SRF) will be introduced, and the relationships between the SRF and the number of turns and the gap interval will be discussed.
- Formulas to predict the solenoid coil AC resistance will be introduced, and the relations between the coil AC resistance and the number of turns and the gap interval will be discussed.
- Formulas to predict the magnetic field distortion in media will be introduced.

Although the coil in the wireless power transfer system is always represented by an inductor L, it is actually much more complicated. A practical equivalent lumped-circuit model of a solenoid coil working in a frequency well below of its self-resonant frequency (SRF) can be shown as Figure 2.3-19.

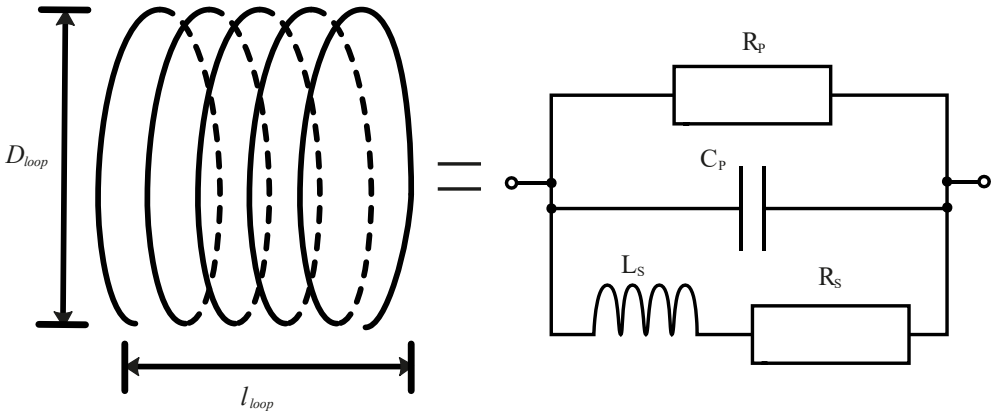

Figure 2.3-19 Complete lumped-circuit model of a coil [174], where D_{loop} is the diameter of the coil and l_{loop} is the length of the coil

There are four components in the complete lumped-circuit model. They are

- The self-inductance L_s of the coil
- The series resistance R_s of the coil which is from heat loss
- The self-capacitance C_p of the coil with additional parasitic capacitance
- The parallel resistance R_p of the coil which is from magnetic loss with additional parasitic resistance

The self-inductance of the coil is determined by the structure of the coil and the existence of a magnetic core. The series resistance R_s of the coil is from the ohmic heat loss, which is dependent on the structure of the coil as well as the frequency of the current passing through the coil. The self-capacitance C_p of the coil is determined by the structure of the coil and the dielectric around the coil. Moreover, parasitic capacitance exists between the coil and the environment. The parallel resistance R_p is from the ferrite core loss. For air-core solenoid coils, there is no magnetic loss, so the parallel resistance R_p can be neglected.

In this thesis, air-core and ferrite-core solenoid coils will be focused. The effect of self-capacitance C_p and the series resistance R_s will be discussed further in detail.

2.3.3.1 Self-capacitance of a solenoid coil

The existence of self-capacitance in the inductor has two major influences on the coil design for wireless power transfer.

a) Firstly, to create a parallel resonant circuit at a certain frequency, the total capacitance should be the value of the additional external capacitor and the value of self-capacitance. Ignoring the self-capacitance will create a lower resonance frequency.
b) Secondly, the self-capacitance, together with the self-inductance, will create resonance themselves at a set of SRFs. As the self-capacitance of the inductor is easily affected by external environments, for the

robustness of the wireless power transfer system, the resonance frequency of the L-C circuits in the wireless power transfer system should be well below the SRF of the coils in the system.

As solenoid coils are used in the proposed wireless power transfer system, the self-capacitance and SRF of a solenoid coil will be calculated.

To calculate the self-capacitance of a solenoid coil, David W. Knight [174], views the coil as a short-circuited transmission line, with which the lowest resonance of the coil occurs when the conductor length of coil equals to half wavelength ($\frac{\lambda}{2}$). At this conductor length, EM wave propagates from one end of the coil to the other end and returns without cancellation, creating a standing wave on the coil and a high output impedance at the terminal. Based on this phenomenon and other researches [175]-[179], David W. Knight points out that the SRF of a solenoid coil is related to the phase velocity factor of the coil, and thus a derivation of phase velocity will lead to the derivation of SRF, which will then lead to the derivation of self-capacitance.

Based on Ollendorff's work [180], on the calculation of phase velocity factor and Medhurst's data for coil self-capacitance (The plots of Ollendorff's formula of velocity factor and Medhust's data can be seen in Appendix A2.), David W. Knight proposed an empirical formula to calculate the solenoid coil self-capacitance with the input argument being the length/diameter (l/D), internal relative permittivity ε_i and external relative permittivity ε_x. This formula is referred to as the Time-Delay Induced Electric-Field (TDE) formula [174],

$$C_L = \frac{4\varepsilon_0\varepsilon_x}{\pi} l_{loop}\left[1+\left(\frac{1}{k_L}-1\right)\frac{1+\frac{\varepsilon_i}{\varepsilon_x}}{2}\right]+\frac{2\varepsilon_0(\varepsilon_x+\varepsilon_i)D_{loop}}{ln\left(1+\frac{\pi^2 l_{loop}}{D_{loop}}\right)} \tag{2.105}$$

where D_{loop} is the diameter of the coil and l_{loop} is the length of the coil as shown in Figure 2.3-19.

k_L is the Nagaoka's coefficient.

$$k_L = Z_k\left[log\left(1+\frac{1}{Z_k}\right)+\frac{1}{-10.632+\frac{3.347}{k_{loop}}+\frac{1.764}{k_{loop}^2}+\frac{-0.47}{\left(0.755+k_{loop}\right)^{1.44}}}\right] \tag{2.106}$$

and

$$Z_k = \frac{2}{\pi k_{loop}} \tag{2.107}$$

$$k_{loop} = \frac{D_{loop}}{l_{loop}} \tag{2.108}$$

$$l_{loop} = Nd_{wire} + (N-1)p \tag{2.109}$$

The formula has two parts.

On part is the transmission-line delay capacitance C_T, which is to model the propagation-delay of EM wave travelling along the conductor of the coil. The capacitance will increase as the coil-length/diameter ratio increases.

$$C_T = \frac{4\varepsilon_0\varepsilon_x}{\pi} l_{loop} \left[1 + \left(\frac{1}{k_L} - 1 \right) \frac{1 + \frac{\varepsilon_i}{\varepsilon_x}}{2} \right] \tag{2.110}$$

The other part is the axial induced-field capacitance C_E, which is to model the induced electric field by the time-varying magnetic field within the coil. The capacitance will decrease as the coil-length/diameter ratio increases.

$$C_E = \frac{2\varepsilon_0(\varepsilon_x + \varepsilon_i)D_{loop}}{ln\left(1 + \frac{\pi^2 l_{loop}}{D_{loop}}\right)} \tag{2.111}$$

In terms of application, the TDE formula is able to have an accurate simulation of self-capacitance for thin-insulated solenoid coils connected in circuits with formers with uniform composition.

Because in a wireless power transfer system, the number of turns and the gap interval, instead of the loop length, are the main variables. The effect of changes in turn number and gap interval on the capacitance is of more interest (As will be discussed in Section 3.2.2, the coil diameter is mainly determined by the transfer distance for maximum magnetic field strength. It is difficult to adjust coil diameter for SRF).

An example of the self-capacitance against the number of coil turns N and against the gap interval p are shown in Figure 2.3-20 and Figure 2.3-21. The parameters of the coil in the example is following the parameters of the coil in the writer's experiment setup in Section 3.2.4.

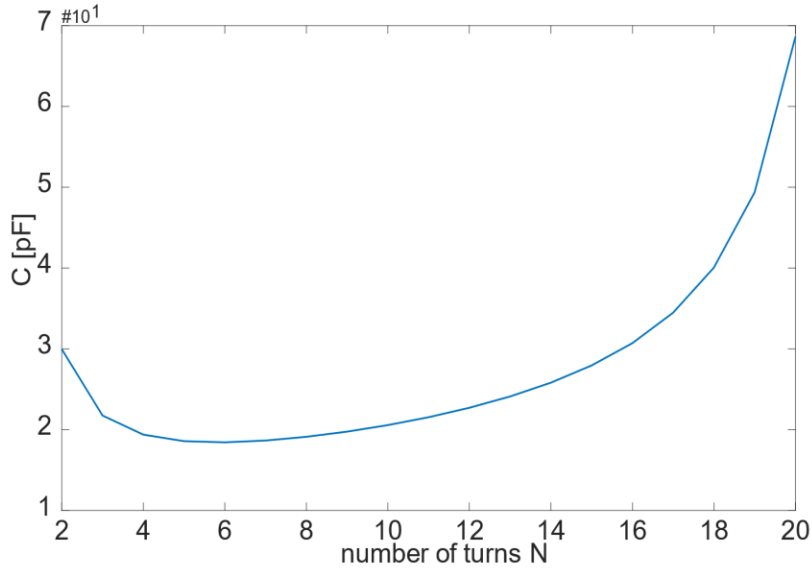

Figure 2.3-20 Calculated self-capacitance against number of coil turns N with diameter of coil D_{loop} = 20 cm, gap interval p = 1.2 cm, internal relative permittivity ε_i = 2.7 (Acrylic) and external relative permittivity = 1 (air)

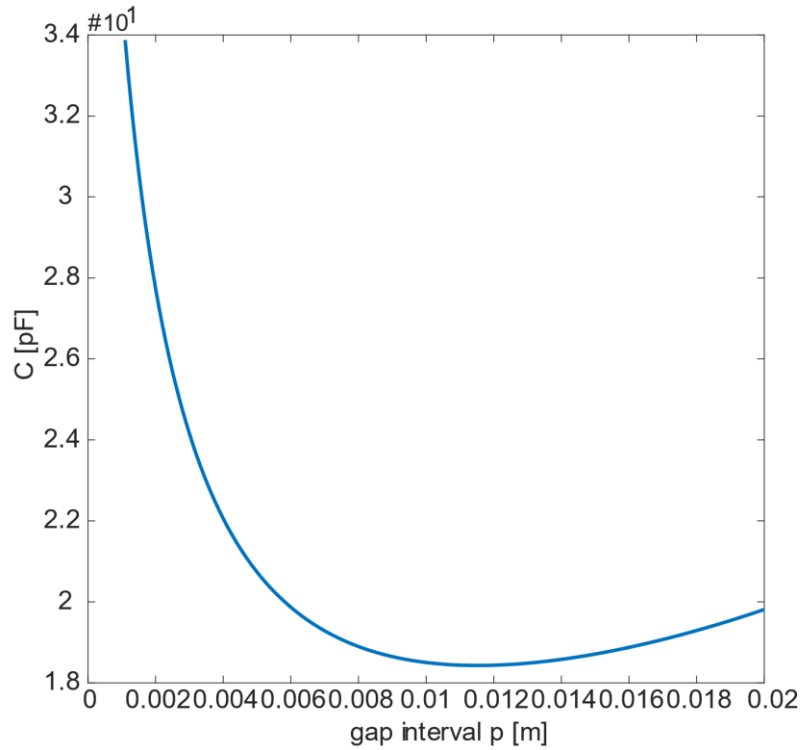

Figure 2.3-21 Self-capacitance against the gap interval p with diameter of coil D_{loop}=20 cm, number of coil turns N = 6, internal relative permittivity ε_i = 2.7 (Acrylic) and external relative permittivity ε_x = 1 (air)

As shown, the capacitance drops from N=2, reaching the bottom at about N=5, then increases exponentially as the N increases. For coil turns less than 10, the capacitance is less than 30 pF. The higher capacitance from N=2 to N=4 is because of the higher axial induced-field component C_E at shorter coil lengths. As the N increases, the coil becomes longer, C_E decreases, and the transmission-line delay capacitance C_T increases as the main contribution of self-capacitance of the coil.

For the gap interval p, as p increases from p=1 mm, the coil capacitance decreases and reaches the bottom when $p=11$ mm. The capacitance increases as the p continues to increase after p=11 mm. Although the decrease of coil capacitance when p is between 1mm and 11mm gives an impression that the electric field exists between adjacent coil turns, the fact is that there is no inter-turn capacitance for solenoid coils. For solenoid coils connected in circuits, the electric field is either in the helical direction along the conductor or the axial direction inside the coil [174]. The decrease of coil capacitance is only owing to the decrease of axial induced-field capacitance C_T as the gap interval increases.

It should be noted that, because of the extra length of wire at the terminals of the coil to connect to the external components, the actual coil is a solenoid shape with wire tails, which will partly distort the electric field in the coil. Thus, the actual capacitance will not be exactly the same as the calculation result. However, the calculation result will be able to provide an estimation of actual capacitance.

2.3.3.2 Self-resonance frequency (SRF) of free solenoid coil

Because the electric field pattern in a free solenoid coil is different from the one in the in-circuit coil, to get an accurate result, the true SRF of a free solenoid coil is calculated based on the simulation of nominal helical velocity factor u_{hx}/c of the coil.

It should be noted that the L-C circuit resonance frequency formula using the self-inductance and self-capacitance is based on the assumption that the capacitance representing the electric field in the coil is parallel to the coil and a uniform current is flowing through the coil, which is not the case for free coils and is only applicable when the operational frequency is much less than the coil's SRF. Moreover, the formula indicates that there is only one SRF for a coil, which is wrong as a coil can have sub-harmonics of SRF in high frequencies.

David W. Knight developed an empirical model called HTL'||C_{EF} to simulate the nominal helical velocity factor u_{hx}/c in a free solenoid coil based on the nominal helical velocity factor data from Drude [178], Pettit [174], Jackson [181] and his own experiment (The comparison of HTL'||C_{EF} and the experiment data can be seen in AppendixA2.).

The steps to obtain the nominal helical phase velocity factor u_{hx}/c of a free solenoid are as follows [174].

1) Calculate the argument of Bessel function

$$k_{loop} = \frac{D_{loop}}{l_{loop}} \tag{2.112}$$

$$x = \frac{\pi}{2} k_{loop} + 0.117 e^{-22 e^{\frac{-0.75}{k_{loop}}}} \tag{2.113}$$

2) Calculate the Nagaoka's Coefficient k_L

$$Z_k = \frac{2}{\pi k_{loop}} \tag{2.114}$$

$$k_L = Z_k \left[log\left(1 + \frac{1}{Z_k}\right) + \frac{1}{-10.632 + \frac{3.347}{k_{loop}} + \frac{1.764}{k_{loop}^2} + \frac{-0.47}{\left(0.755 + k_{loop}\right)^{1.44}}} \right] \tag{2.115}$$

3) Calculate the relative permittivity for radial propagation

$$\varepsilon_{rad} = \frac{\varepsilon_x}{2}\left[1 + k_L + \frac{\varepsilon_i}{\varepsilon_x}(1 - k_L)\right] \tag{2.116}$$

4) Calculate the actual helical velocity factor

$$W(x) = \sqrt{\frac{I_0(x)K_0(x)}{I_1(x)K_1(x)}}, \text{W(x) is Ollendorff's function} \tag{2.117}$$

$$\frac{v_{hx}}{c} = \frac{W(x)}{\sqrt{\varepsilon_{rad}}} \tag{2.118}$$

5) Calculate the fringe field capacitance

$$\frac{C_{EF}}{D_{loop}} = \frac{2\varepsilon_0 \varepsilon_{rad}}{1 + ln\left(1 + \frac{1}{k_{loop}}\right)} \tag{2.119}$$

6) Calculate the axial field capacitance

$$\frac{C_{AF}}{D_{loop}} = \frac{\varepsilon_0(\varepsilon_i + \varepsilon_x)}{ln\left[1.015 + \frac{1}{k_{loop}^2} + \sqrt{\left(1.015 + \frac{1}{k_{loop}^2}\right)^2 - 1}\right]} \tag{2.120}$$

7) Calculate the characteristic impedance of the coil

$$R_0 tan\Psi = \frac{1}{\sqrt{\varepsilon_{rad}}} \frac{Z_0}{2\pi} \sqrt{2I_1(x)K_1(x)I_0(x)K_0(x)} \tag{2.121}$$

8) Calculate the iterative solution for u_{hx}/c

$$a = \frac{\pi}{2\frac{u_{hx}}{c}} \tag{2.122}$$

$$b = \frac{k_{loop}^{-1}}{c\pi\left(\frac{C_{EF}}{D_{loop}} + \frac{C_{AF}}{D_{loop}}\right) R_0 tan\Psi} \tag{2.123}$$

$$y = \frac{1}{a} arctan\left(\frac{b}{z}\right) \text{ to be adjusted until y=z} \tag{2.124}$$

$$\frac{\partial y}{\partial z} = -\frac{b}{a}\frac{1}{z^2 + b^2} \tag{2.125}$$

$$\frac{u_{hx}(nom)}{c} = y \tag{2.126}$$

9) Calculate the SRF of the free solenoid coil

$$SRF = \frac{u_{hx}(nom)}{2l_{wire}} \tag{2.127}$$

The detailed calculation steps are presented in Appendix A7.

It should be noted that the obtained SRF is for free solenoid coils, which means no circuit is connected to the coil. If a shunt impedance is connected at the terminals of the coil, the L-C resonance frequency formula will be applicable at low frequencies until the frequency is close to the SRF of the free coil.

An example of solenoid coil's SRF against the number of turns and against the gap interval between coil turns are shown in Figure 2.3-22 and Figure 2.3-23. The parameters of the coil in the example is following the parameters of the coil in the writer's experiment setup in Section 3.2.4. As the number of turns increases, the SRF of the coil decreases exponentially. For the present sets of coil parameters, the SRF drops to 20 MHz when $\mathrm{N} = 5$. Considering the robustness of wireless power transfer system, the operational frequency should be less than half of the free coil SRF. Therefore, with the present sets of coil parameters, if the operational frequency is set to 10 MHz, the coil should not be more than 5 turns. Compared with the number of turns, the SRF changes "slower" against the change of gap interval p at the present sets of coil parameter. A 10-time change in the gap interval (from 2 mm to 2 cm) only shifts the SRF up by 5 MHz Thus, altering the number of turns is more effective at increasing the SRF than changing the gap interval. Furthermore, as will be discussed in Section 3.1.1, the change of gap interval p has a stronger effect on the magnetic field strength than changing the number of turns. This also indicates the first option when SRF needs to increase to reduce the number of turns N.

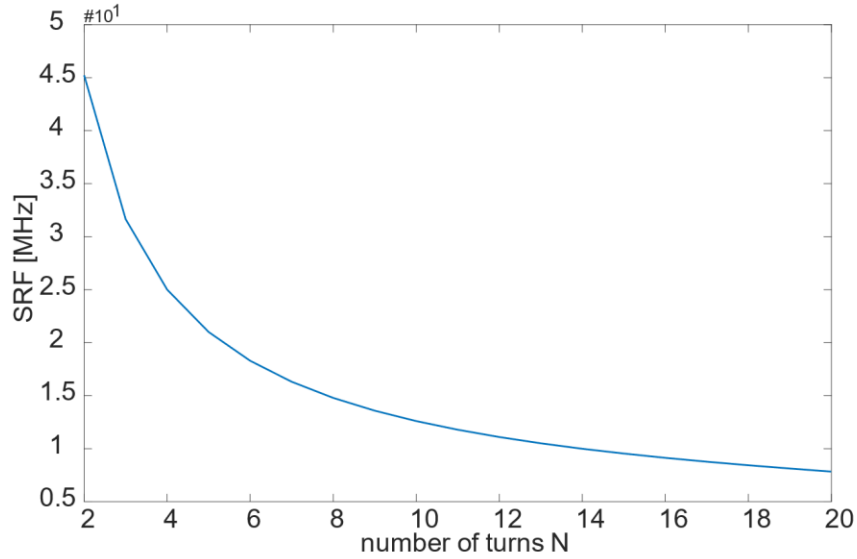

Figure 2.3-22 SRF against number of coil turns N with diameter of coil D_{loop} = 20 cm, gap interval p = 1.2 cm, internal relative permittivity ε_i = 2.7 (Acrylic) and external relative permittivity = 1 (air)

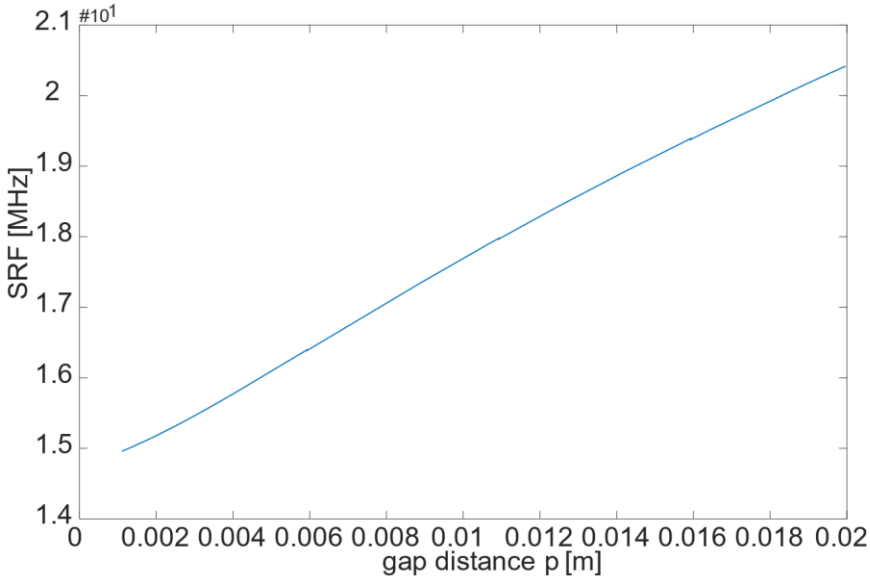

Figure 2.3-23 SRF against gap interval p with diameter of coil D_{loop}=20 cm, number of coil turns N= 6, internal relative permittivity ε_i = 2.7 (Acrylic) and external relative permittivity ε_x = 1 (air)

2.3.3.3 Parasitic capacitance due to environments in proximity

When a coil is near a conductive object, there will be distributed parasitic capacitance between the coil and the object, as shown in the left of Figure 2.3-24. The electric field corresponding to the parasitic capacitance will generate conduction currents on the object and cause heat loss due to the resistance in the object. An equivalent circuit of the solenoid coil with the parasitic capacitance and resistance is shown in the right of Figure 2.3-24. The parasitic capacitance $C_{pr\text{-}eq}$ and resistance $R_{pr\text{-}eq}$ is added in parallel with the coil. Two problems will be caused by $C_{pr\text{-}eq}$ and $R_{pr\text{-}eq}$. Firstly, the parasitic capacitance will be added to the capacitance of the transmitter circuit and change the

resonance frequency of the circuit; Secondly, the resistance $R_{pr\text{-}eq}$ will cause extra heat loss to the transmitter circuit and lower the quality factor.

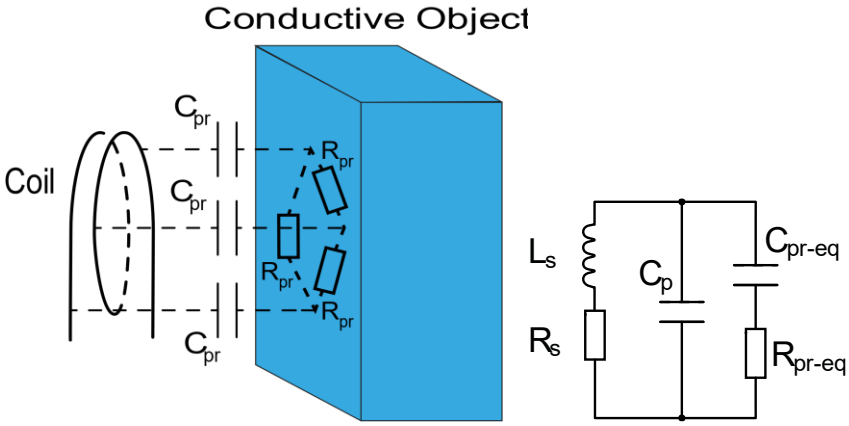

Figure 2.3-24 (Left) distributed parasitic capacitance exists between coil and conductive environment in proximity with parasitic resistance; (right) equivalent circuit for solenoid coil with equivalent parasitic capacitance and parasitic resistance causing by conductive environment in proximity

The parasitic capacitance can be seen as the capacitance between a circular wire and a conductive plate in parallel, which can be calculated as [174][182],

$$C_{pr-eq} = \frac{2\pi\varepsilon l_{wire}}{cosh^{-1}\left(\frac{h}{d_{wire}}\right)} \tag{2.128}$$

where

- l_{wire} is the length of wire in the proximity of the conductive environment
- h is the distance between the wire and the environment
- d_{wire} is the diameter of wire
- ε is the dielectric constant of the medium where the wire is located

In the wireless power transfer system, the circular wire will be the length of conductor of the solenoid coil. As the coil is situated in the air with coil formers, the dielectric constant has to be corrected for the coil former. Due to the complexity of the human body and the scope of the thesis, it is assumed that the electric field corresponding to the parasitic capacitance only exists at the surface of the human body. The distance between the wire and the conductive environment is thus the distance between each turn of the coil and the surface of the human body. As the turns of coil are all parallel to each other and any additional turns will add capacitance to the total parasitic capacitance, the total parasitic capacitance can then be calculated as the superposition of parasitic capacitance between each turn of the coil and the human body.

Because

$$cosh^{-1}(x) = ln\left(x + \sqrt{x^2 - 1}\right) \tag{2.129}$$

The capacitance between the solenoid coil and the human body can thus be roughly estimated as the following in the wireless power transfer system.

$$C_{pr-eq} = \sum_{i=0}^{N-1} \frac{\pi\varepsilon_0(\varepsilon_x + \varepsilon_i)(\pi D_{loop})}{ln\left[\frac{h_{body} + i \cdot p}{d_{wire}} + \sqrt{\left(\frac{h_{body} + i \cdot p}{d_{wire}}\right)^2 - 1}\right]} \tag{2.130}$$

where

- D_{loop} is the diameter of the solenoid coil
- h_{body} is the distance between the coil and the surface of human body
- p is the gap interval between turns of the coil
- N is the number of turns of the solenoid coil
- d_{wire} is the diameter of the wire of the coil
- ε_x is the relative dielectric constant of external environment (air)
- ε_i is the relative dielectric constant of internal environment (coil former)

An example of the amount of parasitic capacitance against the distance between coil and human body is shown in Figure 2.3-25. The parasitic capacitance is more than 20 pF when the distance is less than 1 mm, but it drops more than 50% when the distance increases to more than 1mm. After the drop, as the distance continues to increase, the capacitance decreases slowly. What's more, the capacitance increases as the number of turns increases, which can be easily observed from the formula.

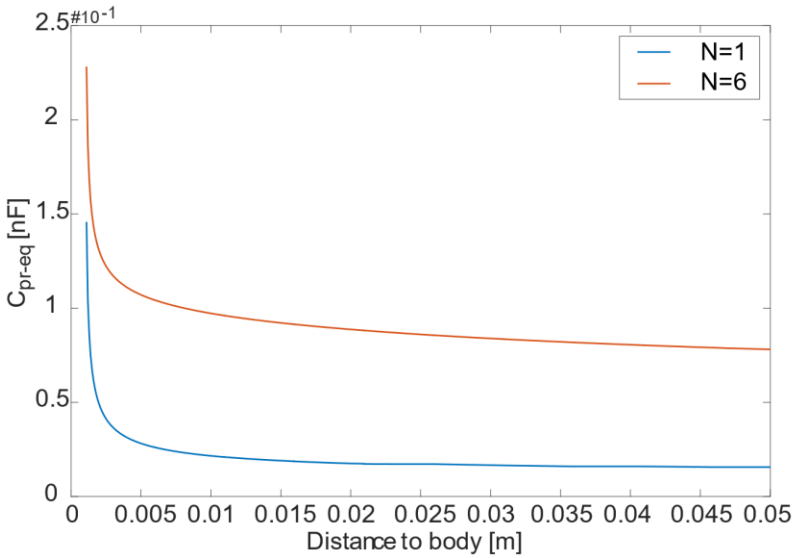

Figure 2.3-25 Parasitic capacitance against distance between coil and human body in different number of coil turns. Diameter of coil D_{loop}=20 cm, gap interval p=1 cm, internal relative permittivity ε_i=2.7 (Acrylic) and external relative permittivity ε_x=1 (air)

Due to the different dielectric constants at different parts of the human body, the capacitance formula will not be able to give an accurate result. However, it can help to estimate the scale of parasitic capacitance and how the capacitance will change due to the change of the distance between the coil and the human body.

The value of equivalent parasitic resistance $R_{pr\text{-}eq}$ is dependent on the medium in the environment. The calculation of the resistance will not be carried out in the thesis.

2.3.3.4 AC resistance with skin effect and proximity effect

The series resistance R_s of a solenoid coil is dependent on the dimensional parameters of coil as well as the frequency of current passing through the coil.

At a DC current, the resistance of a coil is totally dependent on the length of wire and the cross-section area of the wire, which can be calculated as

$$R_{DC} = \frac{\rho l_{wire}}{A_{wire}} \tag{2.131}$$

in which

l_{wire} is the total length of wire that makes the solenoid coil.

$$l_{wire} \approx \sqrt{\left(N\pi D_{loop}\right)^2 + l_{loop}^2} \tag{2.132}$$

l_{loop} is the length of the solenoid coil.

$$l_{loop} = Nd_{wire} + (N-1)p \tag{2.133}$$

A_{wire} is the cross-section area of the wire.

$$A_{wire} = \frac{\pi d_{wire}^2}{4} \tag{2.134}$$

where

- ρ is the resistivity of the conducting wire
- N is the number of turns of the coil
- D_{loop} is the diameter of the solenoid coil
- d_{wire} is the diameter of the wire that wounds the coil
- p is the gap interval between two turns of the solenoid coil

With an AC current, the resistance of the coil to the current will increase due to the skin effect and the proximity effect.

The skin effect is because of the magnetic field generated by the AC current on the wire. The magnetic field expels the current from the centre of the wire, forcing the

current to concentrate near the surface of the wire, forming a current "skin" within the wire [171]. The term skin depth describes the depth under the wire surface where the current density becomes 1/e of the current density on the surface of the wire. The skin depth can be calculated as [183],

$$\delta = \sqrt{\frac{\rho}{\pi f \mu_0}} \tag{2.135}$$

The skin effect reduces the effective cross section area of the wire, which results in an increase of the resistance of the wire.

The proximity effect occurs when AC currents are conducting through adjacent wires. The magnetic field generated by the AC currents of one of the wires expels or attracts the AC currents of another wire [184], forcing the currents to concentrate on one side of the wires, which will also cause an increase of the resistance of the wires.

The AC resistance of a coil caused by the skin effect and proximity effect can be written as [185],

$$R_{AC} = R_{DC} \Xi \Gamma \tag{2.136}$$

where

- R_{DC} is the DC resistance of the solenoid coil
- Ξ is the skin effect factor, $\Xi = \frac{d_{wire}^2}{4(\delta d_{wire} - \delta^2)}$ and δ is the skin depth in (2.135)
- Γ is the proximity factor

To predict the resistance of a long solenoid coil ($N > 30$), R.G. Medhurst [177], summarised a table of values for the proximity factor Γ (as shown in AppendixA3.) for different ratios of solenoid length/solenoid diameter and gap interval/wire diameter.

Based on R.G. Medhurst's empirical data, David W. Knight further develops the formula with short-coil correction, which can be written as [185],

$$R_{AC} = R_{DC}\left[1 + (\Xi - 1)\Gamma \frac{N - 1 + \frac{1}{\Gamma}}{N}\right] \tag{2.137}$$

where N is the number of coil turns.

This formula will be able to give a prediction of AC resistance in less than 3% error for both short and long solenoid coils with a skin-depth/wire diameter ratio ($\frac{\delta}{d_{wire}}$) less than 0.1 and operational frequency below SRF.

An example of the AC resistance against the number of coil turns N and against gap interval p are shown in Figure 2.3-26 and Figure 2.3-27 with coil parameters same as in the lab experiment.

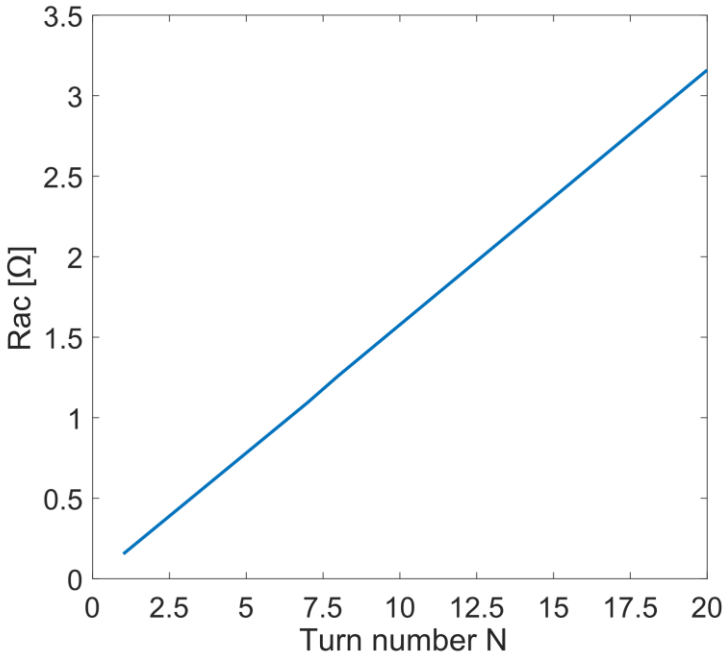

Figure 2.3-26 Calculated AC resistance against number of coil turns N with diameter of coil D_{loop} = 20 cm, gap interval between coil turns p = 1.2 cm, internal relative permittivity ε_i = 2.7 (Acrylic) and external relative permittivity ε_x = 1 (air)

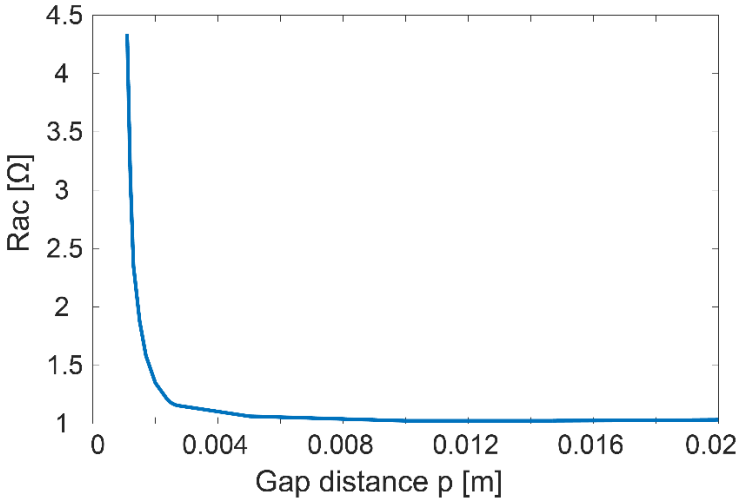

Figure 2.3-27 AC resistance against gap interval between coil turns p with diameter of coil D_{loop} = 20 cm, number of coil turns N = 6, internal relative permittivity ε_i = 2.7 (Acrylic) and external relative permittivity ε_x = 1 (air)

With a fixed diameter and a fix gap interval, the AC resistance of the solenoid coil and the number of turns is in direct proportion, which is expected as any additional turn adds the same amount of resistance to the total resistance.

The curve for the AC resistance against gap interval is not smooth because the table of proximity factor set by Medhurst is discrete between different ratios of solenoid length/solenoid diameter and gap interval/wire diameter. The proximity effect for close

turn coils is rather strong. As seen in Figure 2.3-27, as the gap interval p increases from 1 mm to 6 mm, the AC resistance drops sharply from over 4 Ω to just over 1 Ω.

The AC resistance of a one-turn coupling coil is therefore calculated as

$$R_{AC} = R_{DC}\Xi = \frac{\rho l_{wire}}{A_{wire}} \frac{d_{wire}^2}{4(\delta d_{wire} - \delta^2)} \tag{2.138}$$

The AC resistance of the primary coil is therefore calculated as

$$\begin{aligned} R_{AC} &= R_{DC}\left[1 + (\Xi - 1)\Gamma \frac{N - 1 + \frac{1}{\Gamma}}{N}\right] \\ &= \frac{\rho l_{wire}}{A_{wire}}\left[1 + (\Xi - 1)\Gamma \frac{N - 1 + \frac{1}{\Gamma}}{N}\right] \end{aligned} \tag{2.139}$$

2.3.4 EM regions, EM Wave Attenuation in Tissue and EM exposure Limit

Key points of this section

- The definition of Near field is introduced.
- Electromagnetic field will attenuate in conductive media, such as human tissues.
- IEEE EM field exposure standard limits are introduced.

2.3.4.1 The propagation of EM field from a small circular loop in free space

For a small circular loop ($\frac{D_{loop}}{2} \ll \lambda_0$) in free space, the magnetic field components can be calculated as [186],

$$H_\theta = \frac{m_0 sin\theta e^{j(\omega t - \beta_0 h)}}{4\pi}\left(-\frac{\beta_0^2}{h} + j\frac{\beta_0}{h^2} + \frac{1}{h^3}\right) \tag{2.140}$$

$$H_r = \frac{m_0 cos\theta e^{j(\omega t - \beta_0 h)}}{2\pi}\left(j\frac{\beta_0}{h^2} + \frac{1}{h^3}\right) \tag{2.141}$$

where

- m_0 is the loop current times loop area, $m_0 = I_0\pi(\frac{D_{loop}}{2})^2$
- β_0 is the phase constant of free space, $\beta_0 = \omega/c = 2\pi/\lambda_0$
- h is the transfer distance

In the formula, different components of $1/h^n$ corresponds to different patterns of magnetic field components [186]:

$1/h$ variation: radiation component

$1/h^2$ variation: induction component in the radiating near field

$1/h^3$ variation: magnetostatics component in the reactive near field

At different values of h, the weight of different components of $1/h^n$ will be different, and one of the components will be heavier than the rest of the components.

It can therefore be able to have a rough distinguish on the different regions of generated field, which is shown in Table 2.3-1.

Near field	$h < \lambda_0$
Reactive near field	$h < \frac{\lambda_0}{2\pi}$
Radiative near field	$\frac{\lambda_0}{2\pi} < h < \lambda_0$
Transition field	$\lambda_0 < h < 2\lambda_0$
Far field	$h > 2\lambda_0$

Table 2.3-1 Range of distance for different kinds of fields

If only the reactive near field is considered and it is in a conductive medium with a relative electric constant ε_r, (2.140) and (2.141) will become

$$H_{\theta-m} = \frac{m_0 sin\theta e^{j(\omega t-\gamma h)}}{4\pi h^3} \tag{2.142}$$

$$H_{r-m} = \frac{m_0 cos\theta e^{j(\omega t-\gamma h)}}{2\pi h^3} \tag{2.143}$$

where γ is the propagation constant [186],

$$\gamma = 2\pi f \sqrt{\mu_0 \mu_r \varepsilon_0 \varepsilon_r \left(1 - \frac{j\frac{1}{\rho_m}}{2\pi f \varepsilon_0 \varepsilon_r}\right)} \tag{2.144}$$

- f is the frequency of the generated magnetic field
- μ_0 is the permeability of vacuum
- μ_r is the relative permeability of the media to the permeability of vacuum
- ε_0 is the dielectric constant (permittivity) of vacuum
- ε_r is the relative dielectric constant (permittivity) of the media to the permittivity of vacuum
- ρ_m is the resistivity of the media

As the propagation constant is a complex value, it can be represented by a combination of real component and imaginative component $\gamma = \alpha + j\beta$, where α is the attenuation factor due to power dissipation in the medium,

$$\alpha = 2\pi f \sqrt{\frac{\mu_0 \mu_r \varepsilon_0 \varepsilon_r}{2} \left[\sqrt{1 + \left(\frac{\frac{1}{\rho_m}}{2\pi f \varepsilon_0 \varepsilon_r} \right)^2} - 1 \right]} \tag{2.145}$$

β is phase constant of the medium,

$$\beta = 2\pi f \sqrt{\frac{\mu_0 \mu_r \varepsilon_0 \varepsilon_r}{2} \left[\sqrt{1 + \left(\frac{\frac{1}{\rho_m}}{2\pi f \varepsilon_0 \varepsilon_r} \right)^2} + 1 \right]} \tag{2.146}$$

For an EM field in a conductive media, the phase constant and the wavelength has the following equation [186],

$$\beta_g = 2\pi / \lambda_g \tag{2.147}$$

The wavelength of EM field in a conductive medium with a relative dielectric constant ε_r can therefore be derived [186],

$$\lambda_g \approx \frac{\lambda_0}{\left[\varepsilon_r^2 + \left(\frac{1}{\omega \rho_m \varepsilon_0} \right)^2 \right]^{1/4}} \tag{2.148}$$

Because the relative dielectric ε_r is more than 1, the wavelength λ_g of EM field in a medium is shorter than the wavelength λ_0 in free space.

2.3.4.2 *Attenuation effect in a wireless power transfer system for medical implants*

The same analysis can be applied to the WPT system for medical implants.

If only the area around the receiver coil within the human body is considered, human tissue can be regarded as a homogeneous medium with no sharp edges and rough surfaces with uniform electric and magnetic properties.

An example of electric properties of human tissues can be seen in Table 2.3-2.

Frequency (MHz)	Wavelength in air (m)	Relative permittivity (F/m)	Conductivity (S/m)	Wavelength (m)	Skin depth (cm)
1	300	2000	0.4	347	89
6.7	44.78	300	0.55	115	29
10	30	160	0.625	76	23
13.5	22.22	150	0.615	54	20
27.12	11.06	113	0.612	51	14
40.68	7.38	97.3	0.693	41	11
100	3	71.7	0.889	22.67	6

Table 2.3-2 Properties of Electromagnetic waves in biological media for muscle, skin and tissue of high wave content [187][188]

If only the magnitude of the magnetic field is considered, the actual magnetic field in the human body can be calculated as [186]

$$|H_{z-atn}| = |H_z|e^{-\alpha h} \tag{2.149}$$

where

- h is the transfer distance in the media
- H_z is the magnetic field strength in free space in the axial direction

An example of the attenuation effect of a magnetic field in a medium is shown in Figure 2.3-28 and Figure 2.3-29. As the frequency of the magnetic field increases, the attenuation effect will be stronger, which means the field will become weaker in the medium. This is primarily due to the conduction current $J = \sigma \mathrm{E}$ induced by the magnetic field in the conductive tissues, according to the Faraday's law. The induced electric field will be stronger at a higher frequency, which causes a higher conduction current, and thus a higher heat loss at the tissue. Moreover, the magnetic field will become weaker as the transfer distance into the medium increases. This is called the skin effect because the EM field seems only to exist at the surface or skin of the medium. The reciprocal of the attenuation factor α is called the skin depth, at which the magnetic field strength drops to $1/e$ of the initial strength.

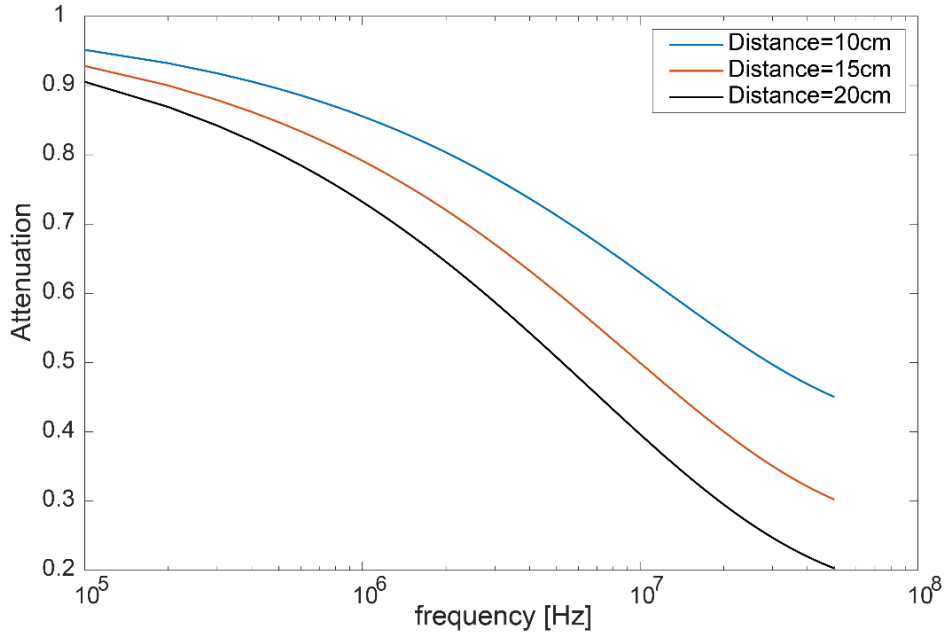

Figure 2.3-28 Attenuation of magnetic field against frequencies at different transfer distances (10 cm, 15 cm, 20 cm) in a uniform conductive material with a frequency-independent high dielectric constant (σ=0.625 S/m, ε_r=160)

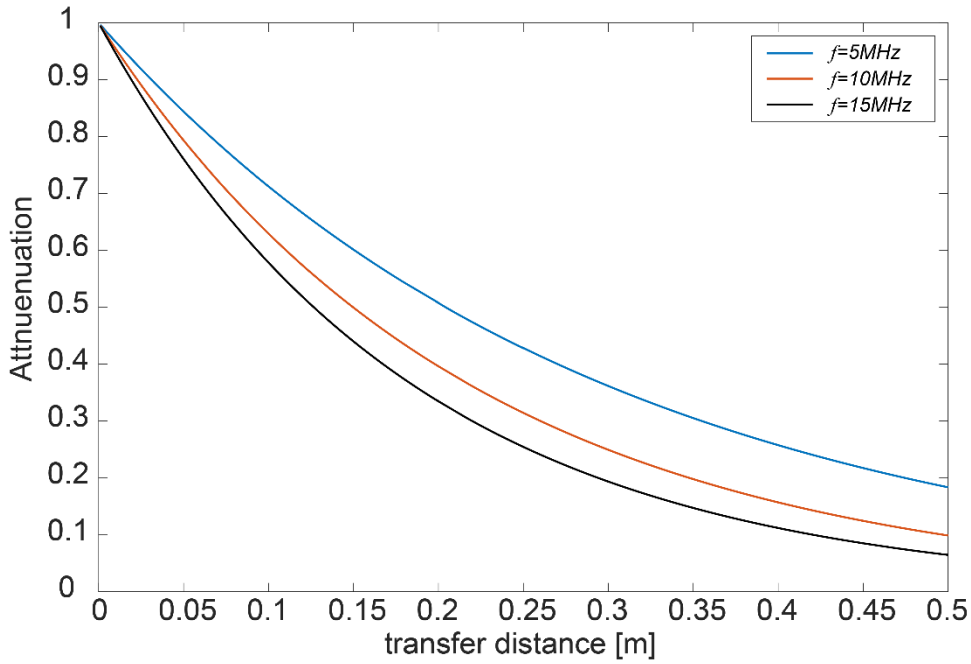

Figure 2.3-29 Attenuation of magnetic field against transfer distance at different frequencies (5 MHz, 10 MHz, 15 MHz) in a uniform conductive material with a frequency-independent high dielectric constant (σ=0.625 S/m, ε_r=160)

Even though the theoretical analysis shows that body tissues will cause severe attenuation effect, some of the previous researches show a different result. In [189], both the experiment and the HFSS analysis show that the tissue attenuation effect is negligible in a 1cm thick layer of beef sirloin. Only 1.7% to 4.3% of efficiency drop has occurred. In [126], it is reported that only a 6.2×10^{-2}% of efficiency decrease has occurred with a pork chop between the TX coil and the RX coil at a transfer distance

of 7 cm. In [122], no noticeable attenuation effect is obtained for a transfer distance up to 15 cm in the body of a rabbit.

Therefore, the theoretical attenuation results will be treated as the worst cases, and the calculation results of magnetic field strength or induced voltage in the later analysis with a consideration of media attenuation will be seen as the bottom-bounded results.

2.3.4.3 The field strength limit on human tissue

As a time-changing magnetic field will induce conduction currents in conductive media, it will lead to heating problems in the human body in the wireless power transfer system for medical implants.

From Faraday's law [171],

$$\oint \boldsymbol{E} \cdot d\boldsymbol{l} = -\iint \frac{\partial \boldsymbol{B}}{\partial t} \cdot d\boldsymbol{S} \tag{2.150}$$

Assume S is a small circular area with diameter D, and l is its circumference, so that the magnetic flux density is uniform across the area. (2.150) becomes,

$$\pi D|E| = -j\omega\pi \left(\frac{D}{2}\right)^2 \mu|H| \tag{2.151}$$

and

$$|E| = \frac{-j\omega D\mu}{4}|H| \tag{2.152}$$

As the current density J is equal to

$$J = \sigma_m E \tag{2.153}$$

where σ_m is the conductivity of the medium,

The power dissipated in the conductive medium can be calculated as [186]

$$P = \frac{1}{2}\iiint \rho_m J^2 dV \tag{2.154}$$

where ρ_m is the resistivity of the medium, $\rho_m = \frac{1}{\sigma_m}$.

This power will be dissipated in the form of heat, causing rising temperature in the tissue of human body, which can lead to serious problems.

The IEEE has introduced EM field exposure standards to limit EM radiation to the public, which can be seen in [144]. According to the IEEE standard C95.1-2005, two restrictions are introduced, basic restrictions (BR) and maximum permissible

exposure (MPE). The basic restrictions are exposure restrictions based on known health effects, while MPE corresponds to the highest root-mean square (RMS) value or peak electric or magnetic field strengths. If an exposure is proven to below the basic restrictions, the MPE can be exceeded [144]. However, the value of BRs should be followed strictly to avoid serious problem. A guidance of MPEs for inductive power transfer is shown in Table 2.3-3. At 8 MHz, the MPE is 40.75 A/m.

Frequency	H_{MaxRMS} (A/m)	Limit
3-3.35kHz	$547/f_{kHz}$	Electrostimulation
3.35kHz-2MHz	163	Electrostimulation
2-30MHz	$326/f_{MHz}$	Heating
30-100MHz	$3166/f_{MHz}^{1.668}$	Heating
100-400MHz	1.588	Heating

Table 2.3-3 MPEs of magnetic field in RMS for inductive power transfer [144], for general population. $f_{MHz}^{1.668}$means the value of frequency in MHz unit to the power of 1.668.

In Table 2.3-4, SAR is the specific absorption rate, which is the time derivative of the differential energy (dW) absorbed by (dissipated in) an differential mass (dm) contained in a differential volume (dV) of a given density (ρ) [144].

		Action level[a] SAR (W/kg)	Persons in controlled environments SAR (W/kg)
Whole-body exposure	Whole-body average	0.08	0.4
Localised exposure	Localised (peak spatial-average)	2[b]	10[b]
Localised exposure	Extremities[c] and pinnae	4[b]	20[b]
[a]BR for the general public when an RF safety program is unavailable			
[b]Average over ang 10 g of tissue (defined as a tissue volume in the shape of a cube)			
[c]The extremities are the arms and legs distal from the elbows and knees, respectively			

Table 2.3-4 BRs for frequencies between 100 kHz and 3 GHz [144]

At a point, it can also be calculated as

$$SAR = \frac{\sigma |E|^2}{\rho} \tag{2.155}$$

where ρ is the mass density of the tissue.

For the wireless power transfer system for medical implants, the localized exposure limit for people in controlled environments is considered. In the IEEE guideline [144], the SAR limits are 4 W/kg for any 10 g of tissues at the limbs for a general public exposure; 1.6 W/kg for any 1 g of tissue in the rest part of the body. In the ICNIRP guideline [190], the SAR limits are 2 W/kg for any 10 g of tissues at the head and trunk for a general public exposure; 4 W/kg for any 10 g of tissues at the limbs.

Although the guidelines relate the SAR limit to the magnetic field strength, researchers do not seem to reach an agreement on the effect of EM field on the human body tissues. In [191], no outstanding health effect was found in the analysis of people who were exposed to high-frequency EM fields with a few mW/cm^2 density. At a frequency less than 20 MHz, the SAR is less than 0.015 W/kg with an EM field of 1 mW/cm^2 density. A similar conclusion is obtained by [192], in which global-Communication-amplitude-level pulsed waves and continuous waves were applied to brain tissues, and no obvious risk effect on health was found.

In this thesis, MPE (i.e., maximum permitted magnetic field strength) will mainly be used to assess the exposure safety of the design of wireless power transmitter.

2.4 Summary of this chapter

In this section, various theories and factors determining/affecting the wireless power transfer system have been discussed.

The basic laws, including Biot-Savart law and Faraday's law, have been introduced. Biot-Savart law describes the strength and direction of the magnetic field generated by an electric current. This is the basis of operation of the transmitter coil in a wireless power transfer system. Faraday's law describes the induction of electromotive force by a time-varying magnetic field, which is the basis of operation of the receiver coil in a wireless power transfer system.

Besides the basic laws, three different factors affect the performance of the wireless power transfer system. The application of an L-C resonant circuit in the transmitter and receiver circuits will minimise the impedance caused by the inductors of the circuits and help to generate

- a higher magnetic field strength in the transmitter
- a higher output voltage at the receiver coil terminal

The practical inductor model helps to predict the self-capacitance, self-resonance frequency, parasitic capacitance and self-resistance of a solenoid coil theoretically. This will be used in the determination of the operational frequency and the generated magnetic field strength in the transmitter. The discussion of propagation of EM field in the chosen medium (the human body) introduces the region of the near field of a transmitter. Moreover, it indicates the attenuation of EM field in conductive media in the form of heat, which means the magnetic field will be weakened inside a human body. The temperature rise caused by the heat loss in the human body could cause a potential hazard to the person. This is why the IEEE exposure limit is introduced.

In the following section, these laws and theories will be applied to calculate the magnetic field strength generated by a solenoid coil theoretically and to analyse how different physical parameters in a solenoid coil will change the field. Based on the analysis, an optimum set of dimensional parameters of a solenoid coil will be presented to achieve a maximum field strength at certain transfer distances. In addition, design flows for a solenoid transmitter coil will be introduced for a weakly coupled wireless power transfer system for medical implants.

Chapter 3 Models and Designs for the Magnetic Coupling Resonance Wireless Power Transfer System for deep implanted medical devices

3.1 Transmitter coil model

Key aims of this section

To maximise the generated magnetic field strength at the receiver,

(1) by maximising the current through the transmitter primary coil

and

(2) by choosing an appropriate coil structure for the transmitter coil

3.1.1 Introduction

For the wireless power system for micro-implants, the design and analysis of the transmitter can be divided into two stages.

- Maximise the current going through the transmitter coil so that the generated magnetic field can be maximised, according to the Biot-Savart law.
- Maximise the generated field strength at the receiver coil, which is between 5cm to 20cm away from the transmitter coil.

With a fixed range of operational frequency and a limited range of input voltage, the first stage is related to the circuit components, impedance matching and the shape of coils in the transmitter; the other one is related to the shape of coils and the media at which the generated field is located.

3.1.2 Maximisation of current in the transmitter primary coil

Key aims of this section

- To maximise the current in the transmitter primary coil, a single-turn coil is used as the coupling coil; the coupling coil and the primary coil are strongly coupled together.
- Both the coupling coil and the primary coil are L-C circuits which resonate at the same frequency to reduce impedance.

- When the mutual inductance between the coupling coil and the primary coil is at a certain value, the resulting current at the primary coil is the highest and will be higher than the current with the primary coil connected directly to the power source.

As shown in the block diagram in Figure 2.1-1, the transmitter consists of two coils, the coupling coil and the primary coil. This forms a 3-coil WPT system with two coils as a transmitter and one coil as a receiver. The reason for a 3-coil WPT system is because of the ease of tuning and impedance matching of the single-turn coupling coil. If the multi-turn primary coil is connected directly to the power source, the values of the tuning inductor and capacitor and even the impedance matching network will have to be recalculated to match the resonant frequency when the parameters of primary coil are changed. What's more, from previous literatures as discussed in Section 1.2.3, a 3-coil WPT system is proved to have a higher efficiency than a 2-coil system if proper designed. Therefore, a 3-coil system is used in this design.

The coupling coil is a one-turn coil connected to the signal generator and a resonator which is basically an L-C circuit. The primary coil is a multi-turn coil connected to a variable capacitor, which forms an L-C resonant circuit. The coupling coil and the primary coil are strongly coupled together. Both the resonator and the variable capacitor are tuned so that the coupling coil circuit and the primary coil circuit resonate at the same frequency. In operation, the coupling coil creates a magnetic field at this frequency. The magnetic field is then coupled with the primary coil, which resonates and creates a corresponding magnetic field. This field will be picked up by the receiver coil and creates a voltage across it. An equivalent circuit of the transmitter is shown in Figure 3.1-1 with the symbols introduced in Table 3.1-1.

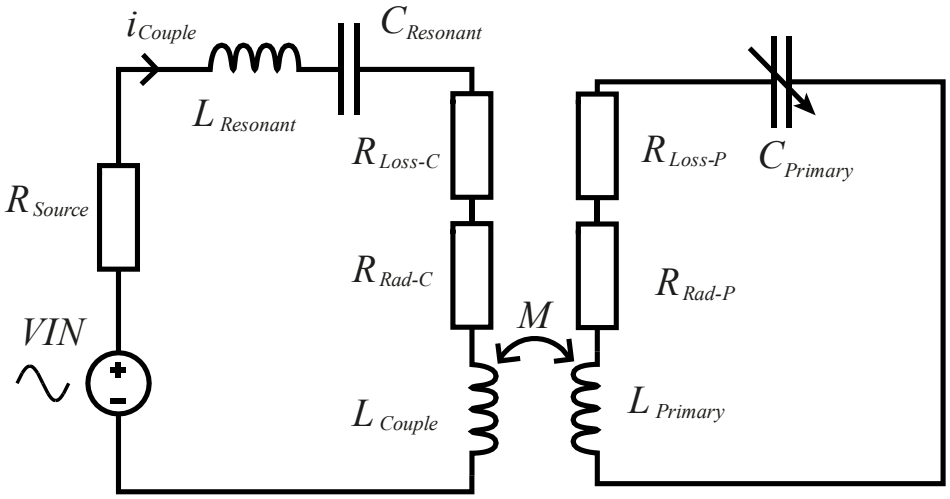

Figure 3.1-1 Equivalent circuit of the transmitter circuit.

Symbol	Component	Symbol	Component
R_{Source}	Output impedance of signal generator	$R_{Rad\text{-}C}$	Equivalent radiation resistor of coupling coil
$L_{Resonant}$	Tuning inductor at coupling coil circuit	$R_{Rad\text{-}P}$	Equivalent radiation resistor of primary coil
$C_{Resonant}$	Tuning capacitor at coupling coil circuit	L_{Couple}	Equivalent inductor of coupling coil
$R_{LOSS\text{-}C}$	Equivalent heat-loss resistor of coupling coil	$L_{Primary}$	Equivalent inductor of primary coil
$R_{LOSS\text{-}P}$	Equivalent heat-loss resistor of primary coil	$C_{Primary}$	Variable capacitor at primary coil circuit
M	Mutual inductance between coupling coil and primary coil		

Table 3.1-1 Symbols and their corresponding components in the transmitter circuit shown in Figure 3.1-1

To simplify the analysis, a bidirectional reflectance impedance analysis is used, with which the voltage source and the impedance of one side of the coupled coils are reflected to the other side [193][194]. The simplified equivalent circuits are shown in Figure 3.1-2 and Figure 3.1-3.

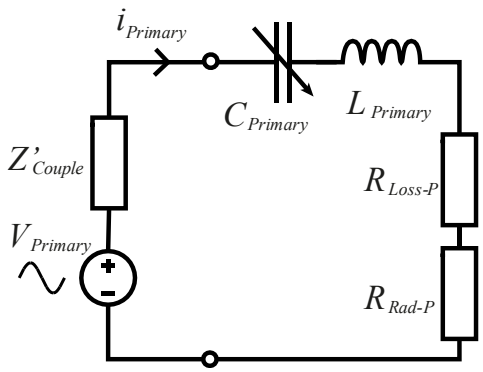

Figure 3.1-2 Equivalent circuit of the transmitter with the coupling coil circuit reflected to the primary coil circuit; $V_{Primary}$ is the voltage at the primary coil circuit, which is linked to the coupling coil circuit; $Z'_{Ccouple}$ is the reflected impedance of the coupling coil circuit to the primary coil circuit.

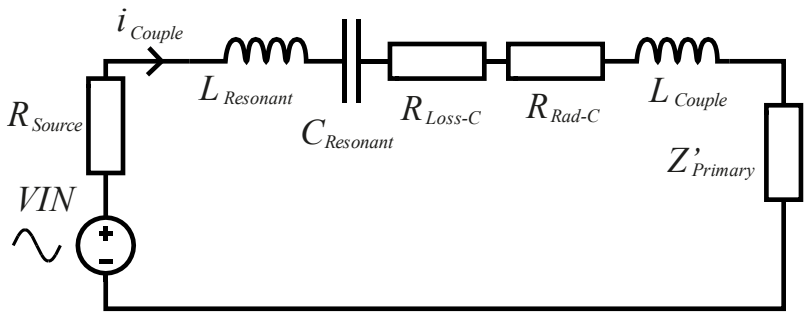

Figure 3.1-3 Equivalent circuit of the transmitter with primary coil circuit reflected to coupling coil circuit; $Z'_{Primary}$ is the reflected impedance of the primary coil circuit to the coupling coil circuit.

According to [193] and [194], in Figure 3.1-2,

$$V_{Primary} = \frac{j\omega M}{Z_{Couple} + R_{Source}} VIN \tag{3.1}$$

$$Z'_{Couple} = \frac{\omega^2 M^2}{Z_{Couple} + R_{Source}} \tag{3.2}$$

$$Z_{Couple} = R_{Loss-C} + R_{Rad-C} \tag{3.3}$$

In Figure 3.1-3,

$$Z'_{Primary} = \frac{\omega^2 M^2}{Z_{Primary}} \tag{3.4}$$

$$Z_{Primary} = R_{Loss-P} + R_{Rad-P} \tag{3.5}$$

The amplitude of current at the primary coil circuit can thus be calculated as

$$I_{Primary} = \frac{V_{Primary}}{Z'_{Couple} + R_{LOSS-P} + R_{Rad-P}} \tag{3.6}$$

By combining (3.1) (3.2) (3.5) and (3.6), the current can be calculated as

$$I_{Primary} = \frac{VIN}{\omega M + \frac{(Z_{Couple} + R_{Source})Z_{Primary}}{\omega M}} \tag{3.7}$$

(3.6) shows that when

$$M = \frac{\sqrt{(Z_{Couple} + R_{Source})Z_{Primary}}}{\omega} \tag{3.8}$$

the current at the primary coil reaches the maximum. By combining (3.6) and (3.8), the maximum current can be calculated as

$$I_{Primary}(MAX) = \frac{VIN}{2\sqrt{(Z_{Couple} + R_{Source})Z_{Primary}}} \tag{3.9}$$

The above analysis, however, cannot guarantee the maximum power is delivered from the signal generator, because the impedance of the source has not yet been matched to the transmitter circuit. To solve this, a T impedance matching network is connected between the source and the transmitter circuit, as shown at the top circuit in Figure 3.1-4.

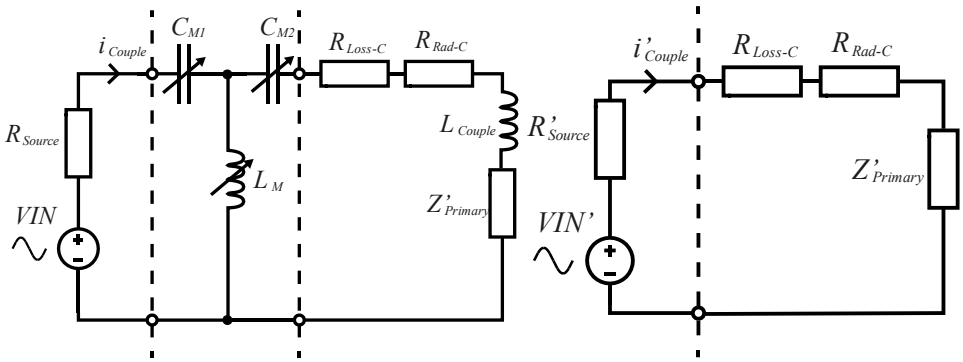

Figure 3.1-4 (Left) equivalent circuit of transmitter with a T impedance matching circuit (C_{M1}, C_{M2}, L_M) and (right) equivalent circuit from transmitter coils side. VIN' is the equivalent input voltage source of the equivalent circuit and Z'_{Source} is the equivalent source impedance.

According to [193] and [194], in Figure 3.1-4,

$$Z'_{Primary} = \frac{\omega^2 M^2}{Z_{Primary}} \tag{3.10}$$

$$Z_{Primary} = R_{Loss-P} + R_{Rad-P} \tag{3.11}$$

$$Z_{Couple} = R_{Loss-C} + R_{Rad-C} \tag{3.12}$$

Because of the impedance matching circuit,

$$R'_{Source} = Z_{Couple} + Z'_{Primary} \tag{3.13}$$

With the impedance matching network, from the transmitter coils side, the signal generator becomes a voltage source in series with a new source resistor R'_{Source}, as shown at the bottom circuit in Figure 3.1-4.

By combining (3.10) (3.11) (3.12) and (3.13),

$$R'_{Source} = R_{Loss-C} + R_{Rad-C} + \frac{\omega^2 M^2}{R_{Loss-P} + R_{Rad-P}} \tag{3.14}$$

Similar to (3.6), the current at the primary coil becomes

$$I'_{Primary} = \frac{VIN'}{\omega M + \frac{\left(R'_{Source} + Z_{Couple}\right) Z_{Primary}}{\omega M}} \tag{3.15}$$

By combining the (3.14) and (3.15), after some arrangements, the current at the primary coil becomes

$$I'_{Primary} = \frac{VIN'}{2\left(\omega M + \frac{Z_{Couple} Z_{Primary}}{\omega M}\right)} \tag{3.16}$$

(3.16) shows that when

$$M = \frac{\sqrt{Z_{Couple} Z_{Primary}}}{\omega} \tag{3.17}$$

the maximum current at the primary coil can be obtained from (3.16), which is

$$I'_{Primary}(MAX) = \frac{VIN'}{4\sqrt{Z_{Couple} Z_{Primary}}} \tag{3.18}$$

The voltage *VIN'* is the equivalent voltage source from the output port of the impedance matching circuit. Its actual value is dependent on the type and the component parameters of the chosen impedance matching circuit, which is discussed in Section 2.3.2.

For solenoid coils, the radiation resistance can be calculated as [195],

$$R_{Rad} = N^2 20\pi^2 \left(\frac{C}{\lambda}\right)^4 \tag{3.19}$$

- N is the number of turns of the solenoid coil
- C is the circumference of the turn of coil
- λ is the wavelength of the operational frequency

For solenoid coils with diameters within 30cm, the radiation resistance at a few MHz is at the milli-ohms level, which is much less than the coil AC resistance caused by heat loss (from a few ohms to a few tens of ohms). Therefore, the current in (3.18) can be simplified as

$$I'_{Primary}(MAX) = \frac{VIN'}{4\sqrt{R_{Loss-C} R_{Loss-P}}} \tag{3.20}$$

Even though the maximum current at the primary coil is obtained, it should be noted that the dependence of coil AC resistance on the coil physical shape parameters (coil diameter, gap interval, wire thickness, number of turns) will be different with different physical shapes.

3.1.3 The maximisation of magnetic field from a solenoid coil as the primary coil

Key aims of this section

- The strength of the magnetic field at the receiver is related to the dimensional parameters of the primary coil, which includes the turn number, the diameter, the gap interval and the wire thickness.
- A model of solenoid coil is built to predict the H_z at a distance from the coil based on the input voltage and the dimensional parameters.

- The magnetic field at the receiver from the primary coil can be regarded as a superposition of generated magnetic fields from multiple single-turn loops.
- Together with the expression of maximum primary coil current, the magnetic field at a distance from the primary coil can be calculated with the expression obtained from Biot-Savart Law.

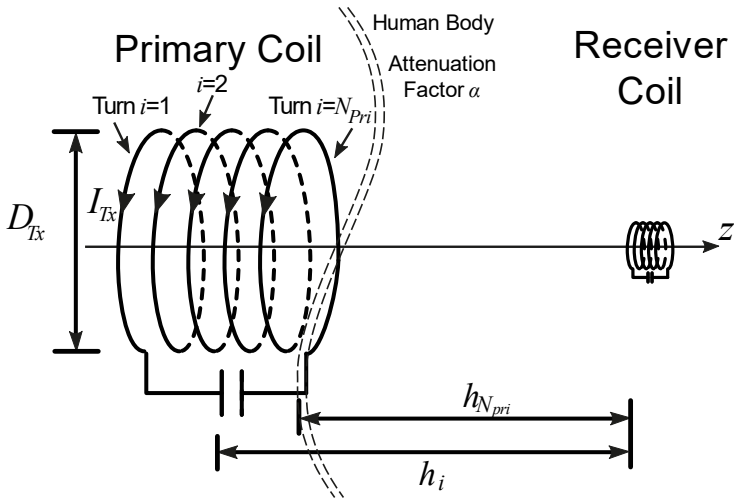

Figure 3.1-5 Schematic illustration of the relative position of primary coil and receiver coil and key parameters for magnetic field strength calculation

According to the Biot-Savart law, the magnetic field at the $\vec{z}$-direction generated by a single-turn loop can be calculated, which is discussed in 2.2.1. For a multiturn circular coil, as the primary coil shown in Figure 3.1-5, the generated magnetic field can be regarded as a superposition of the magnetic fields generated by each turn of coil, while every turn of coil can be regarded as a single-turn circular closed loop. Therefore, with media attenuation considered, the generated magnetic field of the primary coil at a distance h on the $\vec{z}$-axis can be derived from equation (2.17) and (2.149), and thus becomes

$$H_z = \left\{ \sum_{i=1}^{N_{Pri}} \frac{I_{Primary} \left(\frac{D_{Pri}}{2}\right)^2}{2\left[\left(\frac{D_{Pri}}{2}\right)^2 + h_i^2\right]^{\frac{3}{2}}} \right\} e^{-\alpha h_{N_{Pri}}} \tag{3.21}$$

where

- H_z is the magnetic field strength generated by the primary coil at the z-direction
- N_{Pri} is the number of turns of the primary coil
- $I_{Primary}$ is the RMS current flowing at the primary coil
- D_{Pri} is the diameter of the primary coil

- h_i is the distance between the turn i and the receiver
- $h_{N_{Pri}}$ is the distance between the turn N_{pri} and the receiver
- α is the attenuation factor

From (3.20), the current I_{Pri} can be calculated as

$$I'_{Primary} = \frac{VIN'}{4\sqrt{R_{AC-C}R_{AC-P}}} \tag{3.22}$$

In the expression,

- VIN' is the RMS input voltage to the coupling coil
- R_{AC-C} is the AC resistance of the coupling coil
- R_{AC-P} is the AC resistance of the primary coil

By combining (3.21) (3.22), the strength of the magnetic field generated by the primary coil at a distance on the axis from the primary coil can be calculated,

$$H_z = \left\{ \sum_{i=1}^{N_{Pri}} \frac{\frac{VIN'}{4\sqrt{R_{AC-C}R_{AC-P}}} \left(\frac{D_{Pri}}{2}\right)^2}{2\left[\left(\frac{D_{Pri}}{2}\right)^2 + h_i^2\right]^{\frac{3}{2}}} \right\} e^{-\alpha \cdot h_{N_{Pri}}} \tag{3.23}$$

The parameters are categorised in Table 3.1-2.

Parameters from the primary coil		Parameters from the media and conductor	
Name	Symbol	Name	Symbol
wire diameter	d_{wire}	resistivity of the wire	ρ_{wire}
RMS input voltage to the coupling coil	VIN'	resistivity of the media (human body)	ρ_m
operational frequency	f	relative dielectric constant of the media (human body)	ε_r
number of turns of the primary coil	N_{Pri}	relative permeability of the media (human body)	μ_r
gap interval between every two turns at the primary coil	p		
diameter of the primary coil	D_{Pri}		
distance between the end of the primary coil and the receiver coil (transfer distance)	$h_{N_{Pri}}$		

Table 3.1-2 List of parameters of the expression

Now that we have a theoretical model of the magnetic field, it is important to find out how well it reflects reality. In the next section, the theoretical results obtained from

this model will be compared with the experimental results obtained from the measurement of the magnetic field generated by actual solenoid coils in different dimensional parameters.

3.1.4 Comparison of magnetic field strength between theoretical results and measurement

Key aims of this section

- The magnetic field strengths are measured against a range of distance from the primary coil in the experiment.
- Three different parametric setups are done: variable primary coil diameters, variable gap interval between turns and variable number of turns.
- Experimental results are compared against the theoretical results.

3.1.4.1 Experiment apparatus setups and calculation parameters

As shown in Figure 3.1-6, the experiment devices consist of a signal generator, a power amplifier, an impedance matching network, the transmitter coils, a magnetic field probe and a spectrum analyser. The detailed series and functions of the devices are listed in Table 3.1-3. The pictures of the devices are shown in Appendix A1.

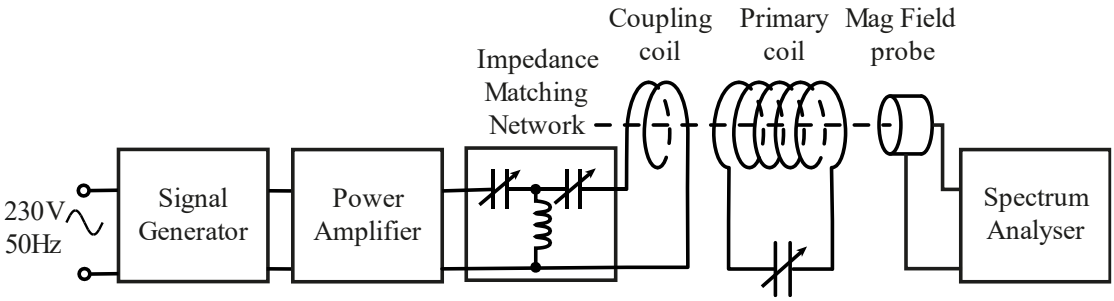

Figure 3.1-6 Experimental setup for measuring magnetic field strength generated by transmitter, with the primary coil in the figure as transmitter coil

During the experiments, the variable capacitor is adjusted for each coil so that the L-C circuit can resonate at the same frequency. The distance between the coupling coil and the primary coil is adjusted for each coil for best coupling. The signal generator and the impedance matching network are set so that the RMS input voltage of the coupling coil is 1 V, and the output frequency is 8.33MHz, which is in the operational range of the power amplifier. The magnetic field probe is located at the axis of the primary coil. The spectrum analyser is set to measure the strength of the magnetic field. The signal generator, power amplifier and the spectrum analyser are grounded. A connection is made with coaxial cables. The parameters in the experiment are listed in Table 3.1-4.

Device	Series	Functions
Signal generator	FeelTech FY3200S	Generate input sinusoidal signals at a specific frequency
Power amplifier	EATON 5001 (0.01 to 10 MHz)	Amplify the power of the input signal
Magnetic field probe	HP11941A	Measure the magnetic field and output the reading at a spectrum analyser
Spectrum analyser	HP8568B (100 Hz to 1.5 GHz)	Obtain the magnetic field strength measurement readings

Table 3.1-3 List of devices used in the experiments. Pictures of the devices are shown in Appendix A1.

Name	Symbol	Value
wire diameter	d_{wire}	1 mm
RMS input voltage to the coupling coil	VIN'	1 V
operational frequency	f	8.33 MHz
resistivity of the wire (copper)	ρ_{wire}	$1.72\times10^{-8}\ \Omega\cdot m$

Table 3.1-4 List of values for parameters in the calculation

3.1.4.2 Variable primary coil diameters

The magnetic field strength against transfer distance is measured from three different primary coil diameters, which are 20 cm, 30 cm and 40 cm, respectively. All the coils have 4 turns and a gap interval of 1 cm between turns. Figure 3.1-7 shows the measurement results and the theoretical results for each test. The measurement results have an error of 0.5 dBA/m, and they agree with the calculation results closely.

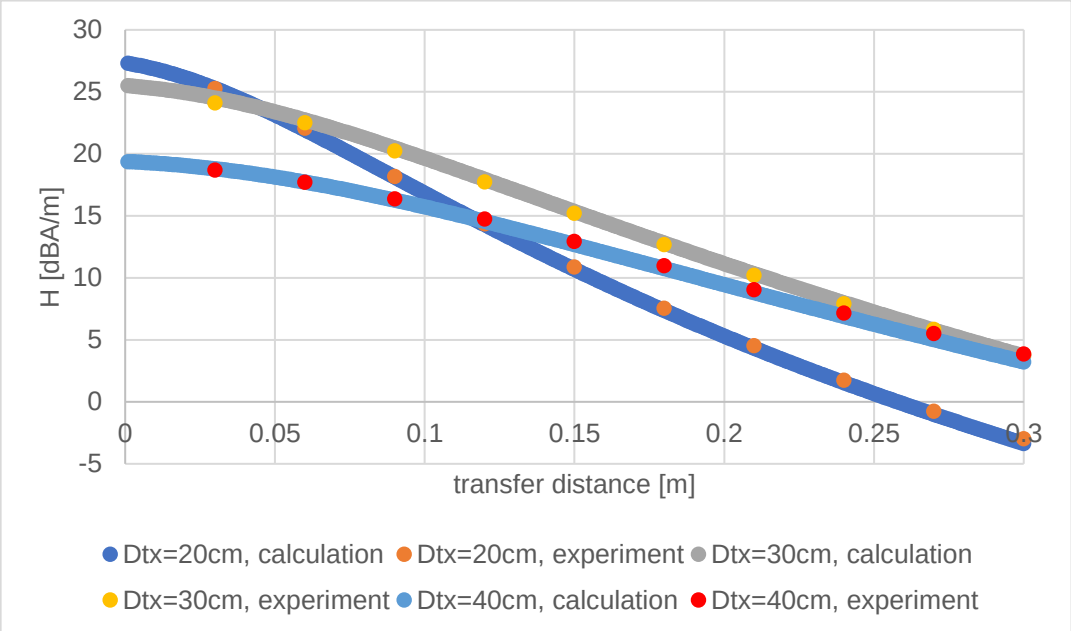

Figure 3.1-7 Comparison of theoretical result and experimental result of magnetic field strength in a transfer distance ranging between 0 and 30 cm from a solenoid transmitter coil with a gap interval of 1 cm, and 4 turns and three different diameters 20 cm 30 cm and 40 cm

As shown in Table 3.1-5, the root-mean-square errors (RMSE) between the measurement results and theoretical results of the three tests are all around 0.1 and

0.2 dBA/m, which is less than 2% of the average of the obtained measurement results. However, RMSE puts higher weight in the results with high values and cannot reflect the difference between results with lower values. To solve this problem, the standardised root-mean-square error (SRMSE) is calculated. It divides the error by the corresponding measurement result before squaring to balance the weight of error for all values. As shown, the SRMSE of D_{Tx}=40 cm is higher because of the higher measurement results in the distance 27 cm and 30 cm.

Experiments	D_{Tx}=20 cm	D_{Tx} =30 cm	D_{Tx} =40 cm
RMSE (dBA/m)	0.106	0.193	0.211
SRMSE	0.037	0.014	0.041

Table 3.1-5 Root-mean-square error (RMSE) and standardised root-mean-square error (SRMSE) between the theoretical results and the experimental results for the variable primary coil diameters test

In a whole, the theoretical model of the primary coil has produced results with good agreement to the experimental results fora transfer distance within 30 cm when N=4 and p=1 cm for solenoid coil.

3.1.4.3 Variable gap interval between turns on primary coil

In this test, the magnetic field strength against transfer distance is measured from three different gap intervals between turns of the primary coil. The gap intervals are 1 cm, 3.5 cm and 5.5 cm, respectively. All the coils have 4 turns and a diameter of 30 cm. As shown in Figure 3.1-8, for all three gap intervals, the measurement results show good agreements with the theoretical results for a distance range within 24 cm.

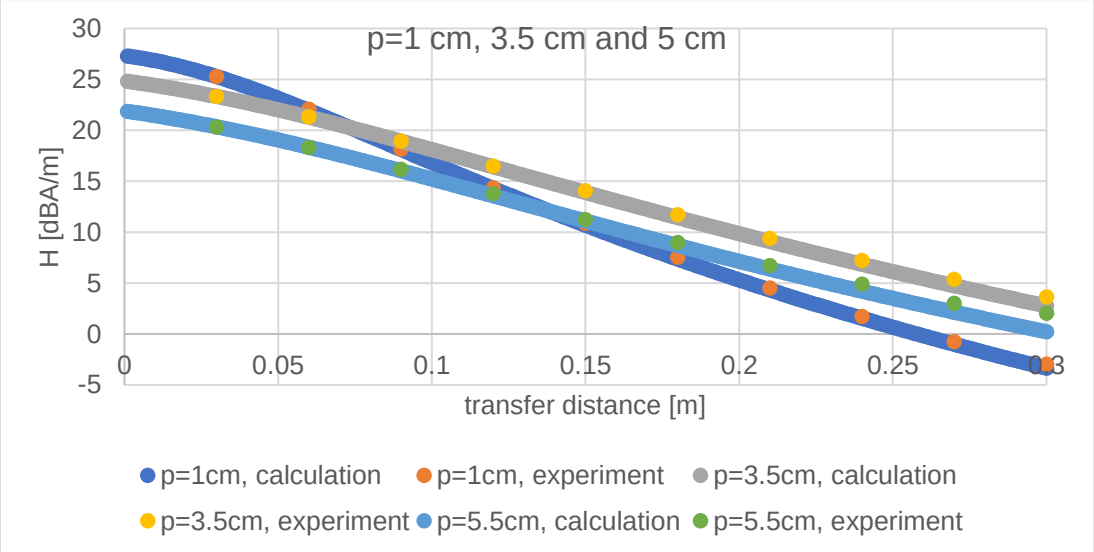

Figure 3.1-8 Comparison of the theoretical result and experimental result of the magnetic field strength in a transfer distance ranging between 0 and 30 cm from a solenoid transmitter coil with a diameter of 30 cm, and 4 turns and three different gap intervals 1 cm, 3.5 cm and 5.5 cm

The experiment results have an error of 0.5 dBA/m. As seen in Table 3.1-6, the SRMSEs within 24 cm for all three gap intervals are very small, which are all less than

2.5%. However, for distance more than 24 cm, the measurements are obviously higher than the theoretical results, especially for p=3.5 cm and p=5.5 cm. These contribute to a much higher overall SRMSE for these two tests, which are almost 5 times and 10 times higher than the SRMSEs within 24 cm, respectively. The reason for these can be that as the length of the solenoid coil becomes larger, the effect from the midfield region components becomes more obvious at the same transfer distance near the midfield region, which is discussed in Section 2.3.4.1. As the theoretical model has not involved the midfield region components, the theoretical results are lower than the measurement results near the midfield region.

Experiments	p=1 cm	p=3.5 cm	p=5.5 cm
RMSE (dBA/m)	0.193	0.319	0.322
SRMSE	0.014	0.074	0.215
SRMSE within 24 cm	0.010	0.015	0.024

Table 3.1-6 RMSE and SRMSE between the theoretical results and the experimental results for the variable primary coil gap interval test

From the comparisons in Section 3.1.4.1 and Section 3.1.4.2, it can be seen that the experiment results and calculation results have better agreement for a smaller coil diameter, a narrower gap interval and a shorter transfer distance. For a gap interval between turns less than 5.5 cm, the measurement results and the theoretical results show good agreement when the transfer distance is less than 24 cm for the solenoid coil with 4 turns and a diameter of 30 cm. The difference between measurement results and calculation results become larger when the value of the parameters (i.e., transfer distance, gap interval, coil diameter) increases. For example, the 40cm-diameter coil will have a large difference between measurement results and calculation results with p=5.5 cm than the 30 cm-diameter coil with the same gap distance at 30 cm transfer distance. Therefore, for accurate prediction of magnetic field strength, the range of parameters of the built model should be constrained. In detail, the transfer distance should be less than 24 cm, the gap interval should be less than 5.5 cm, and the coil diameter should be less than 30 cm.

3.1.4.4 Variable number of turns on primary coil

In this test, the magnetic field strength against transfer distance is measured from four different numbers of primary coil turns. The numbers of turns are 2, 4, 6, and 8, respectively. All the coils have a gap interval 1 cm and a diameter of 20 cm.

Figure 3.1-9 shows the experiment results with an error of 0.5 dBA/m, and the measurements agree well with the calculation results for the tested numbers of turns.

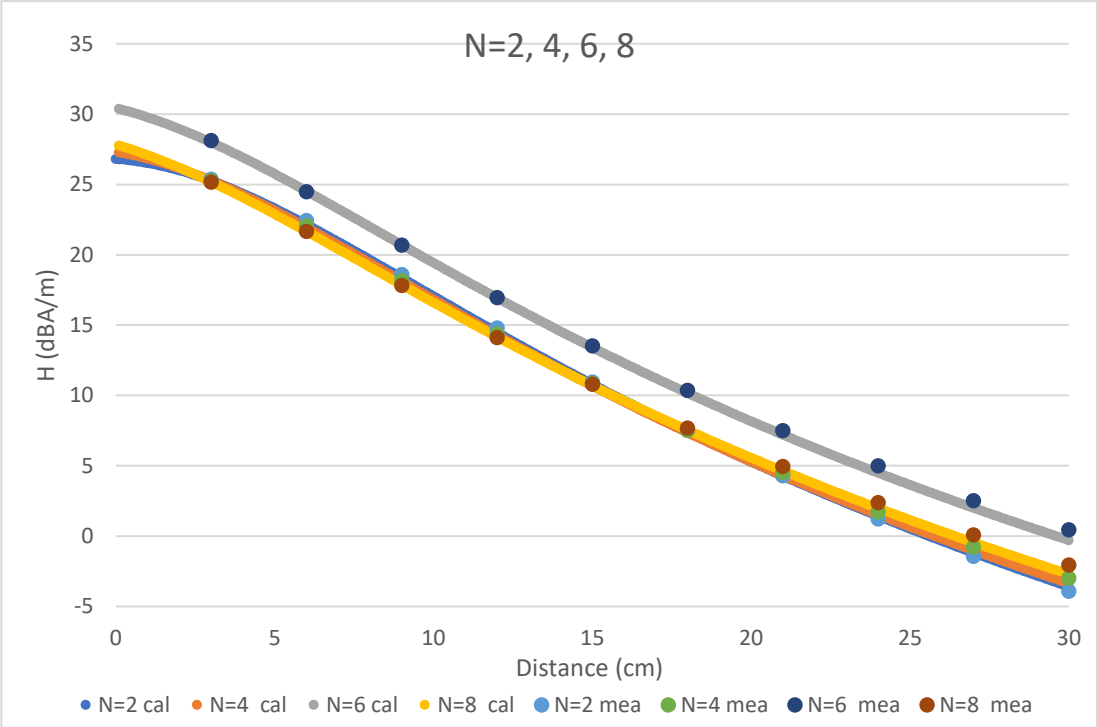

Figure 3.1-9 Comparison of theoretical result and experimental result of magnetic field strength in a transfer distance ranging between 0 and 30 cm from solenoid transmitter coils with a diameter of 20 cm, gap interval of 1 cm and number of turns of 2, 4, 6, and 8. Cal is calculation; Mea is measurement.

However, in the Table 3.1-7, it can be seen that the Standardised Root-Mean-Square Errors (SRMSEs) for the tests of 2, 6, 8 turns are all comparatively high, especially for the test of 8 turns, which reaches up to 1.277. The reason for these owes to the measurement errors at some samples. For example, the difference/measurement result at 27 cm for turns of 8 is up to 16.2, which has pulled up the overall SRMSE value. If the most outstanding error for each test is taken away, a much lower SRMSE value is obtained for each test. As can be seen, the SRMSE of the 8-turn test drops from 1.277 to 0.089, and for the 6-turn test, from 0.322 to 0.035. The SRMSE of 2-turn test, however, remains at around 0.15. If observed carefully, it can be found that there are actually two measurements that are vastly different from theoretical results, which are located at 24 cm and 27 cm. If both of them are taken away, the SRMSE becomes 0.062, which is in the acceptable range.

Experiments	N =2	N =4	N =6	N =8
RMSE (dBA/m)	0.386	0.106	0.250	0.254
SRMSE	0.207	0.037	0.322	1.277
SRMSE without the most outstanding error	0.15	0.024	0.035	0.089

Table 3.1-7 RMSE and SRMSE between the theoretical results and the experimental results for the variable primary coil turn test

Another thing to be noted is that the difference between measurements and theoretical results tends to be larger at a greater transfer distance (>25 cm), which is

similar to the difference of results obtained in different gap interval. As discussed, the reason can be owing to the “heavier” mid-range field component at a far distance, which is not involved in the theoretical model.

Overall, the measurement results and the theoretical results have good agreements in a number of turns ranging from 2 to 8 of the primary coil with a diameter of 20 cm and a gap interval between turns of 1 cm.

3.1.5 Summary of this section

In this section, a theoretical model has been developed to estimate the magnetic field strength at the axis of a solenoid coil with a single-turn coupling coil based on L-C resonance circuit theory and bidirectional reflectance impedance analysis. With the dimensional and electrical parameters of the wire and of the solenoid coil and an input voltage, the magnetic field strength at the axis of the coil can be calculated. The theoretical calculation results are compared with the experiment measurement results in transfer distances between 0 and 30 cm. For variable coil diameters (20 cm, 30 cm, 40 cm), the difference is less than 4.1%; for variable gap intervals between turns (1 cm, 3.5 cm, 5.5 cm), the difference is less than 2.4%; for a variable number of turns (2, 4, 6, 8), the difference is less than 15%. Because of the limited time and resource, only a limited number of variations in coil dimensional parameters have been tried. However, it is shown that the theoretical model is good enough to simulate the magnetic field strength for a solenoid coil with a diameter up to 40 cm, gap interval up to 5.5 cm, number of turns up to 8 at a transfer distance up to 24 cm or 30 cm depending on the length of the coil. These dimensional parameter ranges are sufficient in the design of the weakly coupled wireless power transfer system for micro-implants. Using this model, the optimum dimensional parameters of the solenoid coil can be predicted for a certain transfer distance, which will be discussed in the next section.

3.2 Transmitter design

Key aims of this section

- To determine the optimum set of parameters for the transmitter coil, the dependency relations between the parameters are theoretically analysed based on the formulas developed in Section 3.1.
- Based on the dependency relations between the parameters, a “design flow” for a solenoid transmitter is introduced.
- Optimum sets of parameters for the transmitter coil for different transfer distances are calculated.

3.2.1 Introduction

In the previous section, a theoretical model of the magnetic field around coupled solenoidal coils was introduced and verified by experiment for a range of coil dimensions. Based on this model, it is possible to determine the optimum dimensional parameters to obtain the highest magnetic field strength at specific transfer distances, so that a weakly coupled receiver coil in the wireless power transfer system can receive the highest possible power.

However, before the calculation, it will be helpful to find out how the parameters affect one another to obtain the highest magnetic field strength. In other words, if one of the parameters changes, do the other parameters need to change to obtain the highest field strength? These “co-dependencies” are theoretically predicted using the formulas developed in Section 3.1.

Based on the “co-dependencies” between parameters, a design flow to obtain the optimum dimensional parameters for certain distances can thus be obtained. This also leads to the design flow of the transmitter side of the weakly coupled wireless power transfer system. From this, the optimum parameters of the transmitter for different transfer distances can be calculated.

3.2.2 Co-dependencies between parameters

From Section 3.1.3, it is known that there are eleven parameters in the theoretical model. They are shown again in Table 3.2-1. It should be noted that not all the parameters need to be analysed as the focus in this section is the dimensional parameters of the primary coil. Therefore, the co-dependencies among four of the parameters are especially investigated. They are shown in Table 3.2-2.

Parameters from the primary coil		Parameters from the media and conductor	
Name	**Symbol**	**Name**	**Symbol**
wire diameter	d_{wire}	resistivity of the wire	ρ_{wire}
RMS input voltage to the coupling coil	VIN	resistivity of the media (human body)	ρ_m
operational frequency	f	relative dielectric constant of the media (human body)	ε_r
number of turns of the primary coil	N_{Pri}	relative permeability of the media (human body)	μ_r
gap interval between two turns at the primary coil	p		
diameter of the primary coil	D_{Pri}		
distance between the end of primary coil and the receiver coil (transfer distance)	$h_{N_{Pri}}$		

Table 3.2-1 List of parameters in the theoretical model for generated magnetic field strength in Section 3.1.3

number of turns of the primary coil	N_{Pri}
gap interval between two turns at the primary coil	p
diameter of the primary coil	D_{Tx}
distance between the end of primary coil and the receiver coil (transfer distance)	$h_{N_{Pri}}$

Table 3.2-2 Dimensional parameters of the solenoid coil that are investigated

The co-dependencies among these parameters will be investigated in the following order

(1) D_{Tx}-h_{NPri}, D_{Tx}-N_{pri}, D_{Tx}-p

(2) p-N_{pri}, p-h_{NPri}

(3) N_{pri}-h_{NPri}

The co-dependencies between the primary coil diameter and the transfer distance, the coil turn number and the gap interval between turns will be simulated first. Then, the co-dependencies between gap interval and coil turn number and transfer distance will be simulated. Lastly, the co-dependency between turn number and the transfer distance will be simulated.

Because the attenuation factor in the magnetic field strength model is independent of the dimensional parameters of the primary coil, to simplify the calculation, these

simulations will exclude the attenuation factor in the media. Therefore, the parameters related to the human body will not be involved.

The other parameters will be set as in Table 3.2-3.

Name	Symbol	Value
wire diameter	d_{wire}	1 mm
input voltage to the coupling coil	VIN	1 V_{RMS}
operational frequency	f	8.33 MHz
resistivity of the wire (copper)	ρ_{wire}	$1.72 \times 10^{-8} \Omega \cdot m$

Table 3.2-3 List of values for other parameters in the simulations

3.2.2.1 D_{Tx}-h_{NPri}, D_{Tx}-N_{pri}, D_{Tx}-p

Key points of this section

- The transfer distance between the primary coil and the secondary receiver coil plays a decisive role in determining the optimum primary coil diameter; a longer distance needs a larger size of primary coil.
- With the other parameters being the same, a larger number of coil turns needs a larger optimum size of primary coil; while for the same size of primary coil, a larger number of coil turns does not always mean stronger field strength.
- With the other parameters fixed, a larger coil separation needs a larger size of primary coil to optimise power transfer.

(1) D_{Tx}-h_{NPri}

In this simulation, the primary coil diameter is the primary independent variable, and the transfer distance is the secondary independent variable. The number of turns on the primary coil is set to 4, and the gap interval between turns is set to 1 cm.

Figure 3.2-1 shows that the generated magnetic field strength (H) as a function of primary coil diameters (D_{Tx}) for a range of transfer distances (h_{Npri}). The transfer distances are set to 10 cm, 15 cm, 20 cm and 25 cm, respectively. The primary coil diameter is within the range of 0 to 0.5 m. For example, the top blue line is the magnetic field strength at a transfer distance of 10 cm when the diameter of the primary coil varies from 0 to 0.5 m, with other parameters remaining the same.

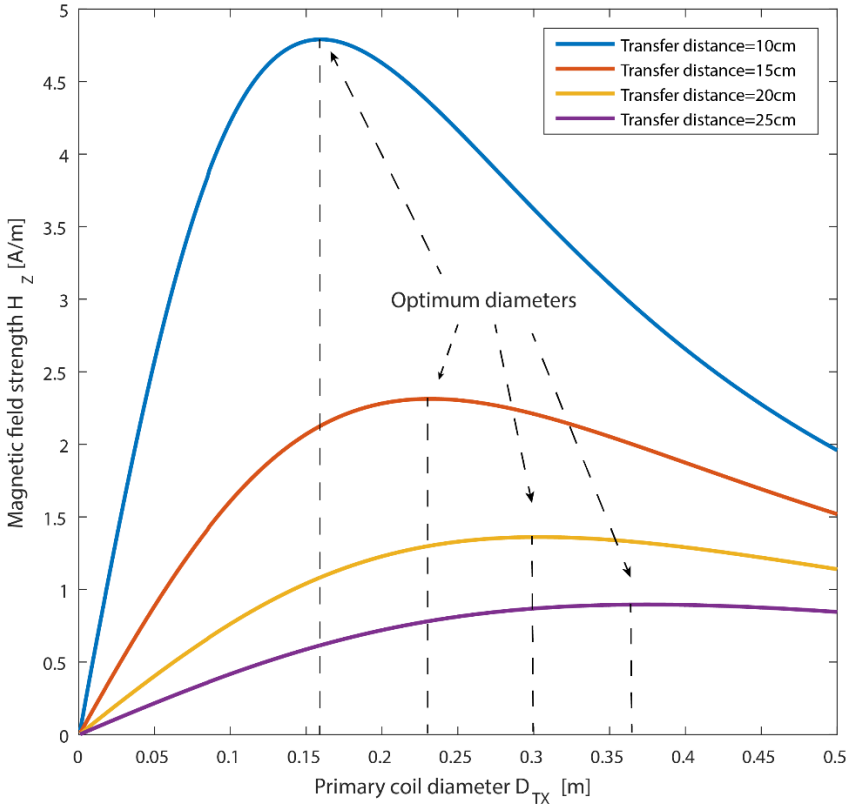

Figure 3.2-1 Magnetic field H_z vesus the primary coil diameter D_{Tx} for different lengths of tansfer distance h_{Npri} with number of coil turns N_{Pri} = 4, gap interval p =1 cm and input voltage VIN = 1 V_{RMS}

For a fixed number of coil-turns and gap interval, the optimum primary coil diameter to achieve the highest magnetic field strength will change with transfer distance. The optimum primary coil diameters are shown in Table 3.2-4. As the target transfer distance increases, the optimum diameter increases. For N_{pri}=4, the ratio between the optimum diameter and the transfer distance D_{TX}/h_{Npri} is around 1.5. The ratio decreases as the transfer distance increases. The value of the ratio is also dependent on the number of turns and gap interval between turns. When the number of turns doubles to 8, the optimum diameter value for each transfer distance increases. The ratio D_{TX}/h_{Npri} decreases from 1.72 to 1.58 as the transfer distance increases from 0.10 m to 0.25 m.

Transfer distance h_{Npri} (m)	0.10	0.15	0.20	0.25
Optimum diameter (m) for N_{Pri} = 4	0.158	0.230	0.300	0.364
D_{TX}/h_{Npri} for N_{Pri} = 4	1.58	1.53	1.5	1.46
Optimum diameter (m) for N_{Pri}=8	0.172	0.254	0.327	0.394
D_{TX}/h_{Npri} for N_{Pri} =8	1.72	1.69	1.64	1.58

Table 3.2-4 Optimum diameter values for different transfer distances with number of coil turn N_{Pri} = 4 and 8, gap interval p = 1 cm and input voltage VIN = 1 V_{RMS}

(2) D_{Tx}-N_{pri}

In this simulation, the primary coil diameter is the primary independent variable, and the number of primary coil turns is the secondary independent variable. The transfer distance is 10cm, and the gap interval between turns is set to 1 cm.

Figure 3.2-2 shows that the generated magnetic field strength at the certain numbers of turns by the transmitter with a range of primary coil diameter. The numbers of turns are set to 1, 3, 5, 7 and 9, respectively. The primary coil diameter is within the range of 0 to 0.5 m. For example, the top green line is the generated magnetic field strength at a transfer distance of 10 cm by a 9-turn primary coil when the diameter of the primary coil varies from 0 to 1 m and the gap interval is set to 1cm.

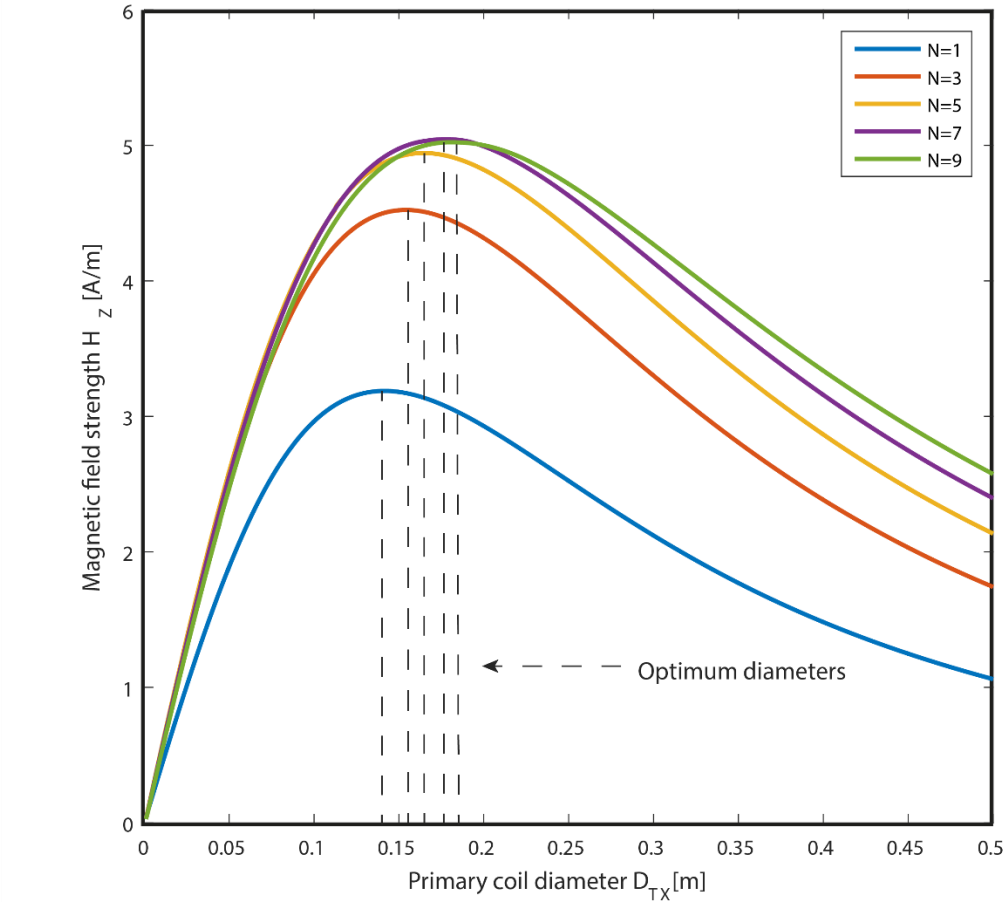

Figure 3.2-2 Magnetic field H_z versus primary coil diameter at different numbers of coil turn N_{Pri} with transfer distance h_{Npri} = 10 cm, gap interval p = 1 cm and input voltage VIN = 1V $_{RMS}$

Table 3.2-5 shows that the optimum diameters increases as the number of primary coil turns increases, which agrees with the result found in Table 3.2-4, where the number of turns changes from 4 to 8. This means that, in the design of primary coil, if the number of coil turns is adjusted, the coil diameter is needed to change as well to achieve the highest generated magnetic field strength.

Turn number N_{Pri}	1	3	5	7	9
Optimum diameter (m)	0.143	0.154	0.164	0.172	0.182

Table 3.2-5 Optimum diameter values for different numbers of coil turn with the transfer distance = 10 cm, the gap interval p = 1 cm and the input voltage VIN = 1 V_{RMS}

Another thing to notice is that the magnetic field strength is not proportional to the number of turns at the same primary coil diameter. When D_{Tx} is less than 0.19 m, the magnetic field strength for N_{pri}=7 is higher than the strength for N_{pri}=9, while for D_{Tx}>0.19 m, the magnetic field strength for N_{pri}=7 is lower than the strength for N_{pri}=9. This indicates that the number of turns is not “the more, the better”, and different values of diameter need different optimum numbers of turns to achieve maximum magnetic field strengths. The reason for this is that the decrease of magnetic field strength caused by the increase of AC resistance of the coil overpowers the increase of magnetic field strength caused by the increase of the number of turns at a high number of turns. Because the gap interval is a finite value, the extra turns are further away from the receiver. The increase of field strength at the receiver caused by the extra turns is thus weaker. The extra AC resistance caused by the extra turns lowers the current amplitude in the primary coil, causing the overall magnetic field to decrease.

Moreover, the difference between two adjacent lines narrows as the number of turns increases, which indicates that the increase of turns will have a saturation effect up to a certain number of turns, with which the increase of turn number will have little effect or even negative effect on the increase of magnetic field strength. The reason for this is the same as the one mentioned in the last paragraph, which is mainly due to the increase in AC resistance when the turn number increases.

(3) D_{Tx}-p

In this simulation, the primary coil diameter is the primary independent variable, and the gap interval is the secondary independent variable. The transfer distance is 10cm, and the number of turns is set to 4.

Figure 3.2-3 shows the generated magnetic field strength by the transmitter at different values of gap interval with a range of primary coil diameters. The gap intervals p is set to 2 mm, 4 mm, 6 mm, 8 mm and 10 mm, respectively. The primary coil diameter is within the range of 0 to 0.5 m. For example, the top red line is the generated magnetic field strength at a transfer distance of 10 cm by a 4-turn primary coil when the diameter of the primary coil varies from 0 to 0.5m, and the gap interval is set to 4 cm.

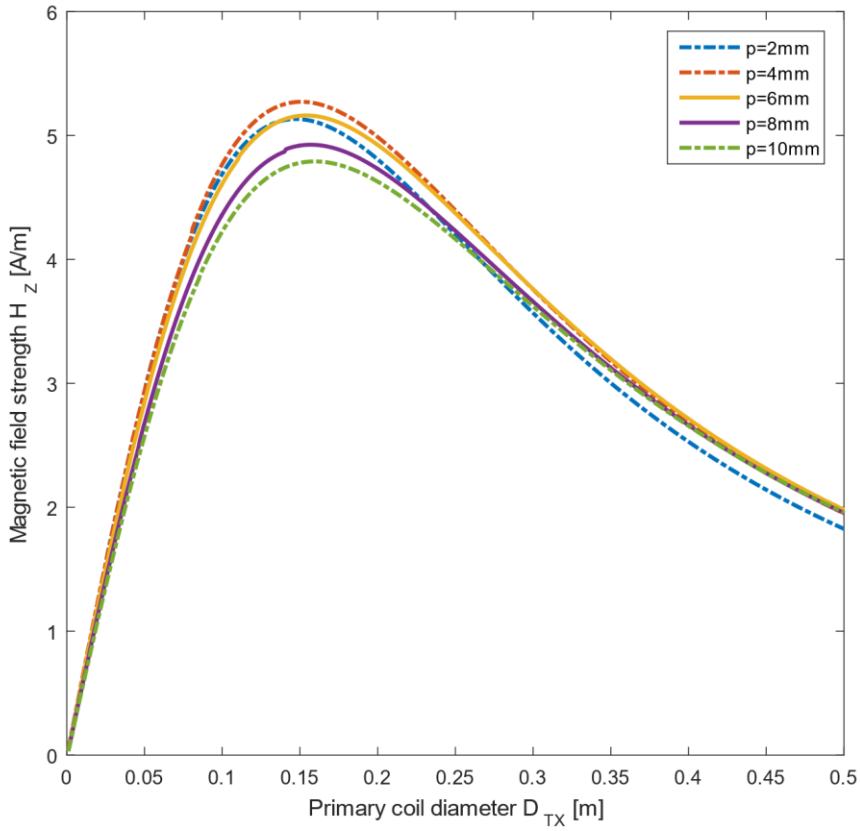

Figure 3.2-3 Magnetic field H_z versus primary coil diameter at different gap interval p with transfer distance h_{Npri} = 10 cm, numbers of coil turn N_{Pri} = 4 and input voltage VIN = 1 V_{RMS}

Table 3.2-6 shows that the optimum primary coil diameter to achieve the highest magnetic field strength increases as the gap interval p increases, which means the optimum gap interval is not independent of the coil diameter. When adjusting the primary coil gap interval, the primary coil diameter will need to adjust correspondingly to get the highest field strength.

Gap interval p (mm)	2	4	6	8	10
Optimum diameter (m)	0.146	0.151	0.155	0.156	0.159

Table 3.2-6 Optimum diameter values for different gap intervals p with the transfer distance = 10 cm, the number of coil turn N_{Pri} = 4 and the input voltage VIN = 1 V_{RMS}

Moreover, Figure 3.2-3 shows that there is a value of gap interval that will achieve a maximum magnetic field strength when other parameters are fixed, while other values of gap interval near the stationary value will have lower magnetic field strengths. As shown in Figure 3.2-3, the highest magnetic field strength is achieved at H_{max}(p=4 mm), while the magnetic field strength of other gap intervals are all lower than this value. This means that as the gap interval p increases from 2 mm, H_{max} will increase first, reach the highest value at a value of gap interval, and then decrease as the gap interval continues to increase. The reason for these is that for the gap interval lower than the stationary value, the proximity effect plays a dominant role, causing the AC resistance to increase “quickly” as the gap interval narrows, which is discussed in

Section 2.3.3.4 and can be observed in Figure 2.3-27; for the gap interval higher than the stationary value, the coil turns become further away from the field measurement point as the gap interval increases, causing the superposition of magnetic field to be weaker. This phenomenon will be revisited in the next section, where the gap interval will be the primary independent variable.

3.2.2.2 p-N, p-h_{NPri}

Key points of this section

- The gap interval between primary coil turns is independent of the transfer distance.
- Because of the proximity effect, close wound coils are not optimum.
- Because the distance between the receiver and the turns of the primary coil increases as the gap interval increases, the magnetic field will become weaker if the gap interval becomes too large.
- With the other parameters being the same, different numbers of turns have the same optimum value of the gap interval. For different values of gap interval, the optimum number of turns can be different.

(1) *p-h_{NPri}*

In this simulation, the gap interval is the primary independent variable, and the transfer distance is the secondary independent variable. The primary coil diameter is 10cm, and the number of turns is set to 4.

Figure 3.2-4 shows the magnetic field strength generated by the transmitter at different transfer distances with a range of primary coil gap intervals. The transfer distances h_{Npri} are set to 10 cm, 15 cm and 20 cm, respectively. The gap interval is within the range of 0 to 0.02 m. For example, the top blue line is the generated magnetic field strength at a transfer distance of 10 cm by a 4-turn primary coil when gap interval varies from 0 to 0.02 m, and the coil diameter is set to 10 cm. The discontinuity of the lines is due to the discrete parameters related to gap interval in the calculation of AC resistance, which has been discussed in Section 2.3.3.

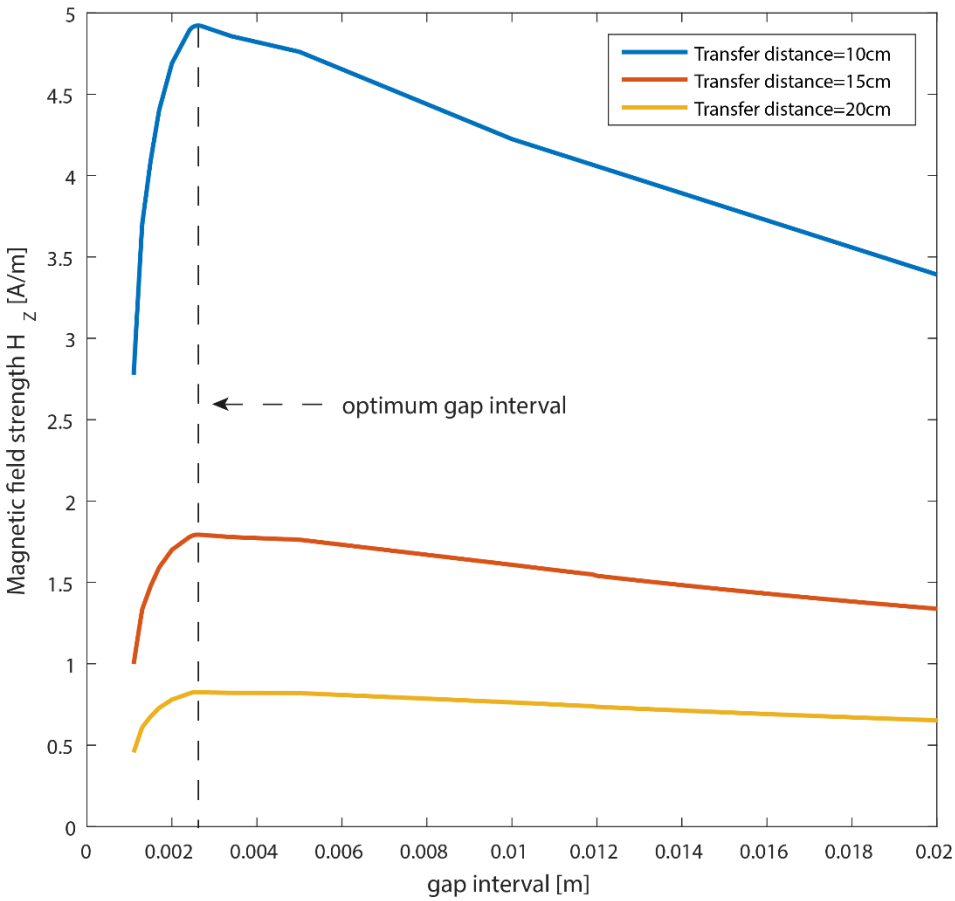

Figure 3.2-4 Magnetic field H_z versus gap interval at different transfer distances with input voltage VIN=1 V_{RMS}, number of turns N_{Pri} = 4 and primary coil diameter=10 cm

The magnetic field strength increases when the gap interval increases from 1 mm to 2.52 mm and then decreases when the gap interval continues to increase. The reason for this has been discussed in the last section. For the transfer distances analysed here, the optimum gap interval is the same. Actually, the optimum gap interval to give the maximum magnetic field strength is the same for the whole range of transfer distance in consideration, which is expected, because with the diameter and coil turn number being the same, there is no additional field for superposition due to the change of gap interval. Because all the magnetic fields experience the same decrease against transfer distance to the power of three on the axis, and the coil with the highest field strength at one position on the axis should also have the highest field strength in all other positions. Therefore, it can be confirmed that the gap interval is independent of the transfer distance.

(2) p-N

In this simulation, the gap interval is the primary independent variable, and the number of turns is the secondary independent variable. The primary coil diameter is 10 cm, and the transfer distance is 10 cm.

Figure 3.2-5 shows the generated magnetic field strength by the transmitter at different numbers of turns with a range of primary coil gap intervals. The numbers of turns are set to 3, 6 and 9, respectively. The gap interval is within the range of 0 to 0.02 m. For example, the top yellow line is the generated magnetic field strength at a transfer distance of 10 cm by a 9-turn primary coil when the gap interval varies from 0 to 0.02 m, and the coil diameter is set to 10 cm.

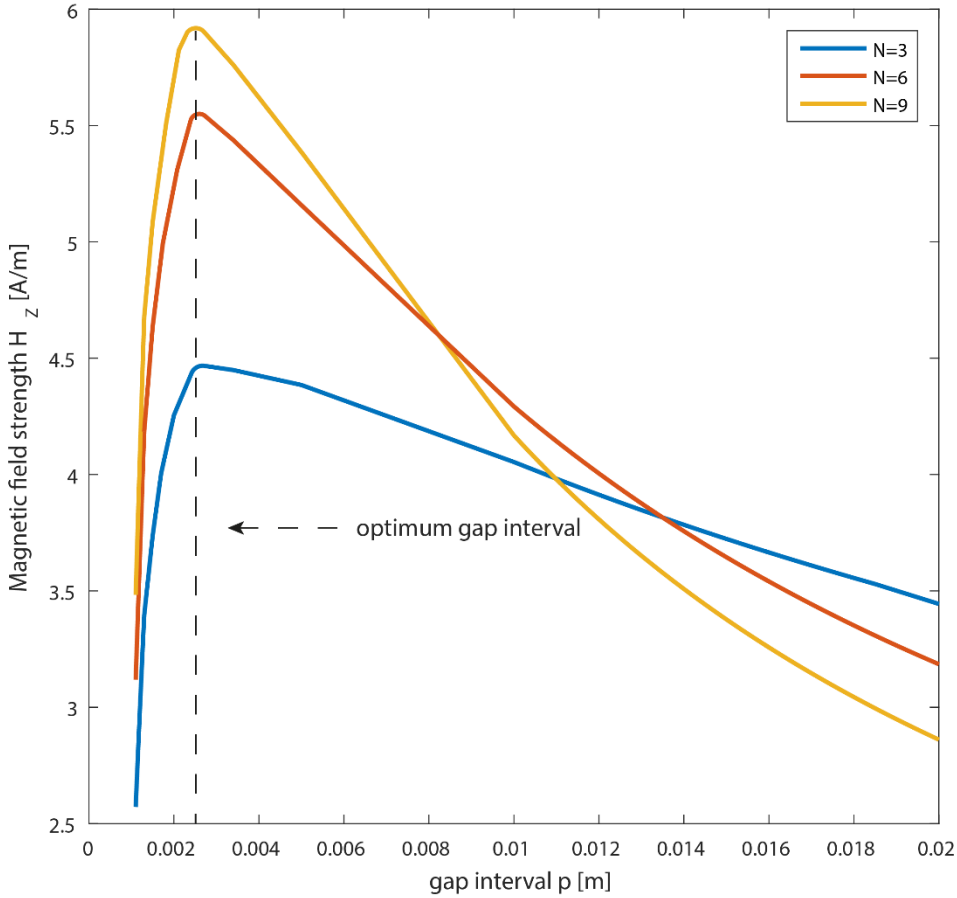

Figure 3.2-5 Magnetic field H_z against gap interval at different numbers of turns N_{Pri} with input voltage VIN=1 V_{RMS}, transfer distance h_{Pri}=10 cm and primary coil diameter D_{Pri} = 10 cm

The optimum gap intervals for the three different numbers of turns analysed here are the same to achieve the maximum magnetic field strength. However, this is not always the case. In Figure 3.2-6, with a diameter of 30 cm, for N_{pri}=3, 4 and 5, the optimum gap interval is 5.01 mm, while for N_{pri}=9, the optimum gap interval is 2.52 mm. By observation of different sets of simulations, it can be found that for coils with small diameters, the optimum gap interval will remain the same as the number of turns increase; for larger coils, the optimum gap interval will be one value for small numbers of turns, but it gradually shifts to another value as the number of turns increases. The problem is that due to the limitation of the theoretical model developed in this thesis, the calculations are presented in a discontinuous manner, which makes it difficult to observe the real trends of the change. However, it can be safely confirmed that the

optimum gap interval will increase for large coils when the number of turns decreases. For smaller coils, the change in the optimum gap interval due to the change of turn number is possibly too small that it is covered by the discontinuity in calculation. Once the change in the turn number is large enough, the change of optimum gap interval will be revealed. Therefore, it can be concluded that the change in the number of turns will affect the value of the optimum gap interval.

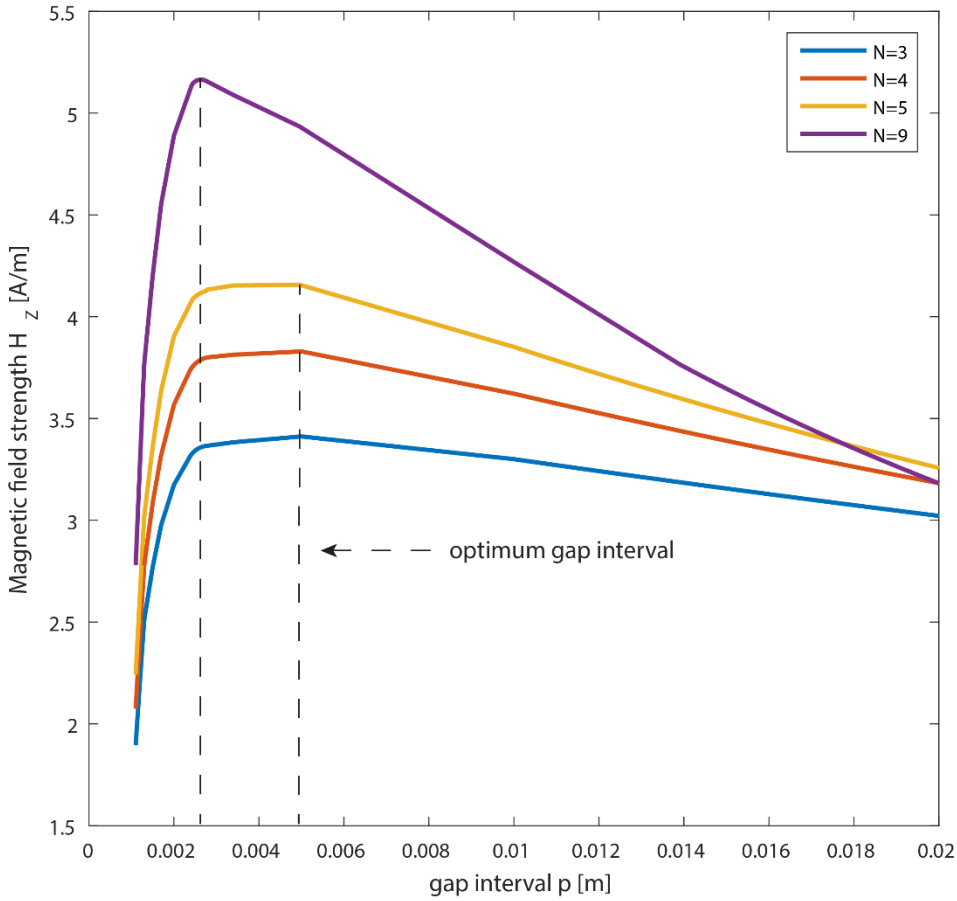

Figure 3.2-6 Magnetic field H_z against the gap interval at different numbers of turns N_{Pri} with input voltage VIN=1 V_{RMS}, transfer distance=10 cm and primary coil diameter = 30 cm

3.2.2.3 N_{pri}-h_{Npri}

Key points of this section

- With the other parameters being the same, different transfer distances have different optimum numbers of turns.

In this simulation, the number of turns is the primary independent variable, and the transfer distance is the secondary independent variable. The primary coil diameter is 10cm, and the gap interval is 1cm.

Figure 3.2-7 shows the magnetic field strength at different transfer distances with a range of numbers of turns. The transfer distances are set to 10 cm, 15 cm and 20 cm, respectively. The number of turns is within the range of 1 to 10. For example, the top

blue line is the magnetic field strength at a transfer distance of 10 cm by a primary coil with 1cm gap interval between turns when the number of turns varies from 1 to 10, and the coil diameter is set to 10 cm.

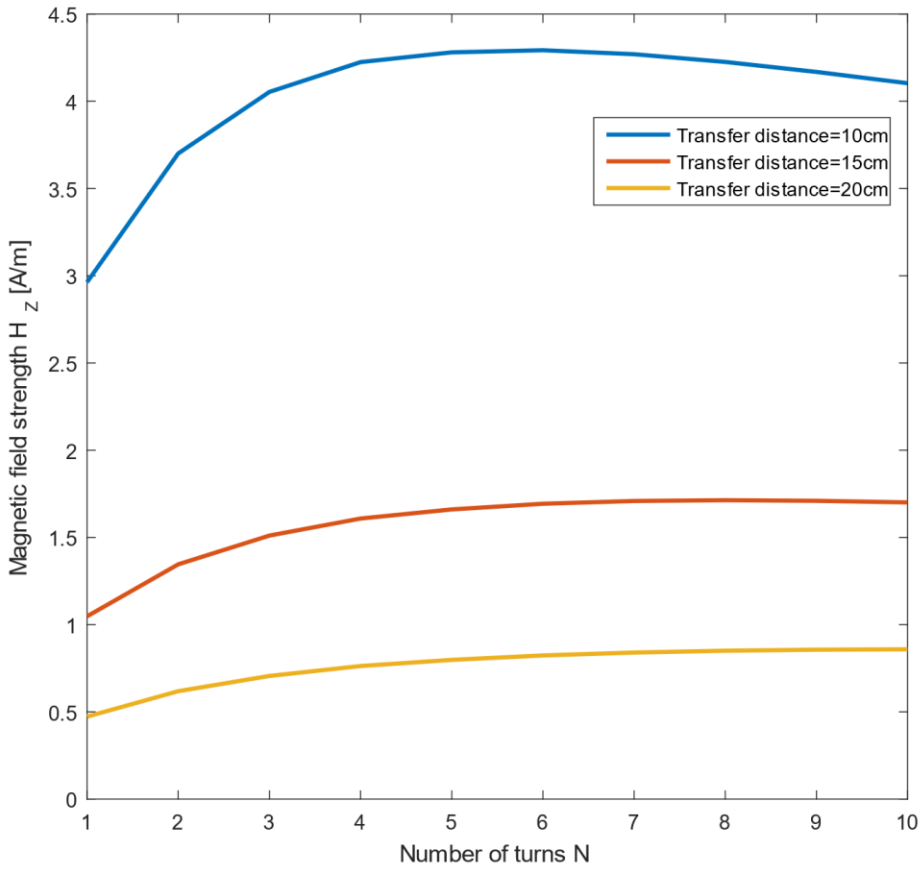

Figure 3.2-7 Magnetic field H_z against the number of turns at different transfer distances with the input voltage VIN = 1 V_{RMS}, the gap interval=1 cm and the primary coil diameter=10 cm

As shown, as the number of turns increases from one, the generated magnetic field will rise to a stationary point and then decrease as the number of turns continuous to increase. The reason for this is that any additional turns on the coil will add an extra magnetic field onto the present one, but it will also add AC resistance into the circuit. The additional AC resistance will cause the current in the coil to decrease and lower the overall field strength. When the number of turns is lower than the stationary point, the effect of additional fields is stronger than the effect of additional AC resistance; when the number of turns becomes higher than the stationary point, because the additional fields are further away from the measurement point, the effect of additional field strength is weaker than the effect of additional AC resistance. Therefore, the overall field strength will decrease.

What is also shown is that the optimum number of turns of the primary coil is different for different transfer distances. As shown in Table 3.2-7, for the presented values of primary coil diameter and gap interval between turns, the optimum number of turns

increases as the transfer distance increases. For the same transfer distance, the optimum number of turns increases as the primary coil diameter increases. With different gap intervals, the optimum number of turns will be hugely different even with the same transfer distance and diameter.

Transfer distance (cm)	10	15	20
Optimum number of turns (D_{Tx}=5 cm, p=1 cm)	5	7	10
Optimum number of turns (D_{Tx} =10 cm, p=1 cm)	6	8	10
Optimum number of turns (D_{Tx} =20 cm, p=1 cm)	8	10	12
Optimum number of turns (D_{Tx} =20 cm, p=4 mm)	16	21	24

Table 3.2-7 Optimum number of the primary coil turns for the analysed transfer distances in Figure 3.2-7

It should be noted that the optimum number of turns of the primary coil may not be the final number of coils in the wireless power transfer system, because the number of turns also affect the self-resonant frequency (SRF) of the coil. As mentioned in Section 2.3.3, if the SRF is less than twice the operational frequency, the system operation will be unstable and heavily affected by the environment. In this case, the number of turns will have to be reduced to meet the frequency requirement. Due to the co-dependency between the number of turns and diameter, the primary coil diameter may need to be adjusted after the reduction of turn number.

3.2.2.4 Summary

In this section, the effect on the magnetic field by the change of each dimensional parameter of the primary coil is observed respectively. The co-dependencies among the dimensional parameters on the decision of optimum parameters have also been analysed.

We can find out that the optimum value of diameter is affected by the transfer distance, the number of turns as well as the gap interval between turns. In order to achieve a maximum magnetic field strength, the transfer distance needs to be adjusted once the other parameters are changed. Of the three parameters (transfer distance, number of turns and the gap interval between turns), the transfer distance has a decisive role in determining the value of optimum coil diameter. The other two parameters have a secondary effect on the value of the optimum coil diameter.

In terms of the optimum gap interval, it can be theoretically proved that a stationary point of gap interval exists to achieve a maximum generated magnetic field strength. Moreover, the change of transfer distance has no profound effect on the optimum gap interval. It is shown that a change of the number of turns will change the optimum gap

interval. Due to the co-dependency found between the diameter and the gap interval, a change in the diameter will also change the optimum gap interval.

In terms of the number of turns, it is found out that for different transfer distances, the optimum number of turns will be different. The optimum values will also be affected by the primary coil diameter and gap interval. Moreover, the self-resonant frequency (SRF) should also be considered in the determination of the actual number of turns.

Based on the above analysis, a design flow for the optimum dimensions of the primary coil in the transmitter system will be developed in the next section. Furthermore, a design flow for the overall transmitter system, including the system component values, will also be presented.

3.2.3 Design flow of solenoid transmitter

The setup of the transmitter system is shown in Figure 3.2-8. The conditions are shown in Table 3.2-8.

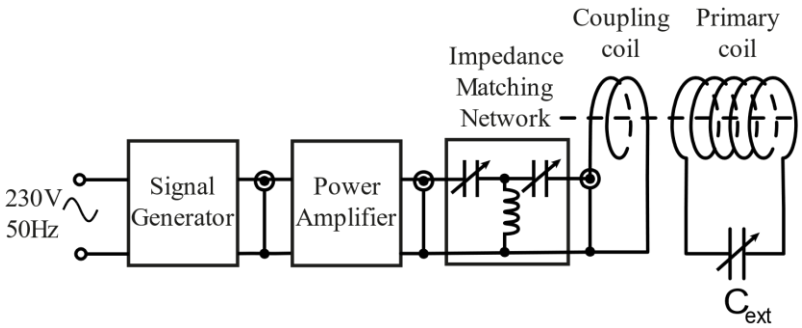

Figure 3.2-8 Setup of the transmitter system

Already known	Should be decided	Need to obtain	Design target
Operational frequency f	Wire diameter d_{wire}	Primary coil SRF	Primary coil number of turns N_{Tx}
Transfer distance h_{npri}	Wire material (resistivity ρ_{wire}, relative permeability μ_r)	Primary coil self-capacitance C_{self}	Primary coil diameter D_{Tx}
RMS Input voltage VIN	Coil former material (dielectric constant ϵ_i)	Primary coil self-inductance L_{self}	Primary coil gap interval p
		Magnetic field strength H at the distance Dis_{Npri}	Resonance capacitor C_{ext}
			Distance between primary coil and coupling coil
			Impedance matching circuit parameters

Table 3.2-8 Conditions and targets for the design of transmitter

3.2.3.1 Design flow of the primary coil

In Figure 3.2-9 and Figure 3.2-10, the design flow for the optimum dimensional parameters of the primary coil is shown.

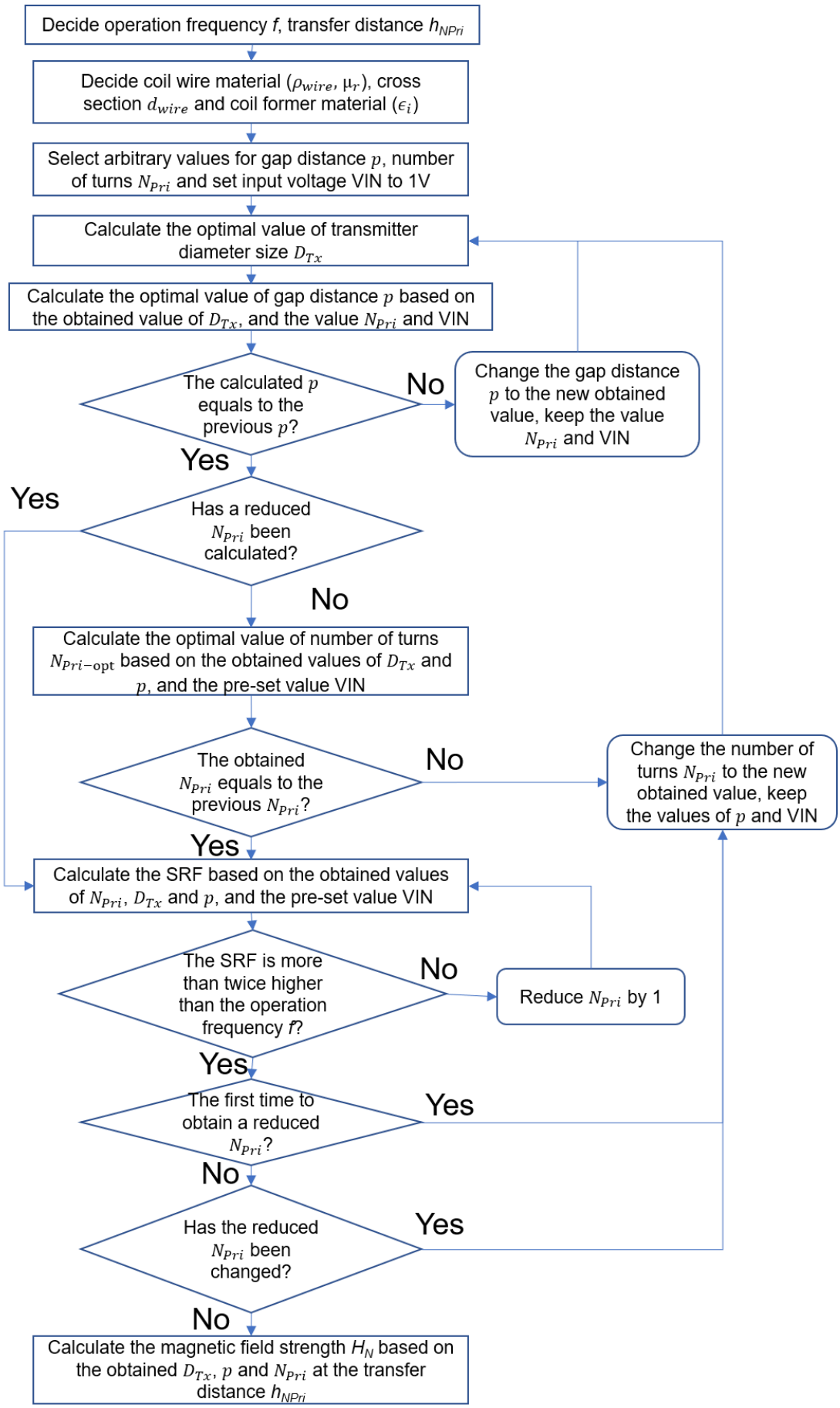

Figure 3.2-9 Design flow of the primary coil-part1

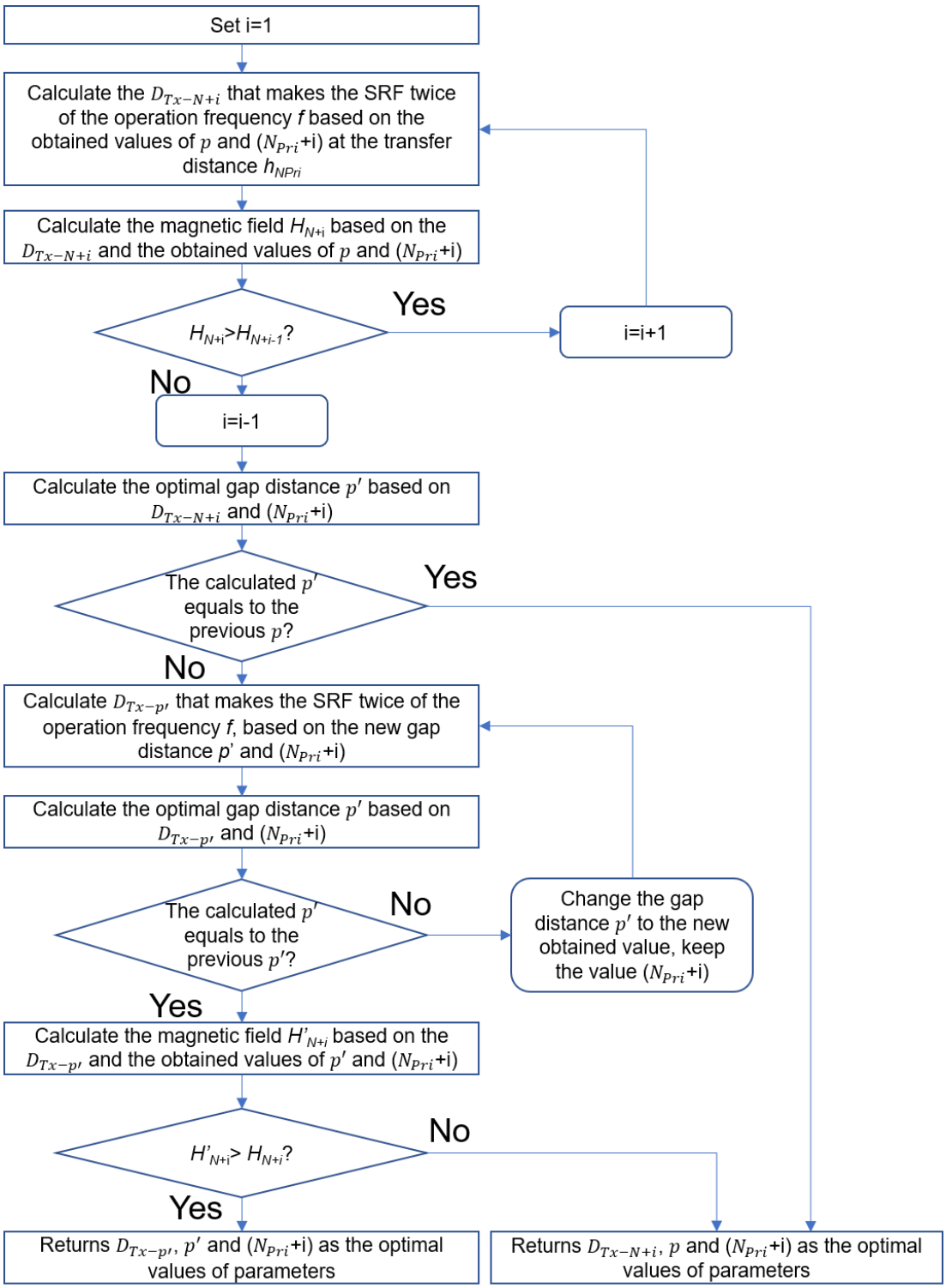

Figure 3.2-10 Design flow of the primary coil-part2

In this design flow, two theoretical models are mainly used. The first one is the theoretical model for the generated magnetic field by a solenoid transmitter developed in Section 3.1.3; the other one is the theoretical model for the calculation of SRF of a free solenoid coil presented in the (2) part of Section 2.3.3.

The process can be divided into two stages. The first stage is mainly to calculate the minimum number of turns based on the magnetic field strength model; the second

stage considers the limits of SRF and aims to find out whether a higher strength value can be achieved with a higher number of turns.

In the first stage, the design flow applies an iterative process. There are three parameters that are needed to calculate, which are the primary coil diameter D_{Tx}, the gap interval p between turns of the primary coil and the number of turns N_{pri} of the primary coil. In each iterative step, the stationary value of one of the parameters will be calculated with the other two parameters being arbitrary values (at the first step) or the previous calculated stationary values (at the later steps). After a number of steps, the parameters will converge into a set of stationary values that will achieve the maximum generated magnetic field strength under the given conditions.

At the start, the operational frequency and transfer distance should be decided. Because the magnetic field strength model is most suitable in the analysis in the near-field region, for a transfer distance between 5 cm and 20 cm, the operational frequency may not exceed 15 MHz with a consideration of the comparatively conductive human body tissue.

After this, the wire used to make the coil should be decided because the resistivity and the cross-section of the wire will be used in the calculation of the magnetic field. Moreover, the material and internal design of the coil former are also needed because this will affect the SRF of the coil.

Once the above parameters are decided, the main iterative process of the design flow can start. Because the primary coil diameter D_{Tx} is mainly decided by the transfer distance h_{NPri}, the stationary value of the primary coil diameter D_{Tx} will be calculated first with the gap interval between turns and number of turns set to arbitrary values.

Once the stationary D_{Tx} is obtained, its value will be applied in the calculation of the stationary value of the gap interval p, with the number of turns N_{pri} being the same arbitrary value. The obtained stationary value of the gap interval will be fed back to calculate the stationary diameter D_{Tx} again because changing the gap interval will change the stationary value of diameter. This is repeated until the calculated stationary value of the gap interval is equal to the previous stationary value of the gap interval.

A similar step is applied to calculate the stationary value of the number of turns N_{pri}.

It should be noted that if the SRF of the coil has been calculated, and the stationary value of the number of turns has been reduced to fit the SRF, there is no need to calculate the stationary value of the number of turns again. The process jumps directly to calculate the SRF with the new gap interval and diameter.

After all the stationary values of the three parameters are obtained, it is necessary to calculate whether the SRF of the coil with these parameters is more than twice the operational frequency f. If not, the number of turns will be reduced until this happens. The reduced number of turns will also change the stationary value of diameter. Therefore, the reduced number of turns will be fed back to calculate the stationary value of D_{Tx} with the obtained stationary value of the gap interval. After some calculation, a new reduced number of turns will be obtained. If this reduced number of turns is equal to the previous one, the first part of the process will be finished, and the stationary values of the two dimensional parameters with the reduced number of turns are obtained. If not, the new reduced number of turns will be fed back until the new one is equal to the old one.

At the first stage of the design flow, we can obtain, at the given operational frequency and transfer distance, the stationary value of diameter D_{Tx} that gives a maximum magnetic field strength with the stationary value of the gap interval p and the number of turns N_{pri} that satisfy the SRF limit.

It should be noted that the number of turns that satisfy the SRF limit is less than the optimised value that gives the highest field strength. In some cases, if all the $D_{Tx,}$ p and N_{pri} are the optimum values that give the highest field strength, the SRF of the primary coil will be lower than the limit. To satisfy the SRF limit, N_{pri} is reduced, and the D_{Tx} and p are then adjusted to be the stationary values that give the highest field strength at the SRF limit.

However, the first stage of the design flow only considers the magnetic field strength H and the SRF at the stationary point of the primary coil diameter D_{Tx}. There is a possibility that, with a higher value of N_{pri} and a non-stationary value of D_{Tx}, a higher magnetic field strength H can be obtained, and the SRF is still at the limit. A demonstrative figure is shown in Figure 3.2-11.

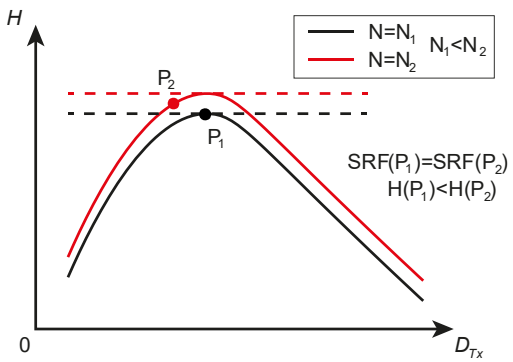

Figure 3.2-11 Demonstrative figure for the situation where the magnetic field strength at non-stationary point P_2 is higher than the magnetic field strength at the stationary point P_1 while the SRFs for both points are the same; the point P_2 is located at a curve where the number of turns N_2 is higher than the number of turns N_1 of the curve where P_1 is located

Therefore, the aim of the second stage of the design flow is to find out the maximum number of turns so that, at this turn number, a non-stationary value of D_{Tx} (i.e. P_2 in Figure 3.2-11) on the curves of D_{Tx}-H can achieve the highest possible magnetic field strength and satisfy the SRF limit. The process is shown in Figure 3.2-10.

To find the maximum turn number, the reduced number of turns obtained in the first stage is increased by 1, which becomes (N_{pri}+1). The primary coil diameter $D_{Tx\text{-}N+1}$ will then be calculated to make the SRF of the primary coil twice the operational frequency f with the obtained stationary value of the gap interval p and the turn number (N_{pri}+1).

The generated magnetic field strength H_{N+1} will be calculated based on $D_{Tx\text{-}N+1,}$ p and (N_{pri}+1). This field strength will be compared with the field strength H_N obtained from the end of the first part. If H_{N+1} is higher than H_N, it means the non-stationary value at a higher number of turns can generate a field at the transfer distance stronger than the stationary value at the original number of turns. Otherwise, H_N is the highest field strength, and the values of parameters obtained from part 1 are the optimum values.

If H_{N+1} is higher than H_N, it is needed to find out whether H_{N+2}, which can be obtained in the same way as H_{N+1}, is higher than H_{N+1}. If this is also true, H_{N+3} will be calculated to compare with H_{N+2}. The loop repeats until H_{N+i}<H_{N+i-1}, where i=1, 2, 3…

Once the $D_{Tx\text{-}N+i}$ and (N_{pri}+i) are obtained, these values will be used to calculate the stationary gap interval p' using the magnetic field strength model. If the value of p' equals to the previously obtained p, the design flow will finish, and the values of $D_{Tx\text{-}N+i}$, (N_{pri}+i) and p will be the optimum values for the primary coil at the frequency and transfer distance.

If not, p' and (N_{pri}+i) will be fed to the SRF model to calculate the diameter $D_{Tx\text{-}p'}$ that makes the SRF twice the operational frequency. The $D_{Tx\text{-}p'}$ and (N_{pri}+i) will then be fed to the magnetic field strength model to calculate a new p'. If the new p' is not equal to the old p', the loop will be repeated until they are the same. Once they are the same, the generated magnetic field strength H'_{N+i} with the new values of $D_{Tx\text{-}p'}$, (N_{pri}+i) and p' will be calculated and compared with the field strength H_{N+i}. If H'_{N+i} is higher, $D_{Tx\text{-}p'}$, (N_{pri}+i) and p' will be the optimum values of the parameters. If H_{N+i} is higher, $D_{Tx\text{-}N+i}$, (N_{pri}+i) and p will be the optimum values of the parameters.

3.2.3.2 Design flow of the transmitter system in the weakly coupled wireless power transfer system

In Figure 3.2-12, the design flow of the transmitter system is shown. During the design, a network analyser with an S-parameter test set will be used to measure the reflected power S_{11} and the resonant frequency of the coils. After the optimum parameters of the primary coil are obtained, it is possible to calculate the self-inductance and self-

capacitance of the coil. (The self-inductance can also be measured after the coil is fabricated.) Based on the L-C circuit resonant frequency formula, the required total capacitance for resonance at frequency f can then be calculated. The external capacitance will then be the difference between the total capacitance and the self-capacitance of the primary coil. The external capacitor should be a variable capacitor whose mid-value is the calculated external capacitance for convenient tuning.

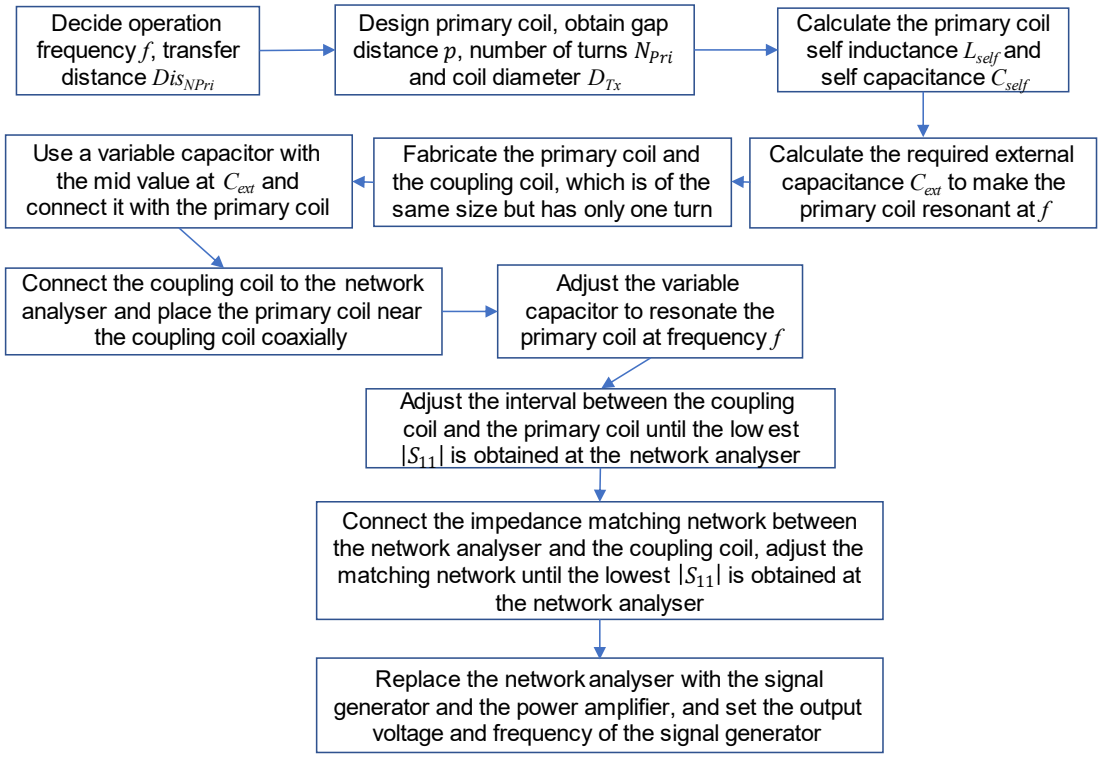

Figure 3.2-12 Design flow of the transmitter system

The coupling coil and the primary coil can then be fabricated. The coupling coil will have the same diameter as the primary coil but with only one turn. The external capacitor, the primary coil, the coupling coil and the network analyser can then be connected as in Figure 3.2-13.

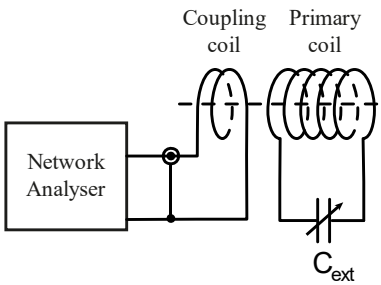

Figure 3.2-13 Primary coil and the coupling coil connected to the network analyser; C_{ext} is the external variable capacitor

With the network analyser, the external capacitor can be tuned to make the circuit resonate at frequency f. The distance between the coupling coil and the primary coil can be adjusted so that the absolute value of $S11$ will be maximised at frequency f.

After tuning and adjusting, disconnect the coupling coil from the network analyser and connect the impedance matching network in between them, as shown in Figure 3.2-14. Adjust the variable capacitors and the variable inductor in the impedance matching network until the maximum absolute value of *S11* is obtained.

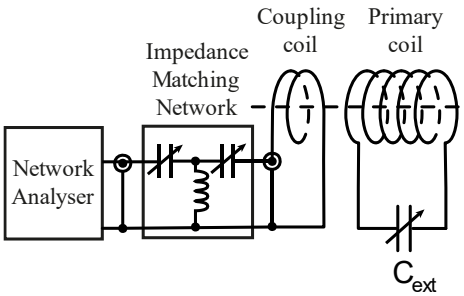

Figure 3.2-14 Setup of the transmitter system with the network analyser

After tuning the impedance matching network, the network analyser can be disconnected and replaced by the signal generator and the power amplifier, as shown in Figure 3.2-15. The design of the transmitter system is finished.

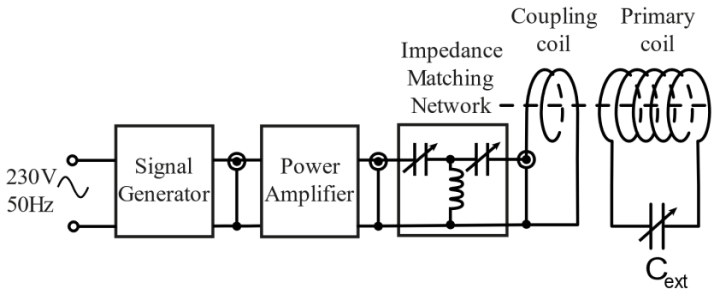

Figure 3.2-15 Setup of the transmitter system

3.2.4 The optimum parameters for the transmitter and its performance

Using the design flow shown in Section 3.2.3.1 and the parameters shown in Table 3.2-9, a list of optimum dimensional parameters of the primary coil for a range of transfer distance is shown in Table 3.2-10.

Name	**Symbol**	**Value**
Wire diameter	d_{wire}	1 mm
RMS input voltage to the coupling coil	VIN	1 V
Operational frequency	f	8 MHz
Resistivity of the wire (copper)	ρ_{wire}	$1.72 \times 10^{-8} \Omega \cdot m$
Coil former relative electric constant (Acrylic)	ε_i	2.35

Table 3.2-9 List of parameters used in the simulations

Transfer distance h_{NPri} (cm)	Optimum diameter D_{Tx} (cm)	Optimum gap interval p (cm)	Optimum number of turns N_{pri}	SRF (MHz)	Generated H at the distance (A/m)
4	7.1	0.20	10	33.7	31.8
8	12.0	0.25	12	16.1	10.3
12	14.6	0.25	9	16.0	4.7
16	17.7	0.25	7	16.0	2.6
20	20.1	0.25	6	16.0	1.5

Table 3.2-10 Optimum dimensional parameters of primary coil for transfer distances ranging from 4 cm to 20 cm with operational frequency at 8 MHz, with predicted SRF and generated magnetic field strength at the distance with 1 V_{RMS} input

As shown, the optimum diameter of the solenoid primary coil increases as the transfer distance increases. However, the ratio between the optimum diameter and the transfer distance decreases from about 2 to almost 1 when the transfer distance increases from 4 cm to 20 cm. Because of the discontinuity in the calculation of AC resistance, the optimum gap interval results as discrete values. For most of the transfer distance range discussed here, the optimum gap interval is 0.25 cm. At a shorter transfer distance, such as 4cm, the optimum gap interval decreases to 0.2 cm. In reality, the optimum gap interval should not be discrete values, but the error (a maximum of 3%) caused by the discontinuity is acceptable in the thesis.

The optimum number of turns increases from 10 to 12 when transfer distance changes from 4 cm to 8 cm, and the optimum number of turns then decreases to 6 at 20 cm transfer distance. The reason for this is that the SRF of the coil is much higher for coils with optimum parameters at shorter transfer distances, such as the 33.7 MHz SRF for the 4 cm transfer distance. For optimum parameters at longer transfer distances, the actual number of turns needed to achieve the highest magnetic field is so high that the resulted SRF is less than the SRF limit. The number of turns is thus reduced to fit the limit. Because the inductance of the coil increases with coil diameter, the optimum number of turns decreases as the transfer distance increases.

It should be noted that these results are predicted when the medium is air, and there is no blocking between the transmitter and the object location. As the receiver of the proposed wireless power transfer system will be implanted inside the human body, there are two situations. For less-conductive tissues such as muscle, fat and skin, the reduction of power delivery caused attenuation effect is less than 5% [122][126][189]. For conductive tissues such as lungs, which have high water content, the attenuation effect cannot be neglected. As discussed in Section 2.3.4.2, the attenuation in magnetic field strength can be more than 50% at a transfer distance of 20 cm. However, because the attenuation effect of the media is independent of the dimensional parameters of the transmitter system, the optimised parameters of the transmitter in the air will still be the optimised parameters in the conductive media. The transmitter design process will still work for conductive media.

For the optimum parameters of 20 cm transfer distance, the coupling coil circuit is shown as in Figure 3.2-16 and the component values are listed in Table 3.2-11.

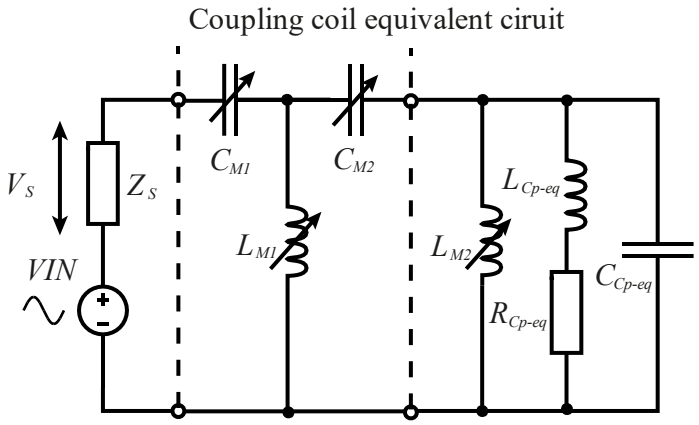

Figure 3.2-16 Coupling coil equivalent circuit with T matching network for optimum TX of 20 cm transfer distance

Symbol	Name	Base Value	Symbol	Name	Base Value
Z_S	Source impedance	50 Ω	L_{M2}	Matching network Inductance	1.4 µH
C_{M1}	Matching network capacitance	0.4 nF	L_{Cp-eq}	Equivalent coupling coil inductance	40 pH
C_{M2}	Matching network capacitance	3.6 nF	R_{Cp-eq}	Equivalent coupling coil resistance	0.3 Ω
L_{M1}	Matching network Inductance	0.1 µH	C_{Cp-eq}	Equivalent coupling coil capacitance	0.28 nF

Table 3.2-11 Impedance matching network component values and calculated coupling coil equivalent values

Because the coupling coil is a single turn coil, the impedance of its self-inductance L_{Cp-eq} is negligible (0.002 Ω) compared with the coupling coil equivalent resistance (0.3 Ω). However, the equivalent capacitance C_{Cp-eq} of the coupling coil cannot be neglected. Therefore, a variable inductor L_{M2} is added in parallel with the coupling coil to resonate with the coil self-capacitance C_{Cp-eq}. The base value of L_{M2} is 1.4 µH. The T matching network is then designed to match the source impedance Z_S and the coupling coil equivalent resistance R_{Cp-eq}. The virtual impedance of the T network is set to 100 Ω, and the corresponding component base values are presented in Table 3.2-11.

From the analysis in Section 3.1.4, it is shown that the developed mathematical model to predict the magnetic field strength from a solenoid coil is only valid for a limited range of values of dimensional parameters. To verify the validity of the calculated optimum results, *COMSOL Multiphysics*, a well-proven simulation software which model the magnetic field using FEA, is used to simulate the magnetic field strengths of the optimum coils for transfer distances of 16 cm and 20 cm.

For the optimum coil for 16 cm transfer distance, the distribution and direction of magnetic field strength are shown in Figure 3.2-17. It is shown that the magnetic field strength is more than 40 A/m in the adjacent spaces of the coil, but it decreases rapidly as the transfer distance increases. A plot of the magnetic field strength along the axis of the coil is shown in Figure 3.2-18. The calculation results and simulation results agree well. For transfer distance between 0 cm and 27.4 cm, the maximum difference between calculation results and simulation results is 4.8% at 0.3 cm and a difference of 1.1% at 16 cm, which means the developed model has an accurate prediction for the target transfer distance. For transfer distance between 27.4 cm and 35 cm, the difference becomes higher, ranging from 4.8% to 8.4%, which owes to higher proportion of mid-field component in the overall magnetic field, as discussed in Section 3.1.4.

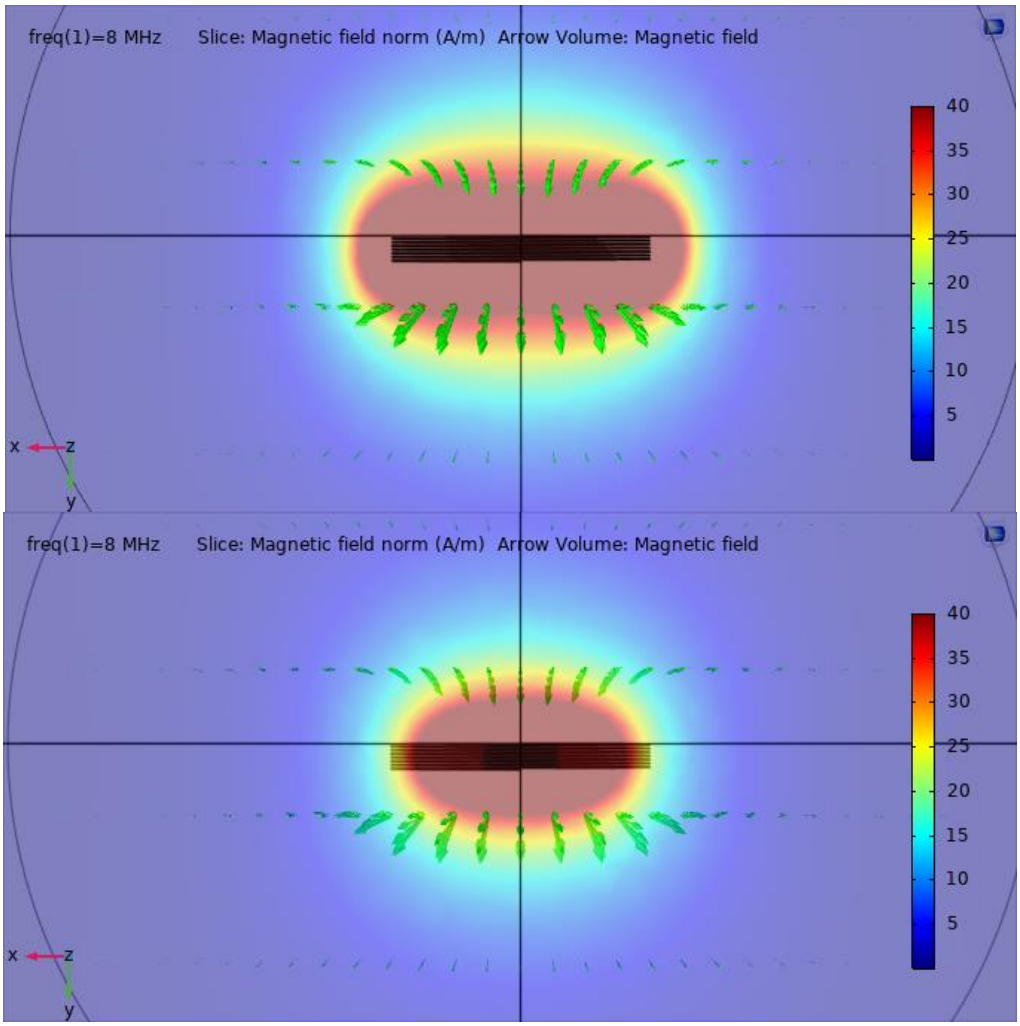

Figure 3.2-17 Distribution (colour table) and direction (green arrows) of magnetic field strength H at the axis plane (top) and at the edge-tangent plane (bottom) parallel to the axis plane of the coil with optimum parameters for 16 cm transfer distance

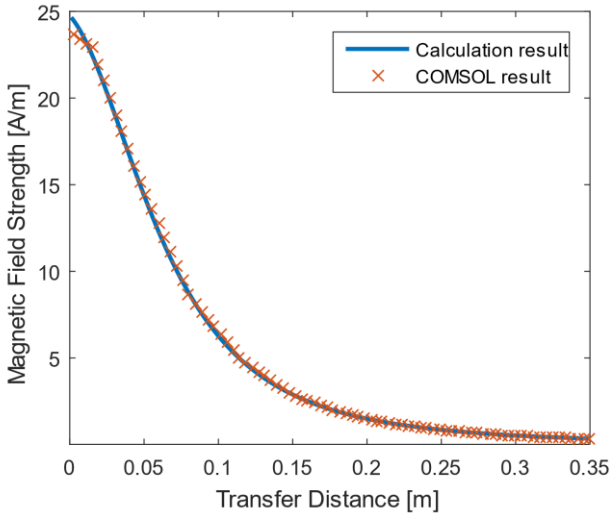

Figure 3.2-18 Calculation results (blue) and COMSOL simulation results (orange) of magnetic field strengths along the axis of the coil of the optimum coil for 16 cm transfer distance

For the optimum coil for 20 cm transfer distance, the distribution and direction of magnetic field strength are shown in Figure 3.2-19. It is shown that the magnetic field strength at the centre of the coil is weaker than the field strength of the optimum coil for 16 cm transfer distance with the same input voltage at the coupling coil. For spaces close to the coil surface, the magnetic field strength can be more than 40 A/m. The calculation results of the magnetic field strength along the transfer distance at the axis are compared with the *COMSOL* simulation results in Figure 3.2-20.

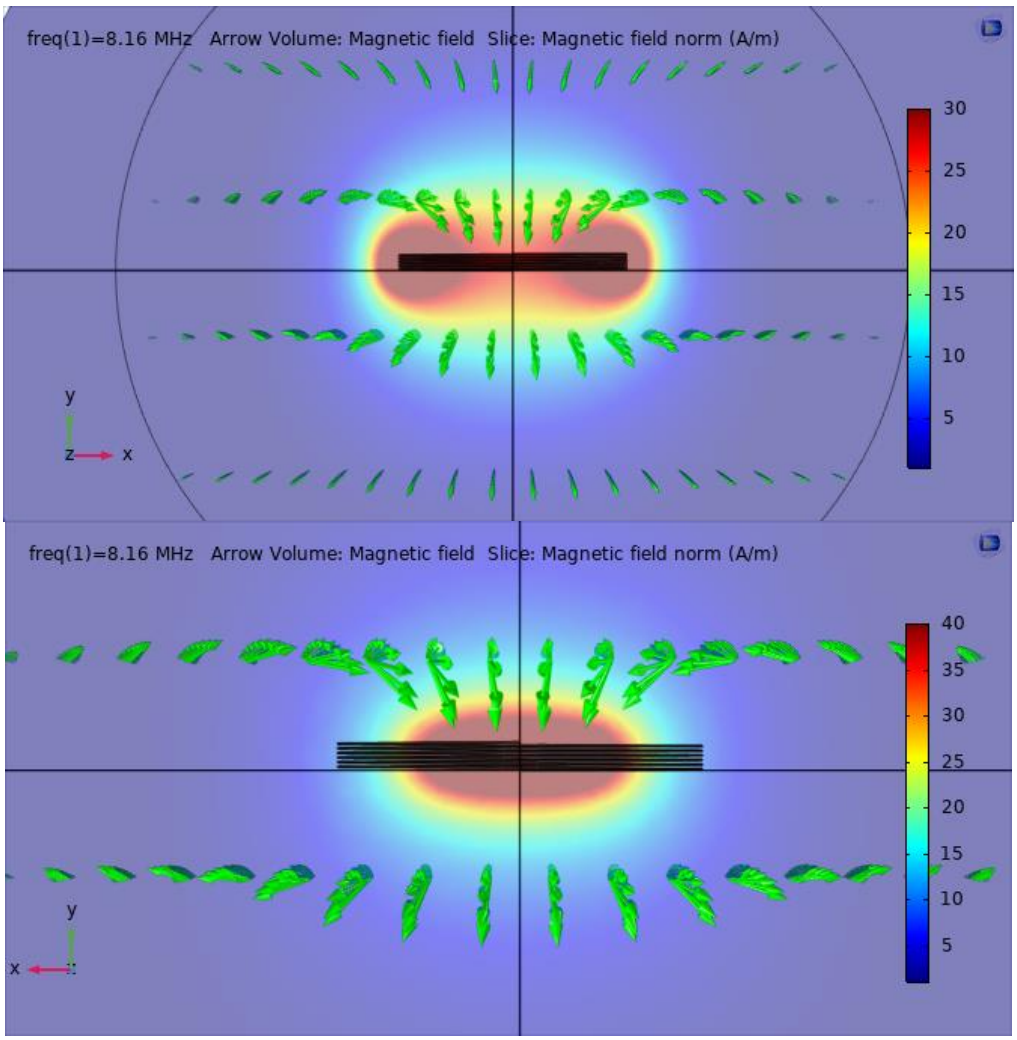

Figure 3.2-19 Distribution (colour table) and direction (green arrows) of magnetic field strength H at the axis plane (top) and at the edge-tangent plane (bottom) parallel to the axis plane of the coil with optimum parameters for 20 cm transfer distance

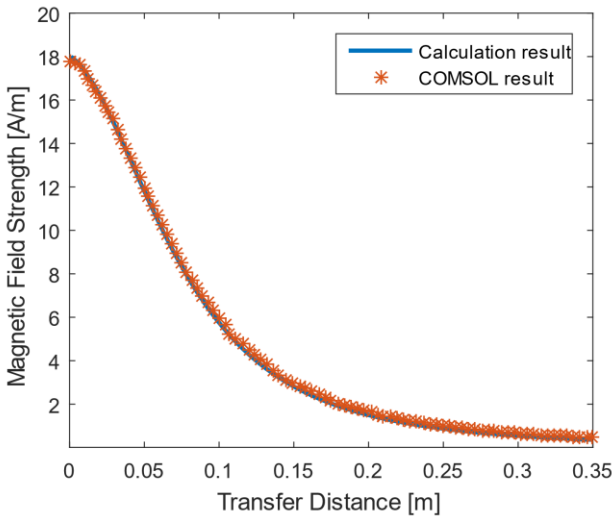

Figure 3.2-20 Calculation results (blue) and COMSOL simulation results (orange) of magnetic field strengths along the axis of the coil of the optimum coil for 20 cm transfer distance

For transfer distance between 0 cm and 5.5 cm, the calculation results are higher than the simulation results, with a maximum difference of 3.0% at 0.1 cm transfer distance

and a minimum difference of 0.5% at 5 cm. For transfer distance between 5.5 cm and 10.7 cm, the calculation results and the simulation results are close to each other and the difference is at a maximum of 5%. For transfer distance between 10.7 cm and 22.7 cm, the simulation results are higher than the calculation results, with a maximum difference of 9.8% at 22.7 cm and a minimum difference of 0.15% at 11.1 cm and a difference of 8% at 20 cm. This shows that the developed model is accurate for prediction for the target transfer distance, and also that the difference increases as the transfer distance increases, which is because that the mid-field component of magnetic field have a higher proportion in the overall magnetic field as is discussed in Section 3.1.4. For transfer distance between 22.7 cm and 35 cm, the difference ranges from 10.9% to 27.5%, which means the developed model is no longer valid because of the large error.

In terms of the magnetic field exposure of the primary coil, according to Table 2.3-3, the maximum permissible exposure (MPE) at frequencies around 8 MHz is H_{MaxRMS}=40.75 A/m. From Figure 3.2-17 and Figure 3.2-19, for 16 cm transfer distance, with 1 V_{RMS} input to the coupling coil, the magnetic field strength is less than 40 A/m when it is 4 cm away from the coil, which means the safe gap interval between the coil surface and the human body skin for the optimum coil for 16 cm transfer distance is about 4 cm; for the optimum coil for 20 cm transfer distance, the safe gap interval is about 2 cm. Once these intervals are satisfied, the proposed optimum coils will work within the exposure limit set by the IEEE standard C95.1-2005 [144].

3.2.5 Summary of this section

In this section, based on the magnetic field strength model developed in Section 3.1.3, the co-dependencies among the three dimensional parameters (coil diameter, number of turns and gap interval between turns) of the primary solenoid coil to obtain a maximum magnetic field strength are obtained. It is found out that the three dimensional parameters are correlated, and when one of the parameters changes, the optimum values of the other two will be changed. Moreover, it is found that the optimum diameter of a coil is heavily dependent on transfer distance. In other words, each transfer distance needs a different value of diameter to achieve a maximum magnetic field, which means each transfer distance needs a different set of optimum parameters of the primary solenoid coil.

Based on the co-dependency analysis, a design flow to obtain the optimum values of dimensional parameters is presented. The first stage of the process aims to find out the stationary values of diameter and gap interval at a maximum number of turns that satisfy the SRF limit. The second stage of the process aims to find out the non-stationary values of diameter and the related stationary value of gap interval at a

higher number of turns that can satisfy the SRF limit and achieve an even higher value of magnetic field strength. Another design flow is also reported to calculate the values of other parameters in the transmitter system and set up the transmitter system. Based on the design flows, the optimum parameters for a range of transfer distance are calculated and discussed.

The main problem in the design comes from the discontinuity of the AC resistance calculation, which causes the gap interval to be discrete values. Improvements in model accuracy will be made if an accurate continuous AC calculation model is applied.

It should be noted that the solenoid transmitter coil can be further optimised. As shown in Table 3.2-10, the optimised diameter of the solenoid primary coil increases as the transfer distance increases. This means that if the length of the primary coil cannot be neglected compared with the transfer distance, the turn of the coil further away from the receiver should have a larger diameter than the turn closer to the receiver for a maximum magnetic field at the receiver position. The shape of the primary coil will then become a conical solenoid instead of a cylindrical solenoid, and a higher magnetic field strength can be achieved at the same transfer distance.

Because a conical solenoid coil can be seen as a cylindrical solenoid coil with a variation of coil diameters, the application of conical solenoid coil can be analysed preliminarily based on the analysis of cylindrical solenoid coil. For the present operational frequency, the conical solenoid coil may be more suitable for a short transfer distance range (around 4 cm), because at this range, as shown in Table 3.2-10, the optimum number of turns is large, and the coil SRF is high, which make it possible and suitable to have turns with large sizes. For a transfer distance range higher than 8 cm, firstly, the SRF of the optimised coil can be lower than the operational frequency if larger turn sizes are used. Secondly, the increase of optimised coil diameter is “slower” for an increase of higher transfer distances. Because of the small optimum gap distances and the low number of turns, the size difference between the first turn and the final turn of an optimised conical coil can be neglected. Therefore, it is unsuitable for large transfer distances at the present operational frequency based on the analysis of optimised parameters of cylindrical coils. However, the conical coil may be useful for a lower operational frequency because a higher turn number is possible, and the optimum sizes of the first turn and final turn of the coil can have a larger difference.

With the optimum parameters of the transmitter system obtained, the focus can be shifted to the receiver. It is of interest to find out the optimum parameters of receiver solenoid coils to supply the maximum power to the load.

3.3 Receiver coil model and design

Key aims of this section

- A circuit model is developed for the receiver coil in the wireless power transfer system.
- Both the air-core solenoid receiver and the ferrite-core solenoid receiver are analysed with the developed theoretical model.
- The induced voltage and the maximum output power are theoretical predicted based on the models with a variety of values of coil parameters. The predicted induced voltage and output power of ferrite-core receivers are compared with the ones of the air-core receivers.
- A design flow of the receiver coil is proposed for the application of the IMPACT program to meet the size and power requirements of micro-implants.

3.3.1 Introduction

In this thesis, one of the aims is to discover, in the proposed wireless power transfer system, how much power a mm-scale receiver can receive and deliver to the load with the optimised transmitter design at a transfer distance greater than 10 cm or even 20 cm inside a patient's body. The cross-section diameter of the receiver should be within 2 mm so that the receiver can be injected into the patient with needles. The length of the receiver is more flexible but should be no more than 5cm.

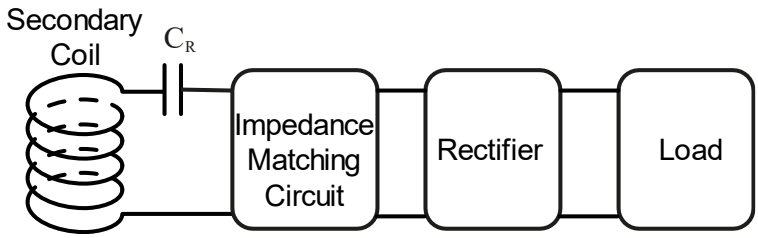

Figure 3.3-1 Block diagram of the receiver in the wireless power transfer system

As shown in Figure 3.3-1, a receiver in the proposed wireless power transfer system includes

- a solenoid coil
- a capacitor
- an impedance matching circuit
- a rectifier to convert AC to DC and a load

The solenoid coil is the secondary coil in the wireless power transfer system. Its main function is to receive the magnetic energy delivered by the transmitter and transferred the energy into electric energy according to the Faraday's Law (as discussed in Section 2.2.2).

The capacitor connects in series with the solenoid coil to form a series L-C circuit. The parallel L-C circuit is not used here because a large amount of current will circulate between the L and C in the circuit (as discussed in Section 2.3.1), which will cause an excessive energy loss in the parasitic resistance of the solenoid coil (which has been discussed in Section 2.3.3.4). The series L-C circuit will have a minimum impedance (mainly the resistance of the coil) at resonance, thus, more power will be delivered to the load.

The impedance matching circuit connects between the series L-C circuit (formed by the receiver solenoid coil and the tuning capacitor) and the rectifier to match the impedances of them so that a maximum output power can be obtained from the series L-C circuit.

The rectifier and the load will be discussed in Chapter 4. In this section, they will be treated as a complex load with an impedance Z_{Rec}. The actual value of impedance can be obtained from simulation or from the measurement of a rectifier circuit.

In this section, the model of the receiver coil will be discussed first. The induced voltage and the maximum output power will be calculated based on the model with the presence of the impedance matching circuit. The performance of the circuit with an air-core solenoid coil will be analysed. Because the performance of air-core solenoid coils cannot meet the power and voltage demands of micro-implants such as the ones developed by the IMPACT program, the receiver circuit with ferrite-core coils are also discussed and analysed.

3.3.2 Model of receiver coil in the receiver circuit

The receiver circuit model is shown in detail in Figure 3.3-2, with the symbols introduced in Table 3.3-1.

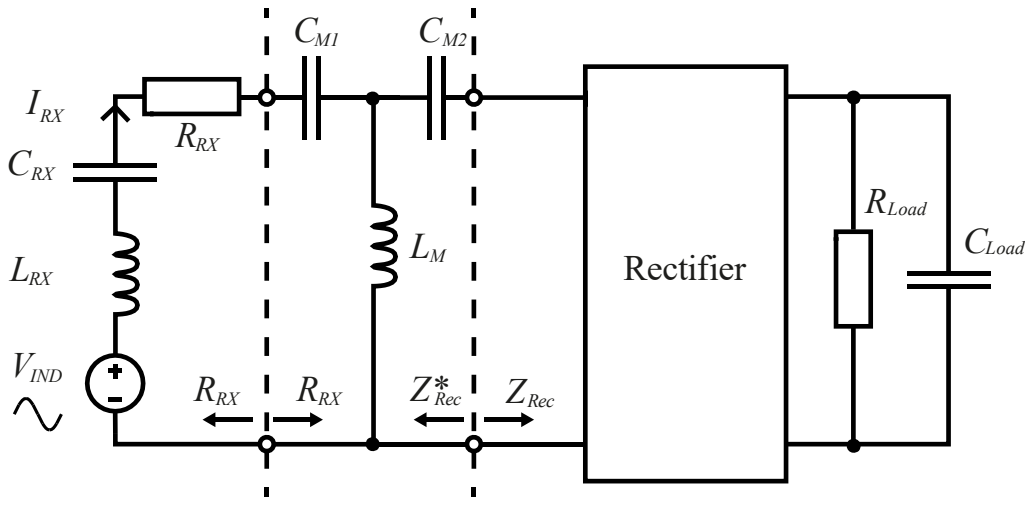

Figure 3.3-2 Circuit diagram of the receiver circuit with a T impedance matching circuit

Symbol	Name	Symbol	Name
V_{IND}	RMS induced voltage on receiver coil	L_M	Inductor of the impedance matching circuit
L_{RX}	Inductance of receiver coil	Z_{Rec}	Impedance of the rectifier
C_{RX}	The tuning capacitor on the receiver	Z^*_{Rec}	Complex conjugate of the impedance of the rectifier
R_{RX}	Total resistance of the receiver coil and the capacitor	R_{Load}	Load resistance
C_{M1}, C_{M2}	Capacitors of the impedance matching circuit	C_{Load}	Load capacitance

Table 3.3-1 Symbols and their corresponding names in the circuit in Figure 3.3-2

Here, the receiver coil is represented by the voltage source V_{IND} and the inductor L_{RX}, with its parasitic resistance added into the resistor R_{RX}, which represents the total resistance of the series L-C circuit.

The impedance matching circuit is a T-section circuit with the capacitors C_{M1} and C_{M2} and the inductor L_M.

The rectifier with the load has an impedance Z_{Rec}.

At the operational frequency, the impedances of L_{RX} and C_{RX} cancel each other. The impedance of the series L-C circuit becomes R_{RX}. Here, the impedance matching circuit is set to match R_{RX} and Z_{Rec}. The impedance of the rectifier is converted to be the same value as the resistance of R_{RX}. Therefore, from the series L-C circuit side, the circuit becomes as shown in Figure 3.3-3.

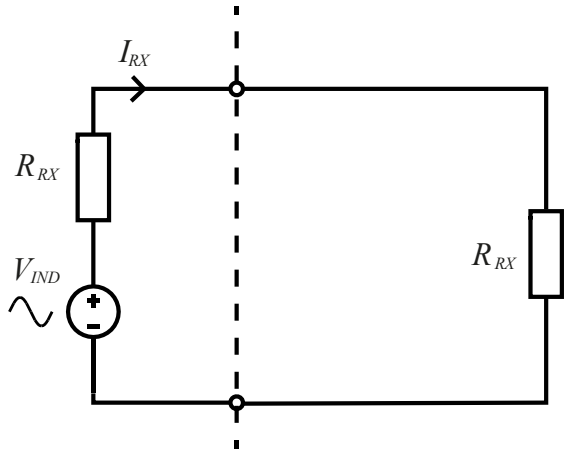

Figure 3.3-3 Equivalent circuit of receiver with impedance matching circuit from the series L-C circuit side; the impedance of the rectifier has been converted to R_{RX}, which is the total resistance of the series L-C circuit; the voltage source VIN equals to the induced voltage across the receiver coil

With this circuit model, the maximum output power from the receiver coil can be calculated based on the parameters of the coil and the magnetic field strength generated by the transmitter, with no consideration of the rest of the circuit.

The input voltage V_{IND} can be calculated with the Faraday's law. Assuming that the magnetic field is uniform through the coil,

$$V_{IND} = j\omega\mu N H_z A_{eff} \tag{3.24}$$

where

- V_{IND} is the RMS induced voltage on the receiver coil
- N is the number of turns of the receiver coil
- A_{eff} is the effective area of the receiver coil
- H_z is the magnetic field strength component which is uniform in the $\mathbf{z}$ direction
- ω is the angular frequency of the magnetic field
- μ is the permeability of the core of coil

The resistance R_{RX} can be calculated as

$$R_{RX} = R_{Core} + R_{AC-Coil} \tag{3.25}$$

where

- R_{Core} is the resistance caused by the loss in the core of the receiver coil
- $R_{AC\text{-}Coil}$ is the AC resistance of the coil itself

From Figure 3.3-3, the output power of the receiver coil can be calculated as

$$P_{OUT} = I_{RX}^2 R_{RX} \tag{3.26}$$

By combining (2.61) (3.24) (3.25) and (3.26), the output power be calculated as

$$P_{OUT} = \left(\frac{V_{IND}}{2R_{Rx}}\right)^2 R_{Rx} = \frac{\left(2\pi f \mu N H_z A_{eff}\right)^2}{4(R_{Core} + R_{AC-Coil})} \tag{3.27}$$

Now that the model of the receiver coil has been built. The air-core solenoid coil will be analysed first as a receiver coil based on its output power performance.

3.3.3 Analysis of receiver with an air-core solenoid coil

3.3.3.1 Model for air-core solenoid coils

For the receiver with an air-core solenoid coil, there are two special conditions

- the core-loss resistance R_{core} is zero
- the relative magnetic permeability μ_r=1

From (3.24), the induced voltage expression thus becomes

$$V_{IND-Air} = j\omega\mu_0 N H_z A_{eff} \tag{3.28}$$

and, from (3.27), the output power expression becomes

$$P_{OUT-Air} = \frac{\left(2\pi f \mu_0 N H_z A_{eff}\right)^2}{4R_{AC-Coil}} \tag{3.29}$$

where, from (2.137) as discussed in Section 2.3.3.4, the AC resistance of the air-core solenoid coil is

$$R_{AC-Air} = R_{DC-Air}\left[1 + (\Xi - 1)\Gamma\frac{N - 1 + \frac{1}{\Gamma}}{N}\right] \tag{3.30}$$

It should be noted that the calculation of AC resistance is only applicable when the coil gap interval between turns is equal to or larger than the wire diameter, but this will not affect our analysis here.

3.3.3.2 Induced voltage and output power analysis for receivers with an air-core coil

As introduced in Section 3.3.1, the induced voltage and output power performance of the receiver coil will be analysed with the following conditions

- The cross-section diameter of receiver coil is of the order of 2 mm.
- The length of receiver coil is no more than 5 cm.
- The receiver operates at the same frequency as the transmitter.
- The target magnetic field strength is between 1.5 A/m and 20 A/m for non-conductive human tissues, and it is approximately half for conductive human tissues.

Because of the limited size of the receiver coil, the scale of the wire diameter becomes equal to the size of coil. The wire diameter should be kept being around 0.1 mm to avoid exceeding the overall length limit of receiver coil.

As a preliminary setting, while the changes of induced voltage and output power with the variation of other parameters are observed, the wire diameter is set to be 0.1 mm, which is approximately the wire width of AWG38 standard. Also, the gap interval is set to be the same as the wire diameter.

The changes in induced voltage and output power will be discussed as follows

- A variation of number of turns from 1 to 200 in different receiver coil diameters (1 mm, 2 mm, 4 mm)
- A variation of magnetic field strength from 0 to 20 A/m in different receiver coil diameters (1 mm, 2 mm, 4 mm)
- A variation of gap intervals between turns from 0.2 mm to 0.5 mm in different wire diameters (0.1 mm, 0.15 mm, 0.2 mm)

It should be noted that the expressions for the induced voltage and output power assume that the magnetic field strength is uniform through the coil. However, as discussed in Section 3.2.4, the magnetic field strength decreases exponentially with the increase of transfer distance. This means the magnetic field is the maximum at the end of the coil nearest to the transmitter (head) and is the minimum at the end most far away from the transmitter (tail). The analysis for the air-core below assumes that the same value of magnetic field strength is uniform through the whole length of the receiver coil as the field strength at the head of the coil. Therefore, the obtained induced voltage and output power from the analysis below will be higher than the actual values. The difference between the values will increase as the receiver coil becomes longer. A more realistic model will be built for the ferrite-core coils, but here, this simpler model for air-core is enough for analysis.

(1) A variation of number of turns from 1 to 200 in different receiver coil diameters (1 mm, 2 mm, 4 mm)

In this analysis, the primary focus is mainly on in what range of turn number the air-core receiver coil can achieve sufficient induced voltage (more than 1 V) and output power (more than 1 mW) under the size limitation (2 mm diameter) and in the target magnetic field strength.

The range of the number of turns, 1 to 200, is determined by the coil length. With a 0.1 mm wire diameter and a 0.1 mm gap interval between turns, a 200 turn coil will have a length about 4 cm, which is within the limit of receiver coil length.

The 2 mm-diameter is chosen based on the requirement mentioned at the beginning of this section. The 1mm and 4mm diameters are chosen for comparison and trend analysis.

The magnetic field strength 1.5 A/m is chosen based on the field strength of the optimised transmitter parameter at 20 cm transfer distance. The operational frequency 8 MHz is also the same as in the analysis of the transmitter.

The changes in induced voltage and output power from the receiver coil with the variation of the number of turns are as shown in Figure 3.3-4.

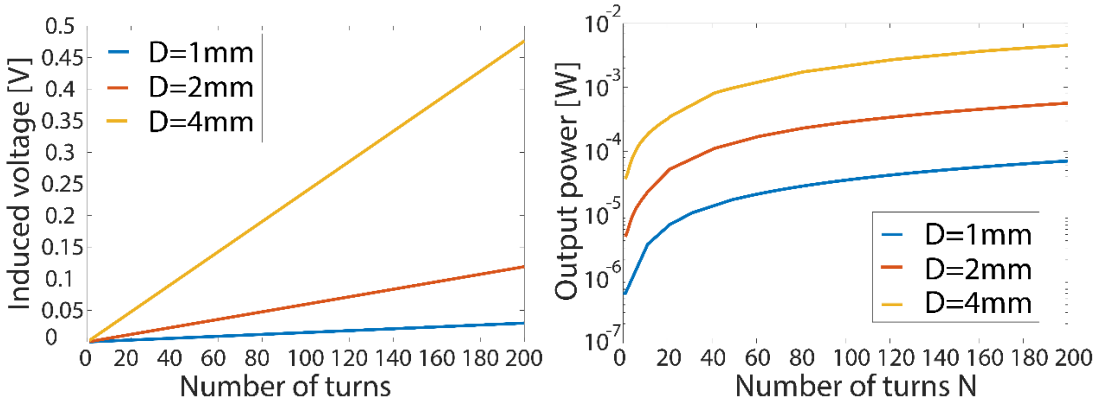

Figure 3.3-4 RMS induced voltage (left) and output power (right) of air-core receiver coil in different receiver coil diameters(1 mm, 2 mm, 4 mm) for a range of number of turns (1 to 200) with gap interval = 0.1 mm, wire diameter=0.1 mm, operational frequency=8MHz and magnetic field=1.5 A/m

As expected from the induced voltage expression, the induced voltage is proportional to the number of turns. However, for a 2 mm-diameter receiver coil, the induced voltage is rather small even with 200 turns when H=1.5 A/m, which is about 0.06 V. Considering how the field strength decreases with the increase transfer distance, the induced voltage will be even lower with a wireless power transmitter. This voltage is obviously not enough for the operation of micro-implants with the presence of the voltage-drop at the rectifier. The 4 mm-diameter receiver coil has an induced voltage about 4 times of the voltage of the 2 mm coil, which is still not high enough for micro-implant applications if a voltage-boost device is not used at the load.

It is apparent that the output power will increase with the number of turns and the coil diameter. The detail is shown in Table 3.3-2. At 200 turns, the output power of a 2 mm coil with 1.5 A/m field strength is about 0.14 mW. The value will be even lower with a wireless power transmitter. For the 4 mm coil, the output power is 1 mW, which is about 7 times the power of the 2 mm coil. This shows the importance of receiver coil diameter in the wireless power transfer system, where a small increase of diameter can result in a large improvement in coil output power. From the analysis, it is found that the 2-mm diameter air-core coil is unable to meet the 1 V induced voltage requirement and 1 mW power requirement with the present range of turn number.

Receiver coil diameter	D_{Rx}=1 mm	D_{Rx} =2 mm	D_{Rx} =4 mm
Output power at N=100	8.8 µW	0.07 mW	0.54 mW
Output power at N=200	17 µW	0.14 mW	1 mW

Table 3.3-2 Corresponding output power of receiver coil at the number of turns with different coil diameters with gap interval = 0.1 mm, wire diameter = 0.1 mm, operational frequency = 8 MHz and magnetic field = 1.5 A/m

(2) A variation of magnetic field strength from 0 to 20 A/m in different receiver coil diameters (1 mm, 2 mm, 4 mm)

In this analysis, the primary focus is on in what range of magnetic field strength the air-core receiver coil can achieve sufficient induced voltage (more than 1 V) and output power (more than 1 mW) under the size limitation (2 mm diameter).

The range of magnetic field strength is chosen based on the magnetic field generated by the optimised transmitter in the wireless power transfer system at a transfer distance between 8 cm and 20 cm. The 2 mm-diameter is chosen based on the requirement mentioned at the beginning of this section. The 1 mm and 4 mm diameters are chosen for comparison and trend analysis. The number of turns 100 is chosen because the resulting coil length will be about 2 cm, which is within the limit of receiver coil length that would be implantable. The changes in induced voltage and output power with the variation of magnetic field strength in different receiver coil diameter are shown in Figure 3.3-5.

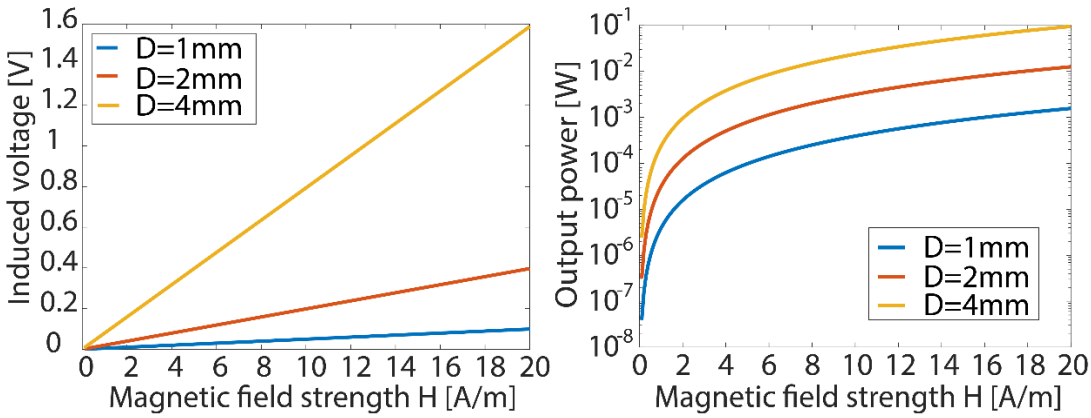

Figure 3.3-5 RMS induced voltage (left) and output power (right) of air-core receiver coil in different coil diameter (1 mm, 2 mm, 4 mm) for a range of magnetic field strength (0 to 20 A/m) with gap interval = 0.1 mm, wire diameter = 0.1 mm, operational frequency = 8 MHz and 100 turns

For the 2 mm-diameter coil, the induced voltage increases from 0.03 V at 1.5 A/m to about 0.4 V at 20 A/m. The 4 mm-diameter coil has an induced voltage 4 times of the induced voltage of the 2 mm-diameter coil at the same magnetic field strength, and the 1 mm-diameter coil induced voltage is a quarter of the 2 mm-diameter coil induced voltage. Again, the 2 mm-diameter receiver coil has a low induced voltage at the target range of magnetic field strength with the present settings. Even with 200 turns, the induced voltage of the 2 mm-diameter coil is 0.8 V at 20 A/m, which is not enough for the application of micro-implants without the use of a voltage-boost device at the load.

The output power at the two magnetic field strengths (1.5 A/m and 20 A/m) for the three coil diameters (1 mm, 2 mm and 4 mm) can be seen in Table 3.3-3. For the 2 mm-diameter receiver coil, the output power meets the 1 mW power requirement when $H \geq 5$ A/m, which corresponds to a transfer distance of less than 11 cm, which is almost half of the target transfer distance (20 cm). The 4 mm-diameter coil has a

much better performance for the range of magnetic field, but it is beyond the size limit of the needle. The 1 mm-diameter coil has minimal output power and is not suitable for this range of magnetic field strength.

Receiver coil diameter	D_{RX} =1 mm	D_{RX} =2 mm	D_{RX} =4 mm
Output power at H=1.5 A/m	8 µW	0.07 mW	0.54 mW
Output power at H=20 A/m	2 mW	13 mW	96 mW

Table 3.3-3 Corresponding output power of receiver coil at the magnetic field strengths with different coil diameters with gap interval = 0.1 mm, wire diameter = 0.1 mm, operational frequency = 8 MHz and 100 turns

(3) A variation of gap intervals between turns from 0.2 mm to 0.5 mm in different wire diameters (0.1 mm, 0.15 mm, 0.2 mm)

In this analysis, the primary focus is to find out how the air-core output power changes when the gap interval changes and when the wire diameter changes.

The coil diameter is chosen to be 2 mm. The magnetic field strength is set to 1.5 A/m. The coils have 100 turns. The changes of output power from the receiver coil with a variation of gap interval between turns with different wire diameters are shown in Figure 3.3-6.

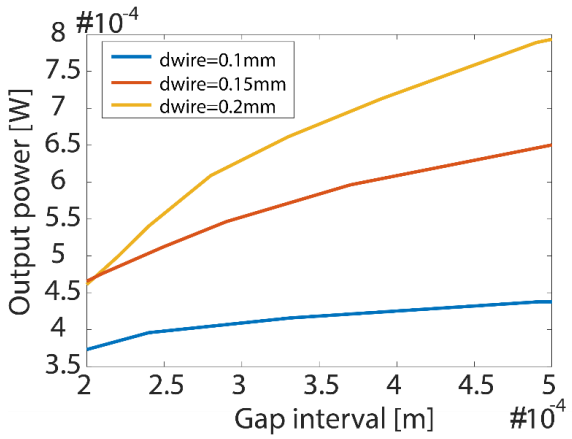

Figure 3.3-6 Output power of air-core receiver coil in different wire diameters (0.1 mm, 0.15 mm and 0.2 mm) for a range of gap intervals between turns (0.2 mm to 0.5 mm) with coil diameter=2 mm, magnetic field strength=1.5 A/m, and operational frequency=8 MHz and 100 turns

As shown, for the same wire diameter, the output power increases as the gap interval increases. For larger wire diameters, the output power increases with higher gradients. That means the output power increases "faster" for thicker wires when the gap interval increases. As shown in Table 3.3-4, only a 0.02 mW increase happens for the 0.1 mm-diameter wire when the gap interval increases from 0.2 mm to 0.5 mm, while for 0.2 mm wire, the increase is 0.08 mW.

Wire diameter	d_{wire}=0.1 mm	d_{wire} =0.15 mm	d_{wire} =0.2 mm
Output power at 0.2 mm interval	0.09 mW	0.11 mW	0.12 mW
Output power at 0.5 mm interval	0.11 mW	0.16 mW	0.20 mW

Table 3.3-4 Corresponding output power of receiver coil at the gap invervals with different wire diameters with magnetic field strength = 1.5 A/m, coil diameter = 2 mm, operational frequency = 8 MHz and 100 turns

For different wire diameters, however, for the present range of gap interval, the increase of wire diameter is not linear to the increase of output power. As shown in Table 3.3-4, while the 0.2 mm d_{wire} is twice than 0.1 mm, the output power of the 0.2 mm d_{wire} coil is less than twice of the output power of the 0.1 mm d_{wire} coil for the same gap interval. What's more, the difference between the output powers of the 0.2 mm d_{wire} coil and of the 0.1 mm d_{wire} coil decreases when the gap interval narrows.

For a narrow gap interval, a thicker wire doesn't always seem to guarantee a higher output power. For a gap interval from 0.2 mm to 0.25 mm, the difference between the output powers of the 0.15 mm wire and the 0.2 mm wire decreases and there is a crossover on the curves. The gap interval of crossover becomes larger for coils with a smaller number of turns, which is shown in Figure 3.3-7 with coils of 20 turns. The curve of 0.2 mm wire crossovers the curve of the 0.15 mm wire at about 0.22 mm gap interval, and crossovers the curve of the 0.1 mm wire at about 0.2 mm gap interval. This shows that the output power of thicker wires can be lower than the output power of thinner wires at a narrow gap interval. Therefore, with a limited coil length and a narrow gap interval, a thin wire is a better option for the air-core coil than a thick wire. Gap interval of 0.1 mm, wire diameter of 0.1 mm is a safe choice.

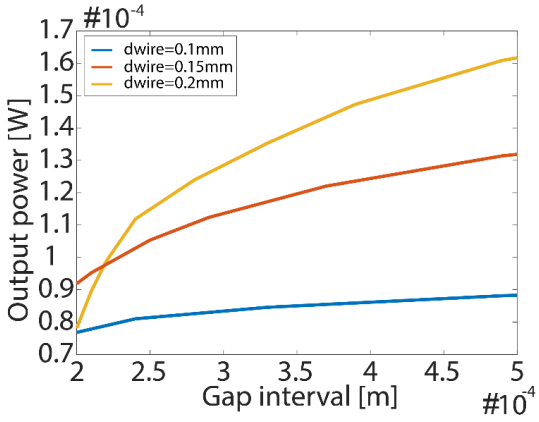

Figure 3.3-7 Output power of air-core receiver coil in different wire diameters (0.1mm, 0.15mm and 0.2mm) for a range of gap intervals between turns (0.2mm to 0.5mm) with coil diameter=2mm, magnetic field strength =1.5A/m, operational frequency=8MHz and 20 turns

3.3.3.3 Summary

The analysis in Section 3.3.3.2 shows that the air-core solenoid receiver coil with 2 mm diameter cannot guarantee sufficient induced voltages and output powers for

the load in the target transfer distances with the optimised wireless power transmitter. Even though the output power from the 2 mm-diameter receiver coil can provide more than 13 mW at close transfer distances (<6 cm), the output power for a long distance (20 cm) is less than 0.1 mW. Moreover, the induced voltage for the 2 mm-diameter receiver is very small (<0.5 V) even with a large number of turns (200 turns) at this transfer distance. With this voltage level, the micro-implants at the load of the receiver will not be able to work properly without voltage-boost devices such as transformers or DC-DC converters, which will cause an increase of the size of the receiver or lower the operation efficiency.

To verify the calculation results from the developed model, a simulation of induced voltage on the receiver coil is done in *COMSOL Multiphysics* with a variation of number of RX turns at a transfer distance of 20 cm. A demonstration of the coils is shown in Figure 3.3-8. The primary coil is the optimum coil for the 20 cm transfer distance with the same magnetic field strength distribution, as mentioned in Section 3.2.4. The receiver coil is an air-core solenoid coil of 2 mm diameter and 0.1 mm gap interval and wire width and is situated at the axis of the primary coil.

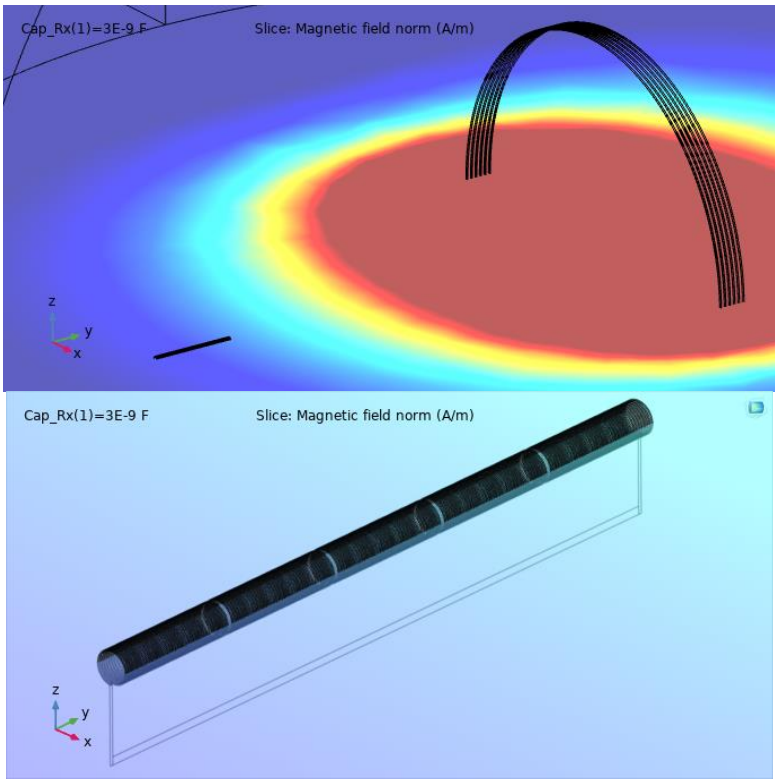

Figure 3.3-8 (top) Demonstration of optimum primary coil and air-core receiver coil (on the bottom-left of the image) at 20 cm transfer distnace in the COMSOL simulation and (bottom) an image of 200-turn receiver coil with 2 mm diameter and 0.1 mm of gap interval and wire width. The receiver coil overall length=4cm.

The simulation results are shown in Figure 3.3-9. The calculation results have the same trend as the simulation results, and the values are also very close to the simulation results in the range of turns, with a standard deviation of 0.47 mV. From

the comparison, the model for the air-core solenoid coil is valid for the present setting of dimensional parameters. Because of the low induced voltage and output power, the air-core solenoid receiver coil is not suitable for the proposed wireless power transfer system. In the next section, the ferrite-core solenoid will be analysed.

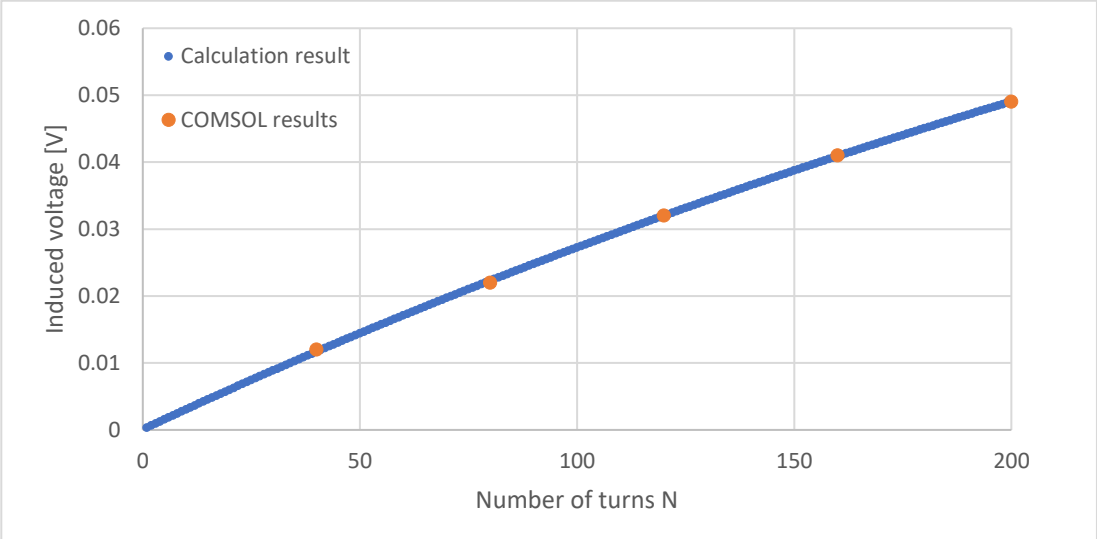

Figure 3.3-9 Comparison of COMSOL simulation results, calculation results of induced voltages on the air-core receiver coil against the number of turns of receiver coil at 20 cm transfer distance

3.3.4 Analysis of receiver with a ferrite-core solenoid coil

3.3.4.1 Ferrite core

In order to improve the induced voltage and the output power performance of the receiver solenoid coil, the ferrite core is used. The model of the ferrite-core solenoid coil refers to the content of *Wireless power transfer for scaled electronic biomedical implants* by P. Theilmann [136], page 89-96.

For closed loop ferrite structures, such as an ideal toroid or infinitely long ferrite rods, if both of the primary coil and the receiver coil are wound tightly on the same ferrite, the induced voltage on the receiver coil can be calculated as [196],

$$V_{IND-CF} = j\omega\mu_0\mu_r N_{RX} H_z A_{eff} \tag{3.31}$$

where

- $V_{IND\text{-}CF}$ is the RMS induced voltage on the receiver coil mount on a closed ferrite
- N_{Rx} is the number of turns of the receiver coil
- A_{eff} is the effective area of the receiver coil
- H_z is the magnetic field strength $\mathbf{z}$-direction component
- ω is the angular frequency of the magnetic field
- μ_0 is the permeability of air space

- μ_r is the relative permeability of the ferrite

However, if the ferrite core is only used at the receiver coil, a reduction of the magnetic flux will occur within the ferrite core because of the air gap at the ends of the ferrite core [197]. From (3.31), the induced voltage on the receiver coil will become

$$V_{IND-F} = j\omega\mu_0\mu_{r-eff}N_{RX}H_zA_{eff} \tag{3.32}$$

where μ_{r-eff} is the effective relative permeability of the ferrite.

For an elliptical ferrite core shown in the left of Figure 3.3-10, the effective relative permeability of a ferrite can be calculated as [198],

$$\mu_{r-eff} = \frac{\mu_r}{1 + D_{fe}(\mu_r - 1)} \tag{3.33}$$

where D_{fe} is the demagnetising factor of the ellipsoid [197][199],

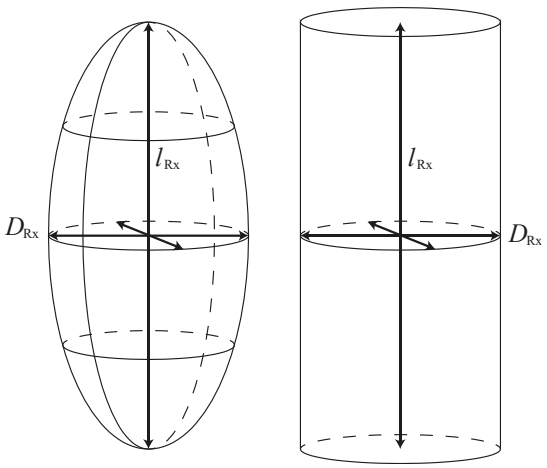

Figure 3.3-10 Demonstration of an elliptical ferrite core and a cylindrical ferrite core with the length of the cores being l_{RX}, the diameter of the cores being D_{RX}.

$$D_{fe} = \frac{l_{RX}D_{RX}^2}{2}A \tag{3.34}$$

$$A = \int_0^\infty \frac{ds}{(s+a^2)R_s}(elliptical\ integral) \tag{3.35}$$

$$R_s = \sqrt{(s+a^2)(s+b^2)(s+c^2)} \tag{3.36}$$

where s is the ellipsoidal coordinate.

For long and thin ellipsoids, with which $\gamma = \frac{l_{Rx}}{D_{Rx}} > 1$ [136],

$$A = \frac{1}{l_{RX}^3 e^3}\left[ln\left(\frac{1+e}{1-e}\right) - 2e\right] \tag{3.37}$$

$$e = \sqrt{1 - \left(\frac{D_{RX}}{l_{RX}}\right)^2} \tag{3.38}$$

Therefore,

$$D_{fe} = \frac{D_{RX}^2}{2l_{RX}^2 e^3}\left[ln\left(\frac{1+e}{1-e}\right) - 2e\right] \tag{3.39}$$

For a cylindrical ferrite core with the same length and diameter as the elliptical core, as shown in the right of Figure 3.3-10, a modification of the demagnetising factor is needed. Based on the empirical analysis in [200], for long and thin cylindrical ferrite cores, the cylindrical demagnetising factor can be calculated as

$$D_{fc} = D_{fe}(0.755\gamma^{0.13}) \tag{3.40}$$

where $\gamma = \frac{l_{Rx}}{D_{Rx}} > 1$.

The effective relative permeability of a cylindrical ferrite core thus can be calculated as [136]

$$\mu_{r-eff} = \frac{\mu_r}{1 + D_{fc}(\mu_r - 1)} \tag{3.41}$$

Because of the losses from magnetic hysteresis and eddy currents in the ferrite core, the relative permeability of a ferrite core is a complex value, which is extended as [171]

$$\mu_r = \mu_r{}' - j\mu_r{}'' \tag{3.42}$$

where

- $\mu_r{}'$ is the real component of the complex magnetic permeability of the ferrite, which is related to the inductance of the ferrite coil.
- $\mu_r{}''$ is the imaginary component of the complex magnetic permeability of the ferrite, which is related to the ferrite loss.

From (3.41) and (3.42), the effective relative permeability can thus be calculated as

$$\mu_{r-eff} = \mu'_{r-eff} + j\mu''_{r-eff} \tag{3.43}$$

where

$$\mu'_{r-eff} = Re\left(\frac{\mu_r}{1 + D_{fc}(\mu_r - 1)}\right) \tag{3.44}$$

$$\mu''_{r-eff} = Im\left(\frac{\mu_r}{1 + D_{fc}(\mu_r - 1)}\right) \tag{3.45}$$

From (3.32) and (3.43), the induced voltage on a cylindrical solenoid receiver coil can thus be calculated as

$$V_{IND-F} = j\omega\mu_0\mu'_{r-eff}N_{RX}H_zA_{eff} \tag{3.46}$$

Based on the analysis above, the circuit model can be built for the ferrite-core cylindrical solenoid receiver coil.

3.3.4.2 Circuit model

In Section 3.3.2, an equivalent circuit has been built for the receiver coil to calculate the maximum output power from the coil. The circuit diagram is shown again here in Figure 3.3-11.

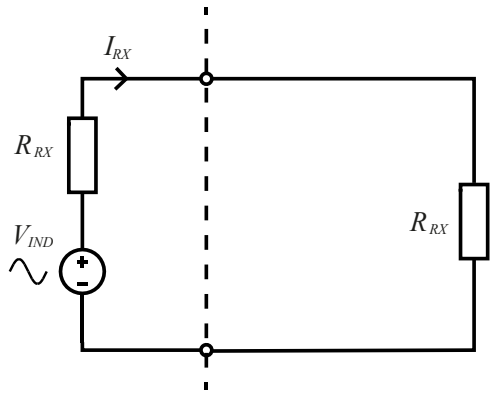

Figure 3.3-11 Equivalent circuit of receiver with impedance matching circuit from the series L-C circuit side; the impedance of the rectifier has been converted to R_{RX}, which is the total resistance of the series L-C circuit; the voltage source VIN equals to the induced voltage across the receiver coil.

As discussed in Section 3.3.4.1, the induced voltage on a cylindrical solenoid coil with a ferrite core can be calculated as

$$V_{IND-F} = j\omega\mu_0\mu'_{r-eff}N_{RX}H_zA_{eff} \tag{3.47}$$

where

- V_{IND-F} is the RMS induced voltage on the receiver coil mount on a ferrite
- N_{Rx} is the number of turns of the receiver coil
- A_{eff} is the effective area of the receiver coil
- H_z is the magnetic field strength z-direction component
- ω is the angular frequency of the magnetic field
- μ_0 is the permeability of air space
- μ'_{r-eff} is the real component of the effective relative permeability of the ferrite

In the circuit, the resistor R_{RX} represents the total resistance of the receiver coil. For a cylindrical solenoid coil with a ferrite core [201],

$$R_{RX} = R_{ferrite} + R_{AC-Coil} \tag{3.48}$$

where $R_{AC\text{-}Coil}$ is the AC resistance of the receiver coil due to the skin effect and the proximity effect, which has been discussed in Section 2.3.3.4.

$R_{ferrite}$ represents the losses in the ferrite core, which can be calculated as [201]

$$R_{ferrite} = \omega L_0 \mu''_{r-eff} \tag{3.49}$$

Here, $\mu''_{r-\mathrm{eff}}$ is the imaginary component of the effective relative permeability of the ferrite. L_0 is the inductance of the coil without the ferrite core, which can be calculated as [202],

$$L_0 = \frac{10\pi\mu_0 N_{RX}^2 \left(\frac{D_{RX}}{2}\right)^2}{9\left(\frac{D_{RX}}{2}\right) + 10 l_{RX}} \tag{3.50}$$

This expression is most accurate when $l_{Rx} >> 0.1 D_{RX}$.

The inductance of the receiver coil with the ferrite core can be calculated as [201]

$$L_{ferrite} = \mu'_{r-eff} L_0 \tag{3.51}$$

As a result, by combining (3.26) (3.47) and (3.48), the output power from a cylindrical solenoid coil with a ferrite core can be calculated as

$$P_{OUT-F} = \frac{\left(2\pi f \mu_0 \mu'_{r-eff} N_{RX} H_z A_{eff}\right)^2}{4\left(R_{ferrite} + R_{AC-Coil}\right)} \tag{3.52}$$

Based on the above analysis, the output power and the induced voltage performances of a cylindrical solenoid receiver coil with a ferrite core can be predicted and analysed.

3.3.4.3 Induced voltage and output power analysis for receivers with a ferrite-core coil

In this analysis, the same conditions are applied as the receivers with an air-core coil, which have been discussed in Section 3.3.3.2. The ferrite used here is the K1 material from TDK Group Company, with the details listed in Figure 3.3-5.

Material name	Base material	Target application	Optimum frequency range	Complex relative permeability at 8MHz and 37°C	Coercive field strength at 25°C
K1	NiZn	Resonant circuit inductor	1.5-12MHz	80-j5, ±25%	380A/m

Table 3.3-5 Material properties for the material K1 from TDK Group Company [203]

As a preliminary setting, while the changes of induced voltage and output power with the variation of other parameters are observed, the wire diameter is set to be 0.1mm, which is approximately the wire width of AWG38 standard. Also, the gap interval is set to be the same as the wire diameter.

The changes in the induced voltage and the output power will be discussed as follows.

- A variation of the magnetic field strength from 0 to 20 A/m in different receiver coil diameters (1 mm, 2 mm, 4 mm)
- A variation of the number of turns from 1 to 200 in different receiver coil diameters (1 mm, 2 mm, 4 mm)
- A variation of the gap intervals between turns from 0.2 mm to 0.5 mm in different wire diameters (0.1 mm, 0.13 mm, 0.16 mm)

In the first analysis with different magnetic field strengths, it is assumed that the magnetic field strength is uniform through the whole length of the receiver coil. In the second and third analysis, the induced voltage and output power of the receiver coil will be analysed with the presence of the optimised wireless power transmitter at the specific transfer distance (20 cm). This means the magnetic field in the receiver coil will not be uniform and will weaken as the distance from the transmitter increases. A more accurate prediction can thus be obtained. The calculation will assume that the transfer media is air.

(1) A variation of magnetic field strength from 0 to 20 A/m in different receiver coil diameters (1 mm, 2 mm, 4 mm)

The dimensional parameters (number of turns N, wire diameter d_{wire} and gap interval p) of the ferrite-core receiver coil are the same as the parameters in the first analysis of the air-core coil in Section 3.3.3.2.

The calculated V_{IND} and P_{OUT} of the receiver coil are shown and compared with the calculated V_{IND} and P_{OUT} of air-core coil in Table 3.3-6. As shown, the induced voltage of the 2 mm ferrite-core receiver coil for the range of magnetic field strength is much higher than the induced voltage of the air-core receiver coil with the same size and the same number of turns. At 1.5 A/m and 20 A/m, the induced voltages of the 2 mm ferrite-core coil are 0.9 V and 12.0 V, respectively, which are more than 30 times higher than the induced voltages of the air-core coil at the corresponding magnetic field strength. These voltages are more than sufficient for the operation of medical micro-implants.

Receiver coil	Ferrite-core, D_{Rx}=2 mm, N =100	Air-core, D_{Rx}=2 mm, N =100
Induced voltage V_{IND} at 1.5 A/m	0.9 V	0.014 V
Induced voltage V_{IND} at 20 A/m	12.0V	0.40 V
Output power P_{out} at 1.5 A/m	2.9 mW	0.07 mW
Output power P_{out} at 20 A/m	517 mW	13.0 mW

Table 3.3-6 (From calculation) comparison of induced voltages and output powers at two different magnetic field strengths between the ferrite-core coil and the air-core coil

In terms of output power, the 2 mm ferrite-core coil has a much better performance than the 2 mm air-core coil. As shown in Table 3.3-6, at 1.5 A/m and 20 A/m, the output powers from the 2 mm ferrite-core coil are 2.9 mW and 517 mW, which are about 40 times higher than the corresponding output power from the 2 mm air-core coil. However, the induced voltage for the ferrite coil with 100 turns is still not enough at 1.5 A/m, higher turns are needed to meet the requirement of the system.

(2) A variation of number of turns from 1 to 200 in different receiver coil diameters (1 mm, 2 mm, 4 mm)

In this analysis, the induced voltage and the output power from the ferrite-core receiver coil are calculated in the situation where the receiver is located at 20 cm distance from the optimised wireless power transmitter. Therefore, the magnetic field inside the receiver coil is not uniform, which is closer to the real situation.

Except for the number of turns, the dimensional parameters (wire diameter d_{wire}, gap interval p) of the ferrite-core receiver coil are the same as the parameters in the second analysis of the air-core coil in Section 3.3.3.2.

The calculated induced voltages and output power with a variation of the number of turns for the ferrite-core receiver coil are shown in Table 3.3-7 and Table 3.3-8.

Number of turns	N =50	N =100	N =200
V_{IND} for D_{RX}=4 mm (V)	0.45	1.70	5.95
V_{IND} for D_{RX}=2 mm (V)	0.22	0.82	2.46
V_{IND} for D_{RX}=1 mm (V)	0.11	0.34	0.81
V_{IND} ratio for D_{RX}=4 mm/D_{RX}=2 mm	2.0	2.07	2.4
V_{IND} ratio for D_{RX}=4 mm/D_{RX}=1 mm	4.1	5.0	7.3

Table 3.3-7 (From calculation) RMS induced voltage on the coils with the three diameters at the three numbers of turns and their ratios

Number of turns	N =50	N =100	N =200
P_{OUT} for D_{RX}=4 mm (mW)	4.7	10.0	16.2
P_{OUT} for D_{RX}=2 mm (mW)	1.3	2.4	3.9
P_{OUT} for D_{RX}=1 mm (mW)	0.32	0.59	0.96
P_{OUT} ratio for D_{RX}=4 mm/D_{RX}=2 mm	3.6	4.2	4.2
P_{OUT} ratio for D_{RX}=4 mm/D_{RX}=1 mm	14.7	16.9	16.9

Table 3.3-8 (From calculation) output power from the coils with the three diameters at the three numbers of turns and their ratios

For ferrite-core coils with larger diameters, the induced voltage and output power are higher, and the ratio of induced voltage between coils of different diameters is higher at a higher number of turns. At 200 turns, the induced voltage ratios are 2.4 (for D_{RX}=4 mm/D_{RX}=2 mm) and 7.3 (for D_{RX}=4 mm/D_{RX}=1 mm). This means that the induced voltage on a single receiver coil with 4mm diameter can be more than the total voltages induced by two 2-mm receiver coils or seven 1-mm receiver coils with the same turn number. For the presented turn numbers, the induced voltage ratio increases as the turn number increases. The output power, however, does not have an apparent trend. The output power ratio for D_{RX}=4 mm/D_{RX}=2 mm varies from 3.6 at 50 turns to 4.2 at 100 and 200 turns. The output power ratio for D_{RX}=4 mm/D_{RX}=1 mm varies from 14.7 at 50 turns to 16.9 at 100 and 200 turns. The reason for the same power ratio at 100 and 200 turns is because as the magnetic field gets weaker at a further transfer distance, the field strength at the far end of the receiver coil is weaker than the field strength at the close end. Therefore, the effect from the increase of AC resistance balances the effect from the increase of induced voltage, causing the output power ratio to remain at the same value.

A comparison of the sizes between a 4 mm-diameter coil and three 2 mm-diameter coils and twelves 1 mm-diameter coils is shown in Figure 3.3-12. Three 2 mm-diameter coils already occupy more spaces than a 4 mm-diameter coil, and twelves 1 mm-diameter coils occupy a similar space as a 4 mm-diameter coil. Therefore, to generate the same output power, with consideration of the proximity effect between coils, much more spaces are required for coils with small diameters than coils with larger diameters. Because the space for the receiver is very limited within the patients' body, with the present parameters, a ferrite-core coil with a larger diameter will be able to induce a higher voltage and provide more output power than a number of smaller coils that take a similar space.

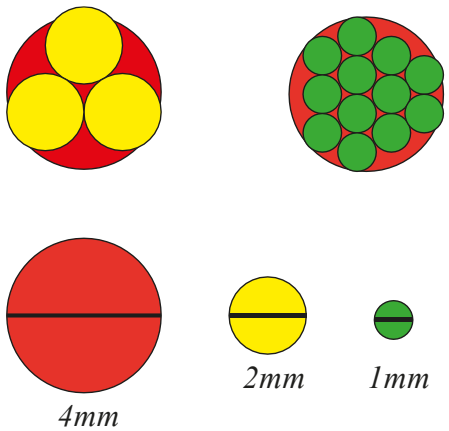

Figure 3.3-12 Size comparison between a 4 mm-diameter circle and three 2 mm-diameter circles and twelve 1 mm-diameter circles

For the 2-mm ferrite-core receiver coil, the maximum induced voltage and output power is achieved when N =250 under the length restriction of the implant. The corresponding induced voltage and the output power are 3.27 V and 4.4 mW, which are sufficient to meet the requirement of implant.

(3) A variation of gap intervals between turns from 0.2 mm to 0.5 mm in different wire diameters (0.1 mm, 0.13 mm, 0.16 mm)

The sizes of wire diameter are chosen based on the diameter of AWG38 (0.101 mm), AWG36 (0.127 mm) and AWG34 (0.160 mm).

The changes in the output power with the variation of the gap interval and different wire diameters are shown in Figure 3.3-13.

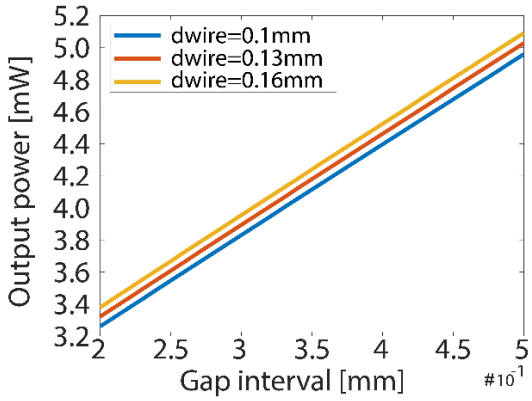

Figure 3.3-13 (From calculation) RMS induced voltage of ferrite-core receiver coil in different wire diameter (0.1 mm, 0.15 mm and 0.2 mm) for a range of gap intervals between turns (0.2 mm to 0.5 mm) with coil diameter = 2 mm, and operational frequency = 8 MHz and 100 turns, at 20 cm transfer distance with the optimised wireless power transmitter

For the same wire diameter, the output power increases linearly with the increase of gap interval at this range of gap interval. The output power is less than doubled when the gap interval increases from 0.2 mm to 0.5 mm for the same wire diameter, which means a 2-time increase in length can cause a 1.37-time increase in the output power for 100 turns. This is less “space-efficient” than the change in the number of turns.

For the same gap interval, a 0.03 mm (30% of 0.1 mm) change in diameter does not have a significant effect on the output power with the present coil parameters. The average difference between the d_{wire}=0.1 mm output power and the d_{wire}=0.13 mm is 0.06 mW (1.4% of the average output power of d_{wire}=0.1 mm at this gap interval range), and it is 0.05 mW (1.3% of the average output power of d_{wire}=0.13 mm at this gap interval range) between the output powers of d_{wire}=0.13 mm and d_{wire}=0.16 mm. The difference between output powers increases as the gap interval increases, but it decreases as the wire diameter increases.

From the above analysis, it shows that the effect of change in wire diameter on output power is insignificant and the effect of change in gap interval on output power is less “effective” than the change in the number of turns.

3.3.4.4 Summary

In Section 3.3.4, the model of a receiver with a ferrite-core coil has been built. The induced voltage and output power from the ferrite-core coil are analysed in different magnetic field strengths, different coil diameters, different numbers of turns, different gap intervals and different wire diameters.

Overall, the ferrite-core coil has a much higher induced voltage (more than 30 times) and a much higher output power (more than 40 times) than the air-core coil with the same parameters and the same magnetic field strength. A 2 mm ferrite-core coil with 250 turns, 0.1 mm wire diameter and 0.1 mm gap interval can induce a voltage more than 3.27 V and has an output power of 4.4 mW at 20 cm transfer distance with the proposed optimised wireless power. These values are sufficient to meet the requirement of the target implant.

The choice of wire diameter and gap interval is less significant for the receiver coil. The change in gap interval has less impact on the output power than the change in the number of turns with the same increase of coil length. The impact of the change in wire diameter is even smaller. A 30% change in wire diameter only results in a 1.4% change in the output power. It shows that the preliminary values of wire diameter (0.1 mm) and gap interval (0.1 mm) are suitable for the receiver coil, and there is no need to change them.

To verify the calculation results from the developed model, a simulation of induced voltage on the ferrite-core receiver coil is done in *COMSOL Multiphysics* with a variation of number of RX turns at a transfer distance of 20 cm. A demonstration of the coils is shown in Figure 3.3-15. The primary coil is the optimum coil for the 20 cm transfer distance with the same magnetic field strength distribution, as mentioned in Section 3.2.4. The receiver coil is a ferrite-core solenoid coil of 2 mm-diameter and 0.1 mm gap interval and wire width. The simulation results are shown in Figure 3.3-14. The calculation results are very close to the simulation results in the range of turns, with a standard difference of 0.19 V. The larger difference between the results in N=80 and 200 is because of the variation of the length of the ferrite-core, which will cause the induced voltage to vary. From the comparison, the model for the ferrite-core solenoid coil is valid.

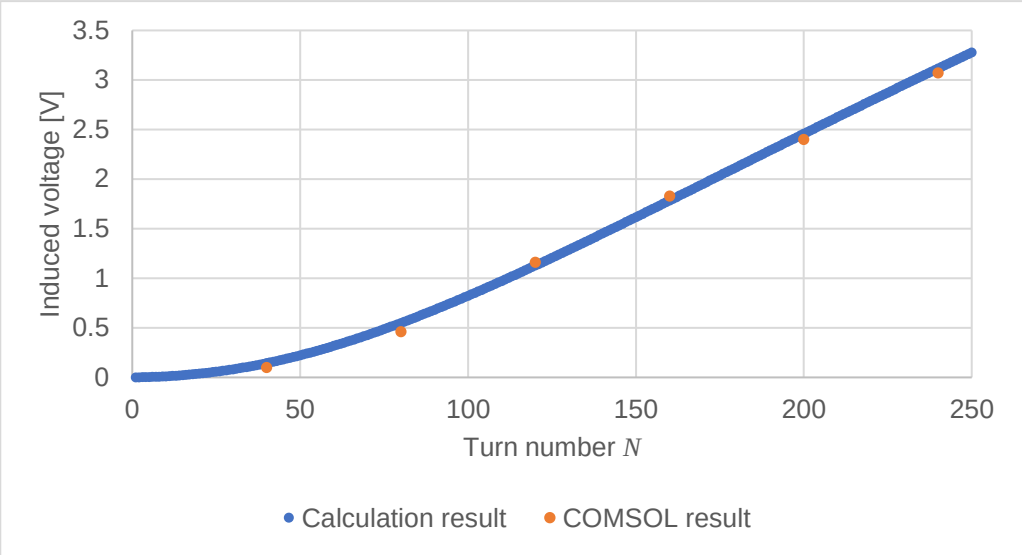

Figure 3.3-14 Comparison of COMSOL simulation results, calculation results of induced voltages on the ferrite-core receiver coil against the number of turns of receiver coil at 20 cm transfer distance

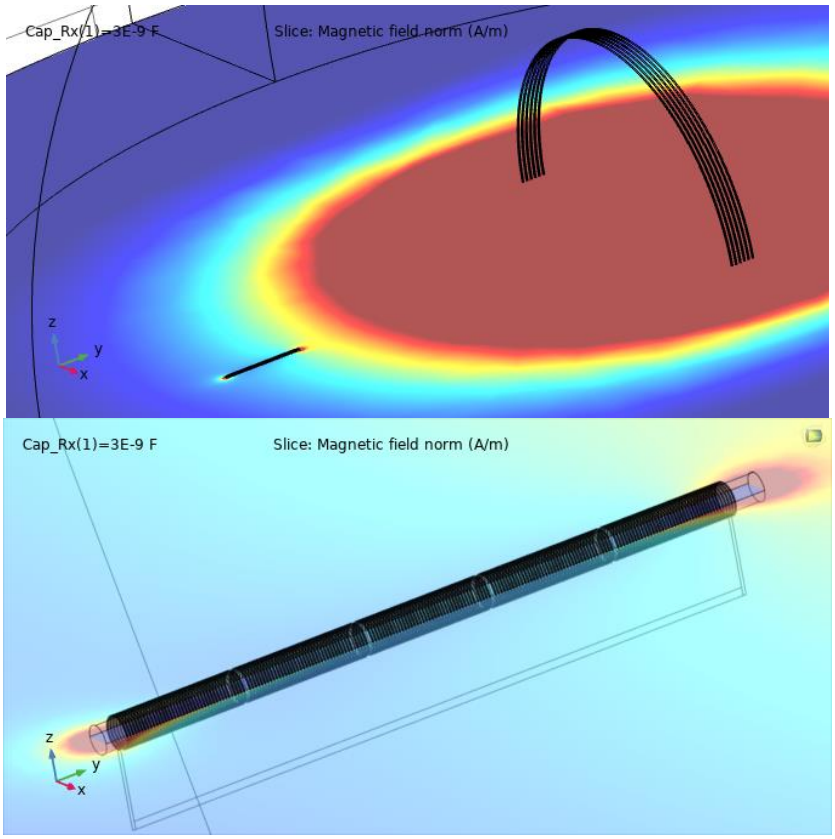

Figure 3.3-15 (Top) Demonstration of the optimum primary and the ferrite-core receiver coil (on the bottom-left of the image) at 20 cm-transfer-distnace in COMSOL simulation and (bottom) a close image of the 200-turn receiver coil with 2 mm diameter, 0.1 mm gap interval and 0.1 mm wire width. The coil overall length is 4 cm.

With the analysis above, it can be decided that ferrite-core coils are suitable to be the receiver coil in the proposed wireless power transfer system for medical micro-implants. Within the size limitation ($\leq$2 mm diameter) and the required transfer distance (10 cm to 20 cm), the ferrite-core coil is likely to provide sufficient induced voltages and output powers for the medical micro-implants.

In the next section, the design of the receiver coil and the receiver circuit will be discussed based on the power requirement of a load.

3.3.5 Receiver design flow

The circuit diagram of the receiver circuit in the proposed wireless power transfer system is shown again in Figure 3.3-16 with the load represented by an equivalent resistor R_{Load} and an equivalent capacitor C_{Load}. The design of the receiver circuit is aimed primarily at meeting the power requirement of the load under the size and transfer distance restrictions. This is not the same as the design of the transmitter, which aims to find the optimum parameters to achieve a maximum magnetic field strength, with no restriction on the physical size.

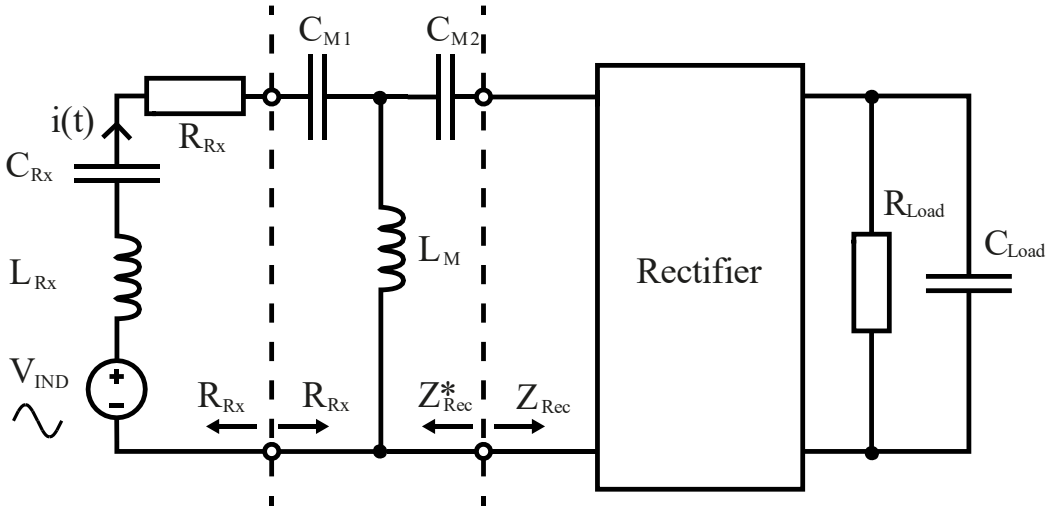

Figure 3.3-16 Circuit diagram of the receiver circuit with a T impedance matching circuit

Before the start of the design process, it is necessary to decide what the conditions are and what results should be obtained. These are shown in Table 3.3-9. Among the conditions, the load is a medical micro-implant with specified working conditions. Thus, the required load power P_{Load} and voltage V_{Load} are known. The diameter of the coil is restricted by the injection needle and the package; therefore, the max coil diameter $D_{Rx\text{-}max}$ will be slightly lower than the inner diameter of the needle. The coil length, however, has no strict restriction, but it should be kept small to minimise its effect on patients. Moreover, the operational frequency f and the maximum transfer distance $h_{Npri\text{-}max}$ are decided when the transmitter is designed. The body tissue parameters depend on the location of the implant inside the body.

Already decided	Should be decided	Need to obtain	Design target
Load (power requirement P_{Load}, Load voltage requirement V_{Load})	Rectifier (power efficiency η, voltage conversion ratio VCR)	Receiver coil target output power $P_{OUT\text{-}coil\text{-}req}$	Coil number of turns N_{RX}
Coil diameter restriction $D_{RX\text{-}max}$	Receiver coil diameter D_{RX}	Rectifier target input voltage $V_{rec\text{-}in\text{-}req}$	Coil length l_{RX}
Coil length restriction $l_{RX\text{-}max}$	Wire diameter d_{wire}	Receiver coil inductance L_{RX}	Resonance capacitor *on the receiver*
Operational frequency f	Receiver gap interval p_{RX}	Receiver coil self-capacitance C_{RX}	Ferrite core length $l_{ferrite}$ and diameter $d_{ferrite}$
Body tissue (dielectric constant $\boldsymbol{\varepsilon_x}$, conductivity $\boldsymbol{\sigma}$)	Ferrite material (complex relative permeability μ_r, dielectric constant $\boldsymbol{\varepsilon_i}$)	Receiver coil self-resistance R_{RX}	Impedance matching circuit C_{M1}, C_{M2}, L_M
Maximum transfer distance $h_{npri\text{-}max}$		Rectifier input impedance Z_{Rec}	
		Impedance matching circuit output voltage $V_{M\text{-}out}$	

Table 3.3-9 Conditions and targets for the design of receiver circuit

Besides these conditions, there are a few more parameters that need to be decided. Firstly, a rectifier should be chosen to convert AC power to DC on the receiver coil. Here, the load required power and voltage will be the output power and output voltage of the rectifier. The power efficiency η and the voltage conversion ratio VCR of the rectifier can thus be obtained based on the output values. Secondly, the receiver coil diameter D_{RX}, wire diameter d_{wire} and gap interval p_{RX} should be decided, because they are either decided by the size restriction (D_{RX}) or having little effect on the output power and induced voltage of the receiver coil (d_{wire}). Because the change in the number of turns N_{RX} has a stronger effect on the change in output power than the gap interval p_{RX}, the gap interval p_{RX} is kept small and constant during the design to keep the overall coil length small. Finally, the ferrite material should be decided. The ferrite material should have a moderate real relative permeability to boost the induced voltage, as well as a low dielectric constant to keep the coil SRF high. The optimum frequency range of the ferrite should also fit the operational frequency f.

The design flow of the receiver circuit is shown in Figure 3.3-17.

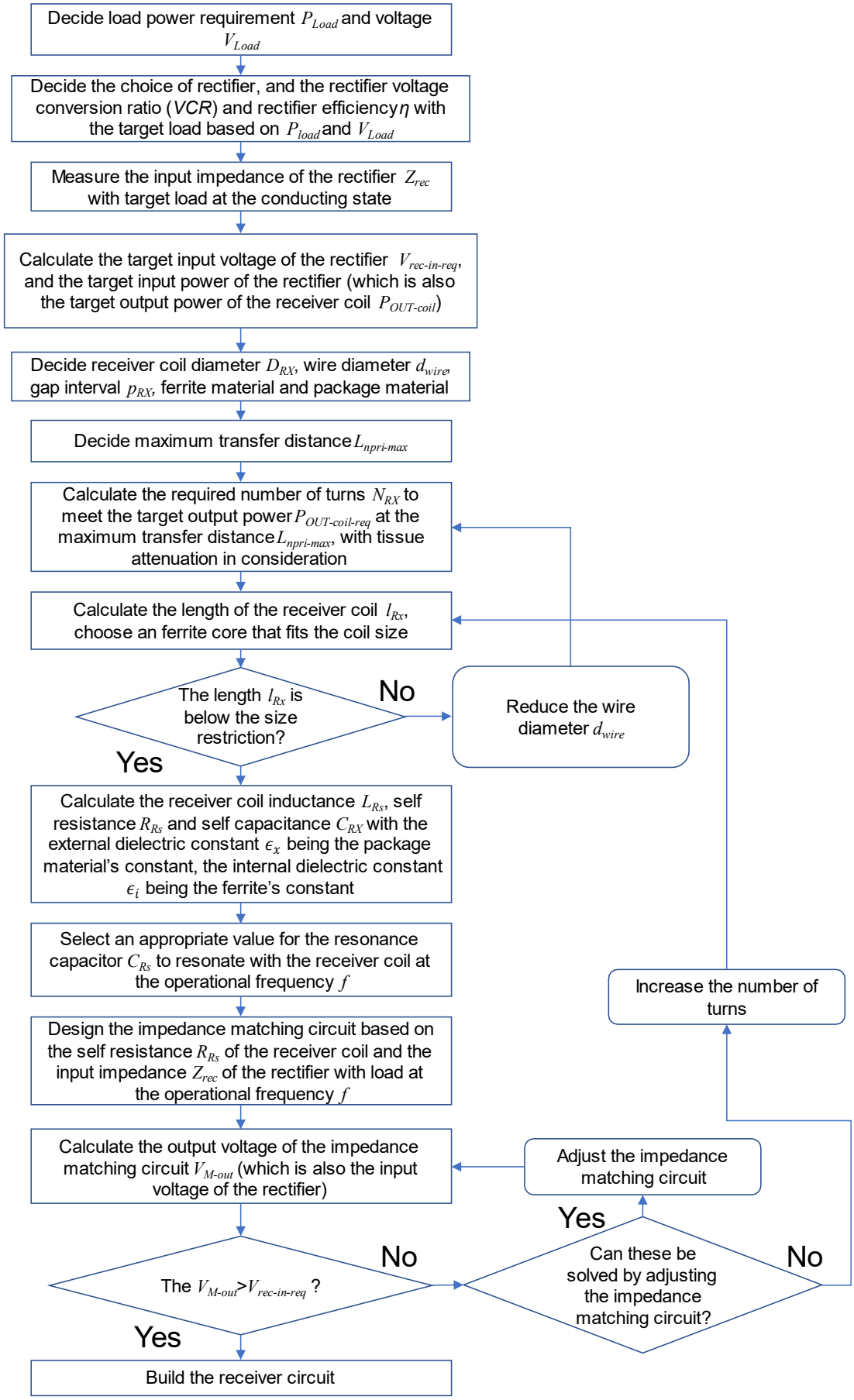

Figure 3.3-17 Design flow of the receiver circuit

The first target is the number of turns, which is the only variable of the receiver coil that has not yet been decided. In order to calculate this, the required output power $P_{OUT\text{-}coil\text{-}req}$ of the receiver coil needs to be obtained. This is calculated from the load power requirement and the rectifier power efficiency, which leads to the required input power of the rectifier. Because the power loss at the impedance matching circuit is negligible, the output power of the receiver coil is the same as the input power of the rectifier. Therefore, the required input power of the rectifier is the required output power $P_{OUT\text{-}coil\text{-}req}$ of the receiver coil. It should be noted that redundancy is needed to decide the value of the load power requirement in case of unexpected losses in the circuit.

Once $P_{OUT\text{-}coil\text{-}req}$ is obtained, the number of turns N_{RX} of the receiver coil can be calculated with the expression (3.52) in Section 3.3.4.2 with the conditions decided in Table 3.3-9. The calculation should consider the worst-case scenario, in which the whole transfer path is filled with conductive human tissues, to make sure enough power can be received by the receiver coil. After this, the length of the receiver coil l_{RX} can be obtained. If the length is under the size restriction, the design can proceed; if not, the wire diameter d_{wire} may have to be reduced to shorten the coil length because the change in wire diameter has the least effect on the change in receiver output power. After changing the wire diameter, the number of turns N_{RX} should be recalculated, and so should the coil length.

Once the coil length is under the size restriction, the electrical parameters of the receiver coil can be calculated, which are the receiver coil inductance L_{RX}, receiver coil self-capacitance C_{RX}, receiver coil self-resistance R_{RX}. With the coil inductance L_{RX} and self-capacitance C_{RX}, the value of the resonance capacitor can be picked up to make the circuit resonant at operational frequency f. It should be noted that the calculation of the coil self-capacitance needs to consider the external media, which is no longer air, but the packaging material surrounded by human body tissues. The external dielectric constant thus is the dielectric material of the packaging material with some adjustments for the human body tissues.

The coil self-resistance R_{RX} is needed in the design of the impedance matching circuit. Because the output of the impedance matching circuit is the rectifier, the input impedance Z_{Rec} of the rectifier with load should be matched to the coil self-resistance R_{RX} at the operational frequency f with the help of the impedance matching circuit. Because the proposed wireless power transfer system only works at one frequency, the bandwidth of the impedance matching circuit can be narrow. However, the output voltage $V_{M\text{-}out}$ of the impedance matching circuit should be higher than the required input voltage $V_{rec\text{-}in\text{-}req}$ of the rectifier to meet the load required voltage V_{Load}. If $V_{M\text{-}out}$

$<V_{rec\text{-}in\text{-}req}$, the impedance matching circuit should be adjusted or the number of turns of the receiver coil should be increased. Otherwise, the circuit can be built and tested.

3.3.6 Summary of the section

In Section 3.3, the receiver in the proposed wireless power transfer system is discussed. The receiver circuit model is built based on air-core solenoid coils and ferrite-core solenoid coils, with a coil diameter within 2 mm. Within the circuit, an impedance matching network is applied for the maximum output power from the receiver coil, which is independent of the load condition.

The induced voltage and the output power of the receiver coil are analysed respectively for air-core solenoid coils and ferrite-core solenoid coils.

For the air-core coils, it shows that for long transfer distances (>4 cm), the induced voltage and the output power from the coil are not sufficient for the operation of the medical micro-implants given the optimum transmitter coils. Both the increases in the number of turns and the gap interval (in a 0.1 mm scale) between turns can improve the induced voltage and the output power but in the compensation of longer coil lengths. Between these two improvement methods, the increase in the number of turns is more effective than the increase of gap interval. However, even with a high number of turns (200), the induced voltage and output power are barely sufficient for micro-implants.

For the ferrite-core coils, it shows that sufficient induced voltage and output power from the coil can be guaranteed even with power attenuation in transfer media. For the same dimensional parameters, the induced voltage from the ferrite-core coils is more than 30 times the induced voltage from the air-core coils, and the output power is more than 40 times. With the strong performance in induced voltage and output power, the diameter and length of the ferrite-core receiver coil can be more flexible in the design of wireless power transfer system.

A design flow of the receiver coil circuit is introduced based on the analysis of the ferrite-core solenoid coil model. The aim is to determine the dimensional parameters of the receiver coil based on the required input power of rectifier and load. With the coil diameter fixed by the clinical situation, the only flexible variable of the receiver coil is the number of turns, because both the wire diameter and the gap interval are less effective in the decision of induced voltage and output power while changing the same length of the coil. Once the dimensional parameters are decided, the impedance matching circuit can be designed based on the AC resistance of the receiver coil and the impedance of rectifier and load.

3.4 Summary of the chapter

In this chapter, a weakly-coupled magnetic resonance wireless power transfer system is developed based on air-core solenoid coils as the transmitter coils and a ferrite-core solenoid coil as the receiver coil.

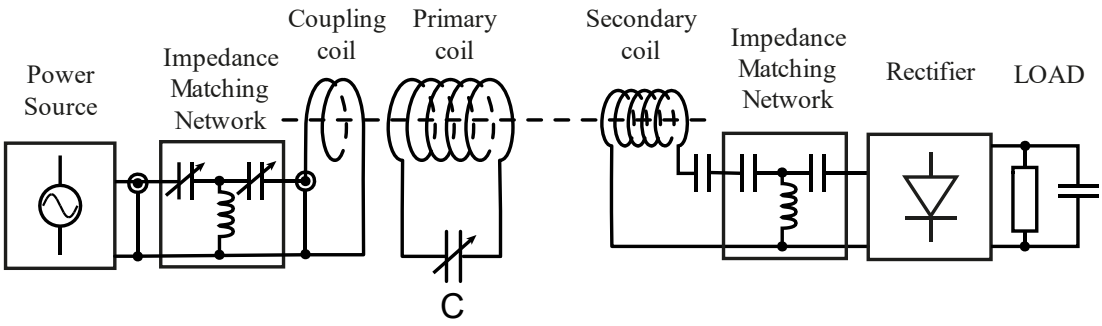

Figure 3.4-1 System diagram of the proposed magnetic coupling resonance WPT system including the magnetic coupling link and the rectifier and load at the receiver

As shown in Figure 3.4-1, the transmitter is a two-coil system: a single-turn coupling coil is connected to a power source with an impedance matching network in between; and a primary coil in the axis of the coupling coil which is resonated by a tuning capacitor. A model is built for the transmitter based on the bidirectional reflectance impedance analysis. Experimental results are compared with the model theoretical results, and good agreements are shown between them. Based on the model, the magnetic field generated by the primary coil is calculated, and the co-dependencies between primary coil parameters in the decision of maximum magnetic field are analysed. The analysis of parameter co-dependencies leads to the fact that a unique set of primary coil dimensional parameters exists to obtain a maximum magnetic field strength for a certain transfer distance and a certain operational frequency. With this understanding, a design flow of the transmitter system is introduced to obtain the optimum set of transmitter parameters for the proposed wireless power transfer system. The analysis also leads to a further discovery that the most effective solenoid structure for near field wireless power transfer system is a conical solenoid. The performance of conical solenoid coil in the wireless power transfer system is worth researching in the future work.

The receiver coil is a solenoid coil whose diameter is fixed to be less than 2 mm by the clinical situation. Circuit models are developed based on air-core solenoid coils and ferrite-core solenoid coils, respectively. The performances of both models are analysed with the wireless power transmitter optimised for 20 cm transfer distance. The analysis shows that the ferrite-core receiver coil is capable of providing enough power to micro-implants within conductive media at a long transfer distance (up to 20 cm) under the size restrictions. The air-core receiver coil, however, will only be able

to provide a similar amount of power in a short transfer distance (<4 cm) within the air. A design flow of the receiver circuit is also introduced to determine the dimensional parameters of the receiver coil based on the required input power of rectifier and load.

The analysis of the weakly-coupled magnetic resonance wireless power transfer system assumes that the operation of the receiver has little effect on the operation of the transmitter. This assumption is acceptable in the analysis of power because the diameter difference between the transmitter and the receiver is quite large (20 cm vs 2 mm) and the transfer distance is much larger than the diameter of the receiver (10-20 cm vs 2 mm). Moreover, any loading effect caused by the receiver at the transmitter can be compensated by the increase of input power of the transmitter. However, the model in this chapter also assumes that the magnetic link is a perfect voltage source with no source impedance. The calculated receiver output power and voltage are thus different from the actual values. In the analysis of the full WPT system in Chapter 5, the circuit model will be developed to combine the transmitter and the receiver so that the actual delivered power to load will be assessed.

In Chapter 4, the rectifier on the receiver circuit will be discussed.

Chapter 4 Rectifier on Chip

4.1 Circuit theory for rectifiers

Key aims of this section

- The operation of a general rectifier will be introduced.
- The energy losses in a general rectifier will be introduced and analysed.
- Ways to calculate the power efficiency of a general rectifier will be introduced.

A rectifier is a device that converts an alternating current (AC) to a direct current (DC). A good rectifier for low voltage on-chip applications should fulfil the following requirements:

- A low voltage drop between input and output
- Small voltage ripples at output
- A high rectification power efficiency

A block diagram of a rectifier is shown in Figure 4.1-1. In general, the efficiency of a rectifier is the overall efficiency over time, which is defined as the ratio of the output energy against the input energy within a certain time.

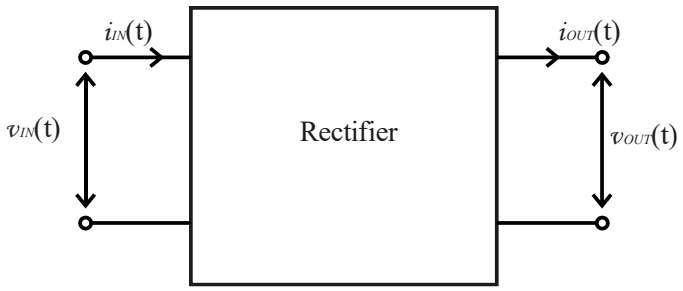

Figure 4.1-1 Block diagram of a rectifier. $v_{IN}(t)$ is the input voltage, $i_{IN}(t)$ is the input current; $v_{OUT}(t)$ is the output voltage, $i_{OUT}(t)$is the output current

In mathematic form, the output energy E_{OUT} and the input energy E_{IN} within a time t_0 are described as follows [209]

$$E_{OUT} = \int_0^{t_0} p_{OUT}(t)\, dt = \int_0^{t_0} v_{OUT}(t)\, i_{OUT}(t) dt \tag{4.1}$$

$$E_{IN} = \int_0^{t_0} p_{IN}(t)\, dt = \int_0^{t_0} v_{IN}(t)\, i_{IN}(t) dt \tag{4.2}$$

where p_{IN} is the instantaneous input power and p_{OUT} is the instantaneous output power.

The overall efficiency of a rectifier is thus described as [209]

$$\eta_{REC} = \frac{E_{OUT}}{E_{IN}} \tag{4.3}$$

For a periodic input (i.e. sine wave input), the overall efficiency of a rectifier in a long enough time is equal to the efficiency of a rectifier within a cycle at steady state. In this case, assuming that the rectifier works in steady state at time t_0, the output energy, input energy and the efficiency of the rectifier can be described as follows [209]

$$E_{OUT}(T) = \int_{t_0}^{t_0+T} p_{OUT}(t)\, dt = \int_{t_0}^{t_0+T} v_{OUT}(t)\, i_{OUT}(t) dt \tag{4.4}$$

$$E_{IN}(T) = \int_{t_0}^{t_0+T} p_{IN}(t)\, dt = \int_{t_0}^{t_0+T} v_{IN}(t)\, i_{IN}(t) dt \tag{4.5}$$

$$\eta_{REC} = \eta_T = \frac{E_{OUT}(T)}{E_{IN}(T)} \tag{4.6}$$

where T is the time of a cycle of the periodic input.

For a practical rectifier, $0 < \eta_{Overrall} < 1$, which means the output energy E_{OUT} will not be able to equal to the input energy E_{IN}. The difference between E_{OUT} and E_{IN} is called loss.

For conventional rectifiers with passive rectification components (i.e. PN-junction diodes in Figure 4.1-2, the triangle with an n), the loss mainly comes from the rectification components [209]. The relation between E_{OUT} and E_{IN} can be written as follows,

$$E_{OUT} = E_{IN} - E_{diode} - E_{other} \tag{4.7}$$

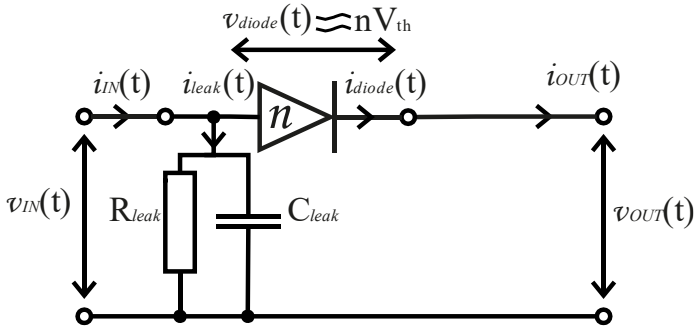

Figure 4.1-2 Illustrative circuit diagram for a conventional rectifier with a number of n working PN-junction diodes at an arbitrary time. $v_{diode}(t)$ is the total voltage across the diodes; $i_{diode}(t)$ is the amount of current through the diodes; V_{th} is the threshold voltage of the diodes

The loss of energy in the diodes can be divided into two parts. One is the heat loss of the diodes and the other one is the leakage loss of the diodes. The heat loss is due to the current through the PN-junction of the diode. The leakage loss is due to the leakage current through the parasitic capacitance between the diode and ground in high frequencies [209].

$$E_{diode} = E_{heat} + E_{leak} \tag{4.8}$$

$$\begin{aligned} E_{heat} &= \int_0^{t_0} v_{diode}(t)\, i_{diode}(t)dt \approx \int_0^{t_0} n\, V_{th} i_{OUT}(t)dt \\ &= nV_{th} \int_0^{t_0} i_{OUT}(t)dt \end{aligned} \tag{4.9}$$

$$E_{leak} = \int_0^{t_0} v_{IN}(t)\, i_{leak}(t)dt \tag{4.10}$$

For rectifiers with active rectification components (i.e. PMOS, P-type Metal-Oxide-Semiconductor, in Figure 4.1-3 and Figure 4.1-4), the loss is mainly from the heat loss of the PMOS, the leakage loss due to the reverse currents from the output, and the energy consumed by the MOSFET control circuit [209].

$$E_{OUT} = E_{IN} - E_{heat} - E_{REV} - E_{CTL} - E_{other} \tag{4.11}$$

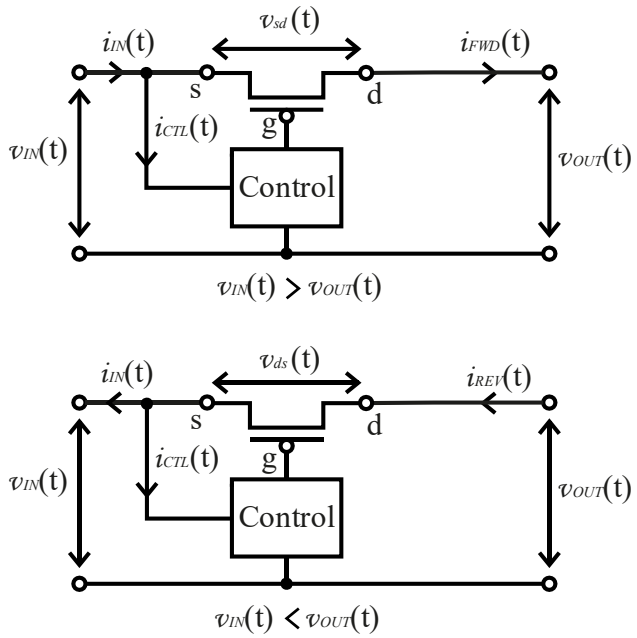

Figure 4.1-3 Illustrative circuit diagram for a PMOS rectifier with the control circuit current from the input. The upper diagram is when $v_{IN}(t) > v_{OUT}(t)$; the bottom diagram is when $v_{IN}(t) < v_{OUT}(t)$. $v_{sd}(t)$ and $v_{ds}(t)$ are the voltage across the source and drain of the PMOS in the two different situations. $i_{REV}(t)$ is the reverse current flowing from the output to the input when $v_{IN}(t) < v_{OUT}(t)$. The block "Control" is the control circuit to control the gate voltage of the PMOS. $i_{CTL}(t)$ is the current from the input to power the control circuit.

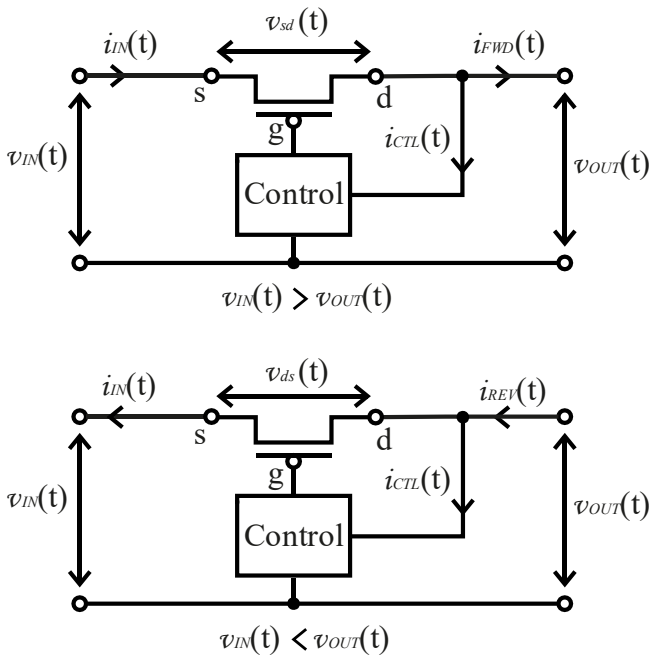

Figure 4.1-4 Illustrative circuit diagram for a PMOS rectifier with the control circuit current from the output. The upper diagram is when $v_{IN}(t)$> $v_{OUT}(t)$; the bottom diagram is when $v_{IN}(t)$< $v_{OUT}(t)$

When $v_{IN}(t)$> $v_{OUT}(t)$, the forward current $i_{sd}(t)$ flows from the source to the drain through the PMOS, there will be a voltage drop $v_{sd}(t)$ across the source and the drain of the PMOS. Like a resistor, in which $(V_R I_R)$ is the heat loss, $i_{sd}(t)v_{sd}(t)$ equals to the instantaneous heat loss of the PMOS. From the author's analysis, the heat loss can be calculated as

$$E_{heat} = \int_0^{t_0} v_{sd}(t)\, i_{sd}(t)dt = \int_0^{t_0} \big(v_{IN}(t) - v_{OUT}(t)\big)\, i_{sd}(t)dt \tag{4.12}$$

For the PMOS rectifier with $i_{CTL}(t)$ from the input in Figure 4.1-3,

$$i_{sd}(t) = i_{FWD}(t) = i_{IN}(t) - i_{CTL}(t) \tag{4.13}$$

$$E_{heat} = \int_0^{t_0} \big(v_{IN}(t) - v_{OUT}(t)\big)\, i_{FWD}(t)dt \tag{4.14}$$

For the PMOS rectifier with $i_{CTL}(t)$ from the output in Figure 4.1-4,

$$i_{sd}(t) = i_{IN}(t) = i_{FWD}(t) + i_{CTL}(t) \tag{4.15}$$

$$E_{heat} = \int_0^{t_0} \big(v_{IN}(t) - v_{OUT}(t)\big)\, i_{IN}(t)dt \tag{4.16}$$

Here, the power capability is introduced to define the ability of the rectifier to supply current to the load. The power capability of rectifiers can be measured by the total amount of forward output current from a rectifier within a certain time for a specific load. With the same load, a higher total amount of forward current means a stronger

power capability. The power capability of a rectifier can also be measured using the forward efficiency η_{FWD}. From author's analysis,

$$\eta_{FWD} = \frac{E_{FWD}}{E_{IN}} \tag{4.17}$$

$$E_{FWD} = \int_0^{t_0} v_{OUT}(t)\, i_{FWD}(t) dt \tag{4.18}$$

$$E_{FWD} = E_{IN} - E_{heat} - E_{CTL} - E_{other} \tag{4.19}$$

The term E_{FWD} describes the maximum amount of energy received by the output (i.e. energy in the forward direction to the output) without considering the reverse leakage loss. The term $\eta_{FWD} = \frac{E_{FWD}}{E_{IN}}$ describes the maximum efficiency the rectifier can achieve if the reverse loss is not considered, which can be used to describe how strong the power capability is for a rectifier in the forward direction. The higher η_{FWD} is, the stronger the power capability will be.

When $v_{IN}(t) < v_{OUT}(t)$, if the PMOS is not able to turn off completely, reverse currents will flow from the output to the input, as illustrated in the bottom figures in Figure 4.1-3 and Figure 4.1-4. Because this current is not used by the load, it is treated as an energy loss and is described as E_{REV}. From author's analysis,

$$E_{REV} = \int_0^{t_0} v_{OUT}(t)\, i_{REV}(t) dt \tag{4.20}$$

The actual output energy E_{OUT} that is consumed and stored by the load is the difference between E_{FWD} and E_{REV},

$$E_{OUT} = E_{FWD} - E_{REV} \tag{4.21}$$

The energy loss E_{CTL} is the total energy loss from the circuits that control the on-off switching of the PMOS and ensure the PMOS works properly. As a circuit used in a power supply, the energy used for controlling the rectifier comes from the rectifier itself. The amount of E_{CTL} is determined by the complexity of the control circuits. In general, the more complex the control of PMOS is, the higher E_{CTL} will be.

For a simple PMOS rectifier such as the self-synchronous rectifier, the heat loss and the leakage loss play a dominant role in the total loss. In order to reduce the heat loss and the leakage loss, complex circuits are added to control the on-off switching of the PMOS. However, this will increase the control energy loss of the rectifier. A balance between the control loss and the heat & leakage loss should be achieved to obtain a high overall efficiency.

To evaluate how efficient a rectifier works, the term efficiency η is introduced, which is the ratio of energy or a loss within the rectifier over the total input energy.

For a junction-diode rectifier, from (4.7), the efficiencies fulfil the following equation.

$$\eta_{OUT} + \eta_{diode} + \eta_{other} = 1 \tag{4.22}$$

where η_{OUT} is the output efficiency, which is the ratio of output energy over the input energy. η_{diode} is the ratio of energy loss through the diodes over the input energy. η_{other} is the ratio of other energy loss over the input energy. The sum of the three efficiencies is 1.

For an active rectifier with MOSFETs, from (4.11) and (4.21), the efficiencies fulfil the following equation.

$$\eta_{OUT} + \eta_{heat} + \eta_{REV} + \eta_{CTL} + \eta_{other} = 1 \tag{4.23}$$

$$\eta_{OUT} = \eta_{FWD} - \eta_{REV} \tag{4.24}$$

In the equation, η_{OUT} is the ratio of output energy over the total input energy; η_{heat} is the ratio of heat energy loss over total input energy; η_{FWD} is the ratio of forward energy to the load over total input energy; η_{REV} is the ratio of reverse leakage energy over the total input energy; η_{CTL} is the ratio of control energy over the total input energy; η_{other} is the ratio of other energy loss over the total input energy. The sum of these efficiencies is 1.

With the definition of parameters of the rectifier circuit, the performance of the rectifiers can be analysed, which will be based on the output efficiency, the output voltage values and the voltage conversion ratio (the output RMS voltage to the input peak voltage).

4.2 Conventional rectifier performance

- A conventional rectifier circuit will be introduced.
- The operation of the rectifier will be analysed.
- The efficiency and voltage conversion ratio of the rectifier will be discussed.

Conventional rectifiers use junction-diodes as rectification components. Because diodes only allow currents to flow in one direction, from its P-junction to its N-junction, it blocks any reverse current.

The simplest form of rectifier is as in Figure 4.2-1.

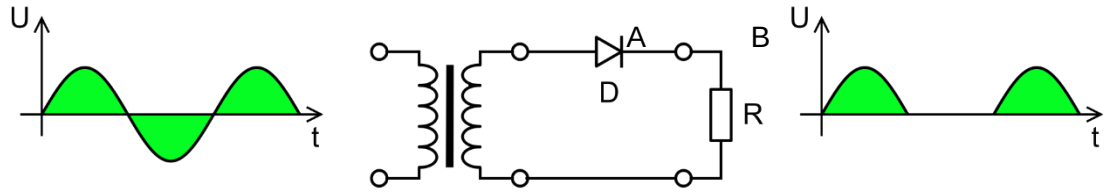

Figure 4.2-1 Half-wave rectifier with a 1:1 transformer as the input source [210]

In this circuit, current will flow only in the positive cycle of the AC source in the direction from A to B, therefore the output voltage will only be in one direction.

The resistor load output voltage of this rectifier is as follows [209],

$$V_{RMS} = \frac{V_{peak} - V_{th}}{2\sqrt{2}} \tag{4.25}$$

$$V_{DC} = \frac{V_{peak} - V_{th}}{\pi} \tag{4.26}$$

where:

- V_{RMS} is the root mean square value of output voltage
- V_{DC} is the average voltage of output voltage
- V_{peak} is the peak voltage of input voltage
- V_{th} is the threshold voltage of diode

Although this simple circuit achieves the rectification function, it has a high voltage drop between input and output in terms of RMS voltage and it has large ripples at the output which requires a large smoothing capacitor, both of which are unacceptable in low voltage on-chip applications.

To increase the output RMS voltage and reduce ripples, full-wave rectifiers can be used, as shown in Figure 4.2-2.

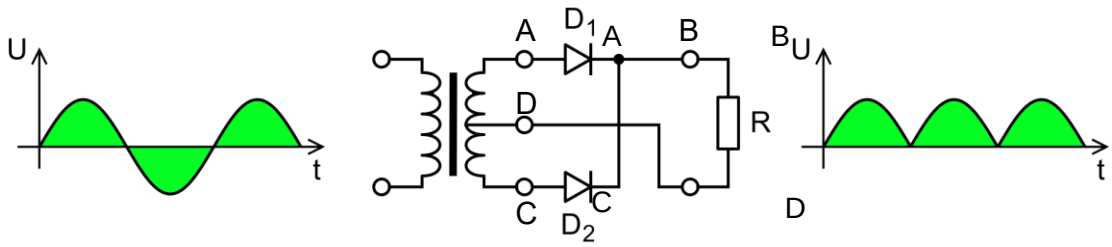

Figure 4.2-2 Full-wave rectifier with a centre-tapped 1:2 transformer [210]

In the source positive cycle, a current will flow in the path A-B-D. In the source negative cycle, a current will flow in the path C-B-D. Therefore, a current will flow to the output load in the whole cycle.

The resistor-load output voltages of this rectifier are as follows [209],

$$V_{RMS} = \frac{V_{peak} - V_{th}}{\sqrt{2}} \tag{4.27}$$

$$V_{DC} = \frac{2(V_{peak} - V_{th})}{\pi} \tag{4.28}$$

The output voltage of this circuit is much improved. The RMS output voltage of the full-wave rectifier is $\sqrt{2}$ times of the RMS output value of the single-phase rectifier. The average output voltage is twice the average output value of the single-phase rectifier. Because there is a current flowing in both the positive cycle and the negative cycle of the source, the ripple level at the output is much reduced, and the smoothing capacitor needed will be much smaller.

For low voltage on-chip applications, the threshold voltage of the diode will have a significant impact on the performance of a rectifier. In the application of wireless powered deep implants, the input terminal voltage of the receiver can be lower than 2V. In this case, the 0.7V threshold voltage of a junction-diode cannot be neglected. According to equations (4.27) and (4.28), at least 35% of input power is lost in the form of heat in the diodes.

Another drawback in the use of silicon junction-diode is the diodes current leakage. This is due to the parasitic capacitance in the diodes. At high operating frequencies, a current will flow through the parasitic capacitor to the substrate, which will cause a loss in power. The amount of loss depends on the size of the diode and the operational frequency. A diode with large size will have a larger parasitic capacitance, which will cause a higher loss. The higher the operational frequency is, the higher the loss will be.

On account of their lower threshold voltage, Schottky diodes can be a good replacement. However, a Schottky diode normally has a higher current leakage than

a normal silicon junction-diode due to a higher parasitic capacitance between the ends of the Schottky diode at a high frequency (as shown in Figure 4.2-3), which will cause larger reduction in the power conversion efficiency.

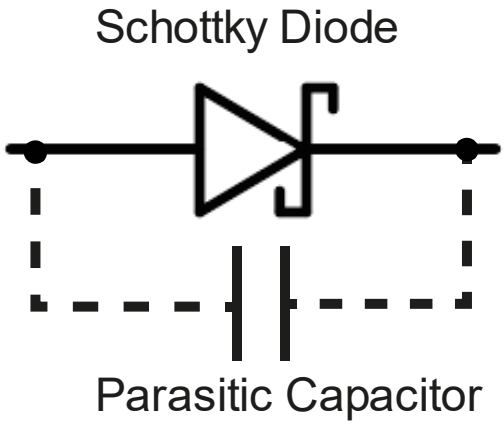

Figure 4.2-3 Schottky diode with parasitic capacitor

In order to avoid the leakage problems of the junction-diode rectifiers, diode-connected MOSFETs are used. The rectifier circuit is as shown in Figure 4.2-4. The gate of the PMOS is connected to its drain.

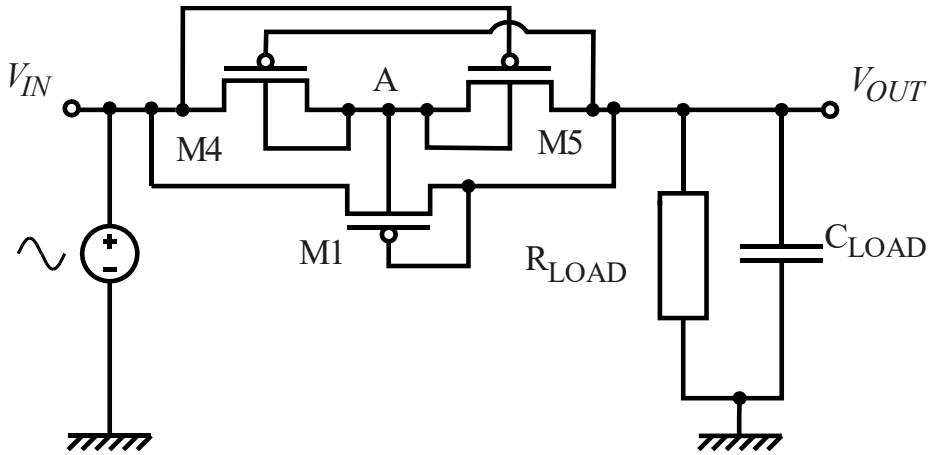

Figure 4.2-4 Rectifier circuit with the diode-connected PMOS M1 as the rectification component

In this circuit, the PMOS M1 is the main rectification component. The PMOSs M4 and M5 are added into the circuit to define the substrate voltage of the PMOS M1. The gate of M5 is connected to the input, and the gate of M4 is connected to the output. The source of M4 is connected to the input, and the source of M5 is connected to the output. The drains of M4 and M5 are connected to each other.

During operation, the voltage at point A will be equal to the difference between the higher voltage of either the input or the output and the voltage drop across the drain and source of a PMOS.

When V_{IN} is more than V_{OUT},

1. M4 will turn on, and M5 will turn off.
2. The voltage V_A at point A will then be equal to V_{IN}. Because M5 is turned off, almost no current will flow through M4. V_{ds} of M4 can then be neglected.

When V_{OUT} is higher than V_{IN},

1. M5 will turn on, and M4 will turn off.
2. V_A will be equal to V_{OUT}. Therefore, the voltage V_A at point A will be equal to the higher voltage of input and output.

The substrates of M1, M4 and M5 are then connected to point A because it is the highest voltage level in the circuit. In this way, the substrate voltage of PMOSs is defined.

The operation of the PMOS M1 is as followed.

According to the 1st order model of PMOS current equation in saturation region,

$$I_{ds} = \frac{\mu C_{ox}}{2} \times \frac{W}{L} \times \left(V_{sg} - |V_{th}|\right)^2 \tag{4.29}$$

$$V_{sg} - |V_{th}| = \sqrt{\frac{2I_{ds}}{\beta}} \tag{4.30}$$

where

- $\beta = \frac{\mu C_{ox}}{2} \times \frac{W}{L}$,
- C_{ox} is the gate capacitance per unit area
- V_{th} is the threshold voltage of the PMOS
- W is the width of the gate of the PMOS
- L is the length of the gate of the PMOS
- μ is the hole mobility in $m^2/(V \cdot s)$

Because $V_{sg} = V_{sd}$,

$$V_{sd} = |V_{th}| + \sqrt{\frac{2I_{ds}}{\beta}} \tag{4.31}$$

When I_{ds} is small,

$$V_{sd} \approx |V_{th}| \tag{4.32}$$

The PMOS M1 is thus acting like a diode. When $V_{IN} > V_{OUT} + V_{thM1}$, PMOS M1 will turn on, and current will flow from the source V_{IN} to the load through M1. When the

voltage $V_{IN} < V_{OUT} + V_{thM1}$, PMOS M1 will turn off, blocking the reversing current from the load.

The voltage waveform of the diode-connected PMOS rectifier is shown in Figure 4.2-5. The simulated performance of the diode-connected PMOS rectifier is shown in Figure 4.2-6 and Figure 4.2-7. In this simulation, the load resistance is 5 kΩ and the load capacitance is 100 pF. This resistance is chosen as the light load condition. When the rectifier RMS output voltage is in the range of 1 V to 5 V, which is also the range of receiver induced voltage of the WPT system, the corresponding rectifier load power is between 0.2 mW and 5 mW, which is around the 1 mW power requirement of the system. The load capacitance is for power storage and is chosen based on the consideration of allowed on-chip capacitance, as the on-chip capacitance should not take too much space of the chip.

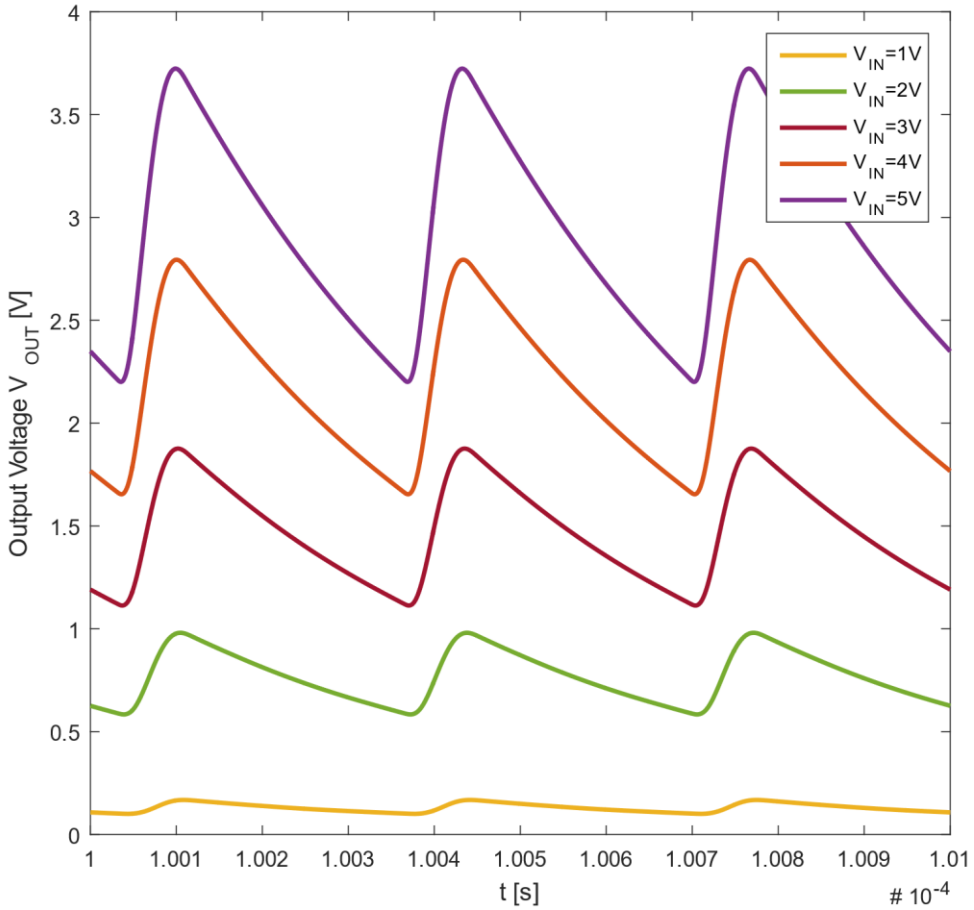

Figure 4.2-5 Waveform of output voltages of the diode-connected PMOS rectifier for peak input voltages from 1V to 5V at the light load condition

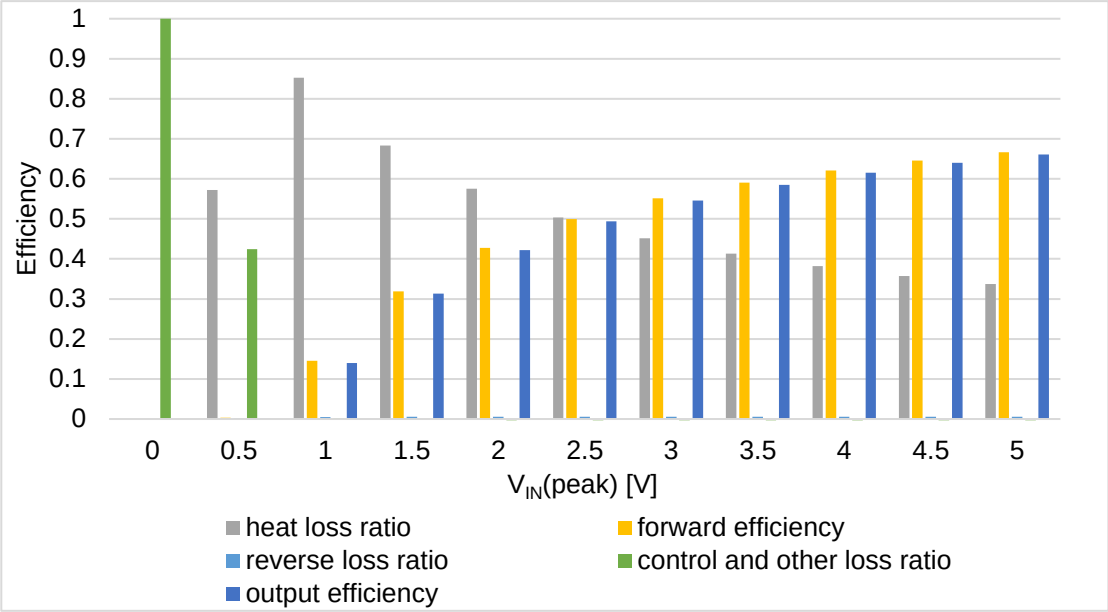

Figure 4.2-6 (From simulation) efficiency of diode-connected PMOS rectifier with 5 kΩ load resistance and 100 pF load capacitance; the simulated waveforms of the output current through the diode-connected PMOS can be seen at in AppendixA5. .

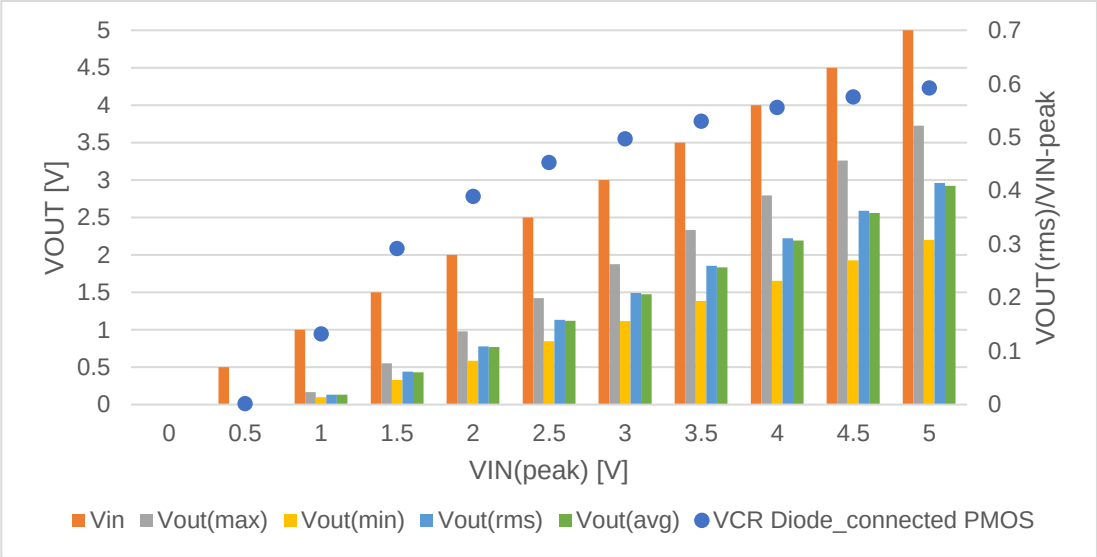

Figure 4.2-7 (From simulation) output voltages of diode-connected PMOS rectifier with 5 kΩ load resistance and 100 pF load capacitance

As shown in Figure 4.2-6, the output efficiency of the rectifier increases as the input voltage increases, from 14% at 1 V_{peak} input to 66% at 5 V_{peak} input. At 0.5 V_{peak} input, the input voltage is lower than the threshold voltage of the PMOS. The PMOS remains closed, and no current will be able to flow through the PMOS. The main energy loss of the rectifier during operation is the heat loss of the PMOS M1. The heat loss ratio decreases as the input voltage increases, from 85% at 1 V_{peak} input to 33% at 5 V_{peak} input. The high heat loss ratio is because of the high forward voltage drop across the PMOS, which can be seen in the output voltage values in Figure 4.2-7.

The forward voltage drop of the PMOS M1 can be obtained by calculating the difference between the peak input voltage $V_{IN}(peak)$ and the max output voltage $V_{OUT}(max)$.

From Table 4.2-1, it can be seen that the ratio of forward voltage drop over the input voltage is 83% at 1 V_{peak} input, which means as much as 83% of input voltage is wasted in the PMOS M1, leaving 17% of input voltage for the load at the output. The forward voltage drop increases as the input voltage increases, but the increment of forward voltage drop is less than the increment of input voltage, so the ratio of forward voltage drop to V_{IN} decreases.

$V_{IN}(peak)$/V	1	2	3	4	5
$V_{OUT}(max)$/V	0.17	0.98	1.88	2.79	3.72
V_{Drop}/V	0.83	1.02	1.12	1.21	1.28
$V_{Drop}/V_{IN}(peak)$	83%	51%	37%	30%	26%

Table 4.2-1 (From simulation) maximum output voltage $V_{OUT}(max)$, forward voltage drops across the PMOS M1 V_{Drop} and the ratio of forward voltage drops over peak input voltages V_{Drop}/V_{IN} at different input voltages

The advantage of the conventional diode-connected PMOS rectifier is that there is almost no reverse leakage loss and no control and other loss. This means the energy delivered to the load will not flow back to the input, and there is negligible capacitive leakage, unlike the junction-diode at high frequencies. However, because of the high heat loss of the diode-connected PMOS, this rectifier is not suitable for the application in the wireless power implants. To reduce the heat loss and increase the rectifier output efficiency, another structure of rectifier—the "*bootstrapping rectifier*"—is introduced.

4.3 Basic bootstrapping rectifier

Key aims of this section

- A basic bootstrapping rectifier (BSR) is introduced with the operation explained.
- The basic rectifier is developed into a practical rectifier.
- The performance of a practical rectifier is analysed in simulation with two load conditions, a 500 Ω load and a 5 kΩ load.
- Experiment analysis are done on the practical rectifier, and the experimental result is compared with the simulation result.

4.3.1 Basic circuit theory and schematic

In order to reduce the voltage-drop in a rectifier, a so-called bootstrapping structure is designed in [166]. Figure 4.3-1 shows a basic bootstrapping structure, where the capacitor will act as a bootstrapping capacitor. Because the capacitor is connected to diode D2 and the gate of PMOS M1, theoretically, current is only allowed to flow into the capacitor, and no current is allowed to flow out of the capacitor. The electric charge is thus "trapped" at the capacitor, which will keep the voltage of the capacitor $V_{CAP} = V_{OUT}(max) - V_{thD2}$, and the capacitor is called as a bootstrapping capacitor.

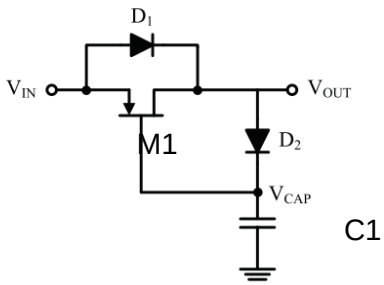

Figure 4.3-1 Basic half-wave bootstrapping Rectifier (basic BSR) [166]

The resistive-load operation of this bootstrapping structure can be described as follows.

At start, V_{CAP} and V_{OUT} are 0 V, and V_{IN} is more than V_{thM1}. The PMOS M1 will turn on, and current will flow from V_{IN} to V_{OUT} via D1 and M1. After start-up, current will flow mainly through M1 and not through D1. When $V_{OUT} \geq |V_{thD2}|$, D2 will conduct, current will flow through D2 and charge the bootstrapping capacitor. V_{CAP} will increase. When

$$V_{CAP} > V_{OUT} - |V_{thD2}| \tag{4.33}$$

the charge will stop. At the same time, V_{CAP} should meet the condition that

$$V_{IN} - V_{CAP} \geq |V_{thM1}| \tag{4.34}$$

to keep M1 on for current to flow. Therefore, from (4.33) and (4.34), the maximum V_{OUT} will be as follows

$$V_{OUT}(max) = V_{IN}(max) - (|V_{thM1}| - |V_{thD2}|) \tag{4.35}$$

When V_{IN} begins to drop, V_{CAP} will remain at $V_{IN}(max) - |V_{thM1}|$ because D2 blocks reversing currents. Therefore, M1 will begin to turn off and less current will flow through M1. Before V_{IN} drops to 0 V, M1 should have turned off completely and no current will flow through M1.

The above process can be summarised as follows.

During a positive input cycle, V_{IN} rises:

1. M1 and D1 turn on.
2. V_{OUT} rises.
3. D2 turns on.
4. V_{CAP} rises.
5. V_{CAP} reaches $V_{OUT} - |V_{thD2}|$.
6. D1 turns off, M1 remains open.
7. V_{OUT} reaches $V_{OUT}(max)$.
8. V_{CAP} reaches $V_{IN} - |V_{thM1}|$.
9. V_{IN} reaches maximum and then drops.
10. V_{CAP} remains $V_{IN}(max) - |V_{thM1}|$.
11. M1 turns off.
12. V_{OUT} follows V_{IN} to drop.

During a negative cycle, when V_{IN} drops below 0 V:

1. In resistive load condition, V_{CAP} will remain at $V_{OUT}(max) - |V_{thD2}|$.
2. The gate voltage will be higher than both the source and the drain voltages of the PMOS M1.
3. M1 will turn off, preventing any reverse current.

In this way, the current will only go from V_{IN} to V_{OUT}. The AC input will be rectified to be DC at the output. The waveform of the output voltage can be seen in the practical bootstrapping rectifier in Figure 4.3-3.

In short, the capacitor C1 will be charged at the start of the rectification process. The voltage of the capacitor will be used to control the PMOS M1 so that this PMOS will turn on at positive cycles and turn off at negative cycles.

The advantage of this circuit is that when the value of V_{thM1} and V_{thD2} is very close and $|V_{thM1}| > |V_{thD2}|$, the voltage drop between input and output can be very low, because the voltage drop is equal to $|V_{thM1}| - |V_{thD2}|$. In this way, the voltage drop will be far less than the one of the conventional rectifiers. This will efficiently reduce the power loss and voltage loss across the rectifier, thus improving the overall power efficiency of the system.

However, there are a few things to be considered in this circuit.

1. As a circuit for a power supply, how should the substrate voltage of the PMOS be defined?
2. If diodes are not available in integrated chip fabrication, what replacement components can be used?

These questions will be answered in the next section.

4.3.2 Practical Basic bootstrapping rectifier and its performance

4.3.2.1 The practical basic bootstrapping rectifier

A practical Half-Wave bootstrapping Rectifier is shown in Figure 4.3-2. In this circuit, PMOS M2 and M3 are used to replace the diodes D1 and D2. The gates of these two PMOSs are connected to their drain.

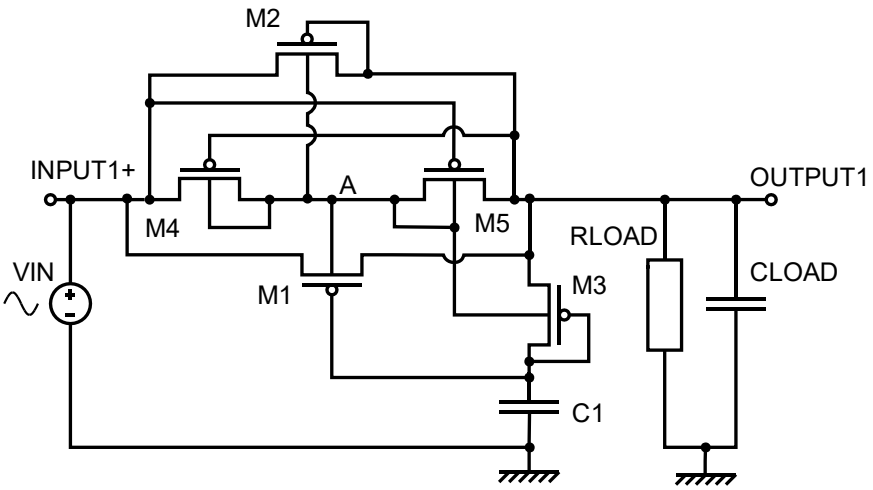

Figure 4.3-2 Practical Half-Wave bootstrapping rectifier

The PMOSs M4 and M5 are added into the circuit to define the substrate voltage of the PMOS M1 and M2, as discussed in Section 4.2.

M3 is a special one among the PMOSs because it is the only PMOS that is not connected to the input. Its highest voltage level is the output voltage. Therefore, the substrate of M3 can be connected to either the output or point A. These two options will cause different threshold voltages because of the PMOS body effect, which can be expressed by the following equation [211]

$$V_{th} = V_{th0} - \gamma(\sqrt{|\phi_B| + V_{BS}} - \sqrt{|\phi_B|}) \quad (4.36)$$

where

- V_{th0} is the threshold voltage when the source and bulk are connected together
- γ is a process parameter, 0.6 $V^{1/2}$
- ϕ_F is another process parameter, 0.3 V

4.3.2.2 Performance of the practical basic bootstrapping rectifier

The performance of the practical basic bootstrapping rectifier is analysed with an input voltage range between 0.5 V and 5 V, which is the expected output voltage range of the receiver coil of the wireless power transfer system. Two load conditions of the rectifier are analysed. A first one is the light load condition, with 5 kΩ load resistance and 100 pF load capacitance. The other one is the heavy load condition, with 500 Ω load resistance and 100 pF load capacitance. In the light load condition, the load current is comparatively small, and the minimum output voltage will be more than 0 V during the operation. In the heavy load condition, the load current is large, and the minimum output voltage will be 0 V.

The performance of the rectifier is analysed based on efficiencies and output voltages. The efficiencies have been introduced in Section 4.1, which includes heat loss ratio, forward efficiency, reverse loss ratio, control & other loss ratio and output efficiency. The output voltages are the maximum output voltage, minimum output voltage, RMS output voltage and average output voltage. The performance of the rectifier is analysed in the steady-state. The efficiencies, the RMS output voltage and the average output voltage are calculated for the whole duration of the steady-state; while the maximum output voltage and the minimum output voltage are measured within a cycle.

The waveform of the output voltage can be seen in Figure 4.3-3. The simulated performance of the practical basic rectifier in the light load condition (with a 5 kΩ load resistor) can be seen in Figure 4.3-4 and Figure 4.3-5.

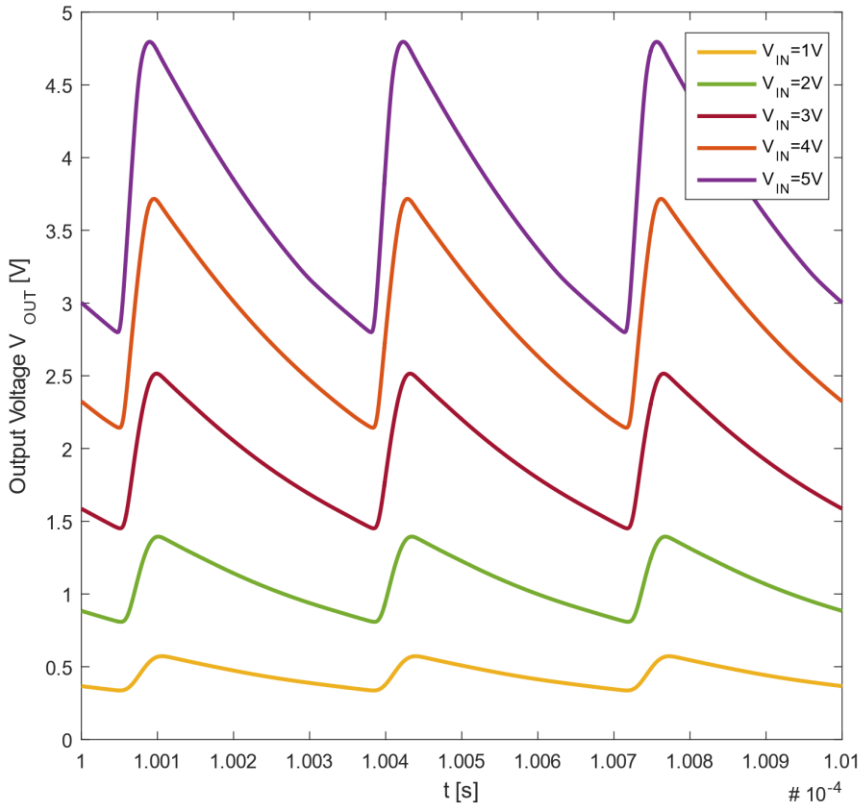

Figure 4.3-3 Waveform of output voltages of basic BSR for peak input voltages from 1 V to 5 V at the light load condition

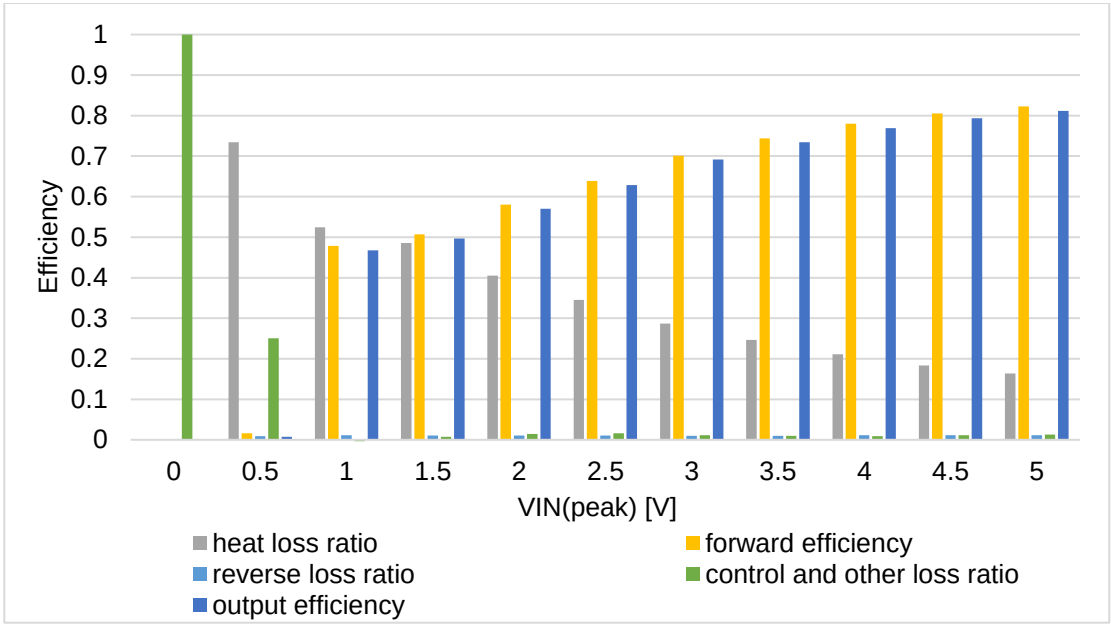

Figure 4.3-4 (From simulation) efficiencies of practical basic bootstrapping rectifier with 5 kΩ load resistance and 100 pF load capacitance. The simulated waveforms of output current through the switch-PMOS can be seen in AppendixA5. .

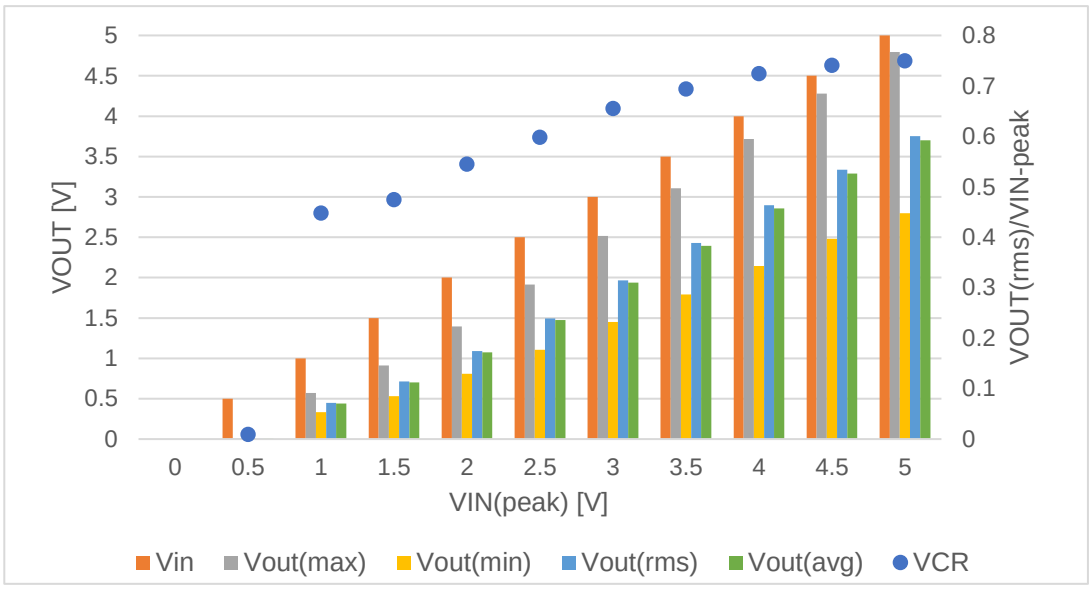

Figure 4.3-5 (From simulation) voltages of practical basic bootstrapping rectifier with 5 kΩ load resistance and 100 pF load capacitance

The output efficiency increases as the input voltage increases, from 46.7% with $V_{IN}(peak)$=1 V to 81.1% with $V_{IN}(peak)$=5 V.

When $V_{IN}(peak)$=0.5 V, the output efficiency is close to 0. This is because the V_{sg} of M1 and M2 are less than V_{thM1} and V_{thM2} respectively at this input voltage, and thus, M1 and M2 are not opened. The input energy is blocked by M1 and M2.

When V_{IN} is between 1 V_{peak} and 2.5 V_{peak}, the efficiency of the rectifier is below 65%. This is mainly because of the comparatively high heat loss ratio for these input voltages. More than 50% of input energy is consumed as heat when $V_{IN}(peak)$=1 V and the heat loss ratio is about 35% when $V_{IN}(peak)$=2.5 V. This is because of the high V_{gM1} at these input voltages, which results in a low V_{sgM1}, and thus, the PMOS M1 is not fully open. When V_{IN} is between 3 V_{peak} and 5 V_{peak}, the output efficiency is over 70% due to the low heat loss ratio. As the input voltage increases, the V_{sg} of M1 increases, and more current is able to go through M1 with the same V_{sdM1}. Therefore, the heat loss ratio in M1 decreases, which results in the increase of forward efficiency and the output efficiency.

In terms of the output voltage values, the maximum output voltage $V_{OUT}(\max)$ for each V_{IN} is higher than the $V_{OUT}(max)$ with the same V_{IN} in the junction-diode rectifier. The voltage difference between $V_{IN}(peak)$ and $V_{OUT}(max)$ is about 0.6 V when V_{IN} is between 1 V_{peak} and 2.5 V_{peak}. The difference decreases when V_{IN} is between 3 V_{peak} and 5 V_{peak}, from 0.5 V at 3 V_{peak} to 0.2 V at 5 V_{peak}. For the minimum output voltage, because the reverse loss ratio is almost 0 for all the input voltages, it can be deduced that the voltage drop is due to the discharging of the load capacitor to the load resistor.

For the heavy load condition (with a 500 Ω load resistor), the output voltage waveform is shown in Figure 4.3-6, and the simulated performance of the rectifier can be seen in Figure 4.3-7 and Figure 4.3-8.

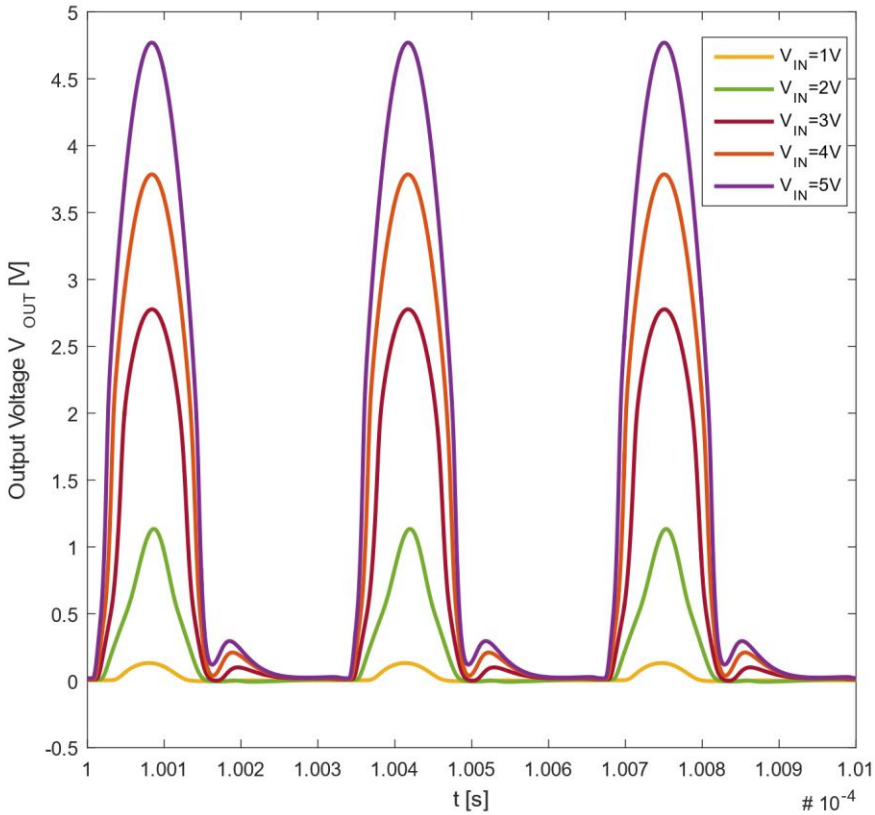

Figure 4.3-6 Waveform of output voltages of basic BSR for peak input voltages from 1 V to 5 V at the heavy load condition

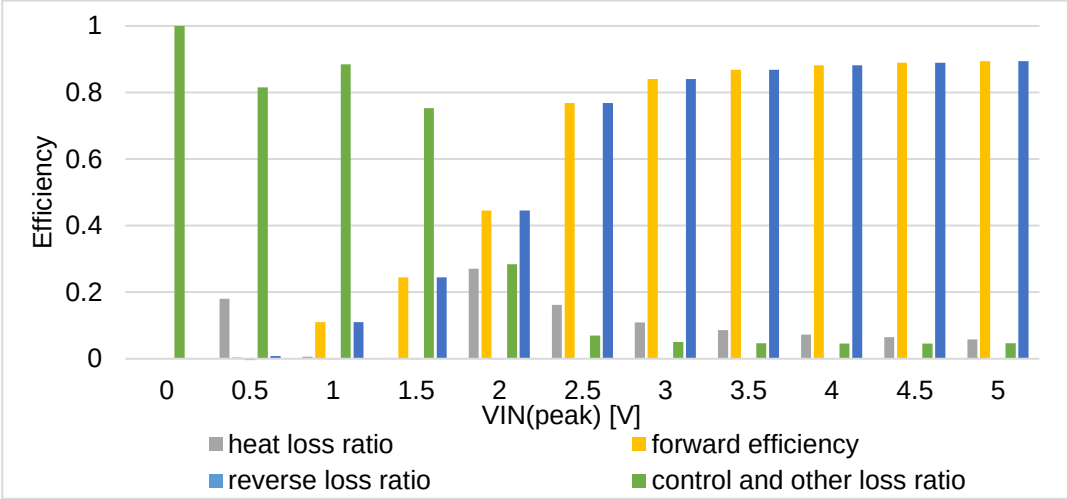

Figure 4.3-7 (From simulation) efficiencies of practical basic bootstrapping rectifier with 500 Ω load resistance and 100 pF load capacitance. The simulated waveforms of the output current through the switch PMOS can be seen in AppendixA5. .

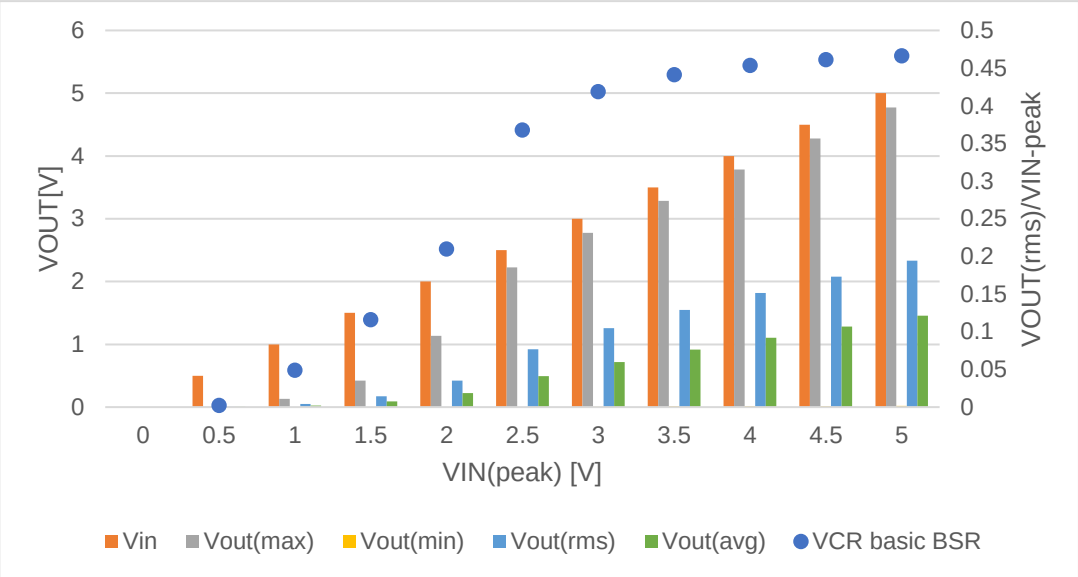

Figure 4.3-8 (From simulation) voltages of practical basic bootstrapping rectifier with 500 Ω load resistance and 100 pF load capacitance

In terms of the efficiencies, the practical basic rectifier has vastly different performance for the input voltage below 2.5 V_{peak} and for the input voltage above 2.5 V_{peak}. When the input voltage is between 0.5 V_{peak} and 2 V_{peak}, the output efficiency is lower than 45%. For input voltages of 1 V_{peak} and 1.5 V_{peak}, the low output efficiency is due to the high control and other loss ratio, which is caused by the low V_{sg} of M1 when V_{IN} is positive. For input voltage of 2 V_{peak}, both the control and other loss ratio and the heat loss ratio are more than 27%. The high heat loss ratio is because of the low V_{sg} of M1, and the high control and other loss ratio is due to the conduction of M2. For input voltages more than 2.5 V_{peak}, the output efficiency is more than 75%. This is because as the input voltage increases, the V_{sg} of M1 increases due to the higher voltage drop across the drain and source of the diode-connected PMOS M3. Therefore, the PMOS M1 is turned more on and thus can conduct more currents with the same V_{sdM1}. In the input voltage range between 2.5 V_{peak} and 5 V_{peak}, the control and other loss ratio is between 4% and 7%. This energy loss is mainly due to the charging of capacitor C1 (3% to 6%) and the bulk voltage setting circuit (1%).

In terms of the output voltages, the values have the same pattern as the efficiencies. For input voltages of 2 V_{peak} and lower, the values of $V_{OUT}(max)$ are much lower than the corresponding $V_{IN}(peak)$. For V_{IN} of 2 V_{peak}, the value of $V_{OUT}(max)$ is 56% of the $V_{IN}(peak)$. For V_{IN} = 1 V_{peak} and 1.5 V_{peak}, the percentage is even lower, which is 13% and 28%. Because the value of $V_{OUT}(min)$ is 0 V due to the high current to the load resistor, the $V_{OUT}(rms)$ and the $V_{OUT}(avg)$ for V_{IN} below 2 V_{peak} are very small (0.42 V_{rms} output for 2 V_{peak} input). For V_{IN} over 2.5 V_{peak}, the values of $V_{OUT}(max)$ is much closer to the corresponding V_{IN}. For V_{IN} of 2.5 V_{peak}, $V_{OUT}(max)$ is 2.2 V, which is 88% of $V_{IN}(peak)$. For V_{IN} of 3 V_{peak} and over, the percentage are all more than 90%.

However, due to the low values of $V_{OUT}(min)$, the $V_{OUT}(rms)$ and the $V_{OUT}(avg)$ are all much lower than the corresponding values at the light load condition (with a 5 kΩ load resistor) with the same input voltage. The larger difference between the values of $V_{OUT}(rms)$ and the $V_{OUT}(avg)$ at the same input voltage is because of the larger voltage ripple due to the lower load resistance.

Compared with the simulated performance of the diode-connected PMOS rectifier, the practical basic bootstrapping rectifier has better performances in all aspects, which is shown in Figure 4.3-9.

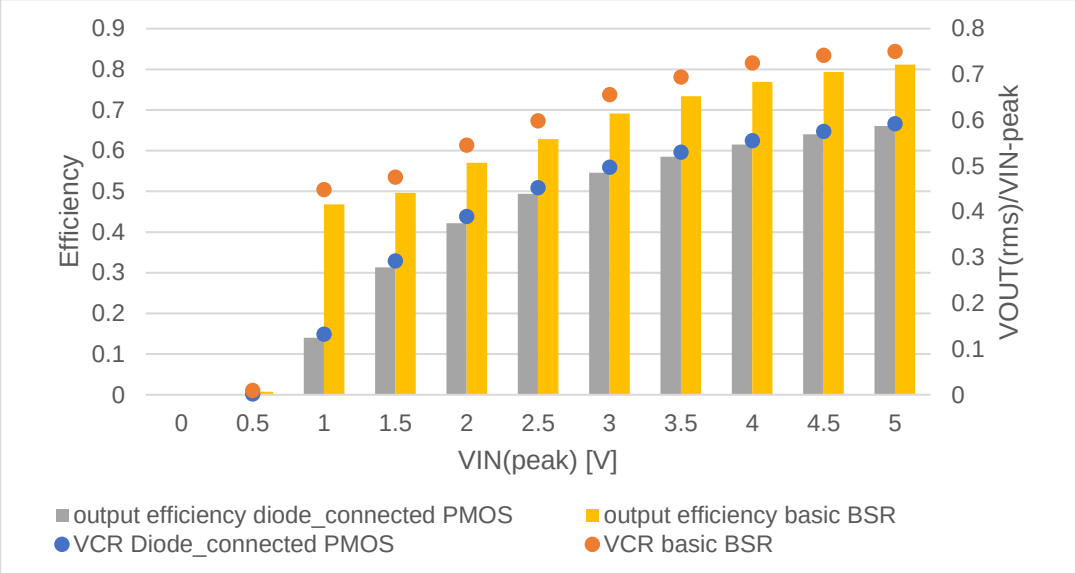

Figure 4.3-9 (From simulation) comparison of voltage conversion ratio (VCR) and output efficiency between practical basic bootstrapping rectifier and diode-connected PMOS rectifier

In terms of the output efficiency, the practical bootstrapping rectifier is 13% to 42% more efficient than the efficiency of the diode-connected PMOS rectifier across the input voltage range. The difference in the efficiency is larger at 1 V_{peak} and 1.5 V_{peak} inputs, in which the diode-connected PMOS has high heat loss ratios; the difference becomes smaller for higher inputs and stays at around 15%.

In terms of output voltages, both the maximum output voltage and RMS output voltage are higher for the practical basic bootstrapping rectifier across the input voltage range. At 1 V_{peak}, the output voltages of the practical basic bootstrapping rectifier are three times more than the output voltages of the diode-connected PMOS rectifier. The difference of the output voltages decreases as input voltage increases, but the output voltages of the practical basic bootstrapping rectifier are 27% to 40% higher than the output voltages of the diode-connected PMOS rectifier at the input voltage range of 1.5 V_{peak} to 5 V_{peak}. Overall, the practical basic bootstrapping rectifier is a big improvement on the diode-connected PMOS rectifier.

The actual performance of the practical basic bootstrapping rectifier will be analysed through experiments on actual integrated chips and compared with the simulation performance, which is shown in the next part.

4.3.2.3 Experiment with the practical basic bootstrapping rectifier

The practical basic bootstrapping rectifier as a full-wave rectifier was fabricated using a TSMC 0.18 CMOS 6-Metal/2-Poly high voltage mixed-signal based 2nd generation BCD process. This chip is mounted in a PLCC 84 package. The PMOSs used are all Pa12_g5a_nbl_mr_mac. This is a high voltage PMOS with a maximum allowed V_{ds} = 12 V, which is sufficient for the wireless power implants. The maximum allowed V_{gs} is 5 V. It is a multi-finger PMOS with a minimum finger of two. The substrate connection of this PMOS is floating and thus can satisfy the requirement of the circuit for substrate voltage definition. The V-I characteristic of the switch PMOS can be seen in AppendixA5. . The same basic size of 10 um width and 400 nm length is used for all PMOSs for easier implementation. The PMOSs M1 and M3 have a multiplier of 8 and the number of fingers of 8 because a much larger current is expected to flow through these PMOSs. All the PMOSs are surrounded by guard rings to isolate them from adjacent cells. The chip was laid out to have a symmetrical structure to minimise the potentially imbalanced parasitic capacitances between the source rails (V_{IN+} and V_{IN-}).

The measurement setup is shown in Figure 4.3-10.

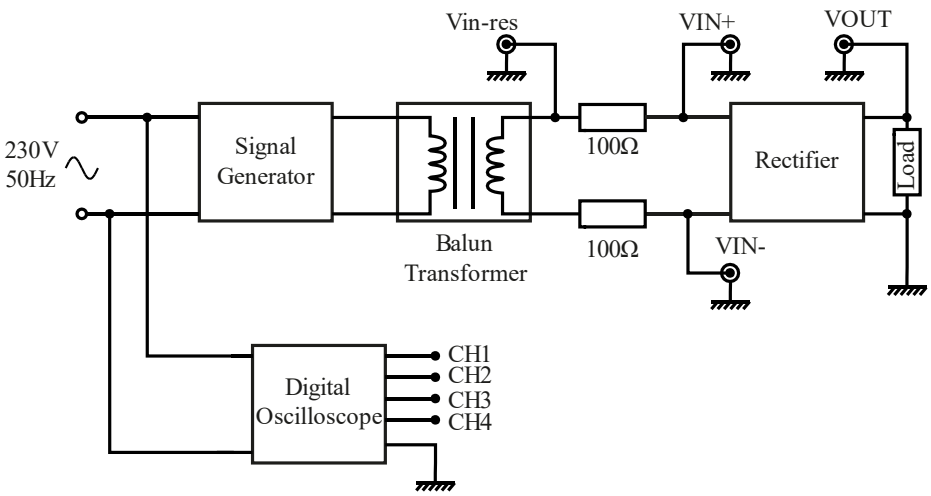

Figure 4.3-10 Measurement setup of the basic BSR

Device	Series	Functions
Signal generator	FeelTech FY3200S	Generate input sinusoidal signals at a specific frequency
Balun Transformer	MURATA DXW21BN2511NL	13.56 MHz 1:1 surface mount wire wound transformer with insertion loss of 1 dB

Table 4.3-1 Device used in the measurement

In the measurement setup, a wideband balun transformer is connected at the output of the signal generator to provide a floating input for the full-wave rectifier. Two 100 Ω resistors are connected between the two output ports of the transformer and the two input ports of the rectifier, respectively, for input current measurement. The probes to measure VIN_{-res} and VIN+ are set to the differential mode for balanced measurement. The input current is thus calculated as $I_{IN} = \frac{V_{IN-RMS} - V_{IN+}}{100\Omega}(A)$.

The input power to the rectifier is $\int_0^T v_{in}(t) i_{in}(t) dt$ at the steady working state. The output power was calculated as the integral of the squared measured output voltage divided by the load resistance over the same period as the input measurement. The voltage conversion ratio VCR was calculated as the ratio of the RMS output voltage to the peak amplitude of input voltage. The amplitude of input voltage at the rectifier ranges from 1.5 V to 5 V. The input frequency is 8 MHz. The load of the rectifier is a 5 kΩ resistor and a 34 pF load capacitor with the output pad parasitic capacitance, package and PCB parasitic capacitance and test probe capacitance in addition.

The measured output efficiency and the measured voltage conversion ratio (VCR) of the full-wave basic BSR are shown in Figure 4.3-11 and Figure 4.3-12, together with the simulated output efficiency and simulated VCR. The measurement data can be seen in AppendixA6. . As shown, the output efficiency of the measurement result is similar, but not identical, to the simulated output efficiency. The output efficiency increases as the input voltage increases and reaches about 80% when V_{IN} reaches 5 V_{peak}. For V_{IN} over 2.5 V_{peak}, the measurement output efficiency is close to the simulated ones, with a maximum difference of 4%. The difference grows bigger as the input voltage decreases. At 2 V_{peak}, the output efficiency difference is about 8% and at 1.5 V_{peak}, the difference reaches about 14%. A similar difference is shown between the simulated VCR and the measured VCR. The measured VCR of the basic BSR increases as the input voltage increases, from 27% at 1.5V_{peak} input to 63% at 5 V_{peak} input. The simulated VCR is about 14% higher than the measured VCR at 1.5 V_{peak}, while at 5 V_{peak}, the two results are only less than 2% different.

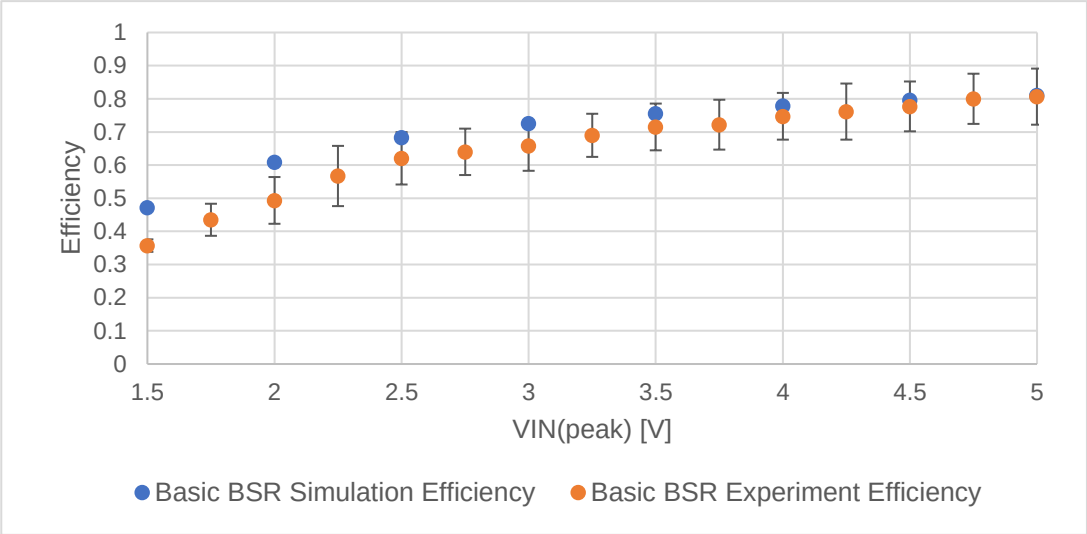

Figure 4.3-11 Comparison of output efficiency between the basic BSR simulation result and the basic BSR experimental result with 5 kΩ R_{load} and 34 pF C_{load}

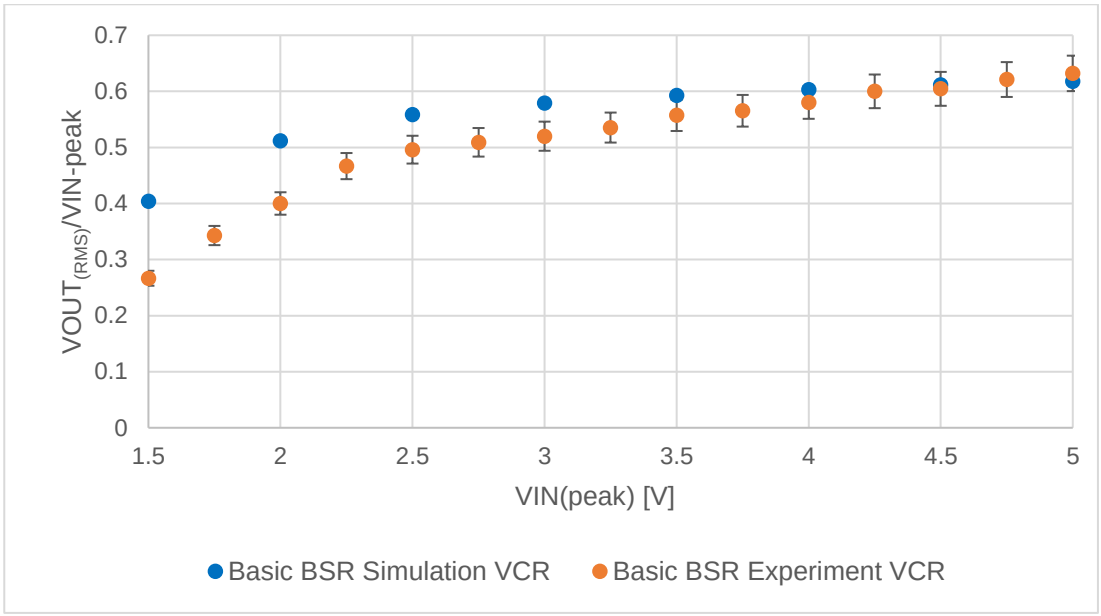

Figure 4.3-12 Comparison of $VOUT_{(RMS)}$ and VCR ($VOUT_{(RMS)}$/VIN-peak) between basic BSR simulation result and basic BSR experimental result with 5 kΩ R_{load} and 34 pF C_{load}

The difference can be firstly because of the parasitic capacitance at the bootstrapping capacitor and at the output of the rectifier, whose effect on the circuit cannot be fully known in the simulator. A second reason can be the variation of the threshold voltages of the main switches PMOS M1 and the diode-connected PMOS M3 on the chip, which results in a higher threshold M1 and lower threshold M3, causing a high V_{gM1}.

A third reason can be that the bootstrapping capacitor becomes over-charged for low input voltages. Because there is no discharging path for the bootstrapping capacitor, the voltage at the bootstrapping capacitor has no way to decrease except for parasitic leakage. Once the capacitor has a high voltage, it will keep the voltage for a certain period before the parasitic leakage of the capacitor drains it out. During the period, whose length depends on the quality of the capacitor, the gate voltage of the PMOS

M1 remains at a high voltage level even if a low voltage is input into the circuit. Therefore, the PMOS M1 will not be able to fully turn on at low input voltages, causing a lower measured output efficiency. In the simulation, the voltage at the bootstrapping capacitor resets to 0 V for each measurement, so this problem will not occur. Further simulations showed that, if an initial voltage of more than 2 V is pre-set at the bootstrapping capacitor or the output capacitor, the RMS output voltage will decrease by 0.1 V to 0.2 V depending on the value of input voltage. The simulated output efficiency of the basic BSR with pre-set bootstrapping capacitor voltage is shown in Figure 4.3-13. A comparison of measured $V_{OUT}(rms)$, measured VCR and simulated $V_{OUT}(rms)$, simulated VCR is shown in Figure 4.3-14.

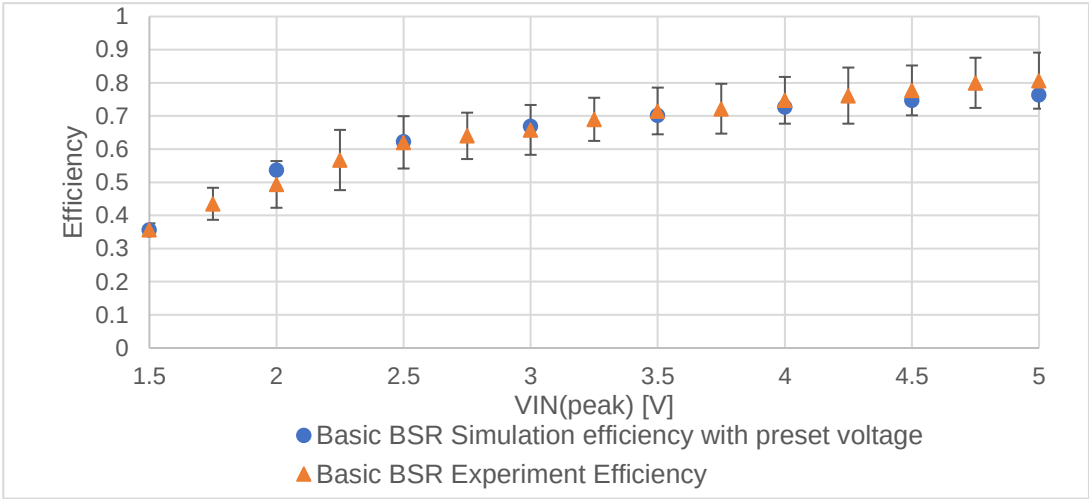

Figure 4.3-13 Comparison of output efficiency between basic BSR simulation result with 2 V pre-set bootstrapping capacitor voltage and basic BSR experimental result with 5 kΩ R_{load} and 34 pF C_{load}

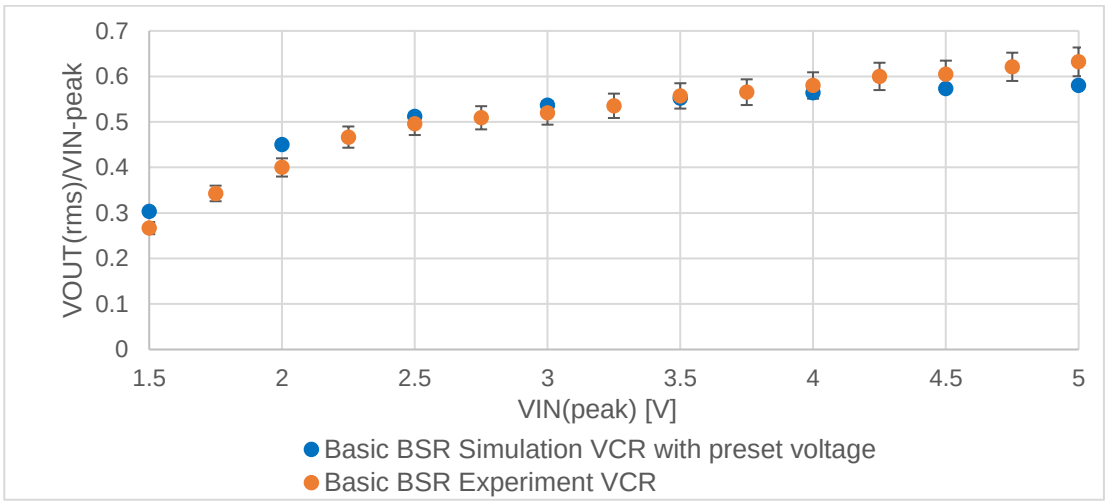

Figure 4.3-14 Comparison of VOUT(rms) and VCR (VOUT(rms)/VIN-peak) between basic BSR simulation result with a pre-set bootstrapping capacitor voltage of 2 V, basic BSR experimental result and diode-connected PMOS Rectifier simulation result with 5 kΩ R_{load} and 34 pF C_{load}

With the pre-set capacitor voltage, both the simulated output efficiency and the simulated VCR have closer results to the measured ones. The maximum difference

of the output efficiency is less than 5% between simulation and measurement results. The most outstanding differences are when V_{IN}=2 V_{peak} and 5 V_{peak}, which have both 4.3% difference of efficiency. The simulated RMS output voltages with a pre-set bootstrapping capacitor voltage agree to the measurement results with less than 5% of VCR difference. The VCR simulation results are closer to the experiment results when V_{IN} is between 2.5 V_{peak} and 4 V_{peak}, with an average difference of 1.3%. For V_{IN} more than 4 V_{peak}, the effect of pre-set voltage is stronger in simulation than in experiment, causing the simulation results to be less than the experiment results. This means the pre-set voltage at the bootstrapping capacitor should be lower for V_{IN} more than 4 V_{peak}. For V_{IN} less than 2.5 V_{peak}, the pre-set voltage can be even higher in the simulation to match the experiment results. For a 2 V pre-set voltage, the VCR difference at this input range is within 5%. Overall, it can be concluded that the over-charged bootstrapping capacitor can cause the difference in efficiency and VCR between the simulated results and the measured results.

4.3.2.4 Summary of the practical basic bootstrapping rectifier

As a summary, a practical basic bootstrapping rectifier is introduced to be used in the application of wireless power system for micro-implants. From the analysis and experimental results, it was found that the rectifier has a better performance than the diode-connected PMOS rectifier but has a low output efficiency and VCR at low input voltages because of the over-charged bootstrapping capacitor. To solve this problem, some alternative bootstrapping rectifiers will be introduced in the next section.

4.4 Augmented Bootstrapping Rectifiers

Key aims of this section

- Two developed rectifiers based on the basic bootstrapping rectifier are introduced to improve the performance in efficiency and VCR.
- The first developed rectifier to be introduced is the static gate-control bootstrapping rectifier. Its operation and performance will be discussed.
- The second one is the dynamic gate-control bootstrapping rectifier, which use an opto-coupler to control the on-off switching of the main rectification-switch MOSFET M1. Its operation and performance will be discussed and compared with the previous rectifiers.

4.4.1 Static gate-control bootstrapping rectifier

4.4.1.1 Structure of the static gate-control bootstrapping rectifier

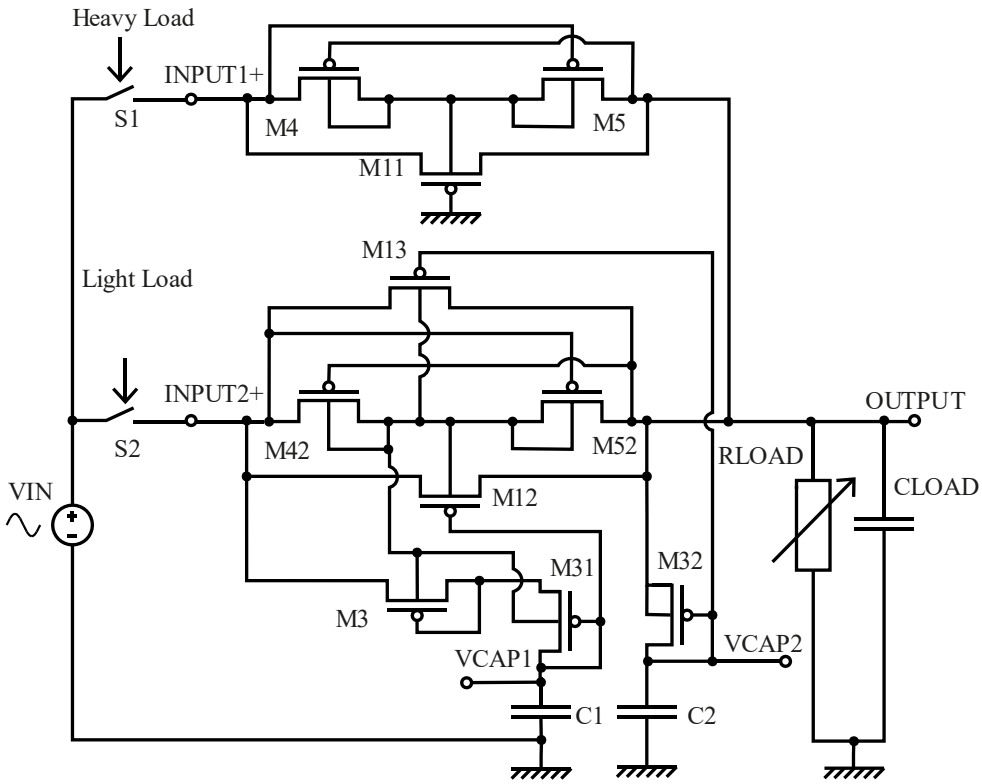

Figure 4.4-1 Circuit diagram of static gate-control bootstrapping rectifier

As shown in Figure 4.4-1, the static gate-control bootstrapping rectifier (static BSR) is combined with two extra circuits. The first one is the heavy load circuit for the heavy load condition (with a small load resistance), which includes the switch S1 and the PMOS M4 M5 and M11. The other one is the light load circuit for the light load condition (with a large load resistance), which includes the switch S2, the capacitor C1 and C2 and the PMOS M12, M13, M3, M31, M32, M42 and M52.

At the heavy load condition, the switch S1 turns on, and the switch S2 turns off. The input voltage will be rectified by the PMOS M11. At the light load condition, the switch

S1 turns off, and the switch S2 turns on. The input voltage will be rectified by the PMOS M12 and M13.

For the heavy load circuit, the PMOS M11 is the rectification component (switch PMOS). The gate of the PMOS M11 is always connected to ground. In this way, the PMOS M11 will conduct as long as the input voltage is higher than V_{thM1} in the heavy load condition. Because the output voltage drops to 0 V quickly after V_{IN} goes negative, the reversing leakage loss will be very limited. The PMOS M4 and M5 form the bulk voltage setting circuit of M11, which sets the bulk of M11 V_{bM1} to be the higher voltage between V_{IN} and V_{OUT}.

For the light load circuit, the PMOS M12 and M13 are the rectification components (switch PMOS). Among other components, M3, M31 and C1 make up a circuit to set the gate voltage V_g of M12; and M32 and C2 make up another circuit to set the gate voltage V_g of M13. M42 and M52 are the bulk voltage setting circuit to set the bulk voltage of M12 M13 M3 and M31.

The rectification circuit formed by M12 M3 M31 and C1 is mainly for low voltage operation, which is between 0.5 V_{peak} and 2.5 V_{peak}. In this circuit, M3 and M31 are two diode-connected PMOSs. Their main purpose is to set the voltage of V_{CAP1} at the capacitor C1. Because the source of M3 is connected to the input, the voltage of V_{CAP1} will be determined by the following equation.

$$V_{CAP1} = V_{IN}(peak) - V_{thM3} - V_{thM31} \tag{4.37}$$

Because the gate of M12 is connected to V_{CAP1}, the voltage between the source and the gate of M12 will thus be as the following equation.

$$V_{gM12} = V_{IN} - V_{CAP1} = V_{thM3} + V_{thM31} \tag{4.38}$$

Because the voltage of V_{CAP1} is entirely determined by the voltage V_{IN}, the voltage of V_{CAP1} will not be affected by the voltage V_{OUT} and will experience less ripple. By adjusting the threshold voltage of M3 and M31, the voltage V_{sgM1} can be set to achieve a high efficiency at low input voltages.

The rectification circuit formed by M13 M32 and C2 is mainly for high voltage operation, which is between 2.5 V_{peak} and 5 V_{peak}. M32 is a diode-connected PMOS. The structure of this circuit is the same as the practical basic bootstrapping rectifier. The source of M32 is connected to the output and the voltage V_{CAP2} at the capacitor is determined by the voltage V_{OUT}. The gate of M13 is connected to V_{CAP2}.

$$V_{gM13} = V_{CAP2} = V_{OUT} - V_{thM32} \tag{4.39}$$

From the analysis in Section 4.3.2.2, the practical basic bootstrapping rectifier has an efficiency of over 62% at an input voltage between 2.5 V_{peak} and 5 V_{peak}. When the voltage is below 2.5 V_{peak}, the efficiency is below 60%. Moreover, the efficiency decreases with the decrease in the input voltage. In the static gate-control bootstrapping rectifier, the PMOS M13 will be working as the practical basic bootstrapping rectifier and have a high rectification efficiency at input voltages between 2.5 V_{peak} and 5 V_{peak}. At input voltages below 2.5 V_{peak}, M12 will operate with a comparatively high rectification efficiency. In this way, the rectifier will be able to work in high efficiencies at the full input voltage range.

4.4.1.2 Performance of the static gate-control bootstrapping rectifier

The simulated performance of the static gate-control bootstrapping rectifier in the light load condition (with a 5 kΩ load resistor) is presented in Figure 4.4-3 and Figure 4.4-4. As introduced in Section 4.4.1.1, the switch S1 will turn off, and S2 will turn on in the light load condition. The PMOS M12 and M13 will be the main rectification components. The efficiency of the static gate-control bootstrapping rectifier will be mainly determined by the gate voltage of M12 and M13.

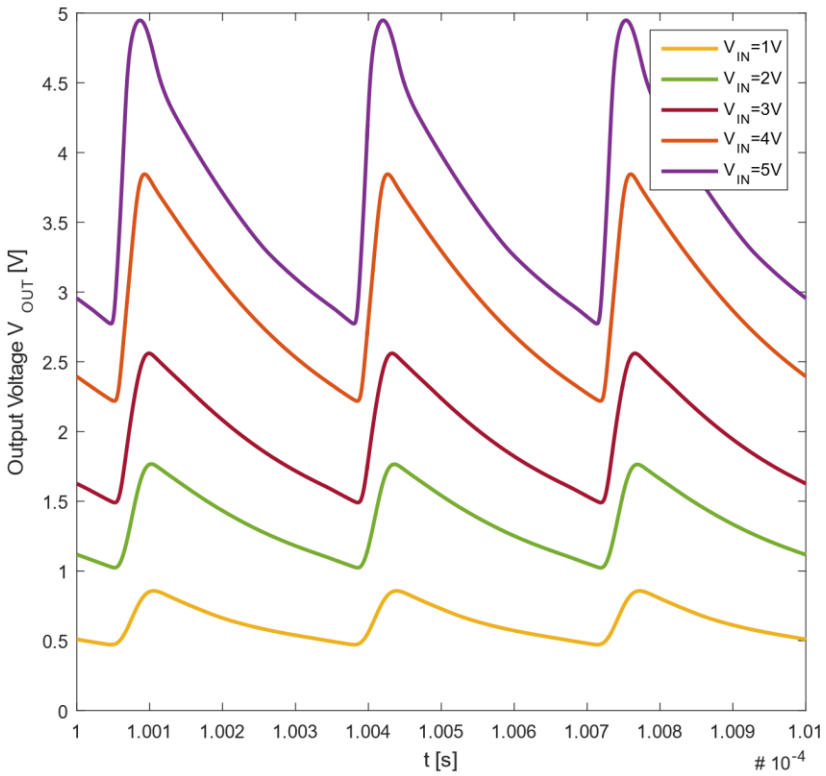

Figure 4.4-2 Waveform of output voltages of static BSR for peak input voltages from 1 V to 5 V at the light load condition

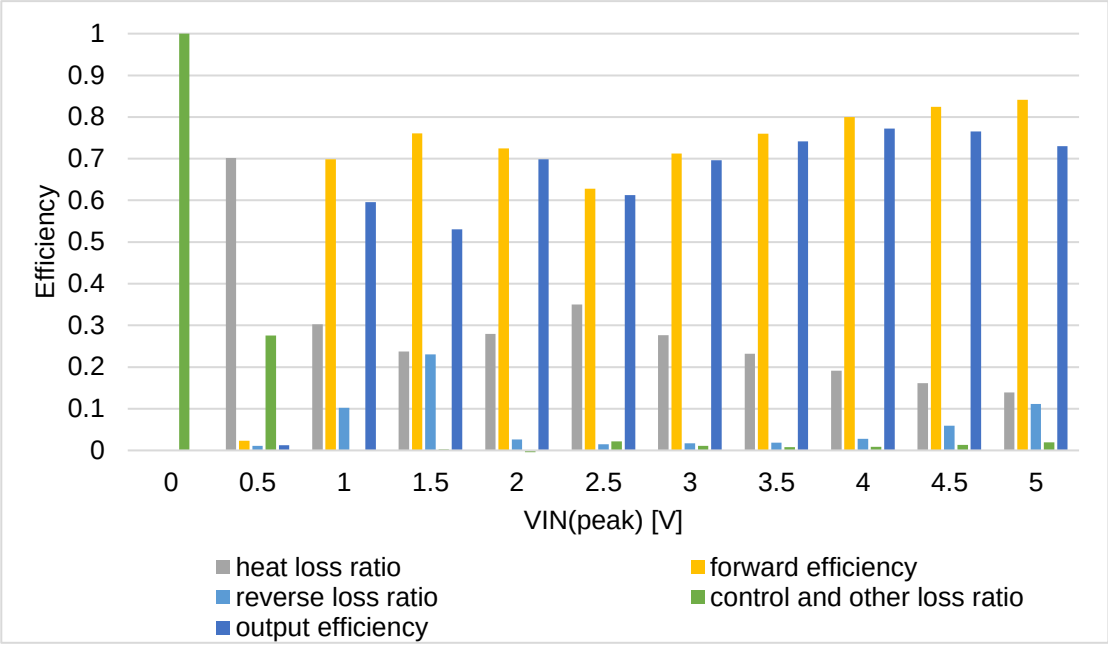

Figure 4.4-3 (From simulation) efficiencies of static gate-control bootstrapping rectifier with 5 kΩ load resistance and 100 pF load capacitance. The simulated waveforms of the output current through the switch PMOS can be seen in AppendixA5. .

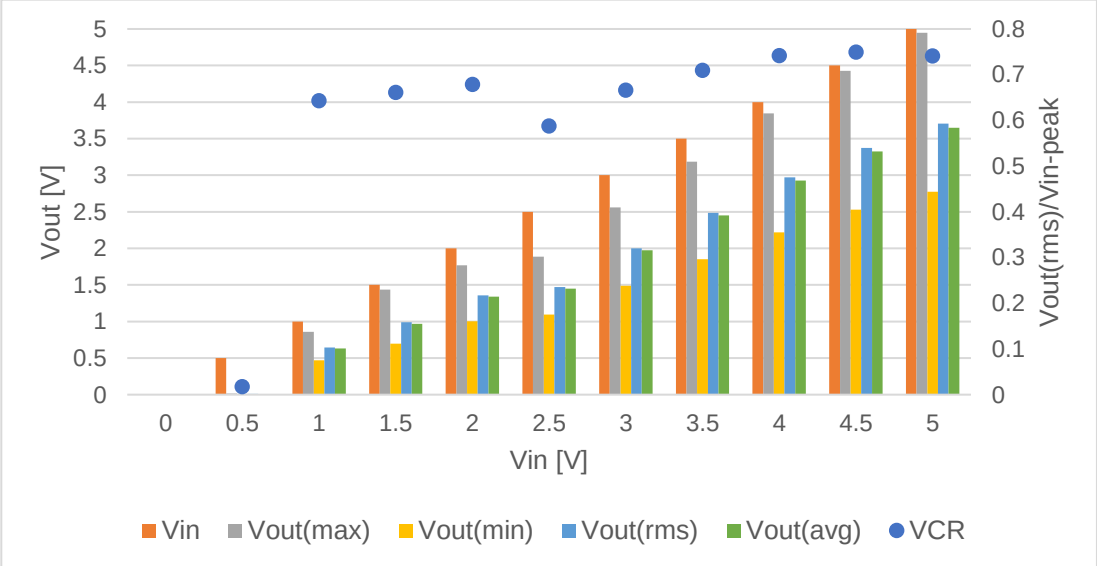

Figure 4.4-4 (From simulation) output voltages and VCR of static gate-control bootstrapping rectifier with 5 kΩ load resistance and 100 pF load capacitance

As shown in Figure 4.4-5, compared with the simulated performance of the practical basic bootstrapping rectifier, the static gate-control bootstrapping rectifier has a slightly lower efficiency for input voltages of 4.5 V_{peak} and 5 V_{peak} but has a much-improved efficiency for input voltages lower than 2.5 V_{peak}.

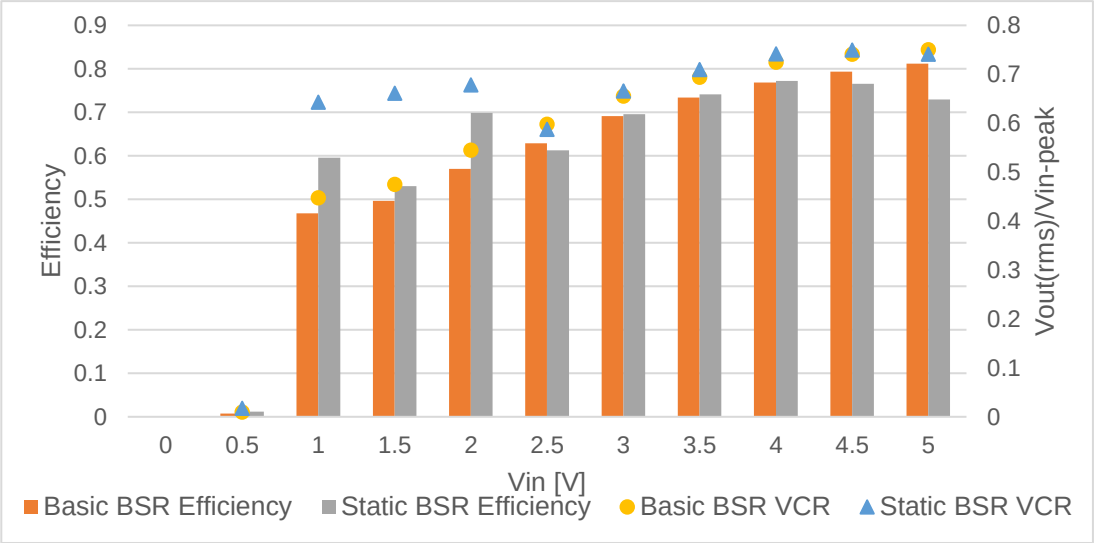

Figure 4.4-5 (From simulation) comparison of voltage conversion ratio (VCR) and output efficiency between static BSR and practical basic BSR at the light load condition

At 4.5 V_{peak} and 5 V_{peak} input, the practical basic bootstrapping rectifier has an output efficiency of 80% and 82%, respectively. In comparison, for the static gate-control bootstrapping rectifier, the corresponding output efficiencies are 76% and 73%, which is 4% and 9% lower. This is because of the higher reverse leakage loss ratio at the static gate-control bootstrapping rectifier, 6% at 4.5 V_{peak} and 11% at 5 V_{peak}. Because the voltage at V_{CAP1} is adjusted to achieve high efficiencies at lower input voltage, the voltage at V_{CAP1} is slightly lower than the optimum gate voltage for the PMOS M12. Therefore, the PMOS M12 will remain open for a short period when V_{OUT}>V_{IN}, which results in the discharging of the load capacitor through M12 to the input.

Even with the lower output efficiencies of the static gate-control bootstrapping rectifier, the output voltages of the static gate-control bootstrapping rectifier are similar to the output voltages of the practical basic bootstrapping rectifier, as shown in Table 4.4-1.

$V_{IN}(peak)$/V	4.5	5
Practical basic BSR V_{OUT}	3.34 V_{rms} 3.29 V_{avg}	3.75 V_{rms} 3.70 V_{avg}
Static BSR V_{OUT}	3.37 V_{rms} 3.32 V_{avg}	3.70 V_{rms} 3.64 V_{avg}

Table 4.4-1 (From simulation) output voltages for practical basic bootstrapping rectifier and static gate-control bootstrapping rectifier at input voltages of 4.5 V_{peak} and 5 V_{peak} at the light load condition

At 4.5 V_{peak} input, the static gate-control bootstrapping rectifier has a higher $V_{OUT}(rms)$ and a higher $V_{OUT}(avg)$ even though the output efficiency is 4% lower than the practical basic bootstrapping rectifier. Both the $V_{OUT}(max)$ and the $V_{OUT}(min)$ are higher for the static gate-control bootstrapping rectifier. The reason for these is because both the PMOSs M12 and M13 are open at this input voltage, and the total PMOS width is twice the PMOS width in the practical basic bootstrapping rectifier, where only M1 are open at the input voltage. Therefore, more current can flow to

charge the load capacitor, resulting in a higher $V_{OUT}(max)$. Moreover, the reverse leakage current is very limited, which causes the $V_{OUT}(min)$ to be comparatively high. The higher $V_{OUT}(max)$ and $V_{OUT}(min)$ contribute to the higher $V_{OUT}(rms)$ and $V_{OUT}(avg)$.

At 5 V_{peak}, the static gate-control bootstrapping rectifier has a higher $V_{OUT}(max)$ (4.94 V, compared with 4.80 V), but a lower $V_{OUT}(min)$ (2.77 V, compared with 2.80 V). Even though the $V_{OUT}(max)$ of the static gate-control bootstrapping rectifier is 0.14 V higher than the $V_{OUT}(max)$ of the practical basic bootstrapping rectifier, because of the reverse leakage, the $V_{OUT}(min)$ is lower, and so are the $V_{OUT}(rms)$ and $V_{OUT}(avg)$. The $V_{OUT}(rms)$ is 1.3% less and the $V_{OUT}(avg)$ is 1.6% less for the static gate-control bootstrapping rectifier.

For the input voltages of 3 V_{peak} 3.5 V_{peak} and 4 V_{peak}, the output efficiencies of the static gate-control bootstrapping rectifier are all higher than the output efficiencies of the practical basic bootstrapping rectifier. The corresponding output voltages of the static gate-control bootstrapping rectifier are also higher.

At 2.5 V_{peak} input, both the output efficiencies and the output voltages are lower for the static gate-control bootstrapping rectifier than the practical basic bootstrapping rectifier. This is because of the higher heat loss ratio (35.0%, compared with 34.4%) and control and other loss ratio (2.2%, compared with 1.6%) at the static gate-control bootstrapping rectifier, which results in a lower forward efficiency 62.7% (compared with 63.9%). The $V_{OUT}(rms)$ is 1.8% less and the $V_{OUT}(avg)$ is 5.4% less for the static gate-control bootstrapping rectifier.

For input voltages of 2 V_{peak} and lower, the static gate-control bootstrapping rectifier has much higher output efficiencies and output voltages than the practical basic bootstrapping rectifier, as shown in Table 4.4-2.

$V_{IN}(peak)$/V	1	1.5	2
Practical basic BSR η_{OUT}	46.8%	49.6%	57.0%
Static BSR η_{OUT}	59.6%	53.0%	69.8%
Practical basic BSR V_{OUT}	0.44 V_{rms} 0.44 V_{avg}	0.71 V_{rms} 0.70 V_{avg}	1.09 V_{rms} 1.08 V_{avg}
Static BSR V_{OUT}	0.64 V_{rms} 0.63 V_{avg}	0.99 V_{rms} 0.97 V_{avg}	1.35 V_{rms} 1.34 V_{avg}

Table 4.4-2 (From simulation) output efficiencies and output voltages of the practical basic bootstrapping rectifier and static gate-control bootstrapping rectifier at input voltages of 1V_{peak}, 1.5V_{peak} and 2V_{peak} at the light load condition

The higher output efficiencies in the static gate-control bootstrapping rectifier at these input voltages are because of the lower heat loss ratio. For the practical basic bootstrapping rectifier, the heat loss ratio at these voltages are more than 40%; while

for the static gate-control bootstrapping rectifier, the highest heat loss ratio is 30% at 1 V_{peak}. The lower heat loss ratio is because of the PMOS M12, of which the gate voltage is adjusted so that the V_{sgM12} can be high for more current flow.

The main drawback from achieving even higher efficiencies is the higher reverse leakage loss ratio at these voltages for the static gate-control bootstrapping rectifier. At 1 V_{peak} and 1.5 V_{peak} input, the reverse loss ratio is 10% and 23%. The reason for these is because the gate voltage of M12 is too low when V_{OUT}>V_{IN}, causing M12 to remain open for a certain time during V_{OUT}>V_{IN}, resulting in the extra discharging of the load capacitor.

Even with the higher reverse leakage loss, the output voltages of the static gate-control bootstrapping rectifier are higher than the practical basic bootstrapping rectifier at these input voltages. The improvement of $V_{OUT}(rms)$ are 45.5%, 39.4% and 23.9% for 1 V_{peak}, 1.5 V_{peak} and 2 V_{peak}, respectively. The improvement of $V_{OUT}(avg)$ are similar to the $V_{OUT}(rms)$. This proves the effectiveness of the addition of the PMOS M12 and its gate-voltage control circuit for rectification improvement.

The performance of the static gate-control bootstrapping rectifier at the heavy load are presented in Figure 4.4-6 and Figure 4.4-7.

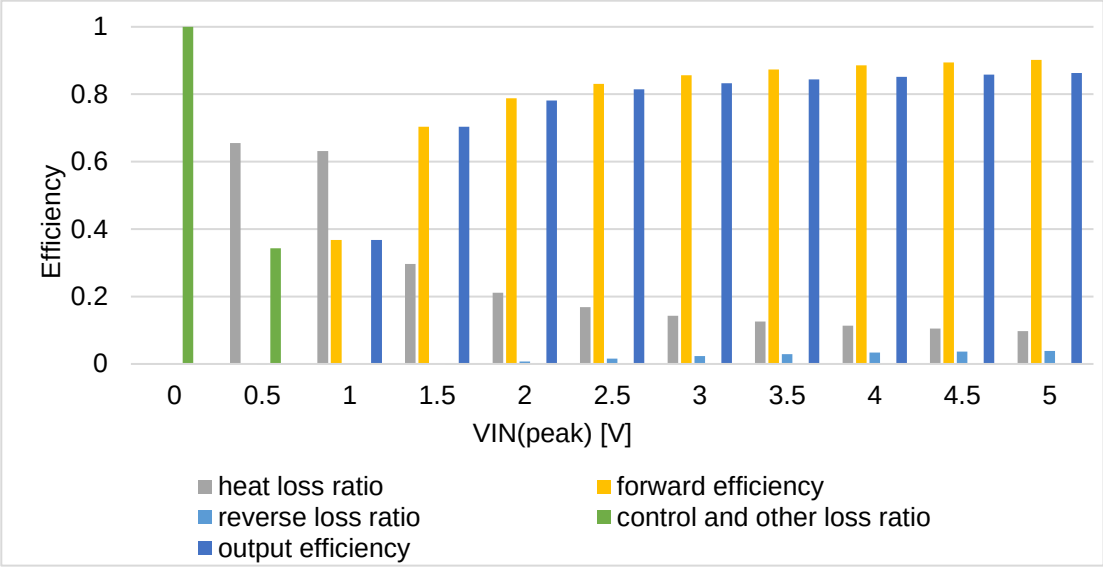

Figure 4.4-6 (From simulation) efficiencies of static BSR with 500 Ω load resistance and 100 pF load capacitance

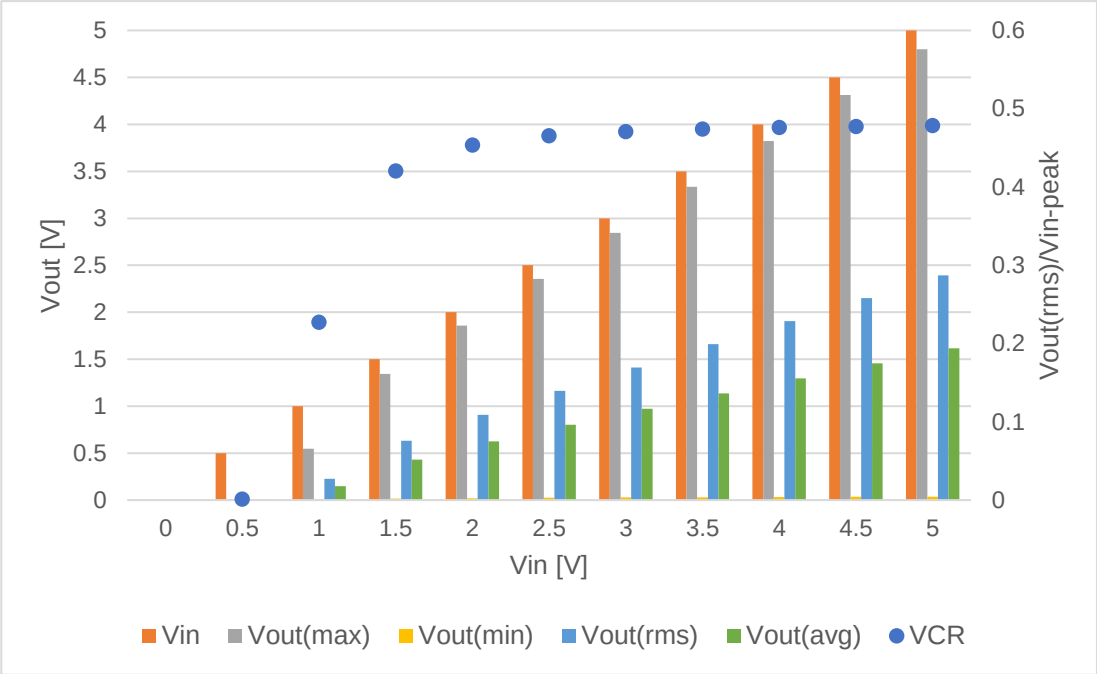

Figure 4.4-7 (From simulation) output voltages and VCR of static BSR with 500 Ω load resistance and 100 pF load capacitance

As introduced in Section 4.4.2.1, the switch S1 will turn on, and S2 will turn off at the heavy load condition. The PMOS M1 will be the main rectification component. Because the gate of M1 is connected to ground, a current will flow through M1 as long as the input voltage is higher than the threshold voltage V_{thM1}.

As shown in Figure 4.4-8, the static gate-control bootstrapping rectifier has much higher output efficiencies than the practical basic bootstrapping rectifier for input voltages below 2.5 V_{peak} but slightly lower output efficiencies for 3 V_{peak} and higher. The output voltages of the static gate-control bootstrapping rectifier are higher than the output voltages of the practical basic bootstrapping rectifier across the input voltage range, especially for input voltages below 2.5 V. At input voltages between 3 V_{peak} and 5 V_{peak}, the output efficiencies of the static gate-control bootstrapping rectifier is lower than the output efficiencies of the practical basic bootstrapping rectifier, as shown in Table 4.4-3.

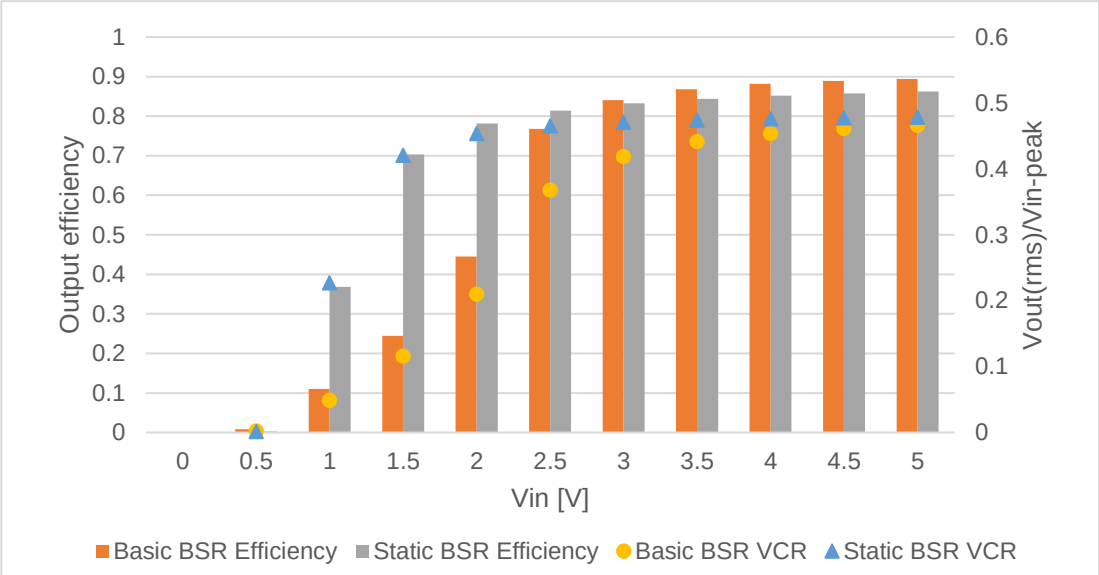

Figure 4.4-8 (From simulation) comparison of voltage conversion ratio (VCR) and output efficiency between static BSR and practical basic BSR at the heavy load condition

$V_{IN}(peak)$/V	3	3.5	4	4.5	5
Practical basic BSR η_{OUT}	84.1%	86.8%	88.2%	88.9%	89.4%
Static BSR η_{OUT}	83.2%	84.3%	85.2%	85.8%	86.3%
Practical basic BSR V_{OUT}	1.26 V_{rms} 0.72 V_{avg}	1.55 V_{rms} 0.92 V_{avg}	1.82 V_{rms} 1.10 V_{avg}	2.08 V_{rms} 1.28 V_{avg}	2.33 V_{rms} 1.45 V_{avg}
Static BSR V_{OUT}	1.41 V_{rms} 0.97 V_{avg}	1.66 V_{rms} 1.14 V_{avg}	1.90 V_{rms} 1.30 V_{avg}	2.15 V_{rms} 1.46 V_{avg}	2.39 V_{rms} 1.62 V_{avg}

Table 4.4-3 (From simulation) output efficiencies and output voltages of practical basic BSR and static BSR at input voltages of 3 V_{peak}, 3.5 V_{peak}, 4 V_{peak}, 4.5 V_{peak} and 5 V_{peak} at the heavy load condition

The lower output efficiencies of the static gate-control bootstrapping rectifier are due to the higher heat loss ratio. This is because of the heat loss at the PMOS M1. Because the gate of M1 is connected to ground, there is no control loss during operation. Another aspect of loss is from the reverse leakage loss, which is because of the low V_{gM1} when V_{OUT}>V_{IN}. Because this period is very short, the reverse leakage loss is comparatively small, less than 4%. By comparing the forward efficiency between the two rectifiers, the forward efficiency of the static gate-control bootstrapping rectifier is actually higher, which means a stronger power capability at the heavy load condition.

Even though the output efficiencies of the static gate-control bootstrapping rectifier are lower, its output voltages are actually higher than the practical basic bootstrapping rectifier when the input voltages are between 3 V_{peak} and 5 V_{peak}. The improvement of $V_{OUT}(rms)$ is from 2.5% at 5 V_{peak} input to 11.9% at 3 V_{peak} input. The improvement of $V_{OUT}(avg)$ is more obvious, from 11.7% at 5 V_{peak} to 24.7% at 3 V_{peak}. The higher

$V_{OUT}(avg)$ shows that the ripple of output voltage is less for the static gate-control bootstrapping rectifier.

At input voltages between 1 V_{peak} and 2.5 V_{peak}, the static gate-control bootstrapping rectifier has much higher output efficiencies than the practical basic bootstrapping rectifier, as shown in Table 4.4-4.

$V_{IN}(peak)$/V	1	1.5	2	2.5
Practical basic BSR η_{OUT}	11.0%	24.4%	44.5%	76.8%
static BSR η_{OUT}	36.8%	70.3%	78.1%	81.4%
Practical basic BSR V_{OUT}	0.05 V_{rms} 0.02 V_{avg}	0.17 V_{rms} 0.09 V_{avg}	0.42 V_{rms} 0.22 V_{avg}	0.92 V_{rms} 0.49 V_{avg}
static BSR V_{OUT}	0.23 V_{rms} 0.15 V_{avg}	0.63 V_{rms} 0.43 V_{avg}	0.91 V_{rms} 0.63 V_{avg}	1.16 V_{rms} 0.80 V_{avg}

Table 4.4-4 (From simulation) output efficiencies and output voltages of practical basic bootstrapping rectifier and static gate-control bootstrapping rectifier at input voltages of 1 V_{peak}, 1.5 V_{peak}, 2 V_{peak}, and 2.5 V_{peak} at the heavy load condition

Because of the high control and other loss ratios of the practical basic bootstrapping rectifier, the forward efficiencies and output efficiencies are comparatively low when the input voltage is between 1 V_{peak} and 2.5 V_{peak}. The high loss ratios are because of the high M1 gate voltage V_{gM1} at these input voltages, which makes the PMOS M1 unable to turn on fully. A portion of the input currents has to flow through the diode-connected PMOS M2, which will cause a higher heat loss because of the larger voltage difference between the source and drain of the PMOS M2. The heat loss of M2 is reflected in the control and other loss ratio. At 1 V_{peak} and 1.5 V_{peak}, there is no heat loss at the practical basic bootstrapping rectifier, but the control and other loss ratio is over 75%. This is because the PMOS M1 is not turned on at these input voltages. The input currents flow entirely through the PMOS M2. The heat loss in M2 is thus reflected as the control and other loss.

For the static gate-control bootstrapping rectifier, because V_{gM1} is 0 V, the PMOS M1 is turned on when the input voltage is between 1 V_{peak} and 2.5 V_{peak}. Because the heat loss in M1 in the static gate-control bootstrapping rectifier is much lower than the heat loss in M2 in the practical basic bootstrapping rectifier, the resulting forward efficiencies are much higher. Because the reverse leakage loss is very limited (less than 1.6%), the actual output efficiencies are also much higher.

The main issue in the static gate-control bootstrapping rectifier at the heavy load condition is the decrease of output efficiency when the input voltage decreases. This is caused by the increase of heat loss in the PMOS M1 when the input voltage decreases. The reason for this is that the source-gate voltage difference V_{sgM1}

decreases when the input voltage decreases as the gate voltage V_{gM1} is constantly 0 V. The solution to this issue will be discussed later in Section 4.4.1.3.

In terms of the output voltages, the performance of the static gate-control bootstrapping rectifier is a big improvement over the performance of the practical basic bootstrapping rectifier. The $V_{OUT}(rms)$ of the static gate-control bootstrapping rectifier is around 4 times the value of the practical basic bootstrapping rectifier at 1 V_{peak} and 1.5 V_{peak} input because of the much higher output efficiencies. The RMS value at 2 V_{peak} is more than twice of the RMS values of the practical basic bootstrapping rectifier. Even for 2.5 V_{peak}, there is a 26% improvement.

At 0.5 V_{peak} input, because the input voltage is under the threshold voltage of M1, M1 is off, and no current will flow in the rectifier.

4.4.1.3 Conclusion

In this section, the novel static gate-control bootstrapping rectifier is developed based on the practical basic bootstrapping rectifier. A circuit, including the PMOS M12 and its gate-control circuit, is added to improve the efficiency at the low input voltage condition with a light load; and a gate-grounded PMOS M1 is added specifically for heavy load conditions. At the light load condition, the static gate-control bootstrapping rectifier has a better output voltage and output efficiency performance in the target input voltage range than the practical basic bootstrapping rectifier except for 5 V_{peak} input, even though the output efficiencies are slightly lower at 4.5 V_{peak} and 5 V_{peak}. At the heavy load condition, the static gate-control bootstrapping rectifier has lower output efficiencies than the practical basic bootstrapping rectifier when the input voltage is between 3 V_{peak} and 5 V_{peak} because of the higher reverse leakage loss ratio. However, the output voltages of the static gate-control bootstrapping rectifier are higher at these input voltages. For the input voltage between 1 V_{peak} and 2.5 V_{peak}, the static gate-control bootstrapping rectifier has a much better performance than the practical basic bootstrapping rectifier. Overall, the static gate-control bootstrapping rectifier is a big improvement over the practical basic bootstrapping rectifier.

However, the static gate-control bootstrapping rectifier is far from being perfect. There are two problems with it. The first problem of the static gate-control bootstrapping rectifier is the decrease of output efficiency when the input voltage decreases below 2 V_{peak} at the heavy load condition, as seen in Figure 4.4-6. This can be improved by connecting the gate of M1 to $-V_{IN}$ in a full-wave rectifier. The source-gate voltage difference V_{sgM1} will thus become $2V_{IN}$. The PMOS M1 will thus turn on fully even with low input voltages. The forward efficiency and the output efficiency will be increased. The waveform of the output voltage is shown in Figure 4.4-9. The performance of the

improved rectifier is shown in Figure 4.4-10 and Figure 4.4-11. As seen, between 1.5 V_{peak} and 5 V_{peak} input, the output efficiency is over 85%; and at 1 V_{peak} V_{IN}, the output efficiency of the improved rectifier has improved to over 80%. Moreover, the improved rectifier will continue to operate when the input voltage drops to 0.5 V_{peak}, with an output efficiency of over 60%. A comparison of the output voltage and output efficiency performance among the discussed rectifiers are presented in Figure 4.4-12.

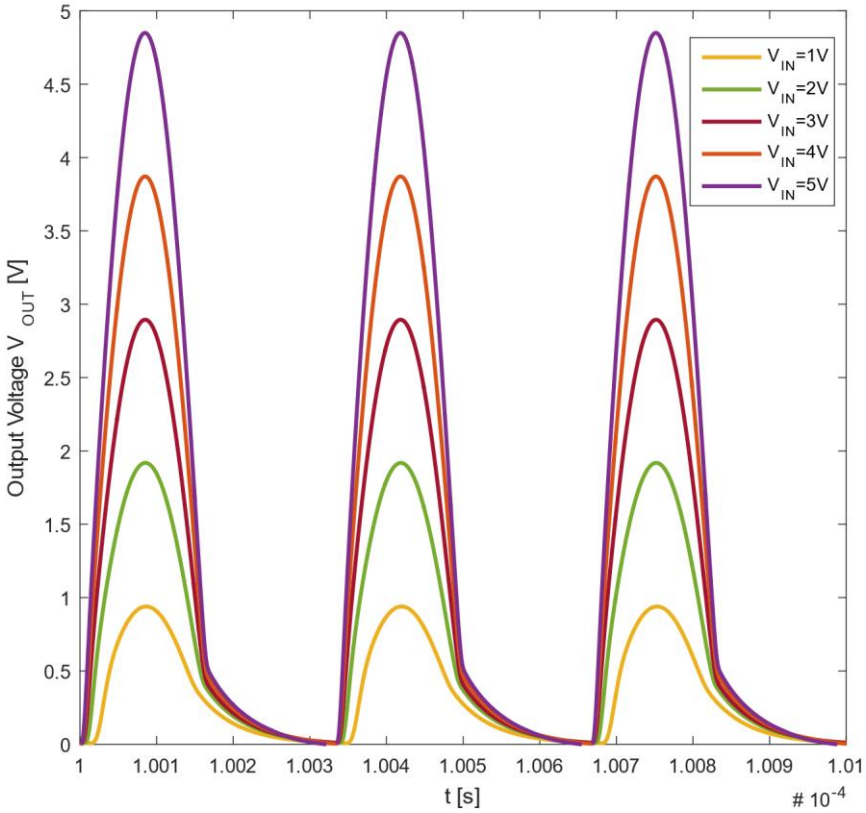

Figure 4.4-9 Waveform of output voltages of improved static BSR for peak input voltages from 1 V to 5 V at the heavy load condition

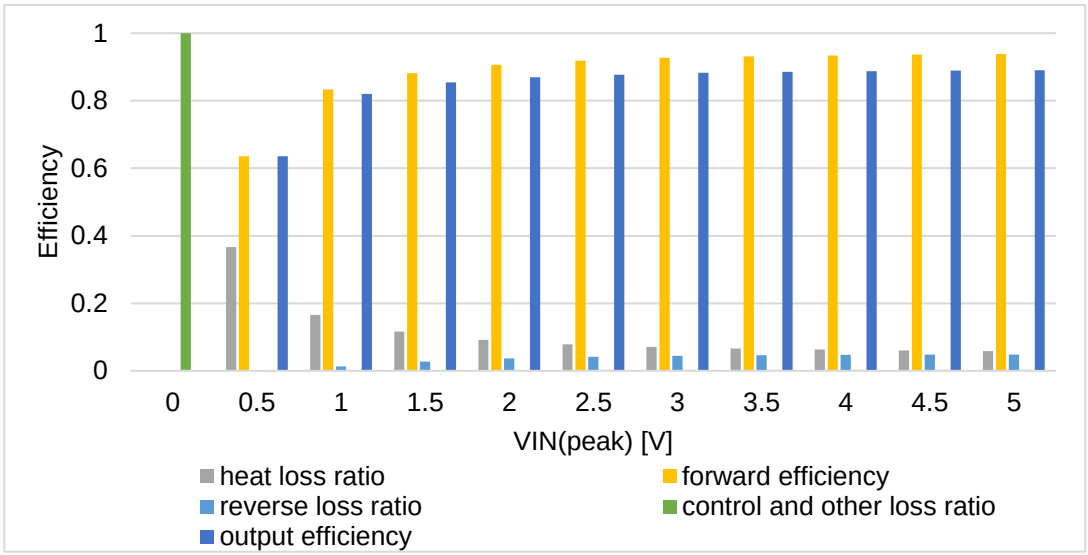

Figure 4.4-10 (From simulation) efficiencies of the improved static gate-control bootstrapping rectifier with 500 Ω load resistance and 100 pF load capacitanc. The simulated waveforms of the output current through the switch PMOS can be seen in AppendixA5. .

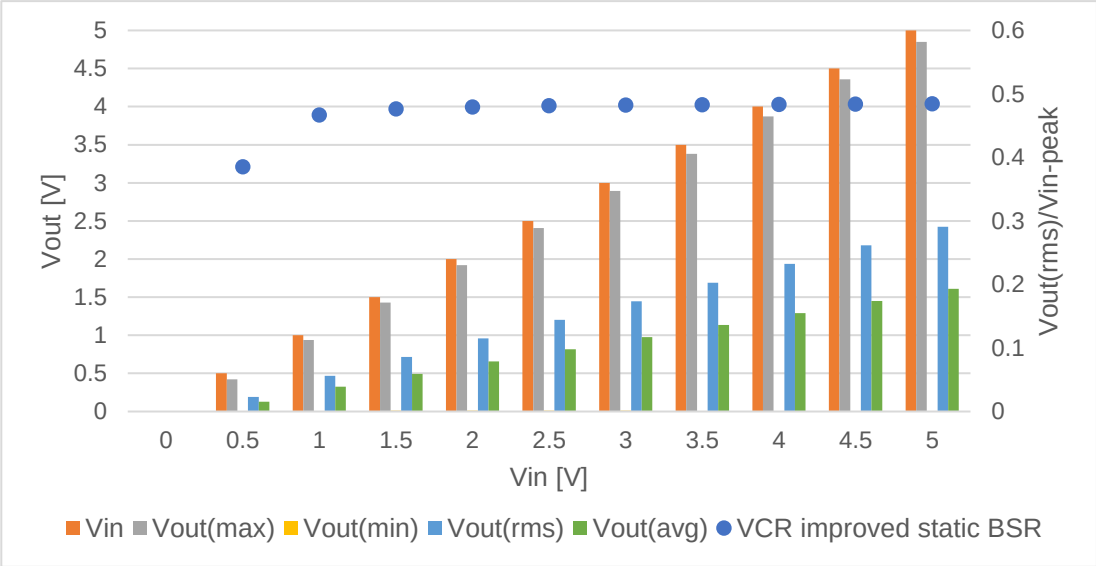

Figure 4.4-11 (From simulation) voltages and VCR of improved static gate-control bootstrapping rectifier with 500 Ω load resistance and 100 pF load capacitance

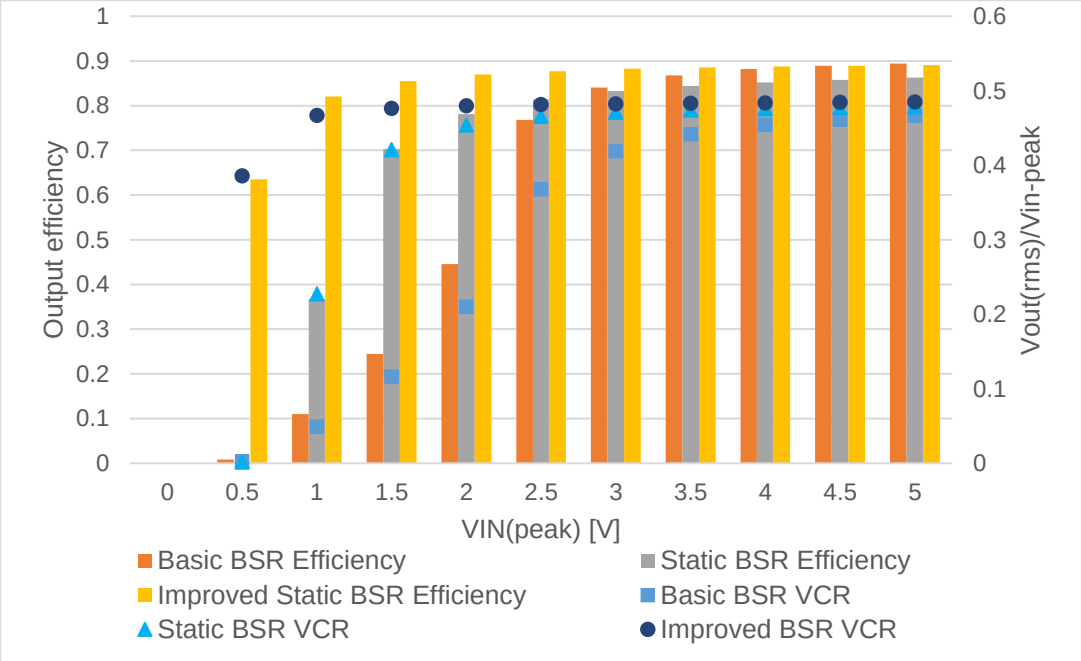

Figure 4.4-12 (From simulation) comparison of voltage conversion ratio (VCR) and output efficiency among static BSR, practical basic BSR and the improved static BSR at the heavy load condition

The other problem comes from the light load condition, where the heat loss ratio and the reverse leakage loss ratio are high across the input voltage range. These high loss ratios are mainly because of the gate voltage values of the main rectification-switch PMOSs M12 and M13. On the one hand, when V_{IN}>V_{OUT}, the gate voltage of these PMOSs should be low to allow maximum current flow; on the other hand, when V_{IN}<V_{OUT}, their gate voltage should be high to block reverse current flow. For M12 and M13 in the static gate-control bootstrapping rectifier, their gate voltage is comparatively fixed at a voltage value so that a compromise on the gate voltage

should be made to balance both situations. Therefore, either the heat loss ratio or the reverse leakage loss ratio will be high to achieve the highest output efficiency.

Another reason is that the gate voltages of the main rectification-switch PMOSs are not always able to match the optimum values for the highest output efficiency. Because the gate voltage of the rectification-switch PMOSs is controlled by the threshold voltages of the PMOSs M3, M31 and M32, there is a conflict between the change of optimum gate voltage in different input voltages and the change of threshold voltage of the PMOSs in different input voltages. While the difference between the input voltage and the optimum gate voltage increases as the input voltage increases, the threshold voltages of the PMOSs remain more or less constant throughout the input voltage range. This makes the matching between the actual gate voltages and the optimum gate voltages only suitable for a small input voltage range, which causes the high loss ratios at some input voltages.

To further improve the efficiency of the bootstrapping rectifier, the gate voltage of the main rectification-switch PMOS must be dynamic, which means the gate voltage should be close to 0 V when V_{IN}>V_{OUT} and should be close to V_{IN} when V_{IN}<V_{OUT}. This will be discussed further in the next section.

4.4.2 Dynamic gate-control rectifier

4.4.2.1 The dynamic gate-control rectifier

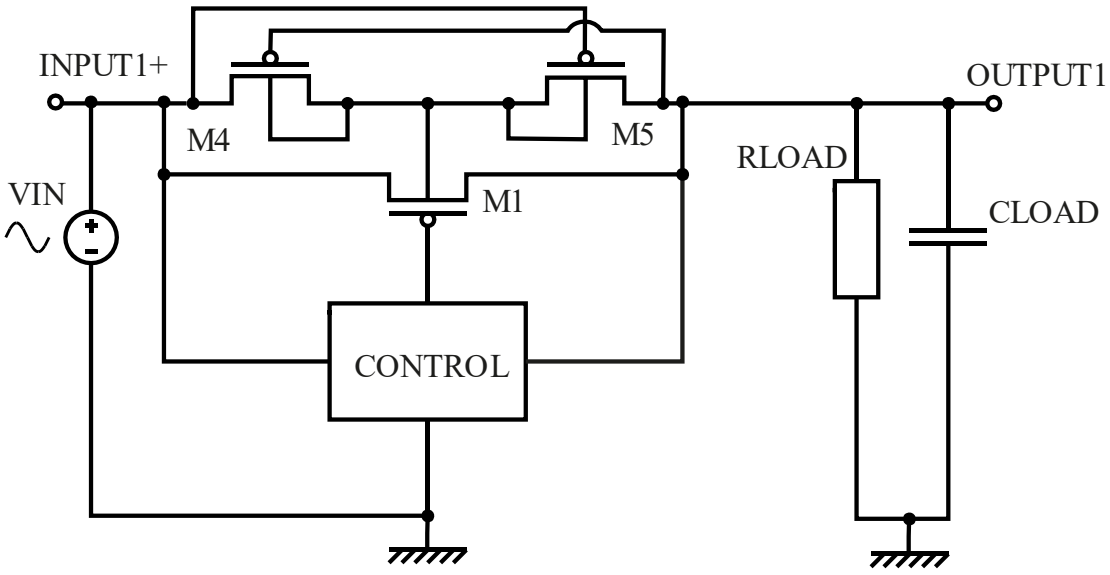

Figure 4.4-13 Circuit structure of dynamic gate-control rectifier

The structure of the dynamic gate-control rectifier is as shown in Figure 4.4-13. A control unit is connected to set the M1 gate voltage value V_{gM1} according to the values of V_{IN} and V_{OUT}. Instead of controlling the gate voltage of M1 with a static value of voltage, a dynamic gate-control rectifier controls the gate of the PMOS M1 with a dynamic voltage. The value of this voltage will be at a low voltage level when V_{IN}>V_{OUT}

to turn on M1 and at a high voltage level when V_{IN}<V_{OUT} to turn off M1. An example simulated waveform is shown in Figure 4.4-14.

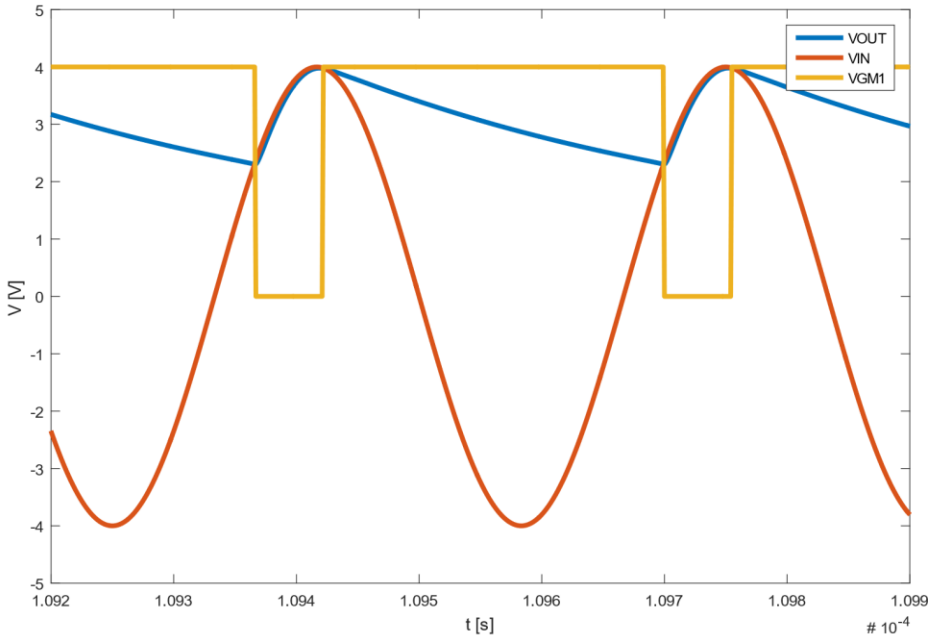

Figure 4.4-14 Simulated waveforms of V_{IN}, V_{OUT} and V_{gM1} in dynamic gate-control rectifier

At the light load condition (with a high load resistance), the dynamic gate-control rectifier has two advantages over the static gate-control bootstrapping rectifier. The first advantage is that the heat loss generated by the main rectification-switch PMOS M1 can be minimised. The second advantage is that the reverse leakage loss can be close to 0% at the same time, making the output efficiency close to the forward efficiency. The static gate-control bootstrapping rectifier can achieve only one of these two conditions at a time, i.e. either a low heat loss ratio but a high leakage loss, or a high heat loss with a low leakage loss.

However, the dynamic gate-control rectifier has a disadvantage. The dynamic gate-control rectifier needs to change the voltage of the switch-gate to a target voltage at the right time to maximise output efficiency. This means a much more complex control circuit is needed for the dynamic gate-control rectifier, which means much more energy will be consumed by the control circuit. Therefore, the dynamic gate-control rectifier will generate a higher control loss ratio than the static gate-control bootstrapping rectifier.

At the heavy load condition, because V_{OUT}>V_{IN} never happens, there will not be any leakage loss and the value of V_{gM1} can stay at 0 V or -V_{IN} for maximum forward efficiency. The dynamic gate-control rectifier has no advantage over the static one.

The simulated performance of an ideal dynamic gate-control rectifier at the light load condition can be seen in Figure 4.4-15 and Figure 4.4-16.

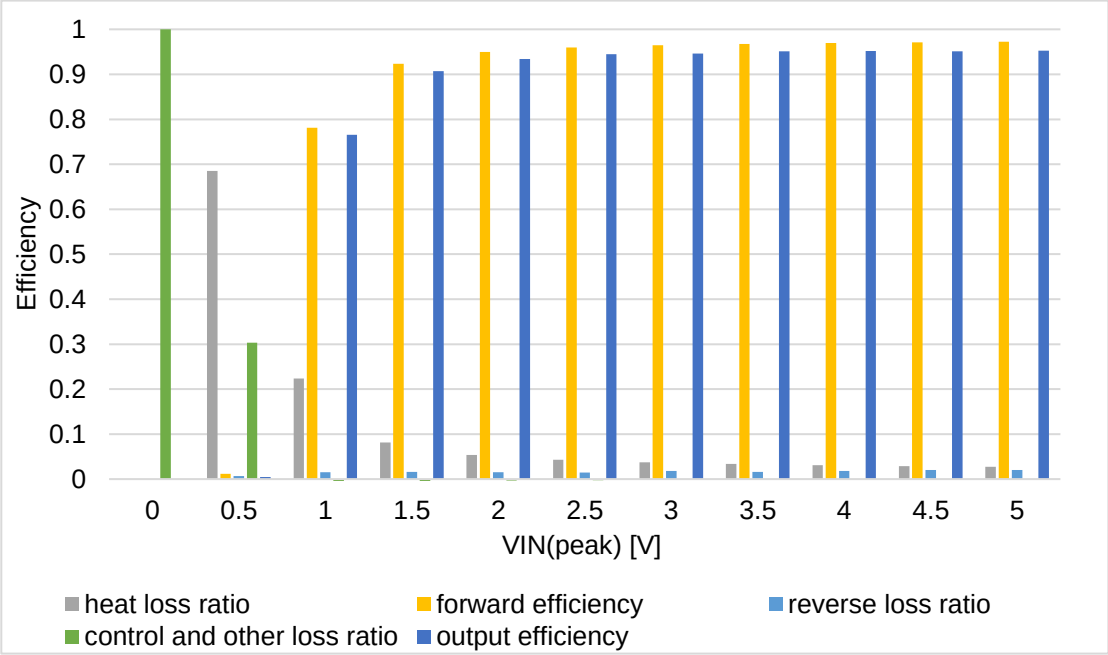

Figure 4.4-15 (From simulation) efficiencies of ideal dynamic gate-control rectifier with 5 kΩ load resistance and 100 pF load capacitance

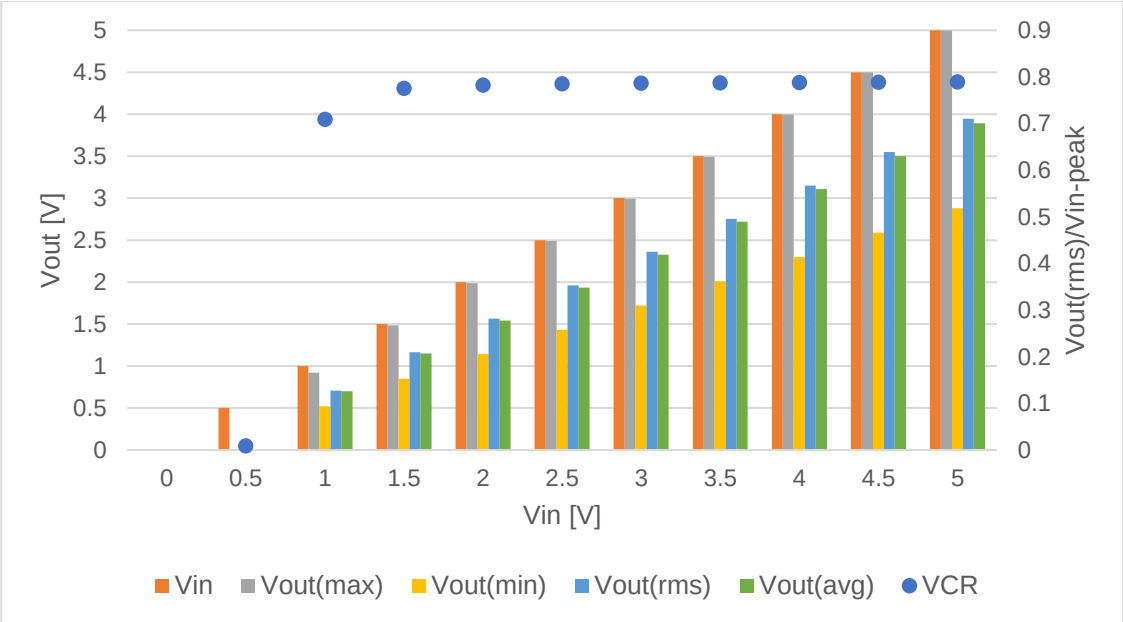

Figure 4.4-16 (From simulation) voltages of ideal dynamic gate-control rectifier with 5 kΩ load resistance and 100 pF load capacitance

From Figure 4.4-15, the output efficiency of the rectifier is all over 90% for V_{IN} from 1.5 V_{peak} to 5 V_{peak}. The output efficiency even reaches over 95% for V_{IN} 3.5 V_{peak} or higher. For V_{IN} = 1 V_{peak}, the output efficiency is 76%, which is because of the smaller V_{sgM1} value. The output efficiency is almost 0% for 0.5 V_{peak} input because the value of V_{IN} is less than the value of threshold voltage V_{thM1}, and the PMOS M1 is not able to turn on. The high output efficiency for V_{IN} over 1.5 V_{peak} is because of the low heat

loss ratios and reverse loss ratios, which are less than 10% in total. The smaller V_{sgM1} value at 1 V_{peak} V_{IN} has caused a higher heat loss at the PMOS M1 and thus reduce the output efficiency.

Because of the higher output efficiency, the dynamic gate-control rectifier has a better output voltage performance than the static gate-control bootstrapping rectifiers, as shown in Figure 4.4-17. Both of the $V_{OUT}(max)$ and the $V_{OUT}(rms)$ are the highest for the dynamic gate-control rectifier when V_{IN} is higher than 0.5 V_{peak}. For V_{IN} between 2.5 V_{peak} and 3.5 V_{peak}, the improvement of $V_{OUT}(rms)$ can be up to 30%.

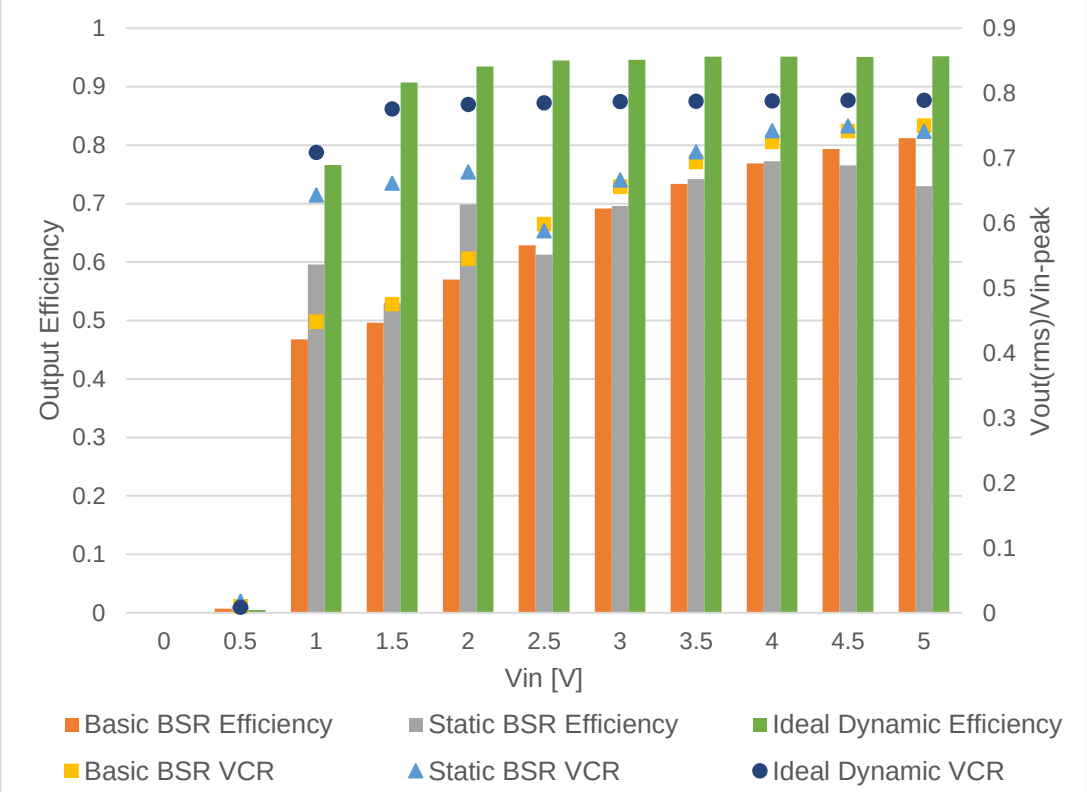

Figure 4.4-17 (From simulation) comparison of voltage conversion ratio (VCR) and output efficiency among static BSR, practical basic BSR and ideal dynamic gate-control rectifier at the light load condition

Practical dynamic gate-control rectifiers generally use comparators as the micro-control unit. As shown in Figure 4.4-18, Comp1 and Comp2 are connected to M_{P1} and M_{P2}, respectively, to set the gate voltages. When IN+ is higher than V_{DC_OUT}, the voltage at the negative input of Comp1 is higher than the voltage at its positive input, and the output of Comp1 is 0 V, causing the PMOS M_{P1} to turn on; when IN+ is lower than V_{DC_OUT}, the voltage at the positive input of Comp1 is higher than the voltage at its negative input, and the output of Comp1 will be close to V_{DC_OUT}, causing the PMOS M_{P1} to turn off. The operation of the Comp2 is the same as Comp1 with the input being IN-.

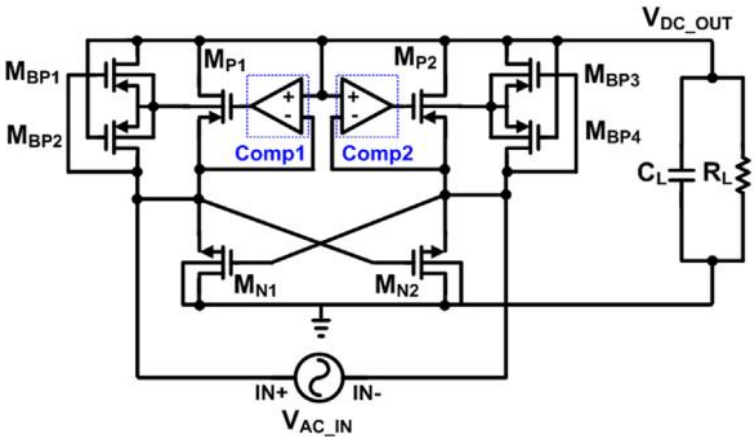

Figure 4.4-18 Full-Wave Gate Cross-Coupled Rectifier with comparators [168]

The use of comparators has two shortcomings.

The first one is the high-power consumption of a comparator. State-of-the-art comparators have a supply current of about 550 uA for a power supply voltage between 2 V and 5 V [TSV7191], which means a large amount of the output power will be consumed by the control circuit if two comparators are used in the rectifier in the wireless power system. The efficiency of the rectifier will thus be much reduced.

The second one is the limited bandwidth of a comparator. For low power comparators that are suitable for the rectifier, their bandwidths are normally quite limited. State of the art low-power comparators normally have bandwidths of less than 1 MHz and the slew rates are normally below 2.5 V/µs. These limitations make it difficult for the comparators to switch the PMOSs at the operational frequency of the wireless power system.

From the above analysis, a dynamic gate-control rectifier has a better performance than the static gate-control bootstrapping rectifiers with less heat loss and reverse leakage loss. However, the control circuit in the dynamic gate-control rectifier is potentially power hungry and limited by the circuit bandwidth, which may reduce the efficiency advantage of the dynamic gate-control rectifier. Therefore, a low power control circuit with an appropriate bandwidth is necessary to make an efficient dynamic gate-control rectifier.

4.4.2.2 Structure and operation of opto-coupled dynamic gate-control bootstrapping rectifier

Based on the structure of the bootstrapping rectifier, an opto-coupled dynamic gate-control (OCDGC) bootstrapping rectifier is developed in simulation. In this circuit, an optocoupler is used to control the gate voltage of the main rectification-switch PMOS, so that the waveform of switch-gate voltage will be dynamic, as the waveform of gate voltage in Figure 4.4-14. The circuit diagram is as shown in Figure 4.4-19.

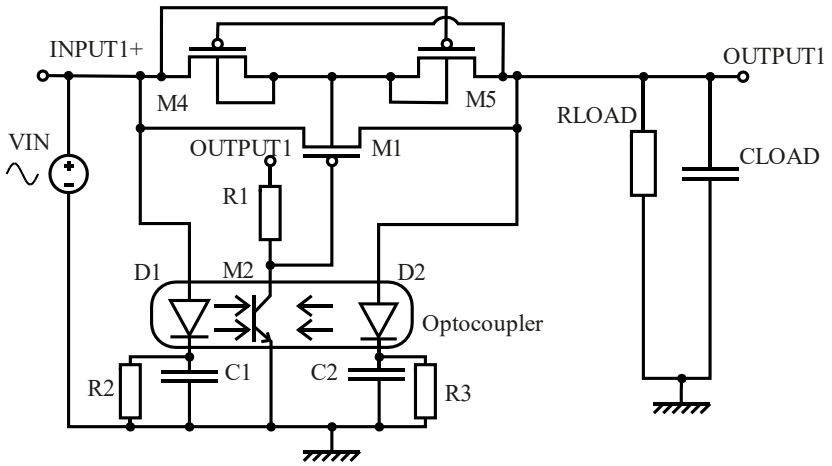

Figure 4.4-19 Circuit diagram of the OCDGC rectifier

An optocoupler is an optical-electrical component that contains LEDs and phototransistors (or photodiode, photoresistor). As shown in Figure 4.4-19, the LEDs D1 and D2 and the phototransistor M2 form an optocoupler.

An LED is a light emitter diode, which will emit light when a current is flowing through it under forward-bias condition. The light output strength from an LED is positively related to the amount of its forward current, as shown in Figure 4.4-20. As a junction-diode, an LED has a threshold voltage, which is related to the colour of the light. Normally, the shorter the wavelength of the colour is, the higher the threshold voltage will be, as shown in Figure 4.4-21.

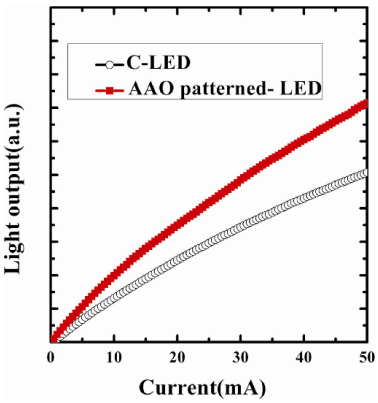

Figure 4.4-20 Two typical light-current responses for LEDs [204]

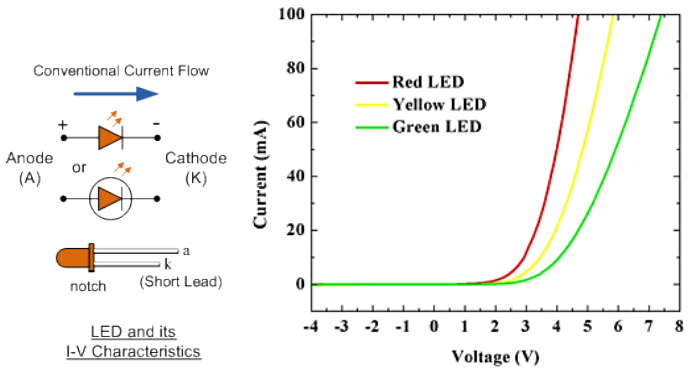

Figure 4.4-21 Typical voltage and current responses for different colours of LEDs [205]

A phototransistor is basically a photodiode with internal amplification, as shown in Figure 4.4-22. The photodiode will allow current to flow under the reverse-biased condition when it senses light with certain frequencies. The light frequency of the LED and the operational frequency of the phototransistor in the optocoupler should, therefore, match so that the phototransistor can turn on when the LED emits light. The V-I response of a photodiode is shown in Figure 4.4-23. The current through the photodiode is proportional to the sensed light strength. The stronger the light is, the higher the current will flow.

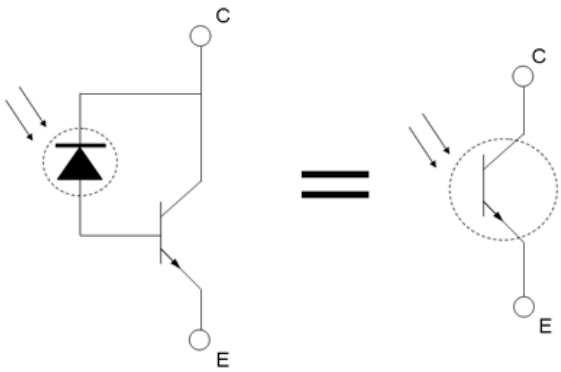

Figure 4.4-22 Phototransistor is basically a photodiode and a bipolar transistor [206]

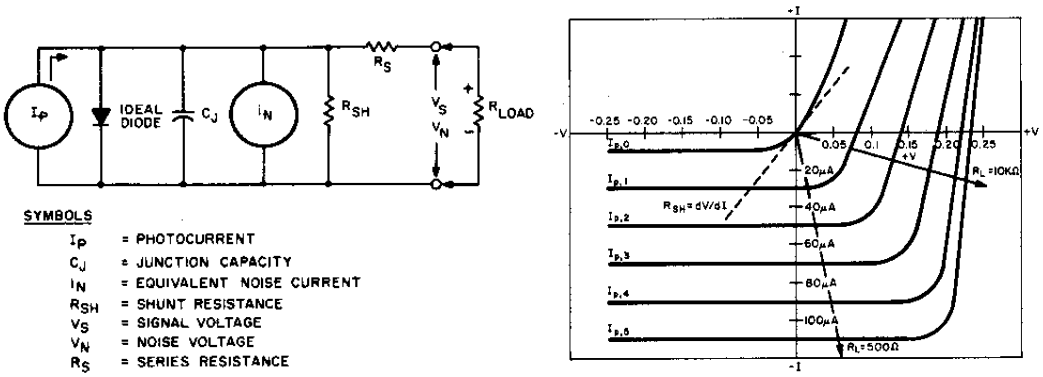

Figure 4.4-23 Equivalent circuit of a photodiode and its V-I responses under different optical energies [207]

The optocoupler works like a current-controlled current source. In an optocoupler, when currents flow through an LED, the LED will emit light of which the strength is proportional to the amount of current. The photodiode will then sense the light and allow a corresponding amount of current to flow through it. This current will then be amplified by the bipolar transistor. The key factors in this operation are the bandwidth and the current gain of the optocoupler. The bandwidth represents how fast the optocoupler can work with input currents; the current gain represents the gain of the output current of the phototransistor over the input current of LEDs.

In the application of OCDGC bootstrapping rectifier, the bandwidth of the optocoupler is 50MHz, and the current gain is 1.

The LEDs D1, D2 and the phototransistor M2 in the optocoupler make the main control circuit in this rectifier. The table of operation process of the OCDGC rectifier can be seen in AppendixA4. . The LED D1 will conduct when the input voltage V_{IN} rises above V_{C1}+V_{thD1}, and will stop as soon as V_{IN} reaches maximum. When D1 conducts, it will emit light and the phototransistor M2 in the optocoupler will be turned on. The gate voltage of the PMOS M1 will be pulled to ground and M1 will thus turn on. The LED D2 will conduct when the output voltage V_{OUT} rises above V_{C2}+V_{thD2}, and will stop as soon as V_{OUT} reaches maximum. Normally V_{OUT} reaches maximum later than V_{IN}, and the LED D2 will continue to emit light when D1 stops, which will extend the M2 conduction time and thus the M1 conduction time. When V_{OUT} reaches maximum, D2 and D1 both are at off stage. The phototransistor M2 in the optocoupler receives no light and thus stop conducting. The gate voltage of the PMOS M1 will be pulled to V_{OUT} and M1 will stop conducting. The time when V_{OUT}>V_{IN} will come after V_{OUT} reaches maximum and M1 is already closed by then, so no reverse current will flow from the load to the input.

The key in the operation of the OCDGC bootstrapping rectifier is the charging and discharging of the capacitor C1 and C2. The capacitor charging current of C1 determines the gate voltage of the PMOS M1, and the C1 discharging-end voltage determines the turn-on time of the PMOS M1.

The capacitor charging current is the inflow current from diode D1 (D2) to the capacitor C1 (C2). The C1 charging current is determined by the input voltage of rectifier as well as the capacitance of C1; the C2 charging current is determined by the output voltage of the rectifier as well as the capacitance of C2. Because the current gain of the optocoupler is 1, a similar amount of current will flow into the collector of the phototransistor M2 as the charging current. Here, the resistor R1 and the phototransistor M2 form a common emitter amplifier. When a current is flowing through the LEDs and the capacitors are being charged, the light-sensed current I_{bM2} at the base of M2 will be amplified by a gain of β, and a current of βI_{bM2} will be outputted at the collector of M2. The voltage V_{gM1} will thus become V_{OUT}-$\beta I_{bM2} \times R_1$; when no current flows through the LEDs, V_{gM1} will rise to near V_{OUT}. The rising time of V_{gM1} is determined by the resistance of R1 and the equivalent capacitance C_{eq} at the collector of M2. Because the time constant for V_{gM1} is calculated as $R_1 \times C_{eq}$, a higher resistance of R1 will result in a longer rising time of V_{gM1}.

The C1 discharging-end voltage is the voltage of C1 when the discharging period of C1 ends. This voltage should be equal to $v_{in}(t)$-V_{thD1} when $v_{in}(t)$= $v_{out}(t)$ at the rising edge of $v_{in}(t)$. Therefore, the capacitor C1 can be charged when $v_{in}(t)$>$v_{out}(t)$

happens, causing M1 to turn on at the right time. The C1 discharging-end voltage is determined by the capacitance of C1 and the resistance of R2. As C1 is fixed in determining the charging current, the resistance of R2 will be set to adjust the C1 discharging-end voltage.

4.4.2.3 The performance of the OCDGC bootstrapping rectifier

The waveform of output voltage is shown in Figure 4.4-24. The simulated performance of the OCDGC bootstrapping rectifier is shown in Figure 4.4-25 and Figure 4.4-26.

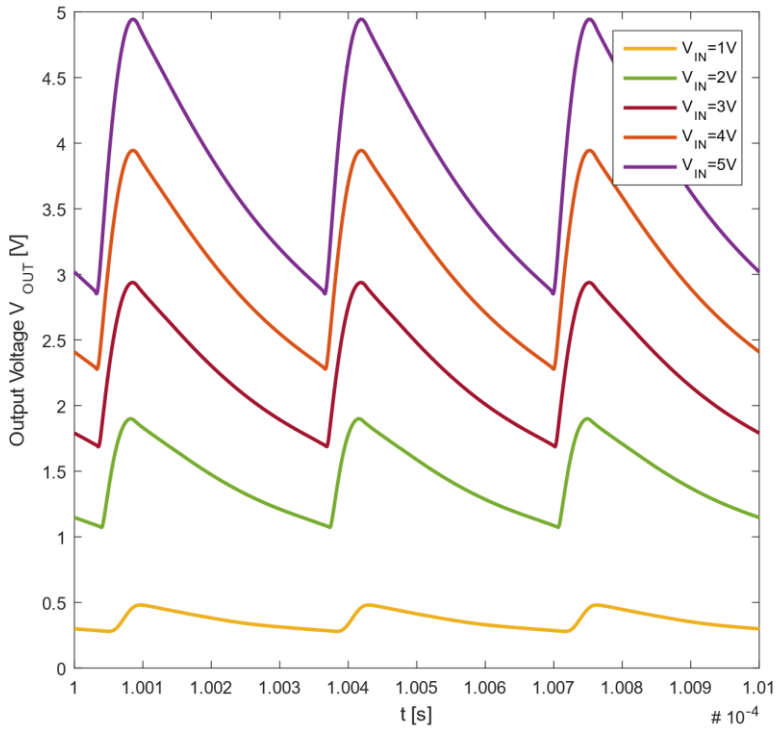

Figure 4.4-24 Waveform of output voltages of OCDGC rectifier for peak input voltages from 1 V to 5 V at the light load condition

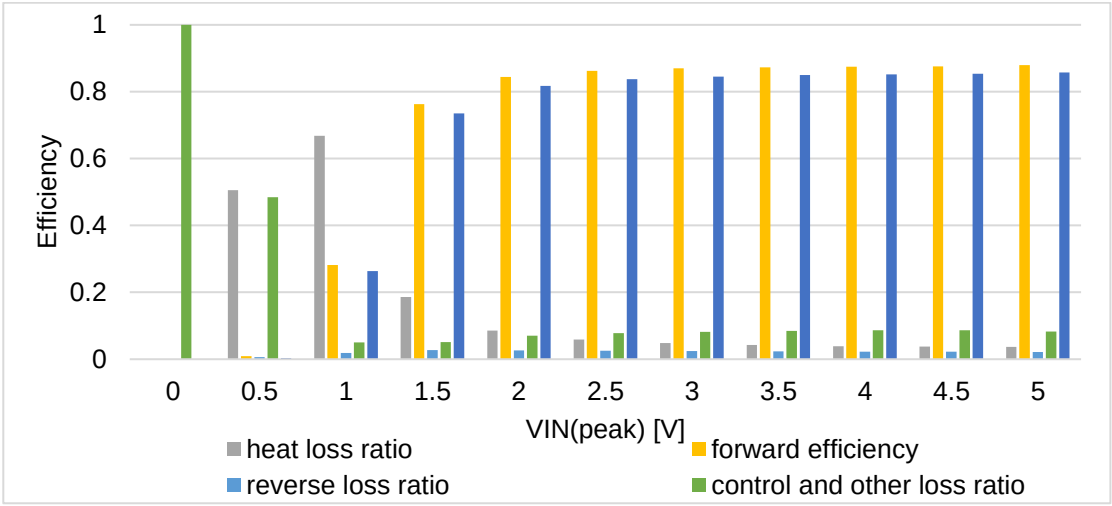

Figure 4.4-25 (From simulation) efficiencies of OCDGC bootstrapping rectifier with 5 kΩ load resistance and 100 pF load capacitance. The simulated waveforms of the current through the switch PMOS can be seen in AppendixA5. .

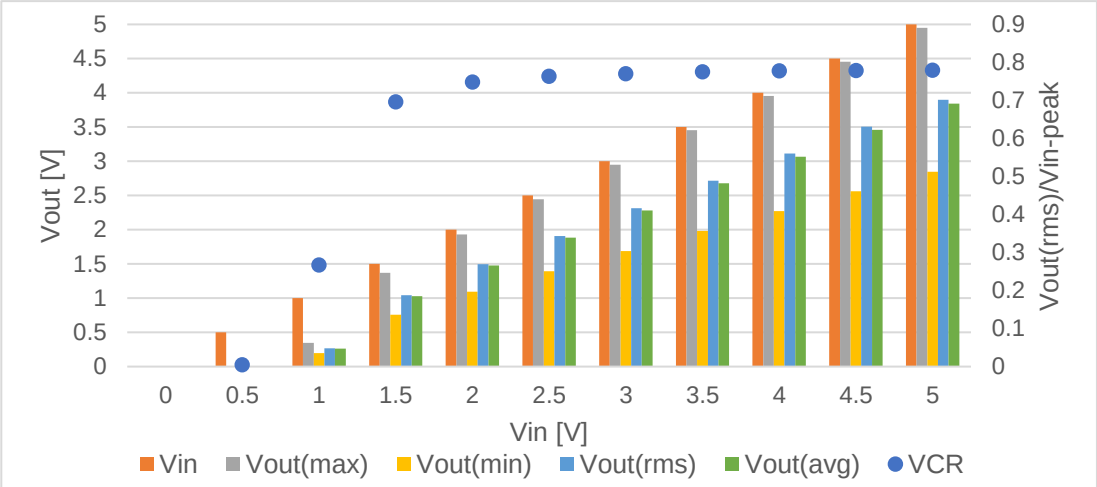

Figure 4.4-26 (From simulation) output voltages and VCR of OCDGC bootstrapping rectifier with 5 kΩ load resistance and 100 pF load capacitance

The output efficiencies of the OCDGC bootstrapping rectifier are over 80% for V_{IN} over 2 V_{peak} but are comparatively low for V_{IN} under 1 V_{peak}. For input voltages of 2 V_{peak} and higher, the output efficiencies are all more than 80%. The main energy loss is the control loss, which is averagely 8%. One part of the control loss is from the capacitor and resistor pairs R2-C1 and R3-C2, which accounts for an average of 30% of the control loss; the other part is from the photo-transistor M2 and the resistor R1, which accounts for the rest of the control loss. The other main energy loss is the heat loss of M1, whose ratio increases from about 3.7% to about 8.6% as the input voltage decreases from 5 V_{peak} to 2 V_{peak}. The reverse loss ratio remains low for this input range, with an average of 2.3%.

At 1.5 V_{peak} input, there is an abrupt output efficiency decrease compared with the output efficiency at 2 V_{peak}. This is due to the increase of heat loss ratio of M1, which is about 19%. This higher loss is because of the shorter switch-on time of the PMOS M1 and the smaller difference between V_{IN} and V_{gM1} when M1 turns on. For 1.5 V_{peak} and lower input voltages, with the same value of resistor R2, the capacitor C1 voltage is not low enough to enable currents to flow through the LED D1 when V_{IN} rises and V_{IN}>V_{OUT} happens. Therefore, the turn-on time of the PMOS M1 is delayed, which causes a shorter M1 overall switch-on time. This can be solved by reducing the value of R2, but a smaller value of R2 will increase the reverse leakage loss for higher input voltages.

The heat loss ratio continues to increase at 1 V_{peak} input to about 67%, causing the output efficiency to drop to 26%. At 0.5 V_{peak} input, the gate voltage of M1 is unable to turn on M1, so the output efficiency is almost 0%.

The voltage performance of the OCDGC bootstrapping rectifier is a big improvement over the static bootstrapping rectifiers, especially at the input voltage range between

2 V_{peak} and 5 V_{peak}. A comparison of $V_{OUT}(max)$ and $V_{OUT}(rms)$ between the OCDGC bootstrapping rectifier and the static gate-control bootstrapping rectifier is shown in Table 4.4-5.

VIN/V	2	2.5	3	3.5	4	4.5	5
$V_{OUT}(max)$ difference/V	0.16	0.56	0.39	0.27	0.11	0.03	0.00
$V_{OUT}(rms)$ difference/V	0.14	0.44	0.31	0.23	0.14	0.13	0.19
$V_{OUT}(max)$ difference ratio	9.3%	29.7%	15.2%	8.3%	2.8%	0.6%	0.0%
$V_{OUT}(rms)$ difference ratio	10.3%	29.9%	15.7%	9.3%	4.8%	3.9%	5.2%

Table 4.4-5 (From simulation) $V_{OUT}(max)$ difference, $V_{OUT}(rms)$ difference and their ratio between the OCDGC bootstrapping rectifier and the static gate-control bootstrapping rectifier at the input voltage range between 2 V_{peak} and 5 V_{peak}

Because of the dynamic voltage at the gate of M1, the OCDGC bootstrapping rectifier has much higher $V_{OUT}(max)$ and $V_{OUT}(rms)$ than the static gate-control bootstrapping rectifier for input voltages between 2 V_{peak} and 3.5 V_{peak}, with at least 8% improvement for the $V_{OUT}(max)$ and 9% for the $V_{OUT}(rms)$. The improvement is less for input voltages between 4 V_{peak} and 5 V_{peak}. The $V_{OUT}(max)$ difference is between 2.8% and 0%. The $V_{OUT}(rms)$ difference is between 3.9% and 5.2%. The improvement of $V_{OUT}(max)$ is due to the larger voltage difference between V_{IN} and V_{gM1} of the OCDGC bootstrapping rectifier; the improvement of $V_{OUT}(rms)$ is due to both the larger V_{IN} and V_{gM1} difference when $V_{IN} > V_{OUT}$ and the V_{OUT} and V_{gM1} difference *when* V_{OUT}>V_{IN}.

For input voltage of 1 V_{peak} and 1.5 V_{peak}, the voltage performance of the OCDGC bootstrapping rectifier is worse than the static gate-control bootstrapping rectifier, as shown in Table 4.4-6. For 1.5 V_{peak} input, the $V_{OUT}(max)$ is lower for OCDGC bootstrapping rectifier but the $V_{OUT}(rms)$ is higher. This is because of the lower reverse leakage loss at the OCDGC bootstrapping rectifier than the static gate-control bootstrapping rectifier. For 1 V_{peak} input, because of the much higher heat loss ratio, the OCDGC bootstrapping rectifier has lower $V_{OUT}(max)$ and $V_{OUT}(rms)$ than the static gate-control bootstrapping rectifier.

VIN/V	1	1.5
$V_{OUT}(max)$ difference/V	-0.51	-0.06
$V_{OUT}(rms)$ difference/V	-0.38	0.05
$V_{OUT}(max)$ difference ratio	-59.7%	-4.5%
$V_{OUT}(rms)$ difference ratio	-58.4%	5.3%

Table 4.4-6 (From simulation) $V_{OUT}(max)$ difference, $V_{OUT}(rms)$ difference and their ratio between the OCDGC bootstrapping rectifier and the static gate-control bootstrapping rectifier at the input voltage range for 1 V_{peak} and 1.5 V_{peak}

A comparison of the output efficiency and output voltages between the OCDGC bootstrapping rectifier and the static gate-control bootstrapping rectifier is shown in Figure 4.4-27. The OCDGC bootstrapping rectifier has the highest output efficiencies and the highest output RMS voltages at input voltages between 1.5 V_{peak} and 5 V_{peak} among the three rectifiers. The OCDGC output maximum voltages are also the highest at input voltages between 2 V_{peak} and 5 V_{peak}. For input voltage of 1 V_{peak}, the output efficiency of the OCDGC bootstrapping rectifier is much less than the other rectifiers, causing much less $V_{OUT}(max)$ and $V_{OUT}(rms)$.

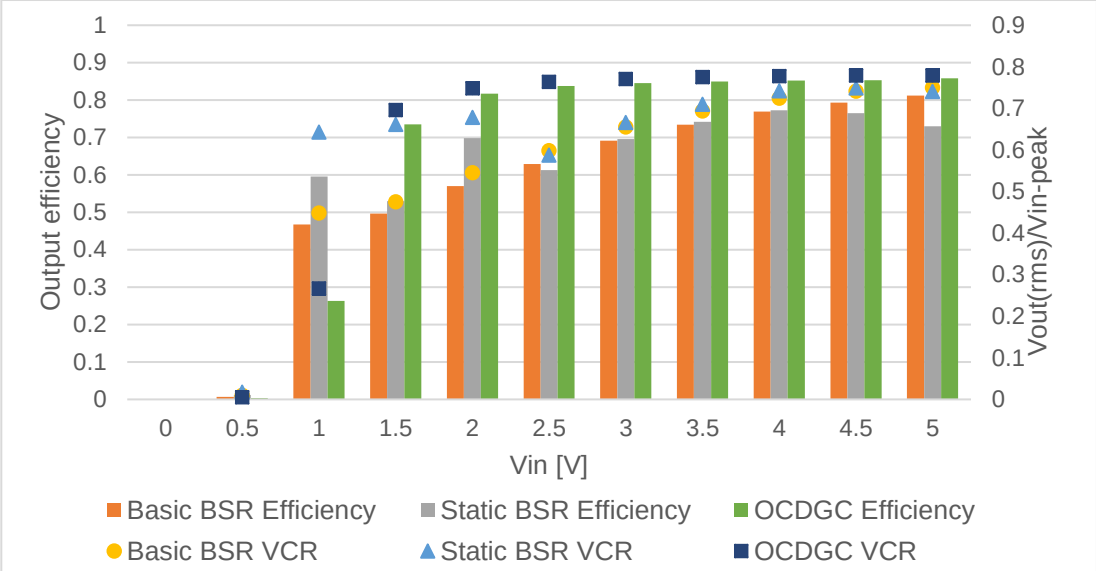

Figure 4.4-27 (From simulation) comparison of voltage conversion ratio (VCR) and output efficiency among the static gate-control bootstrapping rectifier, the practical basic bootstrapping rectifier and the OCDGC bootstrapping rectifier at the light load condition

4.5 Conclusion

In this chapter, the AC-DC rectifier circuits that can be used in the wireless power transfer system for micro-implants are discussed. The simplest form of a rectifier is the junction-diode rectifiers. They are robust and simple and are widely used at high-voltage power systems. However, for the application of high-frequency wireless micro-implants, their high threshold voltages and current leakages at high frequency will stand out and reduce the overall system efficiency. The diode-connected PMOS rectifiers have the same high threshold voltage problem and thus are not suitable for the application.

To improve the overall system efficiency, bootstrapping rectifiers (BSR) are considered. bootstrapping rectifiers use the voltage at the bootstrapping capacitor to control the gate voltage of the main rectification-switch PMOS M1. The capacitor voltage is adjusted to be a set of DC values that turns on the PMOS M1 when V_{IN}>V_{OUT}, and turns off M1 when V_{OUT}>V_{IN}. The practical basic bootstrapping rectifier has better output efficiency and output voltage performances across the input voltage range. However, for low input voltages and in heavy load conditions, the capacitor voltage is not able to turn on the PMOS M1 fully, causing low output efficiencies and output voltages.

To improve the performance, a static gate-control bootstrapping rectifier is designed. This rectifier considers the operation of the rectifier at the heavy load condition (with a load resistance of 500 Ω), in which the output efficiency can be up to 90%. For light load conditions (with a load resistance of 5 kΩ), modifications have been made based on the practical basic bootstrapping rectifier, improving the output efficiency at low input voltages. However, the switch-gate voltage is still in DC form, restricting the performance of the rectifier.

To further improve the performance at the light load conditions, dynamic gate-control bootstrapping rectifiers are introduced. These rectifiers set the gate of the main switch PMOS to a low voltage when V_{IN}>V_{OUT}, and to a high voltage when V_{OUT}>V_{IN}. The problem is that in previous designs, the control circuit normally consumes a comparatively high power and are not suitable for wireless micro-implants. To solve this, the OCDGC bootstrapping rectifier is presented. This rectifier uses an optocoupler to control the gate of the PMOS-switch. The output efficiency and the output voltage performance of the OCDGC rectifier are better than the static gate-control bootstrapping rectifiers at an input voltage range between 1.5 V_{peak} and 5 V_{peak}. At lower input voltages, the performance of the OCDGC rectifier is worse due to the mismatch of resistance.

In the application of wireless power system for micro-implants, a shortcoming of OCDGC bootstrapping rectifier is that the optocoupler may not be able to integrate with the rest of receiver circuit because the LED and phototransistor may not be able to be built in the same process for MOSFETs and other circuit components. In this case, extra common substrates, such as flexible PCBs, may be used for the connection between the optocoupler and the rest of circuits. Even though this may increase the size of the receiver, create extra parasitic capacitance and, more importantly, weaken the robustness of the whole system, the problems can be solved with careful package design.

Overall, the OCDGC bootstrapping rectifier and the static gate-control bootstrapping rectifier are suitable for a wireless power implant with a low power budget (e.g. the IMPACT sensors) because of the following reasons:

- The rectifiers have a low control energy loss ratio (less than 10% for OCDGC and less than 3% for the static BSR) compared with the comparator-based rectifiers.
- They will also be able to work with high efficiencies and low voltage drops for the input voltage ranging from 1 V_{peak} to 5 V_{peak}, which is the induced voltage range of the receiver coil in the proposed WPT system.
- The active switches in the rectifiers can be controlled by MCU on the implant to achieve LSK modulation for signal transmission from the receiver to the transmitter, which can reduce the power loss caused by extra switches.

Because of restriction in time and resource, the OCDGC rectifier and the static BSR are only tested in simulation. In future studies, these rectifiers will be tested on ICs for more detailed analysis.

Chapter 5 The performance of the full proposed magnetic coupling resonance WPT system

5.1 Full proposed magnetic coupling resonance WPT system model

The block diagram of the full magnetic coupling resonance WPT system is shown in Figure 5.1-1. The system involves three parts:

- The coupling coil circuit, which consists of a power source, an impedance matching network, and the coupling coil
- The primary coil circuit, which consists of a variable capacitor, and the primary coil
- The receiver coil circuit, which consists of the receiver (secondary) coil, a tuning capacitor, an impedance matching network, a rectifier, and a load

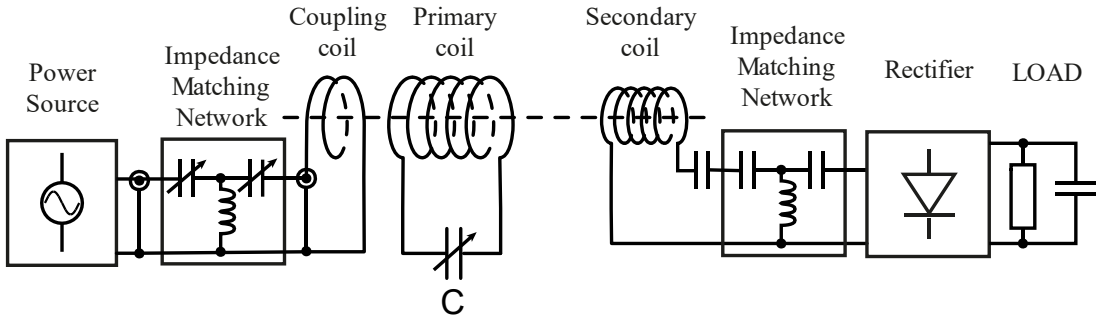

Figure 5.1-1 System diagram of the full proposed magnetic coupling resonance WPT system including the magnetic coupling link, the rectifier and the load at the receiver

It should be noted that, at the receiver, the secondary coil is connected in series with the tuning capacitor, which forms a series L-C circuit to resonate at the operational frequency.

The equivalent circuit of the system is shown in Figure 5.1-2. The explanation of symbols is listed in Table 5.1-1.

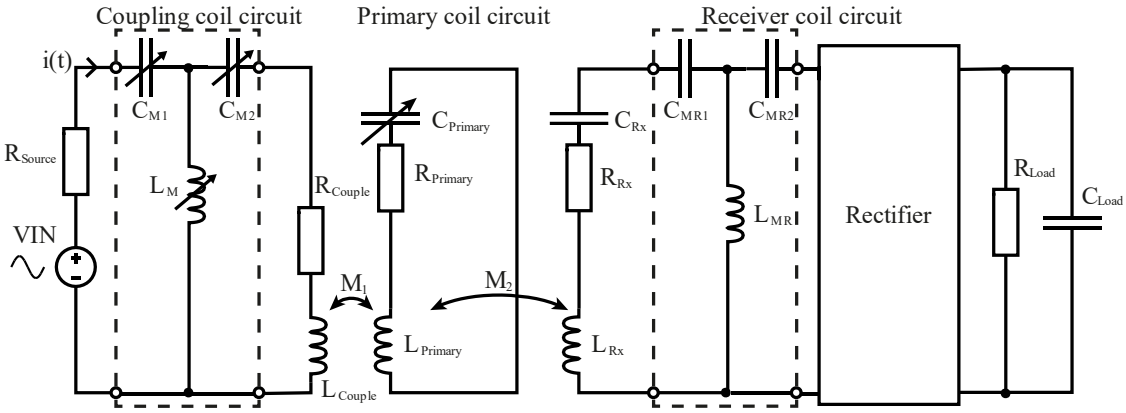

Figure 5.1-2 Equivalent circuit diagram of the proposed WPT system

Coupling coil circuit			
VIN	The output voltage of the power source	C_{M1}, C_{M2} and L_M	The variable capacitors and the multi-tap inductor of the impedance matching network
R_{Source}	The impedance of the power source	L_{Couple}	The inductance of the coupling coil
R_{Couple}	The AC resistance of the coupling coil	M_1	The mutual inductance between the coupling coil and the primary coil
Primary coil circuit			
$R_{Primary}$	The AC resistance of the primary coil	$L_{Primary}$	The inductance of the primary coil
$C_{Primary}$	The variable capacitor connected to the primary coil	M_2	The mutual inductance between the primary coil and the receiver coil
Receiver coil circuit			
L_{RX}	The inductance of the receiver coil	R_{RX}	The AC resistance of the receiver coil
C_{RX}	The tuning capacitor in the receiver coil circuit	C_{MR1}, C_{MR2} and L_{MR}	The impedance matching network in the receiver circuit
R_{Load}	Load resistance	C_{Load}	Load capacitance

Table 5.1-1 Symbols and components in the circuit diagram

In the system, there are two impedance matching networks. One is in the coupling coil circuit. This impedance matching network is a T-section circuit, with two variable capacitors and a variable inductor. The network is set to match the impedances of the power source (R_{Source}) to the total impedance of the coupling coil and the reflected primary coil. The other impedance matching network is in the receiver circuit. This impedance matching circuit is either a normal L-section or a reverse L-section circuit, depending on the condition of the values of the rectifier impedance and the receiver coil impedance. If the receiver coil impedance is higher than the rectifier impedance,

the normal L-section circuit is used; otherwise, the reverse L-section circuit is used. To maximise the power delivered to load (PDL), the network is set to match the impedance of the rectifier in the conduction state to the total impedance of the receiver coil and the reflected primary coil.

The magnetic links are represented by the mutual inductances between coils. Here, M_1 is the mutual inductance between the coupling coil and the primary coil. Its value is chosen to maximise the current at the primary coil, which is discussed in Section 3.1.2. The mutual inductance M_2 is between the primary coil and the receiver coil. Its value is determined by the coupling between the two coils, which is discussed in Section 6.4.1.

To analyse the performance of the full proposed WPT system, the power delivered to the rectifier will be calculated first. Unlike the circuit model in Section 3.3, which treats the magnetic link between the primary coil and the receiver coil as a perfect voltage source at the receiver, the circuit model in this chapter considers the magnetic link as a voltage source with a source impedance, because, in reality, the impedance of the primary coil will also be reflected to the receiver side. With this circuit model, the actual output power of the receiver coil can be analysed.

The second part of the analysis is to calculate the PDL of the full proposed WPT system. Here, the performance of the rectifier will be involved. With consideration of the impedance matching network, the input voltage of the rectifier will be calculated first for a range of rectifier input impedance. The PDL will then be calculated based on the power delivered to the rectifier and the power conversion efficiency of the rectifier at that input voltage.

5.2 The power delivered to the rectifier

5.2.1 Circuit model analysis

To calculate the power delivered to the rectifier, it is necessary to obtain the current at the primary coil. To obtain the current, the steps are as follows.

1. Reflect the impedance of the receiver coil circuit to the primary coil circuit
2. Calculate the equivalent voltage and impedance at the output of the impedance matching network in the coupling coil circuit
3. Reflect the voltage and impedance of the coupling coil circuit to the primary coil circuit
4. Calculate the current at the primary coil circuit

Firstly, the impedance of the receiver coil circuit is reflected to the primary circuit and is noted as $\mathrm{R'_{RX}}$. The circuit diagram thus becomes as Figure 5.2-1. As discussed in Section 3.1.2, the equivalent impedance of the receiver coil circuit is

$$R'_{RX} = \frac{(\omega M_2)^2}{R_{RX} + R'_{Rec}} \tag{5.1}$$

- ω is the angular operational frequency
- $\mathrm{R_{RX}}$ is the AC resistance of the receiver coil
- $\mathrm{R'_{Rec}}$ is the equivalent resistance of the impedance matching network and the rectifier at the receiver coil circuit

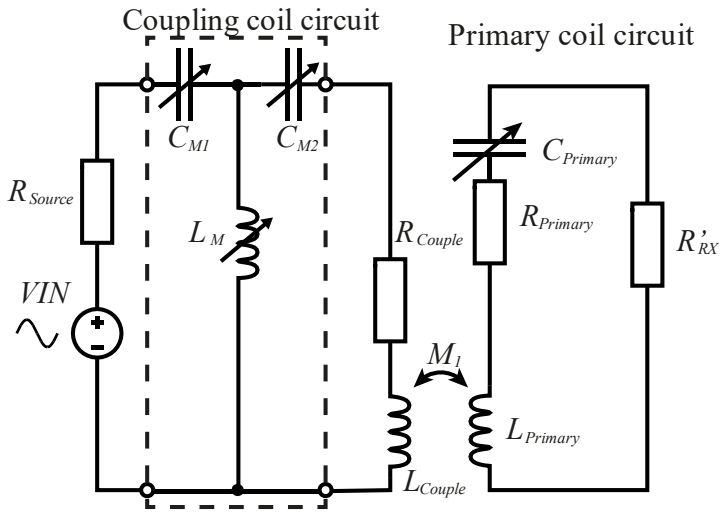

Figure 5.2-1 Equivalent circuit diagram for the proposed WPT system with the receiver circuit reflected to the primary circuit. R'_{RX} is the reflected receiver coil circuit impedance.

Secondly, the equivalent voltage and impedance at the output of the impedance matching network in the coupling coil circuit are calculated. The circuit diagram thus becomes as Figure 5.2-2, where VIN' and R'_{Source} are the equivalent voltage and

impedance. The value of VIN' can be calculated, as shown in the T-section network in Section 2.3.2.2.

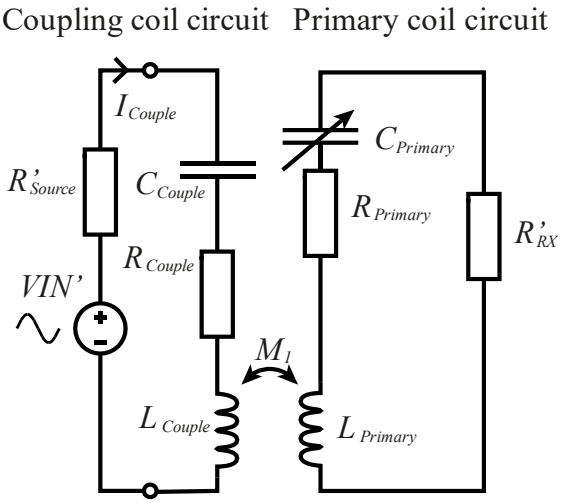

Figure 5.2-2 Equivalent circuit diagram of the proposed WPT system with the magnetic coupling link and the receiver impedance matching circuit represented by an equivalent voltage source VIN' and an equivalent resistor R'_{Source}. R'_{RX} is the receiver equivalent resistance on the primary coil.

The value of R'_{Source} is the complex conjugate of the summation of the impedance of the coupling coil and the impedance of the reflected primary coil circuit. Because the impedance of the coupling coil inductance is cancelled by the impedance of capacitance in the coupling coil circuit, R'_{Source} should be equal to the summation of the AC resistance of the coupling coil and the reflected resistance of the primary coil circuit. As discussed in Section 6.3.2, the reflected resistance of the primary coil circuit is calculated as

$$R'_{Pri\&RX} = \frac{(\omega M_1)^2}{R_{Primary} + R'_{Rec}} = R_{Couple} \tag{5.2}$$

where M_1 is the optimised mutual inductance. As discussed in Section 3.1.2,

$$M_1 = \frac{\sqrt{R_{Couple}\left(R_{Primary} + R'_{RX}\right)}}{\omega} \tag{5.3}$$

Therefore, because of impedance matching, from (2.64) and (5.2),

$$R'_{Source} = R_{Couple} + R'_{Pri\&RX} = 2R_{Couple} \tag{5.4}$$

The circuit diagram in Figure 5.2-2 is similar to the circuit diagram in Figure 3.1-1. Following the calculation in Section 3.1.2, the reflected voltage and impedance of the coupling coil circuit in the primary coil circuit can be calculated.

From (3.18), the maximum current at the primary coil can be obtained, which is

$$I'(Max) = \frac{VIN'}{4\sqrt{R_{Couple}\left(R_{Primary} + R'_{RX}\right)}} \tag{5.5}$$

With the current in the primary coil circuit, the magnetic field strength generated by the primary coil and the induced voltage at the receiver coil can then be generated. The full formula of the magnetic field strength is discussed in Section 6.4.1.

With the induced voltage at the receiver coil, we can then calculate the power delivered to the rectifier. The full receiver circuit diagram is shown in the top of Figure 5.2-3. Because the impedance matching network is set to match the impedance of the rectifier R_{Rec} and R'_{Pri}+R_{RX}, the circuit diagram can be simplified as shown in the bottom of Figure 5.2-3, where the impedance matching network and the rectifier are represented by the resistor $\mathrm{R'_{Rec}}$.

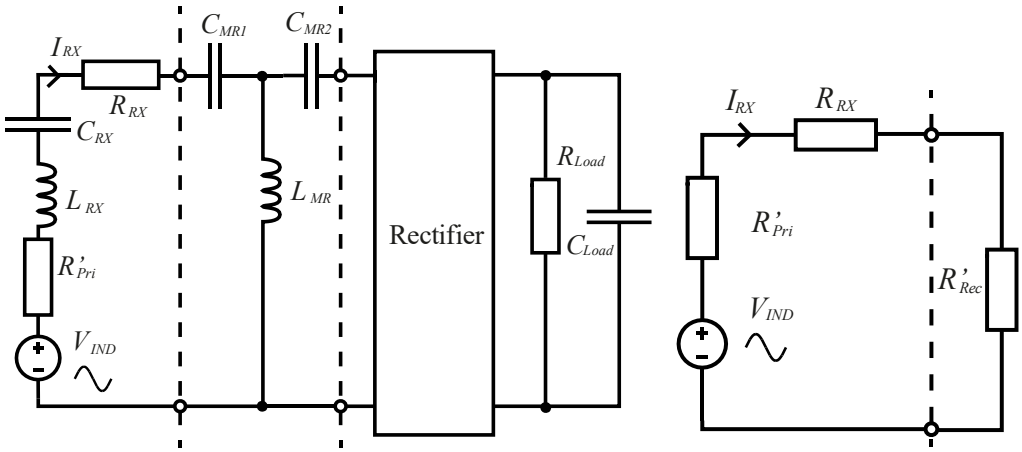

Figure 5.2-3 (Left) full circuit diagram of receiver coil circuit with reflected voltage V_{IND} and impedance R'_{Pri} of primary coil circuit; (right) equivalent circuit diagram with the matched rectifier impedance represented by resistor R'_{Rec}.

Based on the circuit on the right of Figure 5.2-3, from (2.61), the power delivered to the rectifier can thus be calculated as

$$P_{OUT\_RX} = \left(\frac{V_{IND}}{R'_{Pri} + R_{RX} + R'_{Rec}}\right)^2 R'_{Rec} \tag{5.6}$$

- $\mathrm{V_{IND}}$ is the induced voltage at the receiver coil
- $\mathrm{R_{RX}}$ is the receiver coil AC resistance
- $\mathrm{R'_{Rec}}$ is the equivalent resistance of the impedance matching circuit and the rectifier

For impedance matching, $R'_{Rec} = R'_{Pri} + R_{RX}$, and $\mathrm{R'_{Pri}}$ is the reflected resistance of the primary coil in the receiver coil circuit. From (3.4) and (3.5),

$$R'_{Pri} = \frac{(\omega M_2)^2}{R_{Primary} + R'_{Couple}} \tag{5.7}$$

- $\mathrm{R}_{\mathrm{Primary}}$ is the primary coil AC resistance
- M_2 is the mutual inductance between the primary coil and the receiver coil. The value of M_2 is discussed in Section 6.4.1.
- $\mathrm{R}'_{\mathrm{Couple}}$ is the reflected resistance of the coupling coil in the primary coil circuit. From (3.2) and (5.4),

$$R'_{Couple} = \frac{(\omega M_1)^2}{R_{Couple} + R'_{Source}} = \frac{(\omega M_1)^2}{3R_{Couple}} = \frac{1}{3}\left(R_{Primary} + R'_{RX}\right) \quad (5.8)$$

- $\mathrm{R}'_{\mathrm{RX}}$ is the reflected resistance of the receiver coil circuit in the primary coil circuit, as calculated in (5.1)

5.2.2 Calculation result

In this section, calculations are carried out:

- To find out the output impedance of receiver coil
- To find out the maximum induced voltage and RX coil output power
- In different turn numbers and in two different media

To calculate the power delivered to the rectifier, the optimum dimensional parameters of the transmitter and receiver for 20 cm transfer distance and 8 MHz operational frequency are used, which are shown in Table 5.1-1.

Parameter	Gap interval	Coil diameter	Number of turns	Wire diameter	Ferrite permeability		Operational frequency	Transfer distance
Symbol	p (mm)	D (cm)	N	d_{wire} (mm)	μ'_r	μ''_r	f (MHz)	h (cm)
Primary coil	2.54	20.1	6	1	NA	NA	8	20
Receiver coil	0.1	0.2	1-250	0.1	80	5		

Table 5.2-1 Parameters of the full WPT system

The calculations are carried out in two different media, in air and in human tissue. In air, the relative dielectric constant ε_{r_air}=1, and the conductivity σ is 0. In human tissue, as discussed in Section 2.3.4.2, ε_{r_tissue}=160, σ=0.625 S/m.

The calculated induced voltage on RX in the full system in two media is shown in Figure 5.2-4.

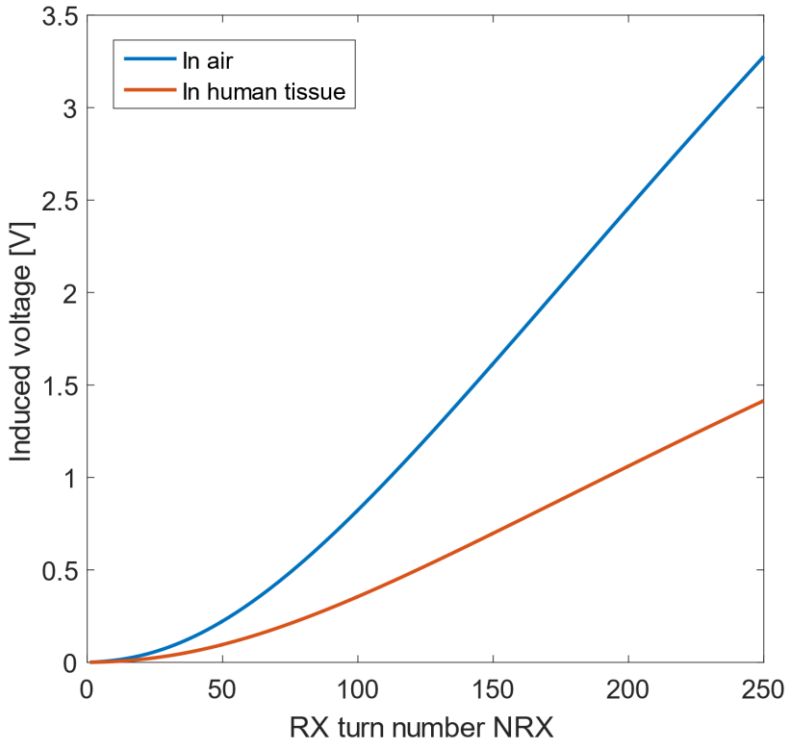

Figure 5.2-4 Induced RMS voltage on RX coil in the full system in air and in human tissue in 20 cm transfer distance with turn number N_{RX} from 1 to 250.

The induced voltage rises exponentially at small turn numbers (from 0 to 50) and linearly at larger turn numbers (from 50 to 250). Compared with the results in Table 3.3-7, it can be seen that the RX induced voltage in air in the full system (in Figure 5.2-4) is the same as the RX induced voltage when the reflected impedance from primary coil to receiver coil R'_{Pri} is not considered (in Table 3.3-7). The reason for this is because R'_{Pri} is negligible compared with the self-resistance of the RX coil, which can be seen in Table 5.2-2. Here, the self-resistance R_{RX} is $R_{ferrite} + R_{AC-Coil}$ as in (3.48).

N_{RX}	R'_{Pri} (Ω)	R_{RX} (Ω)	N_{RX}	R'_{Pri} (Ω)	R_{RX} (Ω)
50	0.09	9.80	200	10.9	385
100	1.23	69.8	250	19.4	606
150	4.74	199			

Table 5.2-2 Comparison of values of reflected impedance from primary coil to receiver coil R'_{Pri} and RX self-resistance R_{RX} in different turn numbers in air

The induced voltage in human tissue is less than half of the induced voltage in air, which is because of the attenuation of magnetic field in the medium. It can be seen that medium attenuation has a serious reduction effect on the performance of WPT system.

To calculate the RX coil output power, the equation (5.6) is referred. Because of impedance matching at the RX circuit, the rectifier equivalent resistance R'_{Rec} is the same as the total resistance of RX coil $R'_{Rec} = R'_{Pri} + R_{RX}$. Because the total resistance of RX coil is different in different turn numbers and in different media, the

rectifier equivalent resistance R'_{Rec} is also different. The values of R'_{Rec} is shown in Table 5.2-3.

N_{RX}	R'_{Rec} (Ω) in air	R'_{Rec} (Ω) in human tissue	N_{RX}	R'_{Rec} (Ω) in air	R'_{Rec} (Ω) in human tissue
50	9.89	9.82	200	395	387
100	71.0	70.0	250	625	610
150	203	200			

Table 5.2-3 Rectifier equivalent resistance R'_{Rec} in different turn numbers in air and in human tissue

It can be seen that the values of R'_{Rec} between air and human tissue has not much difference when turn number N_{RX} is between 50 and 150, and the difference is bigger when N_{RX}= 200 and 250. The reason for this is because the field attenuation in human tissue causes R'_{Pri} to be smaller than the value in air, and the absolute difference between the R'_{Pri} values in human tissue and in air grows bigger when N_{RX} increases. The difference is not obvious at lower N_{RX} is because of the large R_{RX} compared with the small R'_{Pri} value.

With the values of R'_{Pri} in different turn numbers, the output power of RX coil P_{OUT_RX} can be calculated. The result is shown in Table 5.2-4.

N_{RX}	P_{OUT_RX} in air (mW)	P_{OUT_RX} in human tissue (mW)	N_{RX}	P_{OUT_RX} in air (mW)	P_{OUT_RX} in human tissue (mW)
50	1.3	0.23	200	3.8	0.73
100	2.4	0.45	250	4.3	0.82
150	3.2	0.61			

Table 5.2-4 Output power of RX coil P_{OUT_RX} in different turn numbers in air and in human tissue

It can be seen that while the RX coil output power P_{OUT} in air all exceeds 1 mW for N_{RX}>50, in human tissue, P_{OUT_RX} is all lower than 1 mW. In actual application, the value of P_{OUT_RX} will lie between these two values because the calculation parameters chosen for human tissue is of conductive tissues with high water density. If the transfer path contains human tissues with less water density, such as muscle and fat, the value of P_{OUT_RX} will be higher than the results presented for conductive human tissue. However, the results also indicate that, in actual application, the position of implants should be carefully selected so that the power transfer path contains more tissues with low water density to ensure enough received power.

Another thing to notice in the table is that the increase rate of P_{OUT_RX} is lower at higher N_{RX}. In air, from N_{RX}=50 to 250, the increase of P_{OUT_RX} per 50 turns is 1.1 mW (50 to 100), 0.8 mW (100 to 150), 0.6 mW (150 to 200) and 0.5 mW (200 to 250). In human tissue, a similar trend of P_{OUT_RX} also exists. The reason for this is mentioned in Section 3.3.4.3. Because the magnetic field strength from the primary coil gets weaker

as the transfer distance increases, the field strength is weaker at the far end of the RX coil than the field strength at the close end. Moreover, the RX coil resistance will rise when the turn number increases. These two factors cause the increase rate of output power get lower at higher N_{RX}. The lower increase rate of P_{OUT_RX} indicates that the turn number or length of RX coil is not the larger the better. At one turn number, the field strength will become so weak that the increase of RX coil resistance will become the dominant factor, and a further increase of turn number will reduce the output power. From the little increase of P_{OUT_RX} (0.5 mW in air and 0.09 mW in tissue) for N_{RX} from 200 to 250, it can be seen that a further increase of N_{RX} will only result in a less increase on P_{OUT_RX} but will cause a higher risk on the physical robustness of the implant. Therefore, it is not beneficial for the RX coil to exceed the length limit (5 cm).

In the RX coil circuit, because the power consumption of the impedance matching network is negligible, the output power of the RX coil P_{OUT_RX} equals to the power delivered to the rectifier P_{Rec}. In the next section, the power delivered to load (PDL) will be calculated based on P_{Rec} in different turn numbers and in different media to find out under what conditions the PDL will meet the 1 mW power requirement.

5.3 The power delivered to load

Once the power delivered to the rectifier is obtained, the power delivered to load (PDL) can be calculated by multiplying the power delivered to the rectifier with the power conversion efficiency (PCE, i.e. the output efficiency used in Chapter 4) of the rectifier. However, from the discussion in Chapter 4, the PCE of a rectifier is different in different input voltages. Therefore, it is necessary to calculate the input voltage of the rectifier first.

As an impedance matching network is used in the receiver coil circuit, the value of the input voltage of the rectifier will be different with different types of matching networks. For simplicity, two basic types of impedance matching circuits, normal L-section and reverse L-section, will be used as examples. Moreover, the input impedance of the rectifier will also affect the input voltage of the rectifier, which can be seen in the discussion in Section 2.3.2. Because the input impedance of a rectifier is dependent on the rectifier load condition, the rectifier input voltage and PDL in different load resistance will be discussed. Because the rectifier input voltage and input power are different for different RX turn numbers, the PDL will also be discussed for different RX turn numbers.

The analysing steps for the PDL are as follows.

1. Calculate the input voltage of the rectifier in a range of rectifier input impedance
2. Calculate the power delivered to load based on the power delivered to the rectifier and the PCE corresponding to the input voltage

5.3.1 The receiver coil circuit model with the impedance matching circuit

(1) Normal L-section circuit

From the discussion in Section 2.3.2.1, for a normal L-section impedance matching circuit as shown in Figure 5.3-1, the following expressions can be obtained.

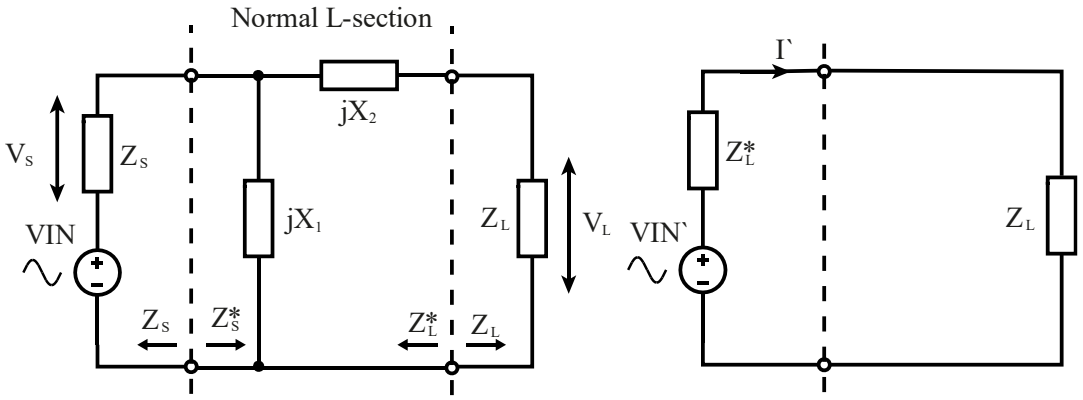

Figure 5.3-1 Normal L-section impedance matching circuit

Assuming that the target input impedance of the rectifier $\mathrm{R_{Rec}}$ is resistive and the summation of $\mathrm{R'_{Pri}}$ and $\mathrm{R_{RX}}$ is higher than the target input impedance of the rectifier $\mathrm{R_{Rec}}$,

$$X_1 = \frac{\pm Z_S}{Q} = \frac{\pm(R'_{Pri} + R_{RX})}{Q} \tag{5.9}$$

$$X_2 = \mp Z_L Q = \mp R_{Rec} Q \tag{5.10}$$

$$Q = \sqrt{\frac{Z_S}{Z_L} - 1} = \sqrt{\frac{R'_{Pri} + R_{RX}}{R_{Rec}} - 1} \tag{5.11}$$

$$VIN' = \frac{jX_1}{jX_1 + (R'_{Pri} + R_{RX})} VIN \tag{5.12}$$

$$V_{Rec} = \frac{1}{2} \frac{jX_1}{jX_1 + (R'_{Pri} + R_{RX})} VIN \tag{5.13}$$

- V_{Rec} is the rectifier input voltage
- $\mathrm{R_{Rec}}$ is the target input impedance of the rectifier for matching

The target input impedance $\mathrm{R_{Rec}}$ of the rectifier for matching is the average input impedance of the rectifier in the conducting state. This value is chosen so that the input impedance of the rectifier can match the output impedance ($\mathrm{R'_{Pri}} + \mathrm{R_{RX}}$) of the receiver coil when the rectifier is conducting. However, the actual input impedance of the rectifier is not a constant, even during the conducting state. Therefore, in reality, a perfect match cannot be guaranteed during the rectifier conducting state. The calculated rectifier input voltage V_{Rec} is thus an approximation of the actual value, which provides a guideline to assess the performance of the WPT system.

(2) Reverse L-section circuit

From the discussion in Section 2.3.2.1, for a reverse L-section impedance matching circuit as shown in Figure 5.3-2, the following expressions can be obtained.

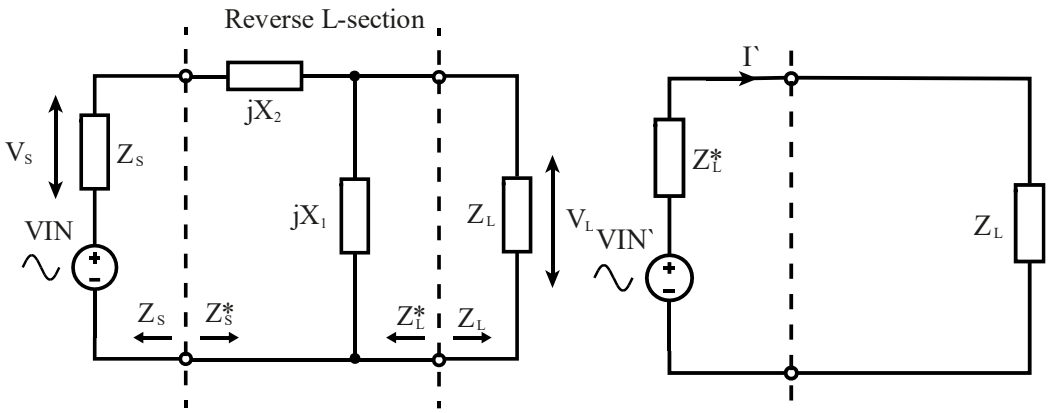

Figure 5.3-2 Reverse L-section impedance matching circuit

Assuming that the target input impedance of the rectifier $\mathrm{R_{Rec}}$ is resistive and the summation of $\mathrm{R'_{Pri}}$ and $\mathrm{R_{RX}}$ is smaller than the target input impedance of the rectifier $\mathrm{R_{Rec}}$,

$$X_1 = \frac{\pm Z_L}{Q} = \frac{\pm R_{Rec}}{Q} \tag{5.14}$$

$$X_2 = \mp Z_S Q = \mp (R'_{Pri} + R_{RX}) Q \tag{5.15}$$

$$Q = \sqrt{\frac{Z_L}{Z_S} - 1} = \sqrt{\frac{R_{Rec}}{R'_{Pri} + R_{RX}} - 1} \tag{5.16}$$

$$VIN' = \frac{jX_1}{jX_1 + jX_2 + (R'_{Pri} + R_{RX})} VIN \tag{5.17}$$

$$V_{Rec} = \frac{1}{2} \frac{jX_1}{jX_1 + jX_2 + (R'_{Pri} + R_{RX})} VIN \tag{5.18}$$

- $\mathrm{V_{Rec}}$ is the rectifier input voltage
- $\mathrm{R_{Rec}}$ is the target input impedance of the rectifier for matching

The relations of $\mathrm{V_{Rec}}$, $\mathrm{R_{Rec}}$ are the same as discussed in the last section.

5.3.2 Power delivered to load (PDL) calculation result

From the above analysis, when $R'_{Pri} + R_{RX} > R_{Rec}$, the normal L-section matching network is used. When $R'_{Pri} + R_{RX} < R_{Rec}$, the reverse L-section matching network is used. Therefore, in different rectifier input resistance, the choice of matching network is different. Moreover, because $R'_{Pri} + R_{RX}$ changes when RX turn number changes, RX turn number also affects the choice of matching network. Therefore, both the RX turn number and the comparison of $R'_{Pri} + R_{RX}$ and $\mathrm{R_{Rec}}$ are needed to consider to calculate the input voltage of rectifier V_{Rec} and also the PDL.

It should be noted that, because the impedance matching network has a negligible power consumption, the input power of the rectifier equals to the RX coil output power, which is only determined by the RX coil turn number. Therefore, for one turn number, the rectifier input power P_{Rec} is constant regardless of the rectifier input resistance R_{Rec}. The rectifier input voltage V_{Rec} is essentially determined by P_{Rec} and R_{Rec}. The resulted V_{Rec} versus R_{Rec} for each N_{RX} is shown in Figure 5.3-3. The corresponding P_{Rec} for each turn number is listed on the right of Figure 5.3-3.

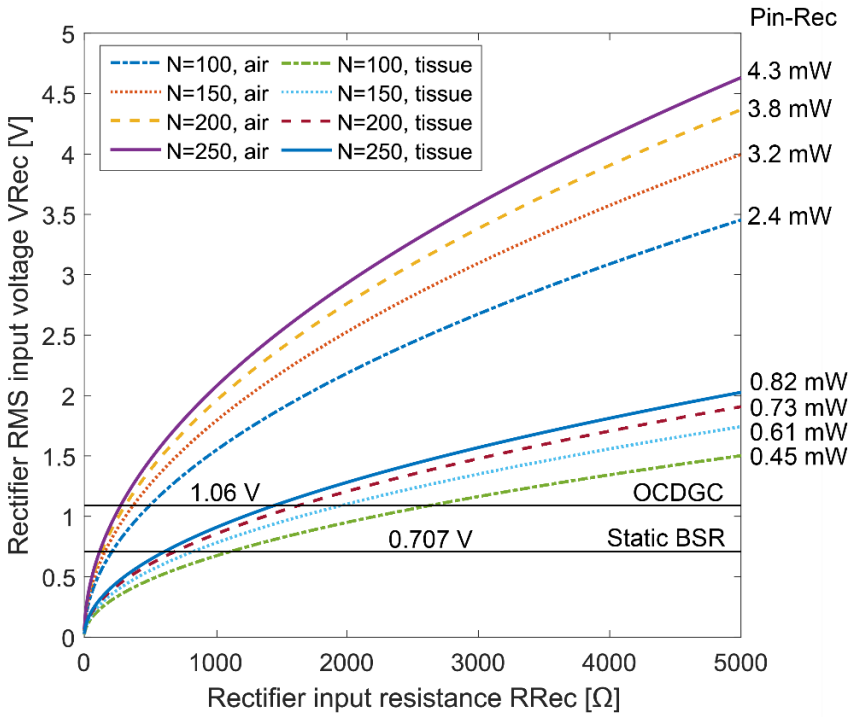

Figure 5.3-3 Rectifier input voltage V_{Rec} versus rectifier input resistance R_{Rec}. Pin-Rec means the input power to the rectifier. The horizontal lines are the minimum working voltages of OCDGC rectifier and static BSR rectifier.

As shown, for a specific turn number, with a constant P_{Rec}, the rectifier input voltage V_{Rec} increases as the rectifier input resistance R_{Rec} increases. With the same input resistance R_{Rec}, a higher turn number N_{RX} (of the presented range 100 to 250) will result in a higher rectifier input voltage V_{Rec}. Due to the presence of conductive human tissue, the rectifier input voltage V_{Rec} is much reduced in tissue because of the lower rectifier input power P_{Rec}. For a high RX turn number, such as N_{RX}=250, V_{Rec} can reach more than 4.5 V in air but only 2 V in human tissue when R_{Rec}=5 kΩ.

In Figure 5.3-3, the two horizontal lines indicate the minimum working voltages for the OCDGC rectifier and the static BSR rectifier developed in Chapter 4. The minimum working voltage means the minimum input RMS voltage with which the rectifier can operate in a high efficiency level. For the OCDGC rectifier, the range of input RMS voltage for high efficiency is from 1.06 V to 3.54 V, which can be seen in Figure 4.4-25. The power conversion efficiency is from 73% to 85% for the light load condition. For the static BSR rectifier, the range is from 0.707 V to 3.54 V, with the power conversion efficiency from 53% to 77% for the light load condition and from 82% to 89% for the heavy load condition, which can be seen in Figure 4.4-3 and Figure 4.4-10.

The crossover between the minimum working voltage V_{Rec_min} line and the V_{Rec}-R_{Rec} curve indicates the required minimum rectifier input resistance R_{Rec_min} for the rectifier to work in the high efficiency range with the full WPT system. The values of R_{Rec_min} for each RX coil turn number are listed in Table 5.3-1.

N_{RX}	100	150	200	250
R_{Rec_min} for OCDGC (Ω)	471 (air) 2489 (tissue)	352 (air) 1851 (tissue)	295 (air) 1544 (tissue)	262 (air) 1369 (tissue)
R_{Rec_min} for static BSR (Ω)	210 (air) 1108 (tissue)	157 (air) 824 (tissue)	132 (air) 687 (tissue)	117 (air) 609 (tissue)

Table 5.3-1 Rectifier input resistance R_{Rec_min} for each N_{RX} to meet the RMS minimum working voltages V_{Rec_min} of the rectifiers. 1.06 V for OCDGC rectifier and 0.707 V for static BSR rectifier.

In the discussion of rectifiers in Chapter 4, the load conditions are divided into light load and heavy load depending on whether the minimum rectifier output voltage will drop to 0 V. This is essentially dependent on both the output resistance value and the output capacitance value. In the analysis of rectifiers, with a 100 pF load capacitance, 500 Ω load resistance is chosen as a representative of the heavy load resistance and 5 kΩ is chosen for the light load. From author's simulation, with 100 pF load capacitance, for R_{Load} <1 kΩ, the output voltage will experience discontinuity (drop to 0 V); for R_{Load} >1 kΩ, the output voltage will be continuous. Because most of the rectifier input power are consumed by the load, it is a safe assumption that the average load resistance is approximately equal to the average rectifier input resistance in this analysis. Therefore, for the present rectifiers and load capacitance, it can be safely assumed that for R_{Rec} <1 kΩ, the rectifiers are at heavy load condition; for R_{Rec} >1 kΩ, the rectifiers are at light load condition.

From Table 5.3-1, the values of R_{Rec_min} in air for OCDGC rectifier are all lower than 1 kΩ. Because OCDGC rectifier is mainly used in the light load condition, its input resistance R_{Rec} will be higher than 1 kΩ, which means the RMS input voltage V_{Rec} of OCDGC rectifier will be higher than V_{Rec_min}=1.06 V during operation in air. Therefore, it can be concluded that, in air, OCDGC rectifier will be able to work in the high efficiency range with the proposed WPT system. For power transfer through conductive human tissue, however, because the values of R_{Rec_min} are all more than 1 kΩ, the rectifier input resistance R_{Rec} have to be more than the corresponding R_{Rec_min} if OCDGC rectifier were to operate in the high efficiency range. For example, for N_{RX} =250, R_{Rec} >1369 Ω should be satisfied if V_{Rec} needs to higher than V_{Rec_min}=1.06 V for OCDGC rectifier to work in the high efficiency range.

A similar analysis can be applied to the static BSR rectifier in the light load condition, which can also lead to the conclusion that static BSR rectifier will be able to work in the high efficiency range with the proposed WPT system in air in the light load condition, but its R_{Rec} should be higher than the corresponding R_{Rec_min} in conductive human tissue. For the static BSR rectifier in the heavy load, because its R_{Rec} is less than 1 kΩ, the rectifier will be able to operate in the high efficiency range when R_{Rec_min}<R_{Rec}<1 kΩ.

By combining the rectifier input power P_{Rec}, the rectifier power conversion efficiency η_{Rec} and the relation between rectifier input voltage V_{Rec} and rectifier input resistance R_{Rec}, the PDL of the proposed WPT system can be calculated and is presented in Table 5.3-2.

N_{RX}	Rectifier	P_{Rec} (mW) air	R_{Rec} (kΩ) air	PDL (mW) air	P_{Rec} (mW) tissue	R_{Rec} (kΩ) tissue	PDL (mW) tissue
100	OCDGC	2.4	>1	1.75 to 2.04	0.45	>2.49	0.33 to 0.38
	Static BSR		>1	1.27 to 1.84		>1.1	0.24 to 0.35
			0.21 to 1	1.97 to 2.14		NA	NA
150	OCDGC	3.2	>1	2.34 to 2.72	0.61	>1.85	0.45 to 0.52
	Static BSR		>1	1.70 to 2.46		>1	0.32 to 0.47
			0.16 to 1	2.62 to 2.85		0.82 to 1	0.50 to 0.54
200	OCDGC	3.8	>1	2.77 to 3.23	0.73	>1.54	0.53 to 0.62
	Static BSR		>1	2.01 to 2.93		>1	0.39 to 0.56
			0.13 to 1	3.12 to 3.38		0.69 to 1	0.60 to 0.65
250	OCDGC	4.3	>1	3.14 to 3.66	0.82	>1.37	0.60 to 0.70
	Static BSR		>1	2.28 to 3.31		>1	0.43 to 0.63
			0.12 to 1	3.53 to 3.83		0.61 to 1	0.67 to 0.73

Table 5.3-2 Predicted PDL for different N_{RX}, different rectifier and in two different media with the input resistance R_{Rec} range. For each N_{RX}, the first row is for OCDGC in light load condition; the second row for static BSR in light load condition; the third row for static BSR in heavy load condition. The efficiency of the rectifier is as shown in Figure 4.4-3, Figure 4.4-10 and Figure 4.4-25.

From Table 5.3-2, it can be seen that for power transfer in air, the PDLs are able to meet the 1 mW requirement for N_{RX} ranging from 100 to 250 with either of the rectifier in either load condition. The proposed rectifiers are able to work in the high efficiency range in the full R_{Rec} range (>1 kΩ) of light load condition, and in most of the R_{Rec} range (from 0.12-1 kΩ to 0.21-1 kΩ) of heavy load condition. The efficiency requirement of rectifier is loose. For N_{RX}=100, the PDL can be 1 mW even when η_{Rec} is as low as 42%. However, for power transfer in conductive human tissue, due to the attenuation effect, the PDLs are all lower than 1 mW. The R_{Rec} range for the operation of rectifiers are also much reduced because of less input power P_{Rec}. For light load condition, the R_{Rec} range for OCDGC is from >1.37 kΩ to >2.49 kΩ. For the heavy load condition, the R_{Rec} range for static BSR is from 0.61-1 kΩ to 0.82-1 kΩ. The highest PDL in conductive human tissue is 0.73 mW with N_{RX}=250 and static BSR in the heavy load condition, which is still lower than the lowest PDL in air (1.27 mW). For N_{RX}=100 with tissue, the static BSR cannot work in the heavy load condition because R_{Rec_min}>1 kΩ, which means that, in the heavy load condition, the highest input voltage V_{Rec} is lower than the minimum required voltage V_{Rec_min} of static BSR. The result shows that the transfer media is extremely vital to the performance of the WPT system. With proper selection of transfer media, the rectifier power budget can be

much increased, the WPT system will be able to work with a wider load range, and the rectifier will be able to work with a higher efficiency.

In conclusion, for power transfer through air, with a 2 mm ferrite-core solenoid RX coil, the proposed WPT system will be able to achieve a PDL of more than 1 mW with N_{RX} from 100 to 250 and with the proposed rectifiers at a 20-cm transfer distance. However, with the same set-up, in conductive human tissue, the highest achieved PDL is less than 1 mW, which is mainly due to the magnetic field attenuation in media. A further increase of N_{RX} will not help to improve the situation because the increase of power will be very limited as is discussed in Section 5.2.2. The most efficient way to increase PDL is by proper selection of power transfer path, so that the path contains less conductive tissues. By increasing the proportion of non-conductive tissues in the path, the PDL of the system will approach the values obtained in air and meet the 1 mW power requirement.

5.4 Summary of this chapter

In this chapter, the full proposed magnetic coupling resonance WPT system is presented and analysed with a target transfer distance of 20 cm and an operational frequency of 8 MHz.

Overall, it can be concluded that, with a proper selection of transfer media, with a 2-mm ferrite-core solenoid RX coil, the proposed WPT system will be able to achieve a PDL of more than 1 mW with the proposed rectifiers at a 20-cm transfer distance.

In this chapter, a circuit model has been built for the full system with the application of impedance matching networks. The matching networks are set to maximise the magnetic field strength generated by the primary coil and to maximise the power delivered to the rectifier.

The power link between the primary coil and the receiver coil has been treated as a practical power source in the receiver, which is represented by a voltage source V_{IND} and a source impedance R'_{Pri}.

The changes of V_{IND} and R'_{Pri} have been analysed with a range of RX turn number N_{RX}. Calculation result shows that the induced voltage rises exponentially at small turn numbers (from 0 to 50) and linearly at larger turn numbers (from 50 to 250). The induced voltage V_{IND} in air is the same as the results obtained in Section 3.3.4.3. However, V_{IND} in conductive human tissue is less than half of the value in air under the same N_{RX}, which is because of the field attenuation in tissue.

With the induced voltage V_{IND} and the reflected impedance R'_{Pri} obtained, the input power of the rectifier P_{Rec} can be calculated. Because of the impedance matching circuit at the RX circuit, the equivalent rectifier resistance R'_{Rec} is the same to $R'_{Pri} + R_{RX}$. Analysis of P_{Rec} shows that, for power transfer in air, P_{Rec} is sufficient to meet the 1 mW power requirement; for power transfer in conductive human tissue, P_{Rec} is less than 1 mW. Moreover, the increase of N_{RX} is inefficient to increase P_{Rec} at a high N_{RX} value because of the weaker field strength at the extra coil turns.

After the rectifier input power P_{Rec} is obtained for different N_{RX}, with the analysis of impedance matching network, the rectifier input voltage V_{Rec} versus rectifier input resistance R_{Rec} for different N_{RX} is obtained. The values of V_{Rec}, together with the working input voltages V_{Rec_min} of the rectifiers developed in Chapter 4, determines the required input resistance R_{Rec_min} for the rectifiers to work in a high efficiency range with the proposed WPT system. Results show that, for power transfer in air, the proposed rectifiers are able to work in the high efficiency range in the full R_{Rec} range of light load condition, and in most of the R_{Rec} range of heavy load condition. However,

for power transfer in conductive human tissue, the R_{Rec} range for the operation of rectifiers are much reduced because of less input power P_{Rec}. As a result, the PDL for power transfer in air is able to meet the 1 mW power requirement, while the PDL in conductive human tissue is less than the power requirement. The result shows that the transfer media is extremely vital to the performance of the WPT system.

Chapter 6 Wireless signal transfer in the wireless power transfer system

6.1 Introduction

Besides delivering electrical energy to the micro-implants, another aim of the proposed wireless power transfer system is to transmit data from the micro-implant during the power transfer using the same sets of coils. For the IMPACT project, the data rate can be as low as 1 byte/second. The data transfer will not have a significant effect on power delivery because the frequency for power delivery is up to 8 MHz.

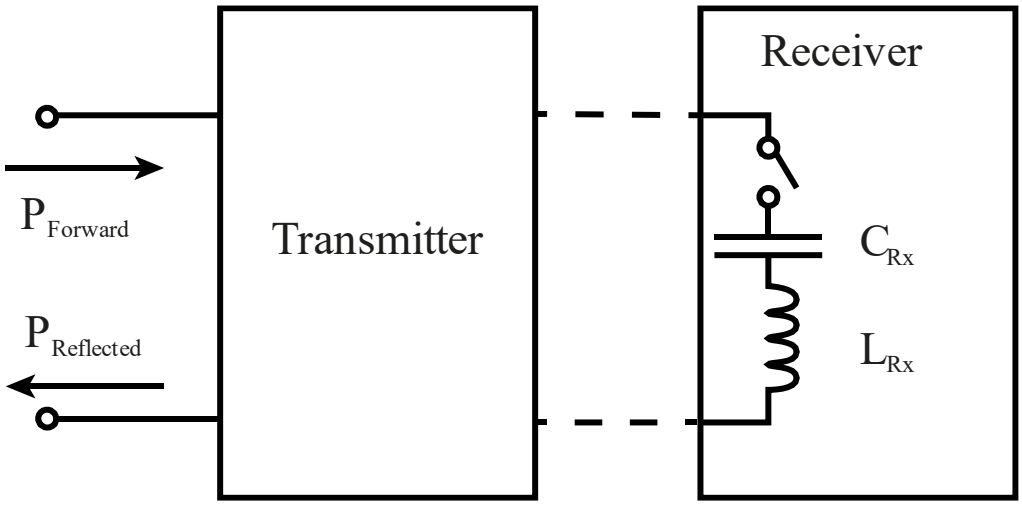

Figure 6.1-1 Illustrative block diagram for the wireless signal transfer scheme

The proposed wireless signal transfer scheme uses a method similar to the one used to measure S-parameters with a network analyser. As shown in Figure 6.1-1, during the wireless power transfer, there will be forward power from the power source and reflected power from the wireless power system. With these two powers, the reflection coefficient can be obtained, which is the S-parameter S_{11}. The power receiver is a tuned series L-C circuit feeding the rectifier circuit. If the rectifier is turned off and on by the data stream, this can be detected by monitoring the reflection coefficient (S_{11}) of the transmitter coil. If the data from the micro-implant can be digitised and used to turn the power receiver rectifier on and off using a suitable coding scheme, this data can be recovered by measuring or demodulating S_{11} at the transmitter power source.

The study of wireless data transfer will focus on determining the feasibility of data transfer using the proposed wireless power transfer system with a transfer distance up to 20 cm. In other words, this chapter is trying to prove, at least theoretically, that a detectable change in S_{11} will occur at the transmitter side over a transfer distance as much as 20 cm. This is equivalent to assess the data transfer sensitivity of the system at the transfer distance.

In Section 6.2, the background to S-parameters and the operation of network analysers will be introduced. Models will be built in Section 6.3 for wireless power transfer in two situations: with impedance matching and without impedance matching at the coupling coil circuit. The models will be analysed in Section 6.4 with the optimised parameters of power transmitter coils and power receiver coils in a range of transfer distance.

6.2 Basics for S-parameters

Key aims of this section

- The definitions of one-port and two-port networks are introduced
- The reflection coefficient S_{11} of a network is introduced, and its relationship with the network dissipated power is discussed
- The operation of a network analyser is briefly introduced

Any circuit can be represented as a "black-box", and its properties can be described in terms of the signals at its terminals [186]. Depending on the presence of inputs and outputs, a system or a circuit can be seen as a one-port network or a two-port network, as shown in Figure 6.2-1. For example, the whole wireless power transfer system including the power transmitter circuit and the power receiver can be seen as a one-port network, while the transmitter circuit alone (including the coupling coil circuit and the primary coil circuit) can be seen as a two-port network because it has an output terminal.

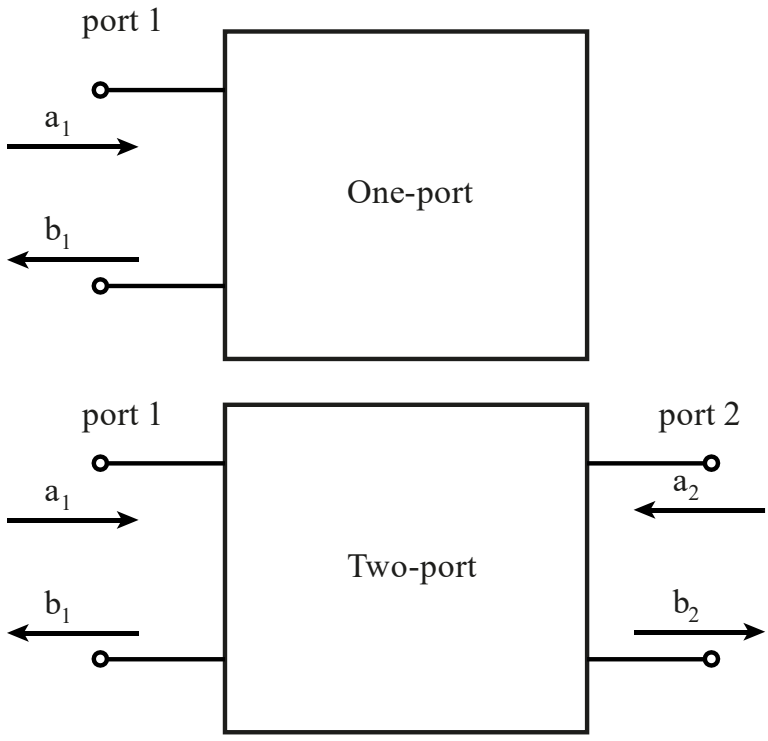

Figure 6.2-1 Block diagram for a one-port network and a two-port network;a_1 and b_1 are the incident wave and the reflected wave of port 1; a_2 and b_2 are the incident wave and the reflected wave of port 2 [186]

For an electric circuit, the analysis of the performance of the circuit depends on the measurement of voltage and current at the terminal of the circuit. In a high-frequency system, such as the proposed wireless power transfer system, its performance can be analysed by the measurement of its forward wave and reflected wave. As shown in Figure 6.2-2, a_1 is the forward wave, and b_1 is the reflected wave.

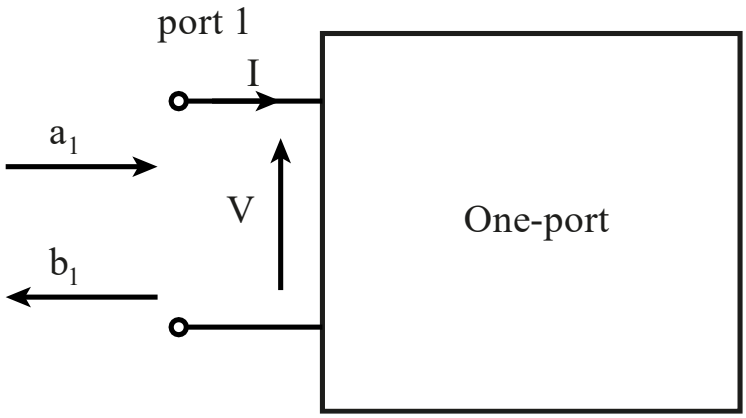

Figure 6.2-2 Block diagram of a one-port network with terminal voltage V and current I, a_1 is the forward wave and b_1 is the reflected wave [186]

The forward wave and the reflected wave can be calculated as [186]

$$a_1 = \frac{1}{2}\left(\frac{V}{\sqrt{R_0}} + \sqrt{R_0}I\right) \tag{6.1}$$

$$b_1 = \frac{1}{2}\left(\frac{V}{\sqrt{R_0}} - \sqrt{R_0}I\right) \tag{6.2}$$

where R_0 is the reference impedance of the network.

From (6.1) and (6.2), the terminal voltage and current can be calculated as

$$V = \sqrt{R_0}(a_1 + b_1) \tag{6.3}$$

$$I = \frac{1}{\sqrt{R_0}}(a_1 - b_1) \tag{6.4}$$

The power dissipated in the one-port network can be calculated as [186]

$$P = \frac{1}{2}RE(VI^*) \tag{6.5}$$

By combining (6.3), (6.4) and (6.5), it can be obtained that

$$P = \frac{1}{2}|a_1|^2 - \frac{1}{2}|b_1|^2 \tag{6.6}$$

The term $\frac{1}{2}|a_1|^2$ can be interpreted as the power of forward wave, the incident power.

The term $\frac{1}{2}|b_1|^2$ can be interpreted as the power of reflected wave, the reflected power.

The difference of them is thus the power dissipated in the one-port network.

Because the S-parameter S_{11} can be calculated as [186]

$$S_{11} = \frac{b_1}{a_1} \tag{6.7}$$

From (6.6) and (6.7), the power dissipated in the one-port network can thus be calculated as

$$P = \frac{1 - |S_{11}|^2}{2} |a_1|^2 \tag{6.8}$$

The value of S_{11} can be measured by a network analyser. A block diagram of a network analyser is shown in Figure 6.2-3. As shown, the ports of the two-port Device Under Test (DUT) is connected to the Test ports of the network analyser. If the DUT is a one-port device, only the left Test port is connected. The network analyser feeds signal to the DUT with the voltage sources VIN-A and VIN-B. To obtain the reflection coefficient S_{11}, the Reference Channel is connected to port a_1 at the dual directional coupler to measure the incident wave from the voltage source VIN-A, and the Test Channel is connected to the port b_1 to measure the reflected wave from the DUT. S_{11} is then calculated using the formula (6.7).

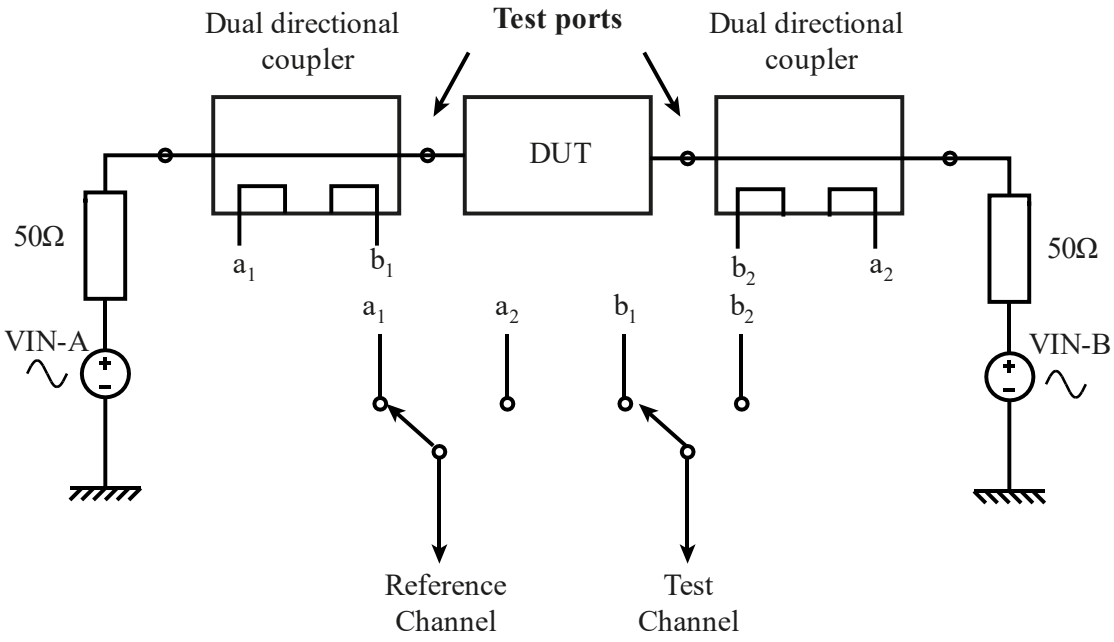

Figure 6.2-3 Block diagram for the network analyser

Using a network analyser (or a test set similar to a network analyser) to measure the reflection coefficient S_{11}, the changes in the power receiver coil load impedance can theoretically be detected as the power dissipated in the whole system changes. A theoretical model will be built in Section 6.3 to explain the concept in detail.

6.3 Models for wireless signal transfer

Key aims of the section

- To minimise the power consumption for data transfer, a single-link LSK modulation scheme (introduced in Section 1.2.2.1) is a preferable option.
- Two circuit models are developed based on the full WPT system. The aim of the model analysis is to find out the relation between the change of S_{11} at the power source and the change of impedance in the power receiver.
- The first model is for the case with no impedance matching network between the coupling coil and the power source. The second model is for the case with an impedance matching network between the coupling coil and the power source.

6.3.1 The circuit model with no impedance matching network between the coupling coil and the power source

To find out the effect of changes in the power receiver on the S_{11} at the voltage source, the circuit model in Figure 5.1-2 is simplified and becomes as shown in Figure 6.3-1.

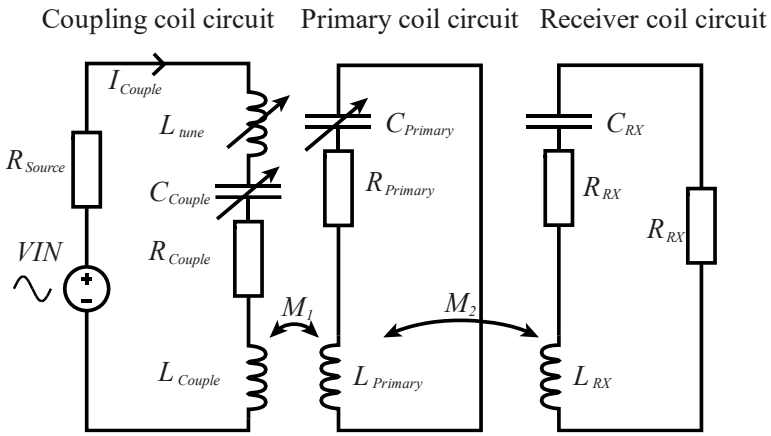

Symbol	Name	Symbol	Name
R_{Source}	The output impedance of the voltage source	L_{Couple}	The self-inductance of the coupling coil
L_{tune}	The tuning inductor at the primary coil circuit	$L_{Primary}$	The self-inductance of the primary coil
C_{Couple}	The tuning capacitor at the primary coil circuit	$C_{Primary}$	The tuning capacitor at the primary coil circuit
R_{Couple}	The AC resistance of the coupling coil	M_1	The mutual inductance between the coupling coil and the primary coil
$R_{Primary}$	The AC resistance of the primary coil	M_2	The mutual inductance between the primary coil and the receiver coil
L_{Rx}	The self-inductance of the receiver coil	C_{Rx}	The capacitance at the receiver coil circuit for resonance
R_{Rx}	The AC resistance of the receiver coil	VIN	The voltage source

Figure 6.3-1 Circuit diagram of the wireless power transfer system including the coupling coil circuit, the primary coil circuit and the power receiver coil circuit

Because of the impedance matching network at the power receiver, the power receiver coil circuit can be simplified by replacing the rectifier and the load with the complex conjugate of the power receiver coil impedance. Because the power receiver coil inductance L_{RX} and capacitance C_{RX} are resonating, the power receiver coil impedance becomes the AC resistance R_{RX} of the power receiver coil. For simplicity, the equivalent resistance of the rectifier and load becomes the same as R_{RX}. It should be noted that the impedance matching network at the power receiver coil circuit is designed to match the impedance of the rectifier and load when the rectifier is in the on-state. Therefore, when the rectifier is in the off-state, the impedance of the rectifier and load will become infinite, which will increase the output impedance of the power receiver coil greatly and detune the power receiver coil. Therefore, the received power of the power receiver will be much less than power in the on-state.

The mutual inductance between the primary coil and the power receiver coil is M_2. The mutual inductance between the coupling coil and the power receiver coil is negligible due to the long distance between the coupling coil and the power receiver coil as well as the difference in the number of turns between the coupling coil and the primary coil.

In order to find the effect of change in the power receiver load impedance R_{Rx} on the voltage source VIN, the primary coil circuit and the power receiver coil circuit need to be combined with the coupling coil circuit.

To simplify the analysis, the bidirectional reflectance impedance analysis is used, which has been discussed in Section 3.1.2. Here, the power receiver coil impedance is reflected to the primary coil circuit first, as shown in the left of Figure 6.3-2. A similar step is taken to reflect the impedance of the primary coil to the coupling coil circuit, which leads to the circuit in the right of Figure 6.3-2

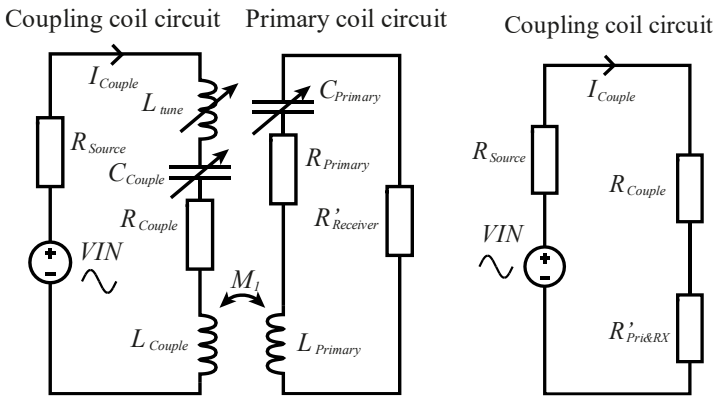

Figure 6.3-2 (Left) equivalent circuit of the wireless power transfer system with the impedance of the power receiver coil circuit reflected to the primary coil circuit; (right) equivalent circuit of the wireless power transfer system with the impedance of the primary coil circuit reflected to the coupling coil circuit

According to [193] and [194], the equivalent power receiver impedance is noted as $R'_{Receiver}$,

$$R'_{Receiver} = \frac{(\omega M_2)^2}{2R_{RX}} \tag{6.9}$$

- R_{RX} is the power receiver coil AC resistance
- ω is the angular operational frequency
- M_2 is the mutual inductance between the primary coil and the power receiver coil

Because the primary coil inductance $L_{Primary}$ and capacitance $C_{Primary}$ are in resonance, the impedance of the primary coil equals to its AC resistance $R_{Primary}$. According to [193] and [194], the reflected impedance of the primary coil in the coupling coil circuit is $R'_{Pri\&RX}$,

$$R'_{Pri\&RX} = \frac{(\omega M_1)^2}{R_{Primary} + R'_{Receiver}} \tag{6.10}$$

M_1 is the optimum mutual impedance between the coupling coil and the primary coil. From (3.7) as discussed in Section 3.1.2,

$$M_1 = \frac{\sqrt{(R_{Source} + R_{Couple})(R_{Primary} + R'_{Receiver})}}{\omega} \tag{6.11}$$

By combining (6.10) and (6.11), $R'_{Pri\&RX}$ becomes

$$R'_{Pri\&RX} = \frac{(\omega M_1)^2}{R_{Primary} + \frac{(\omega M_2)^2}{2R_{RX}}} = R_{Source} + R_{Couple} \tag{6.12}$$

The output power of the voltage source (also the total dissipated power in the wireless power transfer system) can thus be calculated. From (6.12), when the power receiver rectifier is in the on-state, based on the circuit on the right of Figure 6.3-2, the total dissipated power P_1 can be calculate as,

$$P_1 = \frac{VIN^2}{R_{Source} + R_{Couple} + R'_{Pri\&RX}} = \frac{VIN^2}{2(R_{Source} + R_{Couple})} \tag{6.13}$$

When the power receiver rectifier is in the off-state, the power receiver is detuned and the impedance of the power receiver becomes much higher, the equivalent impedance $R'_{Receiver}$ is thus negligible. From (6.12),

$$R'_{Pri\&RX} = R'_{Pri} = \frac{(\omega M_1)^2}{R_{Primary}} \tag{6.14}$$

Similar to (6.13), the total dissipated power P_2 thus can be calculated as,

$$P_2 = \frac{VIN^2}{R_{Source} + R_{Couple} + R'_{Pri}} = \frac{VIN^2}{R_{Source} + R_{Couple} + \frac{(\omega M_1)^2}{R_{Primary}}} \quad (6.15)$$

From (6.13) and (6.15), the ratio of P_2 over P_1 can thus be calculated as,

$$G_1 = \frac{P_2}{P_1} = \frac{1}{1 + \frac{R'_{Receiver}}{2R_{Primary}}} \quad (6.16)$$

From (6.6), the dissipated power is related to the reflection coefficient,

$$P_1 = \frac{1 - |S_{11}|_1^2}{2} |a_1|^2 \quad (6.17)$$

$$P_2 = \frac{1 - |S_{11}|_2^2}{2} |a_1|^2 \quad (6.18)$$

By combining (6.16) (6.17) and (6.18), the ratio of the off-state-receiver reflection coefficient $|S_{11}|_1$ and the on-state-receiver reflection coefficient $|S_{11}|_2$ can thus be calculated as,

$$\frac{|S_{11}|_2}{|S_{11}|_1} = \sqrt{\frac{1 - G_1}{|S_{11}|_1^2} + G_1} \quad (6.19)$$

or in the log form,

$$20log\left(\frac{|S_{11}|_2}{|S_{11}|_1}\right) = 10log\left(\frac{1 - G_1}{|S_{11}|_1^2} + G_1\right) \quad (6.20)$$

The difference in the reflection coefficient $|S_{11}|$ caused by the change of the power receiver impedance can thus be calculated when the coupling coil has no impedance matching circuit.

6.3.2 The circuit model with an impedance matching circuit at the coupling coil

When the coupling coil circuit has an impedance matching circuit such as the one in the upper graph of Figure 6.3-3, the model must be modified.

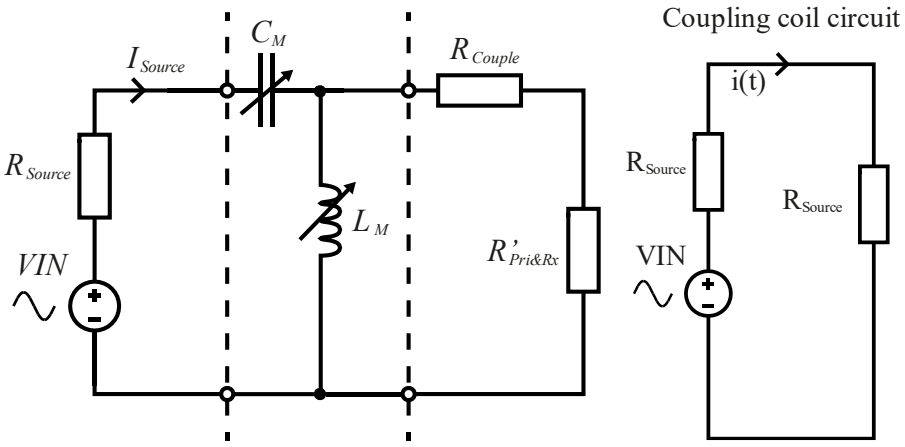

Figure 6.3-3 Equivalent circuits of the wireless power transfer system with an L-section impedance matching circuit; (left) the impedance of the primary coil circuit reflected to the coupling coil circuit; (right) the impedance at the output terminal of the impedance matching circuit converted to its input terminal

Here in Figure 6.3-3, the primary coil and the power receiver coil have already been reflected to the coupling coil. However, the equivalent impedance $R'_{Pri\&RX}$ of the primary coil at the coupling coil is different from the one mentioned in Section 6.3.1.

From (3.17) as discussed in Section 3.1.2, the optimum mutual inductance M_1 is

$$M_1 = \frac{\sqrt{R_{Couple}\left(R_{Primary} + R'_{Receiver}\right)}}{\omega} \tag{6.21}$$

According to [193] and [194], the equivalent impedance $R'_{Pri\&RX}$ is calculated as

$$R'_{Pri\&RX} = \frac{(\omega M_1)^2}{R_{Primary} + R'_{Receiver}} \tag{6.22}$$

By combining (6.9) (6.19) and (6.20), $R'_{Pri\&RX}$ can be calculated as

$$R'_{Pri\&RX} = \frac{(\omega M_1)^2}{R_{Primary} + \frac{(\omega M_2)^2}{2R_{RX}}} = R_{Couple} \tag{6.23}$$

From (6.26) and (2.64), the total impedance on the output terminal of the impedance matching circuit is

$$R_{Couple} + R'_{Pri\&RX} = 2R_{Couple} \tag{6.24}$$

When the power receiver rectifier is in the on-state, the input impedance of the impedance matching network at the coupling coil matches the output impedance of the network, the equivalent impedance of the matching network and the output impedance of the network is equal to the input impedance of the network, which is the source impedance R_{Source}.

Based on the circuit on the right of Figure 6.3-3, the output power of the voltage source P_1 (also the total dissipated power of the wireless power transfer system) for the on-state power receiver rectifier can thus be calculated as,

$$P_1 = \frac{VIN^2}{2R_{Source}} \tag{6.25}$$

From (2.90), in a reverse L-section matching network, R_{Couple} and R_{Source} have the following relation

$$Q = \sqrt{\frac{R_{Couple} + R'_{Pri\&RX}}{R_{Source}} - 1} \tag{6.26}$$

where Q is the quality factor of the impedance matching network at the coupling coil.

By combining (6.23) (6.25) and (6.26), P_1 can thus be calculated as

$$P_1 = \frac{VIN^2}{4R_{Couple}}(1 + Q^2) \tag{6.27}$$

When the power receiver rectifier is in the off-state, with (6.14) and (6.26), the total dissipated power P_2 can be calculated as,

$$P_2 = \frac{VIN^2}{R_{Source} + \frac{R_{Couple} + \frac{(\omega M_1)^2}{R_{Primary}}}{1 + Q^2}} = \frac{VIN^2(1 + Q^2)}{3R_{Couple} + \frac{(\omega M_1)^2}{R_{Primary}}} \tag{6.28}$$

From (6.27) and (6.28), the ratio of P_2 over P_1 can thus be calculate as,

$$G_2 = \frac{P_2}{P_1} = \frac{1}{1 + \frac{R'_{Receiver}}{4R_{Primary}}} \tag{6.29}$$

where $R`_{Receiver}$ is the impedance of power receiver reflected to the primary coil and can be calculated from (6.9).

Because when the power receiver rectifier is in the on-state, the source impedance R_{Source} is fully matched by the impedance matching network, the reflection coefficient $|S_{11}|_1$ is zero. Therefore, from (6.6), the total dissipated power P_1 is the incident power,

$$P_1 = \frac{1}{2}|a_1|^2 \ (|S_{11}|_1 = 0) \tag{6.30}$$

When the power receiver rectifier is in the off-state, the total dissipated power P_2 is equal to,

$$P_2 = \frac{1 - |S_{11}|_2^2}{2} |a_1|^2 \tag{6.31}$$

Therefore, by combining (6.30) and (6.31), the off-state reflection coefficient $|S_{11}|_2$ can be calculated as,

$$|S_{11}|_2 = \sqrt{1 - G_2} \tag{6.32}$$

or the log form,

$$20log(|S_{11}|_2) = 10log(1 - G_2) \tag{6.33}$$

Therefore, with the impedance matching network at the coupling circuit, the off-state reflection coefficient $|S_{11}|_2$ is dependent only on the ratio of the equivalent power receiver coil impedance at the primary coil $R'_{Receiver}$ and the primary coil AC resistance $R_{Primary}$.

In summary, it is shown that the changes in the power receiver impedance can be detected by the change of reflection coefficient at the source of the wireless power transfer system. If there is no impedance matching network at the coupling coil circuit, the changes in the power receiver impedance are reflected at the change of $|S_{11}|$, where

$$20log\left(\frac{|S_{11}|_2}{|S_{11}|_1}\right) = 10log\left(\frac{1 - G_1}{|S_{11}|_1^2} + G_1\right) \tag{6.20}$$

where G_1 is the ratio of dissipated power in the case of no impedance matching at the coupling coil,

$$G_1 = \frac{P_2}{P_1} = \frac{1}{1 + \frac{R'_{Receiver}}{2R_{Primary}}} \tag{6.16}$$

If there is an impedance matching network at the coupling coil circuit, the changes in the power receiver impedance is directly linked to $|S_{11}|$, where

$$20log(|S_{11}|_2) = 10log(1 - G_2) \tag{6.33}$$

where G_2 is the ratio of dissipated power in the case when the coupling coil circuit has impedance matching,

$$G_2 = \frac{P_2}{P_1} = \frac{1}{1 + \frac{R'_{Receiver}}{4R_{Primary}}} \tag{6.29}$$

The ratio G_2 is less than the ratio G_1 for the same value of $R'_{Receiver}$ and $R_{Primary}$. More detailed analysis of the wireless signal transfer models will be given in Section 6.4.

6.4 Analysis of wireless signal transfer model

Key aims of this section

- The parameters used in the calculation of the models will be introduced.
- The $|S_{11}|$ ratio will be the figure of merit (FOM) to analyse the performance of the no-impedance-matching case, and the magnitude of off-state $|S_{11}|$ will be the FOM of the performance of the with-impedance-matching case.
- The FOMs will be analysed in a range of transfer distance (0 m to 20 cm), in two media (conductive human-tissue and air) and with two representative numbers of power receiver turns (100 and 200).
- The $|S_{11}|$ ratio will also be analysed in different on-state $|S_{11}|s$.

6.4.1 Model parameters

As discussed in Section 6.3, to find out the $|S_{11}|$ (with impedance matching in the coupling coil circuit) or the ratio of $|S_{11}|s$ (with no impedance matching in the coupling coil circuit) due to the impedance change in the power receiver, it is necessary to obtain the value of primary coil AC resistance $R_{Primary}$ and the value of the equivalent resistance of the power receiver coil at the primary coil $R'_{Receiver}$. As discussed in Section 2.3.3.4, the primary coil AC resistance $R_{Primary}$ and the AC resistance of the power receiver coil R_{RX} can be calculated given the dimensional parameters of the primary coil. The value of power receiver coil equivalent resistance $R'_{Receiver}$, however, is also dependent on the mutual inductance between the primary coil and the power receiver coil.

According to Electromagnetic Theory [199], as current flows through a coil, a magnetic flux is generated. When another coil is nearby, the magnetic flux generated by the first coil through the effective area of the second coil. The ratio of the amount of magnetic flux through the second coil to the current flowing through the first coil is noted as the mutual inductance between the two coils, which can be calculated as

$$M_{TX/RX} = \frac{\Psi_{TX/RX}}{I_{TX}} \tag{6.34}$$

- $\Psi_{TX/RX}$ is the magnetic flux generated by the transmitter coil through the power receiver coil
- I_{TX} is the current flowing through the transmitter coil

The magnetic flux created by one coil and through the other coil is [199]

$$\Psi_{TX/RX} = \oint B_{TX/RX}(I_{TX}) dA_{RX} = \oint \mu H_{TX/RX}(I_{TX}) dA_{RX} \tag{6.35}$$

Assuming that magnetic field is uniform at the effective area of the power receiver coil and through the coil, the magnetic flux expression (6.23) can be simplified as

$$\Psi_{TX/RX} = \mu H_{TX/RX}(I_{TX}) N_{RX} A_{RX} \tag{6.36}$$

By combining (6.30) and (6.32), the mutual inductance between the two coils can be calculated

$$M_{TX/RX} = \frac{\mu H_{TX/RX}(I_{TX}) N_{RX} A_{RX}}{I_{TX}} \tag{6.37}$$

As discussed in Section 3.1.3 and Section 3.3.4, the magnetic field generated by the primary coil of the wireless power transfer system at the power receiver, with consideration of the non-uniformity of field strength along the axis of power receiver coil, can be calculated as

$$N_{RX} H_{TX/RX} = \sum_{t=0}^{N_{RX}-1} \left\{ \sum_{i=1}^{N_{Pri}} \frac{I_{Pri} \left(\frac{D_{Pri}}{2}\right)^2}{2\left[\left(\frac{D_{Pri}}{2}\right)^2 + (p_{RX} t + d_{wire-RX} t + h_i)^2\right]^{\frac{3}{2}}} \right\} e^{-\alpha \cdot h_{N_{P_1}}} \tag{6.38}$$

By combining (6.37) and (6.38), the mutual inductance between the primary coil and the power receiver coil is thus calculated as

$$M_2 = \mu\pi \left(\frac{D_{RX}}{2}\right)^2 \sum_{t=0}^{N_{RX}-1} \left\{ \sum_{i=1}^{N_{Pri}} \frac{\left(\frac{D_{Pri}}{2}\right)^2}{2\left[\left(\frac{D_{Pri}}{2}\right)^2 + (p_{RX} t + d_{wire-RX} t + h_i)^2\right]^{\frac{3}{2}}} \right\} e^{-\alpha \cdot h_{N_{Pri}}} \tag{6.39}$$

With the mutual inductance available for calculation, $|S_{11}|$ (with impedance matching in the coupling coil circuit) or the ratio $|S_{11}|_2/|S_{11}|_1$ (with no impedance matching in the coupling coil circuit) due to the change in the power receiver can be calculated. In the following analysis, the parameters of the transmitter coils (the coupling coil and the primary coil) and the power receiver coil are chosen as in Table 6.4-1.

The ratio $|S_{11}|_2/|S_{11}|_1$ and magnitude $|S_{11}|$ due to change of power receiver will be analysed against the transfer distance, which will give a prediction on the performance of the wireless data transfer scheme under the wireless power transfer system.

Parameter	Gap interval	Coil diameter	Number of turns	Wire diameter	Ferrite permeability		Operational frequency	Transfer distance
Symbol	*p (mm)*	*D (cm)*	*N*	d_{wire} *(mm)*	$\mu`_r$	$\mu``_r$	*f (MHz)*	*Dis (cm)*
Primary coil	2.52	20.1	6	1	NA	NA	8	0-20
Receiver coil	0.1	0.2	100 or 200	0.1	80	5		

Table 6.4-1 Parameter values for the wireless power transfer system

6.4.2 Analysis of the model with no impedance matching at the coupling coil

6.4.2.1 The calculated ratio $|S_{11}|_2/|S_{11}|_1$ in different numbers of turns and different media

The calculated ratios $|S_{11}|_2/|S_{11}|_1$ in dB against transfer distance are shown in Figure 6.4-1 in two different transfer media (air and conductive human-tissue) and with two different numbers of turns (100 and 200). In the figure, the more negative the value is, the larger the ratio will be.

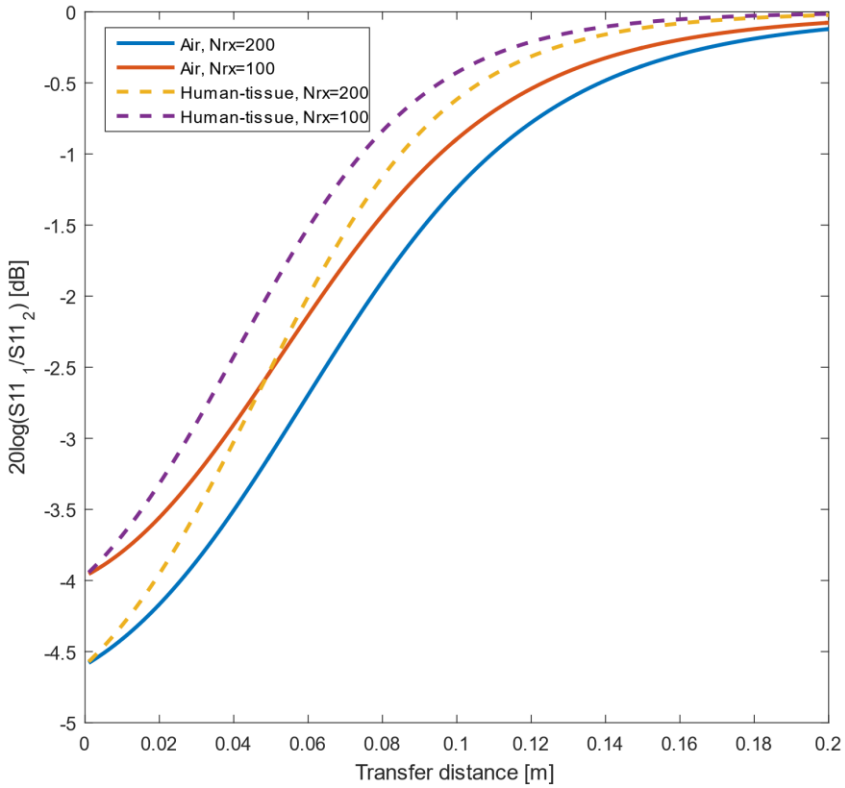

Figure 6.4-1 Calculated ratio ($|S_{11}|_1/|S_{11}|_2$) in dB with $|S_{11}|_1$ of on-state receiver and $|S_{11}|_2$ of off-state receiver in a range of transfer distance from 0 m to 0.2 m with the chosen parameters of the transmitter coils and the receiver coil with no impedance matching at the coupling coil circuit; the magnitude of $|S_{11}|_1$ is 0.5. (Dash lines) the whole transfer path with conductive human-tissues; (solid lines) the whole transfer path in air or non-conductive human-tissues.

As shown, for the same media and same number of turns, $|S_{11}|_1/|S_{11}|_2$ increases when the transfer distance decreases. This is because, at a shorter distance, the magnetic field strength generated by the primary coil is higher, resulting in a higher mutual inductance between the power receiver coil and the primary coil. The difference in the dissipated power between the on-state-receiver case and the off-state-receiver case

will thus become larger, and the ratio of the dissipated powers G_1 will thus become smaller. According to equation (6.20), $|S_{11}|_1/|S_{11}|_2$ will thus become higher.

In terms of transfer media, $|S_{11}|_1/|S_{11}|_2$ is higher when the medium is air. This is because the magnetic field generated by the primary coil is attenuated in conductive media, which is discussed in Section 2.3.4.2. It should be noted that the calculation of conductive human-tissue is an extreme case because it is assumed that the whole transfer path is filled with conductive human-tissue, which is usually not the case. Therefore, in reality, $|S_{11}|_1/|S_{11}|_2$ will be between the air-line and the human-tissue-line with the same number of turns.

In terms of the number of turns, it shows that a higher number of turns of the power receiver coil causes a higher $|S_{11}|_1/|S_{11}|_2$. This is because the number of turns of the power receiver coil is proportional to the mutual inductance between the primary coil and the power receiver coil, which is shown in equation (6.39).

The calculated $|S_{11}|_1/|S_{11}|_2$ at transfer distances 20 cm and 10 cm are shown in Table 6.4-2. It shows that at 20 cm, a 0.4% to 2% change in $|S_{11}|$ can be detected by the network analyser when the power receiver rectifier changes its state when the power receiver coil has 200 turns. When the transfer distance becomes shorter, the percentage increases. At 10 cm transfer distance, a 10.2% to 20.6% change in $|S_{11}|$ can be detected for 200 turns, depending on the composition of the transfer media.

	Air, N_{Rx}=200	Human tissue, N_{Rx}=200	Air, N_{Rx}=100	Human tissue, N_{Rx}=100
$\|S_{11}\|$ ratio at 20 cm transfer distance (dB)	-0.12 (2.0%)	-0.02 (0.4%)	-0.08 (1.3%)	-0.02 (0.2%)
Signal level at 20 cm (dB)	-37.0	-51.5	-41.0	-55.5
$\|S_{11}\|$ ratio at 10 cm transfer distance (dB)	-1.24 (20.6%)	-0.62 (10.2%)	-0.90 (14.9%)	-0.43 (7.1%)
Signal level at 10 cm (dB)	-16.3	-22.7	-19.3	-26.0

Table 6.4-2 Calculated ratio ($|S_{11}|_1/|S_{11}|_2$) in dB for different media and number of turns at 20 cm transfe distance and 10 cm transfer distance for coupling coil circuits with no impedance matching. The percentage number in the bracket is the calculated ratio of the $|S_{11}|$ ratio in dB over the $|S_{11}|_1$ dB value, which is equal to $20log_{10}(0.5)$=-6.02; the signal level is equal to the dB value of ($|S_{11}|_2$-$|S_{11}|_1$)/$|S_{11}|_1$.

The calculated dB value of ($|S_{11}|_2$-$|S_{11}|_1$)/ $|S_{11}|_1$ for each case is also listed. This value is equivalent to the signal level of the wireless data transfer system. In the system, the signal level should be higher than the noise level for signal transmission. As shown, in order to detect the change in $|S_{11}|$ at 20 cm with a 200-turn power receiver coil in conductive human tissue, the network analyser noise level for the measurement of

$|S_{11}|$ should be equal to or lower than -51.5 dB. Otherwise, the signal from the power receiver coil cannot be distinguished from the noise. The required noise level is even lower for a 100-turn power receiver coil.

6.4.2.2 The calculated $|S_{11}|$ ratio in different $|S_{11}|_1$ values and different media

The calculated ratios of $|S_{11}|s$ in dB against transfer distance are shown in Figure 6.4-2 in two different transfer media (air and conductive human-tissue) and with three different $|S_{11}|_1$ magnitudes (0.2, 0.5 and 0.8).

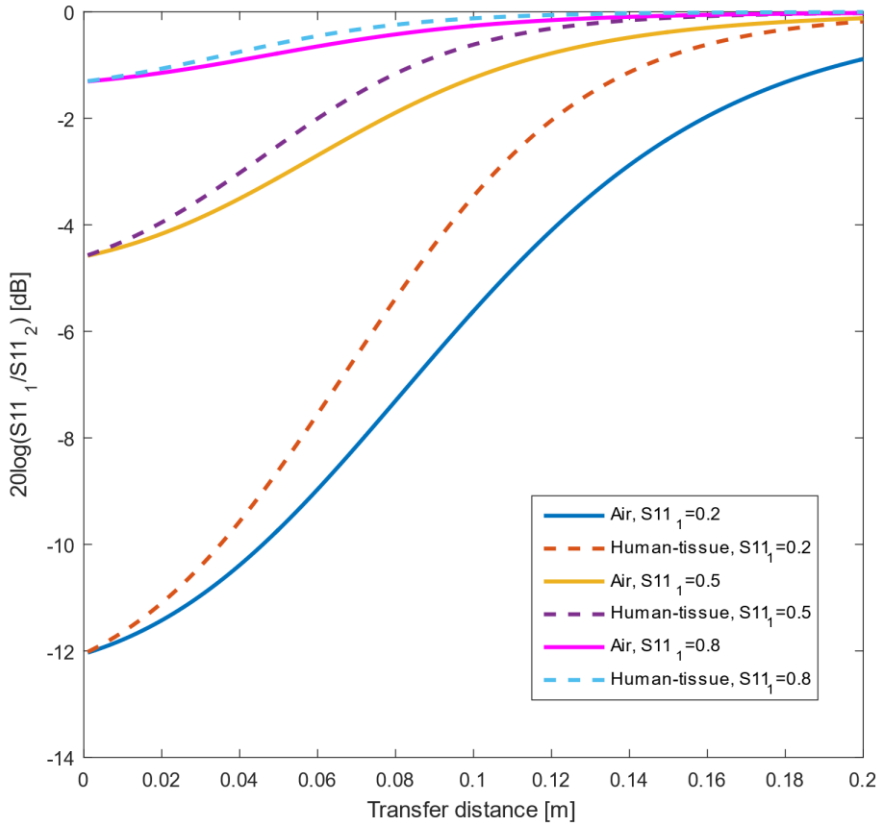

Figure 6.4-2 Calculated ratio ($|S_{11}|_1$/ $|S_{11}|_2$) of the $|S_{11}|$ with the on-state receiver ($|S_{11}|_1$) and the $|S_{11}|$ with the off-state receiver ($|S_{11}|_2$) in dB in a range of transfer distance from 0 m to 0.2 m with different $|S_{11}|_1$ values with the chosen parameters of the transmitter coils and the receiver coil with no impedance matching at the coupling coil circuit; the number of turns is 200. (dash lines) the whole transfer path with conductive human-tissues; (solid lines) the whole transfer path in air or non-conductive human-tissues

As shown, with the same power receiver, the same transfer distance and the same transfer media, a smaller on-state-receiver reflection coefficient $|S_{11}|_1$ will result in a higher $|S_{11}|$ ratio.

As discussed in Section 6.3.1, the magnitude of off-state-receiver reflection coefficient $|S_{11}|_2$ can be calculated as

$$|S_{11}|_2 = \sqrt{1 - G_1 + G_1|S_{11}|_1^2} \tag{6.40}$$

As shown, when the magnitude of $|S_{11}|_1$ approaches 1, the magnitude of $|S_{11}|_2$ will also approach 1. This means that if most of the incident power from the power source is reflected, the change in the power receiver state will be less noticeable from the observation of $|S_{11}|$ values, because little power is received at the power receiver, and the on-state received power and off-state received power have little difference in values. Therefore, the $|S_{11}|$ ratio will become smaller when $|S_{11}|_1$ approaches 1.

When $|S_{11}|_1$ decreases and approaches 0, which means the source and the wireless power system approaches perfect impedance matching, more power will be received by the power receiver, and the change of power receiver state will cause a larger difference in the received power. When $|S_{11}|_1$ approaches 0, $|S_{11}|_2$ will approach $\sqrt{1-G_1}$. As discussed in Section 6.3.1, the value of G_1 is only dependent on the equivalent impedance of the on-state receiver at the primary coil $R'_{Receiver}$ and the primary coil impedance $R_{Primary}$, which are independent of the change of power receiver state. As $|S_{11}|_1$ approaches 0, the ratio $|S_{11}|_2/|S_{11}|_1$ will approach infinity. Therefore, the $|S_{11}|$ ratio will become higher when $|S_{11}|_1$ becomes smaller.

The $|S_{11}|$ ratio at transfer distances 10 cm and 20 cm are shown in Table 6.4-3 with the percentage ratios of the $|S_{11}|$ ratio (in dB) over the corresponding $|S_{11}|_1$ dB value and the signal level of the wireless data transfer system. As shown, for $|S_{11}|_1$=0.2, a 1.3% to 6.3% of the change in the dB $|S_{11}|$ can be detected at 20 cm when the power receiver changes states with the chosen parameters of the wireless power transfer system. The variation of the change is dependent on the composition of media. The change in dB $|S_{11}|$ is even greater for shorter transfer distances. For $|S_{11}|_1$=0.8, the change is from 0.2% to 1.2%, which is much less than the changes in $|S_{11}|_1$=0.2 and 0.5.

	Air, $\|S_{11}\|_1$=0.2	Human tissue, $\|S_{11}\|_1$=0.2	Air, $\|S_{11}\|_1$=0.5	Human tissue, $\|S_{11}\|_1$=0.5	Air, $\|S_{11}\|_1$=0.8	Human tissue, $\|S_{11}\|_1$=0.8
$\|S_{11}\|$ ratio at 20 cm transfer distance (dB)	-0.89 (6.3%)	-0.18 (1.3%)	-0.12 (2%)	-0.02 (0.4%)	-0.02 (1.2%)	-0.004 (0.2%)
Signal level at 20 cm (dB)	-19.4	-33.5	-37.0	-51.5	-51.5	-66.0
$\|S_{11}\|$ ratio at 10 cm transfer distance (dB)	-5.62 (40.1%)	-3.46 (24.8%)	-1.24 (20.6%)	-0.62 (10.2%)	-0.26 (13.5%)	-0.12 (6.3%)
Signal level at 10 cm (dB)	-0.8	-6.2	-16.7	-22.7	-30.3	-37.0

Table 6.4-3 Calculated ratio ($|S_{11}|_1/|S_{11}|_2$) in dB for different media and different $|S_{11}|_1$ at 20 cm transfe distance and 10 cm transfer distance for coupling coil circuits with no impedance matching. The percentage number in the bracket is the ratio of the $|S_{11}|$ ratio in dB over the corresponding $|S_{11}|_1$ dB value; the signal level is equal to the dB value of ($|S_{11}|_2$-$|S_{11}|_1$)/ $|S_{11}|_1$.

In terms of signal level, a lower $|S_{11}|_1$ has a huge advantage of the required noise level than a high $|S_{11}|_1$. As shown, at 20 cm, the signal level for $|S_{11}|_1$=0.2 in full conductive human-tissue is -33.5 dB, which is 18 dB higher than the signal level for $|S_{11}|_1$=0.5, and 32.5 dB higher than the one for $|S_{11}|_1$=0.8. The requirement in the noise level of network analyser is thus much less strict for $|S_{11}|_1$=0.2.

From the above analysis, the magnitude of on-state-receiver reflection coefficient $|S_{11}|_1$ is a vital parameter in the performance of the wireless data transfer system. A lower $|S_{11}|_1$ will result in a less strict required noise level. Therefore, it is of interest to find out the performance of the wireless data transfer system with impedance matching at the coupling coil circuit.

6.4.3 Analysis of the model with impedance matching at the coupling coil circuit

With an impedance matching network at the coupling coil circuit, the amplitude of the on-state-receiver reflection coefficient $|S_{11}|_1$ is 0, and its dB value will be theoretically $(-\infty)$. In practical case, due to noise, the actual dB value will be around -80 dB. Therefore, the performance of the wireless data transfer will be analysed through the off-state-receiver reflection coefficient $|S_{11}|_2$. This is actually an advantage because it provides a straightforward criterion to assess the high level (1s) and low level (0s) in digitised data transmission, given the dimensional parameters of the wireless power transfer system. As discussed in Section 6.3.2, the $|S_{11}|_2$ in dB can be calculated as

$$20log(|S_{11}|_2) = 10log(1 - G_2) \tag{6.33}$$

where

$$G_2 = \frac{1}{1 + \frac{R'_{Receiver}}{4R_{Primary}}} \tag{6.29}$$

$|S_{11}|_2$ in dB at a transfer distance between 0 cm to 20 cm are shown in Figure 6.4-3 in two different transfer media and two different numbers of turns.

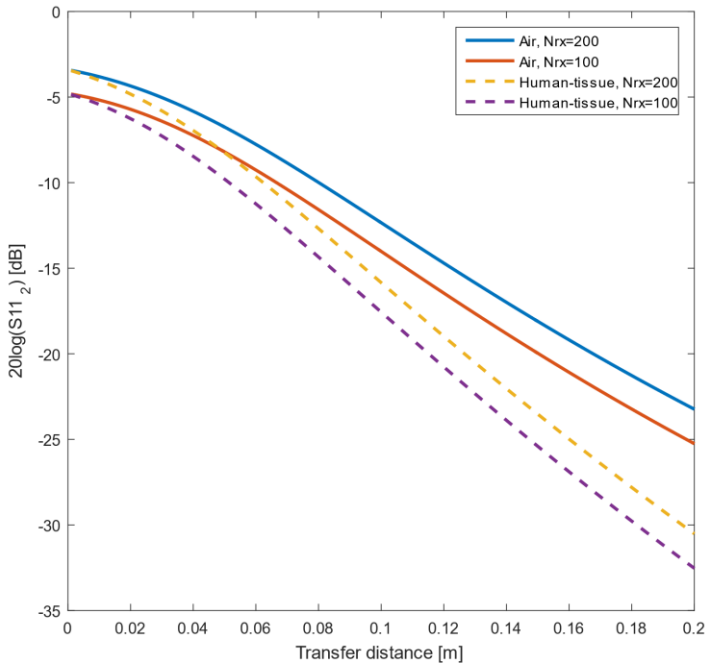

Figure 6.4-3 Calculated value of $|S_{11}|_2$ in dB in a range of transfer distance from 0 m to 0.2 m with the chosen parameters of the transmitter coils and the receiver coil with impedance matching at the coupling coil circuit; (dash lines) the whole transfer path with conductive human-tissues; (solid lines) the whole transfer path in air or non-conductive human-tissues

As shown, with the same transfer media and the same number of turns, $|S_{11}|_2$ in dB decreases as the transfer distance increases. Because $|S_{11}|_1$ in dB is supposed to be minus infinity, a smaller absolute value of $|S_{11}|_2$ in dB means a stronger effect due to the change of power receiver state. Therefore, as the transfer distance increases, the effect due to the change in the power receiver state is weaker.

In terms of transfer media, the attenuation effect in conductive human-tissue becomes more apparent as the transfer distance increases. In reality, $|S_{11}|_2$ in dB should be lying between the air-line and the human-tissue line for the same number of turns depending on the composition of transfer media.

In terms of the number of turns in the power receiver, a higher number of turns corresponds to a lower dB value of $|S_{11}|_1$. The reason for this is discussed in Section 6.4.2.1. The value of $|S_{11}|_2$ for transfer distances 20 cm and 10 cm are shown in Table 6.4-4.

	Air, N_{Rx}=200	Human tissue, N_{Rx}=200	Air, N_{Rx}=100	Human tissue, N_{Rx}=100
$\|S_{11}\|_2$ at 20 cm transfer distance (dB)	-23.24	-30.51	-25.25	-32.53
$\|S_{11}\|_2$ at 10 cm transfer distance (dB)	-12.34	-15.84	-14.02	-17.56

Table 6.4-4 Calculated $|S_{11}|_2$ in dB for different media and number of turns at 20 cm transfer distance and 10 cm transfer distance for coupling coil circuits with impedance matching

6.5 Summary of this chapter

In this chapter, a wireless data transfer scheme is developed based on the wireless power transfer system. The data transfer scheme uses the same coils as the wireless power transfer system and is suitable for low-speed data transmission (around 1 byte/second). The data transfer scheme detects the change of received power in the power receiver coil circuit by observing the reflection coefficient $|S_{11}|$ at the power source. Because the impedance of the power receiver coil circuit when the rectifier is in the on-state is much less than the impedance when the rectifier is in the off-state, the on-state received power will be much higher than the off-state received power, which can be reflected in $|S_{11}|$ at the power source. In practice, the forward power and the backward power from the power source of the WPT system will be measured by a specially-designed demodulator, which then calculate the $|S_{11}|$ from the measurements and demodulate the signal sent from the power receiver.

Theoretical models are built for two conditions: with and without impedance matching at the coupling coil circuit. In both cases, the transfer media and the number of turns in the power receiver coil will affect the performance of the data transfer scheme by changing the mutual inductance between the primary coil and the power receiver coil. In terms of the number of turns, as the mutual inductance is basically the induced voltage on the power receiver coil divided by the current at the primary coil, the idea to increase of mutual inductance can refer to the analysis of primary coil in Section 3.2.2 and the analysis of power receiver coil in Section 3.3.4. In terms of transfer media, the conductive tissue will lower the signal level of the data transfer scheme by attenuation effect of the magnetic field. The effect is stronger when the transfer distance becomes longer.

In the case that the coupling coil circuit has no impedance matching, the $|S_{11}|$ ratio between on-state and off-state is dependent on the on-state reflection coefficient $|S_{11}|_1$. The analysis shows that a lower $|S_{11}|_1$ will result in a higher $|S_{11}|$ ratio and a less strict required noise level. In the case that the coupling coil circuit has impedance matching, the off-state reflection coefficient $|S_{11}|_2$ represents the performance of the data transfer scheme. Once the parameters of the wireless power transfer system are determined, the magnitude of $|S_{11}|_2$ will not change under the same transfer distance and the same media, which give a straightforward criterion to assess the high level (1s) and low level (0s) in digitised data transmission.

From the analysis above, it can be concluded that the proposed wireless power transfer system is feasible to transfer data with the same set of coils for power transfer using the LSK modulation scheme and the basic idea of network analyser at a transfer distance up to 20 cm. The sensitivity of data transfer is essentially determined by the

ratio between the power receiver input power and the source output power at the transmitter. The higher the ratio is (i.e. more power receiver input power for the same source output power), the higher the sensitivity will be. For the proposed WPT system with optimum transmitter parameters, the data transfer sensitivity is affected by four factors:

- the impedance matching between the source (including the signal generator and the power amplifier) and the coupling coil
- the transfer distances
- the power attenuation in transfer media
- the dimensional parameter of the power receiver, e.g. number of turns, coil diameter

Therefore, to achieve a high data transfer sensitivity, we can improve the impedance matching between the source and the coupling coil, shorten the transfer distance, find an alternative path of power transfer with lower power attenuation, or increase the power receiver number of turns (if the power receiver diameter is fixed).

For the IMPACT sensors, which have fixed positions inside the body of patients and a fixed power receiver diameter (2 mm), a good impedance matching and a high number of turns of power receiver coils are the keys to achieving a high sensitivity of data transfer. As discussed in Section 6.4.2.2, the predicted dB value of $|S_{11}|$ ratio ($|S_{11}|_1$/ $|S_{11}|_2$) for $|S_{11}|_1$=0.2 when N_{RX}=200 is between -0.18 dB and -0.89 dB, which can be detected by state-of-the-art network analysers in a low noise environment. As discussed in Section 6.4.3, the predicted value of $|S_{11}|_2$ in the perfect match condition ($|S_{11}|_1$=0) at 20 cm transfer distance when N_{RX}=200 is between -30.51 dB and -23.24 dB, which is in the measurable range of state-of-the-art network analysers. Therefore, the transferred signals of the proposed WPT system can be detected by external devices at 20 cm transfer distance. From the above analysis, it can be preliminarily concluded that the LSK modulation scheme of the proposed WPT system can meet the data transfer distance requirement of the IMPACT sensors. In terms of data rate, according to the works of literature in Section 1.2.2.1, the state-of-the-art LSK modulation schemes can achieve a data rate more than 1 Mbps, which can meet the requirement of the IMPACT sensor system. In future studies, a practical WPT system with data transfer will be developed based on the proposed model of the system, which can be used with the IMPACT systems.

Chapter 7 Conclusion

7.1 Summary

This project set out to examine the hypothesis that:

- ***Power of more than 1 mW can be received by the microsystem inside a human body through a wireless magnetic coupling link with the receiver diameter less than 2 mm at a transfer distance as much as 20 cm.***
- ***Data can be transmitted wirelessly from the microsystem to an external reader using the same magnetic coupling link as the wireless power system.***

To examine the hypothesis, the following works have been done:

In Chapter 1

- Two suitable wireless data transfer schemes for micro-implants have been reviewed and discussed, which are the single-carrier scheme and the multiple-carrier scheme. The single-carrier scheme, which applies the LSK modulation, is more suitable for the proposed WPT system, because of its lower power consumption of data transfer at the required data rate (at least 1 byte/second).
- Different kinds of wireless power transfer options have been reviewed and discussed, including magnetic coupling resonance, ultrasonic wave power, EM radiation, etc. The magnetic coupling resonance WPT is chosen because of its relatively long transfer distance (up to 20 cm) and low radiation exposure risk.
- Different rectifier structures commonly used in the receiver of WPT systems have been reviewed and discussed, including junction-diode rectifiers, basic bootstrapping rectifiers and comparator-based rectifiers. The bootstrapping structure is chosen in this thesis for further discussion because of its low forward voltage drop (<0.7 V) and low control power loss compared with the comparator-based rectifier.

In Chapter 2

- The basic laws and theories behind the magnetic coupling resonance wireless power transfer system are discussed, including the Biot-Savart law and the Faraday's law.

- The factors that affect the performance of the WPT system are discussed, including *L*-*C* resonant circuits, impedance matching circuits, the inductor AC resistance, self-capacitance and SRF, and the properties of high-frequency EM fields and waves in the air and media.

In Chapter 3

- An analytical model of solenoid transmitter coils is built to calculate the magnetic field strength generated by the proposed WPT system based on the dimensional parameters of the coils. The transmitter mainly utilises a power source, an impedance matching network, a coupling coil circuit and a primary coil circuit. The idea of the model is to maximise the primary coil current by matching the impedance of the coupling coil circuit and the primary coil circuit through the adjustment of the mutual inductance between the coils; and by matching the power source impedance and the coupling coil circuit through the adjustment of the impedance matching circuit. The calculation results of the model are in good agreement with the experimental results.
- The co-dependencies between the dimensional parameters of the solenoid coils are discussed. With the co-dependencies, a design flow to obtain the optimum dimensional parameters of the solenoid transmitter is presented based on the operational frequency and the target transfer distance. Some examples of optimum dimensional parameters are shown for target transfer distances of 4 cm, 8 cm, 12 cm, 16 cm and 20 cm.
- Analytical models of solenoid receiver coils (ferrite-core and air-core) are built to calculate the induced voltage and received power for the proposed WPT system based on the dimensional parameters of the receiver coil and the magnetic field strength from the transmitter coil. The receiver utilises a receiver coil, an impedance matching circuit, a rectifier and load. The received power is maximised by matching the receiver coil impedance and the rectifier input impedance.
- The induced voltages and the received power of the ferrite-core receiver and the air-core receiver with 2 mm diameter are calculated in different numbers of turns, gap intervals and wire widths, with the magnetic field strength from the optimum transmitter at 20 cm transfer distance. Results show that the ferrite-core receiver has much better performances than the air-core receiver with the same dimensional parameters. A design flow of the ferrite-core solenoid receiver is also presented.

In Chapter 4

- The performance of different kinds of rectifiers suitable for the implanted receivers are discussed and compared in two different load conditions.
- The performance of the practical basic bootstrapping rectifier is tested on integrated chips. Experimental results show that the PCE and VCR of the rectifier are in good agreement with the simulation results.
- A novel static switch gate-control rectifier (improved static BSR) and a OCDGC rectifier based on the bootstrapping structure for the proposed wireless power transfer system are introduced and analysed. Results show that the proposed rectifiers can operate at high efficiencies at the target input voltages and load conditions.

In Chapter 5

- A circuit model for the full proposed wireless power transfer system including the optimum transmitters, the ferrite-core receivers and the proposed rectifiers is built. This model considers the receiver coil as a non-ideal voltage source with a non-zero source impedance, which is related to the mutual inductance between the primary coil and the receiver coil and the impedances of the primary coil and coupling coil. The impedance matching circuit at the receiver thus matches the total receiver coil impedance and the rectifier input impedance.
- The rectifier input voltage is calculated in a range of rectifier input resistance based on the full model with a 20 cm transfer distance and a 2 mm-diameter receiver coil. The PDL of the system is analysed and presented with a consideration of rectifier efficiencies at the corresponding input voltages and load conditions.

In Chapter 6

- A mathematical model for data transfer sensitivity prediction is developed based on LSK modulation for the data transfer using the same sets of coils in the proposed wireless power transfer system. The model uses the idea of network analysers and compares the reflection coefficients at the power source of the proposed system in two receiver states (on and off) to distinguish digital “1” and “0”. Depending on the presence of the impedance matching circuit at the coupling coil circuit, the model uses different figure of merits to assess the data transfer sensitivity. With the impedance matching circuit, the FOM is the $|S_{11}|$ values at off-state of the receiver (at on-state, $|S_{11}|$ is 0). Without the impedance matching circuit, the FOM is the ratio of $|S_{11}|$ values between the on-state and off-state of the receiver.

- The data transfer sensitivity of the proposed wireless power and data transfer system has been assessed with a transfer distance of 20 cm and a 2 mm-diameter receiver in the air and conductive human tissues. The required signal levels of the network analyser at the power source are presented for different media, different receiver number of turns and different initial situations.

7.2 Conclusions

As summarised, it is shown that the hypothesis put forward in this thesis is feasible.

In other words, the concept has been proved as follows:

- With the proposed wireless power system, using a solenoid transmitter with optimum parameters and a receiver coil of a diameter of 2 mm, more than 1mW electrical power can be received by the load through human tissue at a transfer distance of 20 cm, if the human tissue mainly consists of skin, muscle and fat, which are less conductive. The turns of receiver coil can vary from 100 to 250, which is under the length limit. In fact, up to 3.8 mW can be received by the implant in air or non-conductive tissues when N_{RX}=250. This power will be sufficient for micro-implants for medical use. If the human tissue consists mainly of conductive tissues, however, the power delivered to the implants can be lower than the requirement. Therefore, the selection of transfer path is extremely vital for the operation of the proposed WPT system. Overall, with the proposed wireless power system, the electronic medical implants at the mm scale, such as the ones developed by the IMPACT program [66], will be able to operate deep inside the body of patients without wires going into the body. In this way, the risk of infection will be reduced, and the patient's everyday life will not be affected.

- With the limited power budget (1mW) and the requirement for high efficiency, two novel rectifiers are specially designed for the proposed WPT system. The proposed OCDGC bootstrapping rectifier will be able to operate at an efficiency of over 80% with a 5 kΩ-load condition with a VCR of more than 0.75 for an input voltage ranging from 1.5 V to 5 V. For input voltages between 1 V and 1.5 V, a practical static gate-control bootstrapping rectifier has been proposed with an efficiency of up to 60% for a 5 kΩ-load and over 90% for a 500 Ω-load. These rectifiers will be able to convert the received power from AC to DC efficiently at the receiver with a low power budget. However, it should be noted that, while the static gate-control bootstrapping rectifier will be able to operate at more than 50 MHz, the OCDGC bootstrapping rectifier will only be able to work up to 10 MHz due to the frequency limitation of the opto-coupler units. Moreover, the opto-coupler units may not be able to integrate with the rest of the receiver circuits, which could increase the overall size of the receiver system. In wireless powered micro-implant applications, the proposed rectifiers will be able to operate at high efficiency at a wide range

of load and input voltage conditions. For special implants, such as the ones developed by the IMPACT program [66], data will also be transferred from the receiver to the transmitter. In this case, the gate voltage of the main-path PMOSs of the rectifier can be controlled to switch the power on/off to achieve the function of ASK. Therefore, no extra switching component is needed, which will save the space on the integrated circuit and improve the power efficiency during data transmission.

- The proposed wireless data transfer scheme is based on the idea that a change in the impedance of the receiver coil can be detected by an amplitude shift of the reflection coefficient $|S_{11}|$ at the power source. This data transfer method has been well studied, but no research has investigated the capability of the method for a 2-mm implant at a 20 cm transfer distance with the proposed WPT system. The analysis shows that, with the optimised transmitter structure and a properly designed receiver, a change in $|S_{11}|$ can be detected at a 20 cm transfer distance when the noise level of the network analyser is below the corresponding signal level. For example, for a 200-turn receiver with a diameter of 2 mm, the noise level of the network analyser should be no higher than -30.5 dB (with respect to the fully reflected situation where $|S_{11}|$=1) to detect the impedance change at the receiver. This shows that data can be transferred, using the same coils as the power delivery for a transfer distance of up to 20 cm. In practice, the forward power and the backward power from the power source of the WPT system will be measured by a specially designed demodulator, which then calculate the $|S_{11}|$ from the measurements and demodulate the signal sent from the power receiver. To achieve a high data transfer sensitivity, we can improve the impedance matching between the source and the coupling coil, shorten the transfer distance, find an alternative path of power transfer with lower power attenuation, or increase the receiver number of turns (if receiver diameter is fixed). However, the speed for data transfer is limited to 1Mbyte/second due to the limitation of operational frequency. For wireless powered implants that only require a low data rate, such as the ones developed by the IMPACT program, this speed of data transfer is acceptable, as relatively small amounts of data will be transmitted.

However, the proof has not been extended to address the shortcomings expressed above, and to address the following issues:

- For micro-implants in lungs and other organs where the water density is high, the generated magnetic field may be attenuated by a further factor of two. A higher input power will be needed for the receiver to operate. The increase of magnetic field strength may exceed the SAR limit and cause a temperature rise on patients, which is potentially a hazard.
- For patients with large body sizes, the implants may be so deep inside the body that the transfer distance will be over 20 cm. In this case, the amount of delivered power may not be able to meet the requirement of the load in the receiver. The data will also not be able to transfer.
- In the thesis, the discussions are based on the setting that the direction of the receiver coil is coaxial to the transmitter. In the actual application, this may not always be happening. The effect of misalignment between the transmitter and receiver at this range of transfer distance has not been investigated in terms of power and data transfer. This can be solved in theory by using multiple coils in different directions and positions. However, the analysis of multiple coils on power transfer and data transmission is beyond the scope of this thesis.
- Even though it is proved that a change in the amplitude shift can be observed for a single magnetic coupling link with the proposed wireless power transfer system, it is still far away from being used in the actual application. The limitation of data transfer speed (1Mbyte/second) is also a restriction for some applications.

Therefore, before this set of techniques can be used in the proposed application, more work is needed, as described in 7.3.

7.3 Further Work

- Misalignment analysis

In this work, the analysis of power transfer is assumed that the primary coil and the receiver coil are in coaxial. In the actual application, the coils will not be able to align perfectly all the time. It can be expected that the induced voltage and the received power at the receiver coil will be reduced by misalignments. In the future works, the effect of angular and lateral misalignments between the primary coil and the receiver coil on long transfer distances (up to 20 cm) and the limits of tolerable amounts of misalignment is necessary to find out.

- Multi-transmitter coil analysis with power and data transfer

To compensate the reduction of received power at the receiver coil caused by the misalignments, multiple transmitter coils in different positions can be used. In the future works, the interference between transmitter coils of different sizes and positions on power and data transfer for long transfer distances (up to 20 cm) will be studied. The optimum number of transmitter coils and their optimum relative positions to provide the maximum power to an implant will be found out.

- Experiment analysis of the improved static BSR rectifier and the OCDGC rectifier

Due to limitation of resources, the improved static BSR rectifier and the OCDGC rectifier were unable to be tested on chips to compare the simulation results and experimental results. In future works, these rectifier circuits will be fabricated on chips, and their performance will be analysed with experiments.

- Implementation of the data transfer system

In this work, the sensitivity of data transfer is calculated with the proposed WPT system. In future works, a data transfer system will be developed, where the implants' data are digitised by an on-chip system to control the switches in the rectifier with a coding scheme, and the external devices can receive and demodulate the data in real-time.

Appendix

A1. Picture of experiment devices

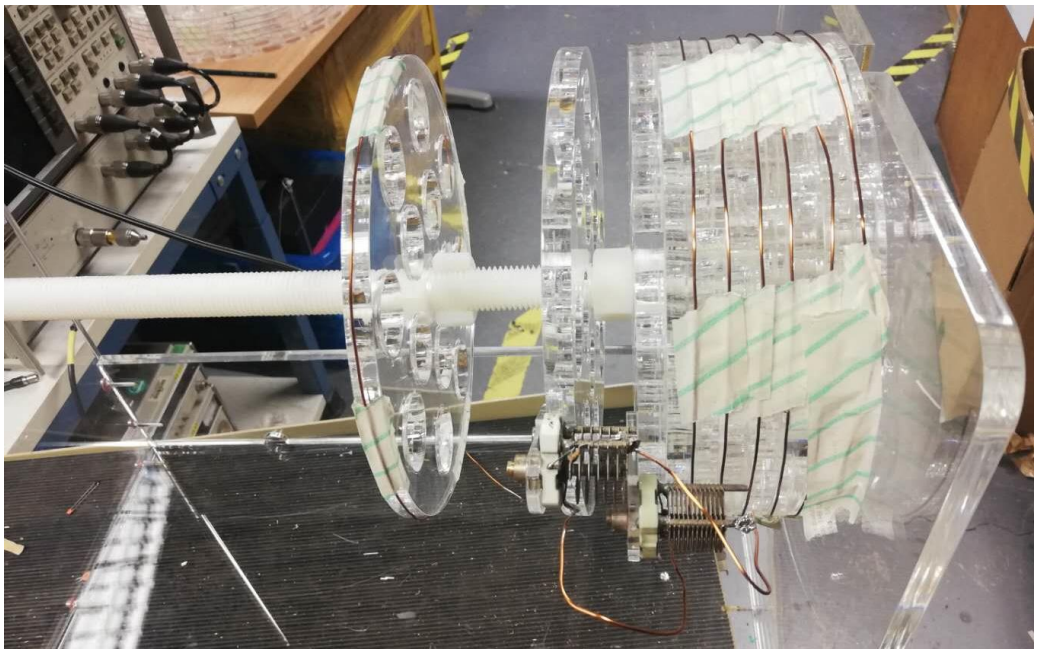

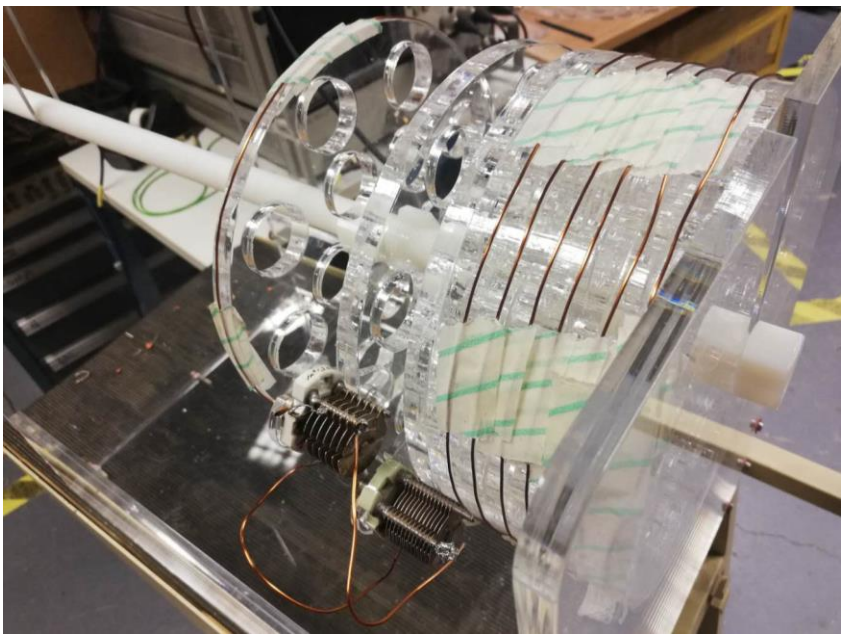

Photos for the coils for the experiments

Magnetic field probe HP11941A

Network analyser HP8753C (300KHz to 3Gz) and the S-parameter test set HP 85046A

Broadband power amplifier EATON 5001 (0.01 to 10MHz)

FeelTech FY3200S dual channel arbitrary function signal generator/counter

Spectrum analyser HP8568B (100Hz to 1.5GHz)

A2. Self-capacitance and SRF prediction

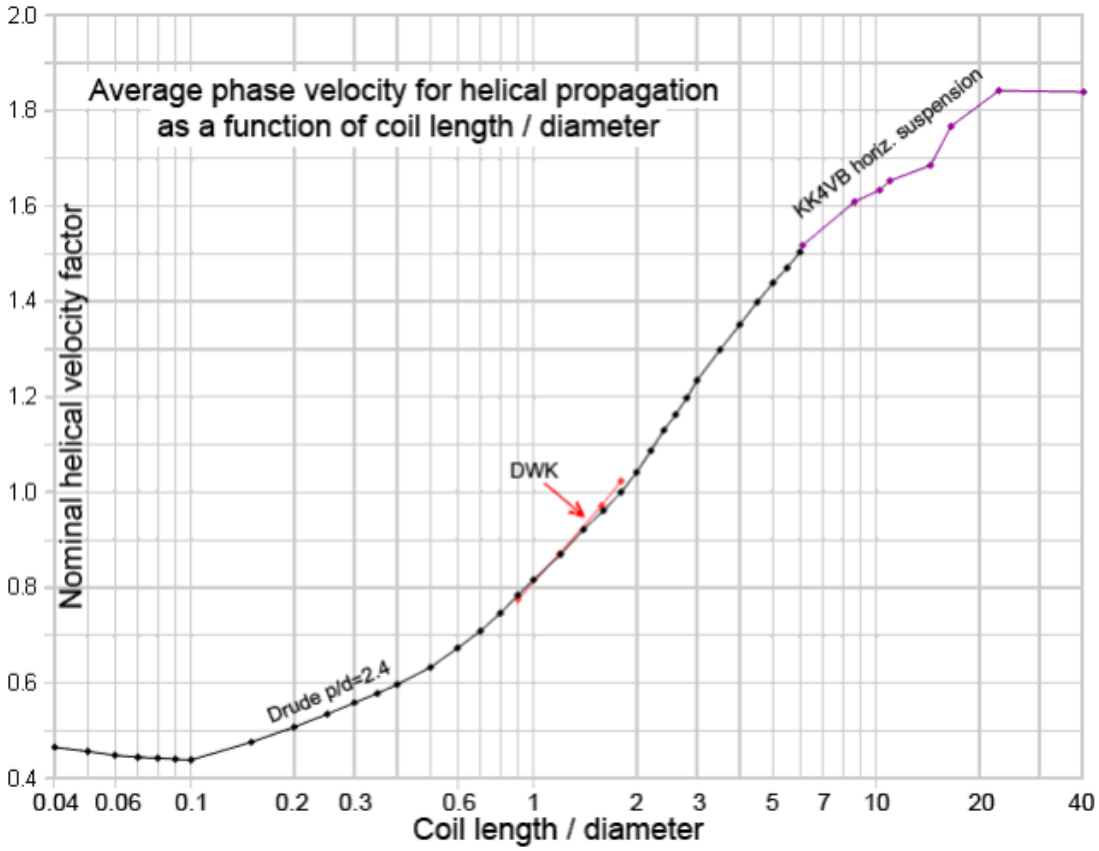

Experiment data of apparent velocity factor for air-cored solenoids at the first SRF, including Drude's data [178], DWK data and Alex's data [174].These data is used to develop the empircal formula for SRF in (2.127). This figure is obtained from [174].

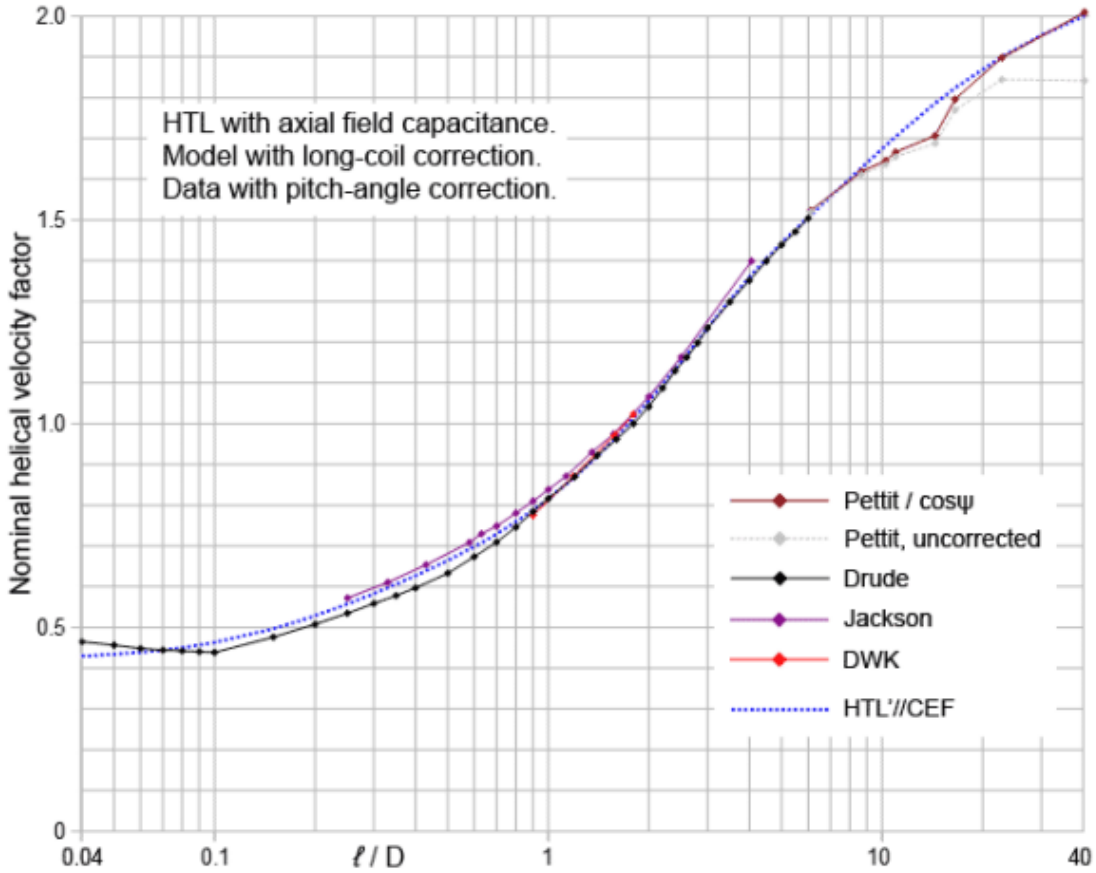

Comparison of experiment datas with the empirical formula for apparent velocity factor HTL'//CEF, which involves the modelling of axial field capacitance, long-coil correction and pitch-angle correction. This figure is obtained from [174].

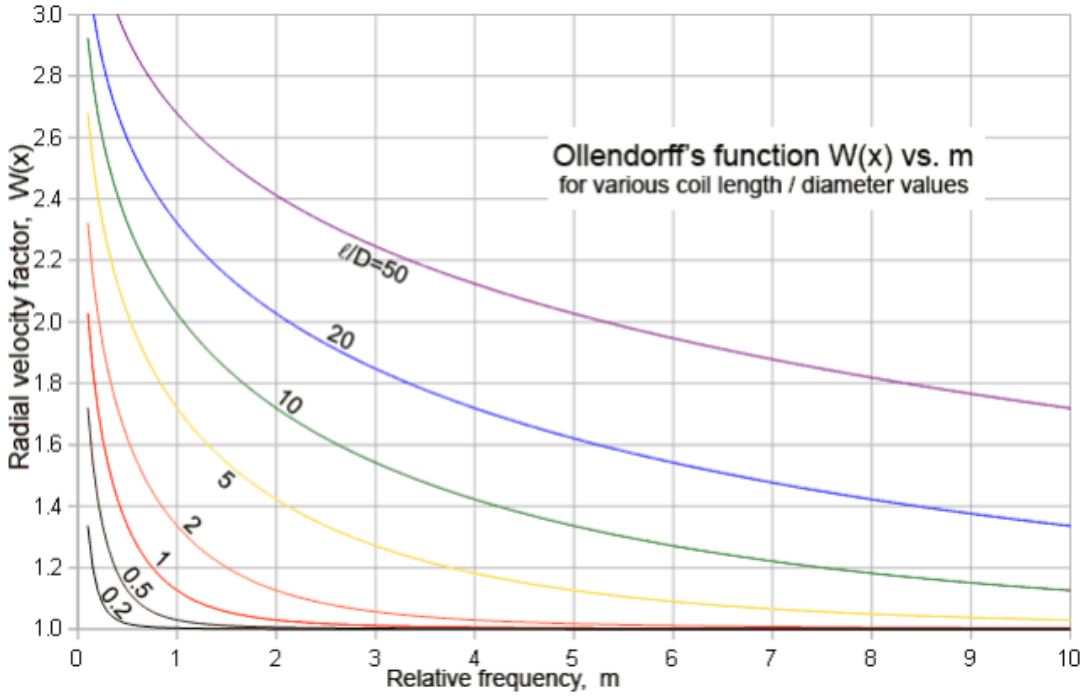

Ollendorff's function (radial velocity factor) against relative frequency for various coil length/ coil diameter, from 0.2 to 50. This function implies that the velocity factor declines with frequency. This figure is obtained from [174].

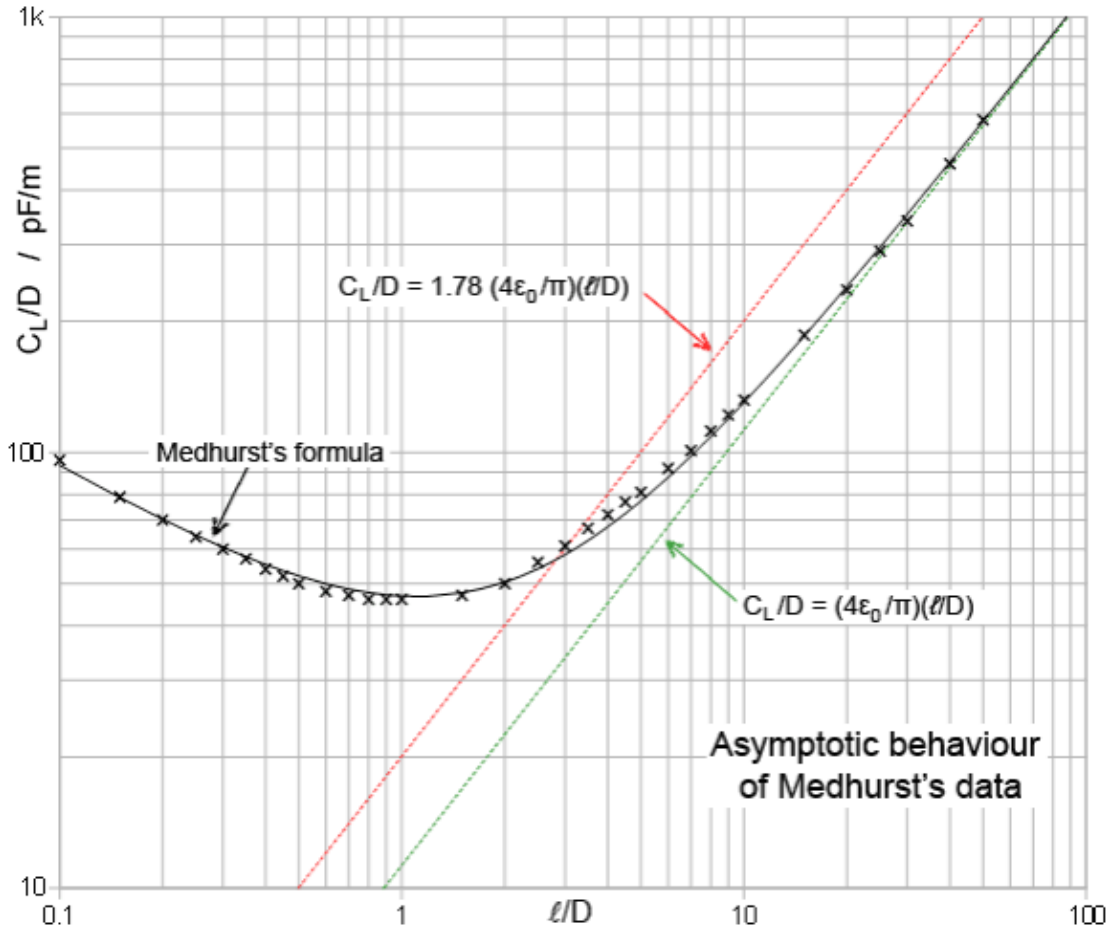

Medhurst's data for solenoid coil capacitance/ coil diameter against coil length/ coil diameter, with approximation formulas to calculate capacitance/ coil diameter. This figure is obtained from [174].

A3. Proximity factor for AC resistance calculation

p/d→ l/D↓	1	1.111	1.25	1.429	1.667	2	2.5	3.333	5	10
0	5.31	3.73	2.74	2.12	1.74	1.44	1.20	1.16	1.07	1.02
0.2	5.45	3.84	2.83	2.20	1.77	1.48	1.29	1.19	1.08	1.02
0.4	5.65	3.99	2.97	2.28	1.83	1.54	1.33	1.21	1.08	1.03
0.6	5.80	4.11	3.10	2.38	1.89	1.60	1.38	1.22	1.10	1.03
0.8	5.80	4.17	3.20	2.44	1.92	1.64	1.42	1.23	1.10	1.03
1	5.55	4.10	3.17	2.47	1.94	1.67	1.45	1.24	1.10	1.03
2	4.10	3.36	2.74	2.32	1.98	1.74	1.50	1.28	1.13	1.04
4	3.54	3.05	2.60	2.27	2.01	1.78	1.54	1.32	1.15	1.04
6	3.31	2.92	2.60	2.29	2.03	1.80	1.56	1.34	1.16	1.04
8	3.20	2.90	2.62	2.34	2.08	1.81	1.57	1.34	1.165	1.04
10	3.23	2.93	2.65	2.27	2.10	1.83	1.58	1.35	1.17	1.04
∞	3.41	3.11	2.815	2.51	2.22	1.93	1.65	1.395	1.19	1.05

Ratio of solenoid coil AC resistance to the AC resistance of the straightened wire in the while-colour cells from Medhurst's paper [177], with calculation results for long coils and wide spaced coils in the coloured cells from DWK [185]. The data can be used to predict solenoid coil AC resistance within 3% error when the operational frequency is lower than the SRF and the skin depth is less than 1/10 of the wire diameter. An end correction is needed to calculate AC resistance of coils with number of turns less than 30. p/d is the gap interval/ wire diameter ratio; l/D is the coil length/ coil diameter ratio.

A4. OCDGC rectifier operation process

$No.$	V_{IN}/V	V_{OUT}/V	$D1, D2, M2$, V_{C1}, V_{C2}	V_{gM1}/V	$i_{M1}, i_{RLOAD}, i_{CLOAD}$/A
1	Rises, V_{IN}=V_{OUT}, V_{IN}=V_{C1}+V_{thD1}	Drops, >0	D1, D2, no light V_{C1}, V_{C2} drops, M2 off	High, V_{OUT}	$\|i_{CLOAD}\|$=i_{RLOAD}=V_{OUT}/R_{LOAD}, i_{M1}=0
2	Rises, V_{IN}>V_{OUT}, V_{IN}>V_{C1}+V_{thD1}	Drops, >0	D1 light, D2 no light, M2 turns on, V_{C1} rises, V_{C2} drops	Low, 0V	i_{M1}< i_{RLOAD}, i_{RLOAD}=$\|i_{CLOAD}\|$+i_{M1}
3		Min, >0		Low, 0V	i_{RLOAD}=i_{M1}, $\|i_{CLOAD}\|$=0
4		Rises, >0		Low, 0V	i_{RLOAD}>0, rises; i_{CLOAD}>0, rises; i_{M1}>0, rises; i_{M1}=i_{CLOAD}+i_{RLOAD}.
5		V_{OUT}>V_{C2}+V_{thD2}	D1, D2 light, M2 on, V_{C1}, V_{C2} rise	Low, 0V	i_{RLOAD}>0, rises; i_{CLOAD}>0, rises; i_{M1}>0, rises; i_{M1}=i_{CLOAD}+i_{RLOAD}+i_{D2}.
6		Rises, >0		Low, 0V	
7	V_{IN}-V_{OUT} is max	Rises, >0		Low, 0V	i_{RLOAD}>0, rises; i_{CLOAD}=max; i_{M1}=max, i_{M1}=i_{CLOAD}+i_{RLOAD}+i_{D2}.
8	Rises, V_{IN}>V_{OUT}, V_{IN}>V_{C1}+V_{thD1}	Rises, >0		Low, 0V	i_{RLOAD}>0, rises; i_{CLOAD}>0, drops; i_{M1}>0, drops
9	V_{IN}= $V_{IN}(max)$ V_{IN}=V_{C1}+V_{thD1}	Rises, >0	D2 light, D1 no light, M2 on, V_{C2} rises, V_{C1} max	Low, 0V	
10	V_{IN}>V_{OUT}, V_{IN} drops from V_{IN}= $V_{IN}(max)$ till V_{IN}=V_{OUT}	Rises, >0	D2 light, D1 no light, M2 on, V_{C2} rises, V_{C1} drops	Low, 0V	
11		Max, >0 V_{OUT}=V_{C2}+V_{thD2}	D1, D2 no light, M2 turns off, V_{C2} max, V_{C1} drops	High, V_{OUT}	i_{M1}=0; i_{RLOAD}=$\|i_{CLOAD}\|$>0, drops; i_{CLOAD}<0
12		Drops, >0	D1, D2 no light, M2 turns	High, V_{OUT}	

13	V_{IN}<V_{OUT}	Drops, >0	off, V_{C1}, V_{C2} drop	High, V_{OUT}	

Operation of the OCDGC bootstrapping rectifier

A5. Rectifier performance

(1) Diode_connected PMOS rectifier

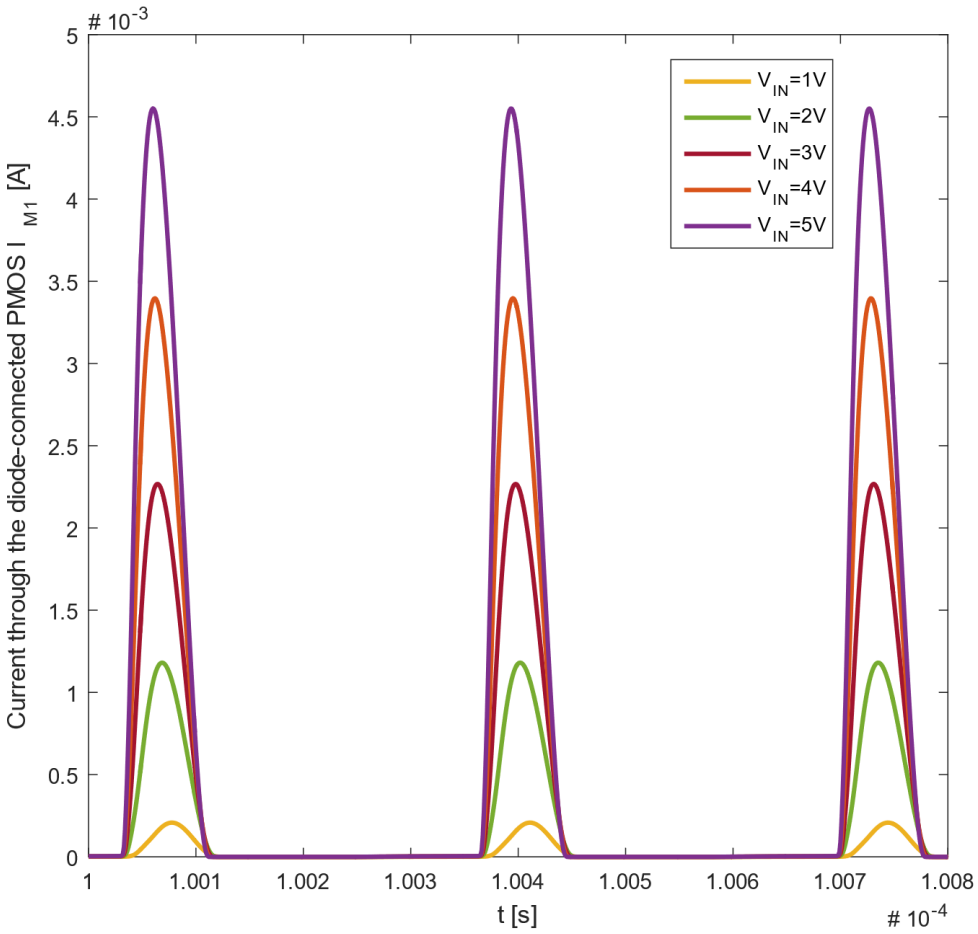

Waveform of the current through the diode-connected PMOS of the diode-connected PMOS rectifier for peak input voltages from 1V to 5V at the light load condition

(2) PMOS Pa12_g5a_nbl_mr_mac

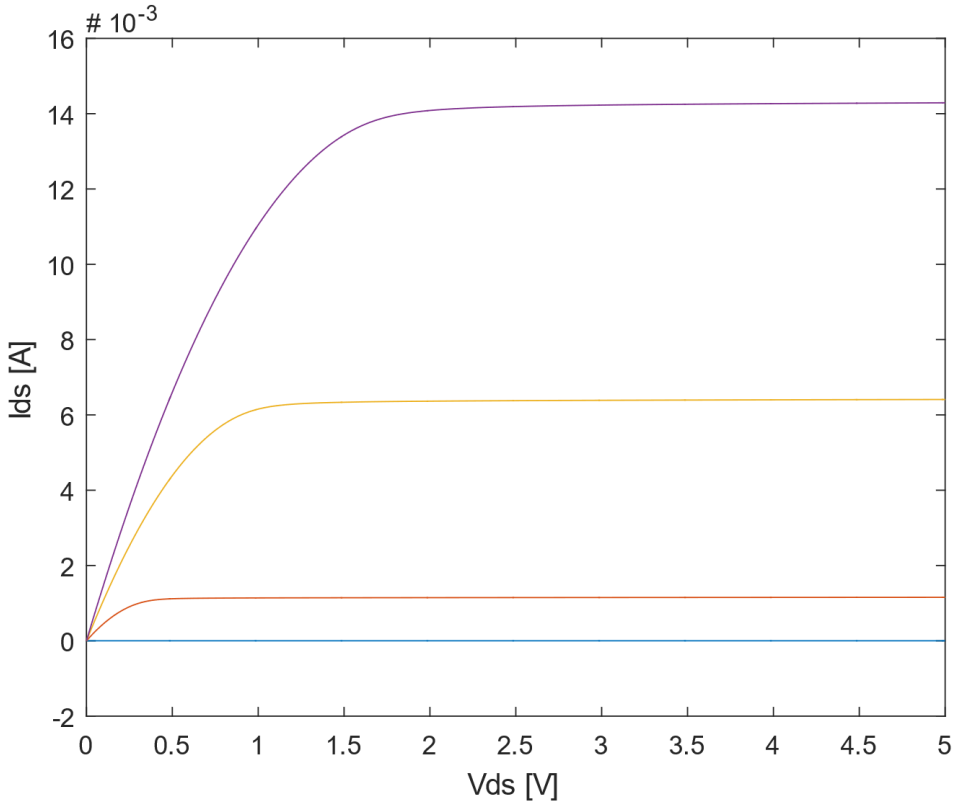

V-I characteristic of the PMOS Pa12_g5a_nbl_mr_mac, I_{sd} against V_{sd} (0-5V) with varying V_{sg} (0.5V blue, 1V red, 1.5V yellow, 2V pruple)

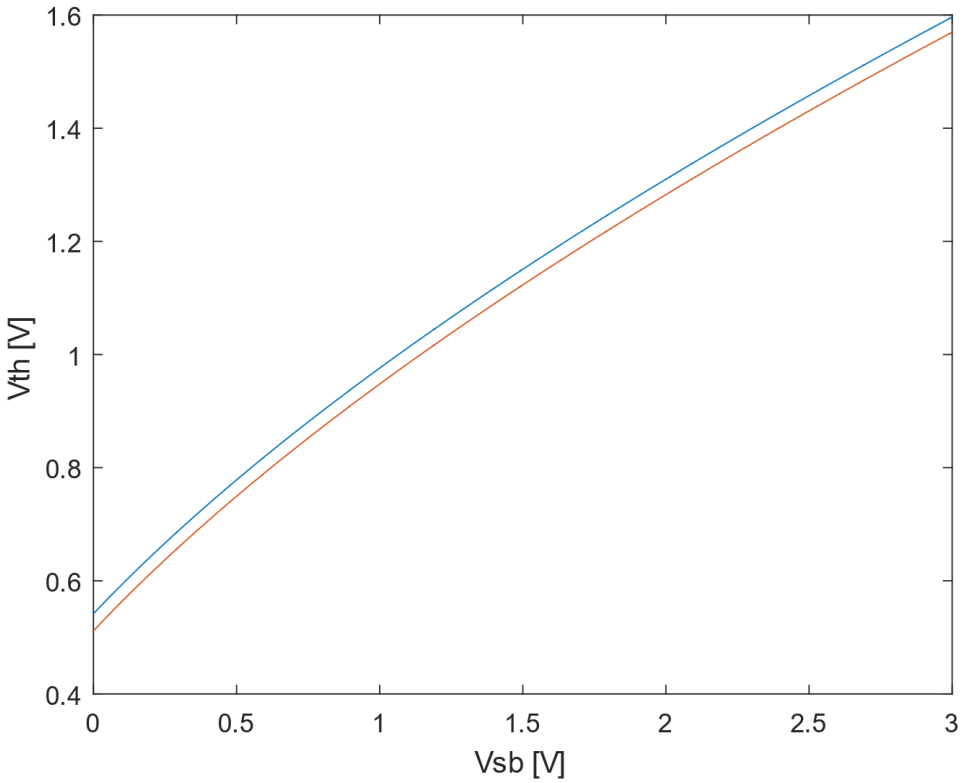

Threshold voltage V_{th} against V_{sb} (0 to 3V) of the PMOS Pa12_g5a_nbl_mr_mac in different number of fingers. (Red) number of fingers is 4, and multiplier is 8; (Blue) number of fingers is 2, and multiplier is 8.

(3) Basic BSR

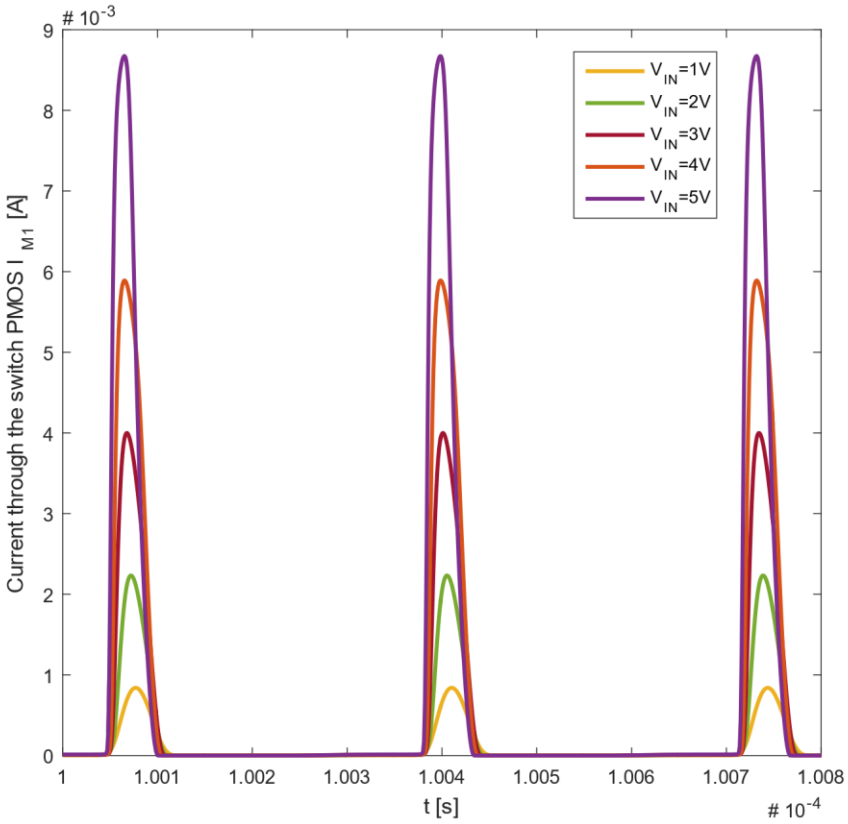

Waveform of current through the switch PMOS M1 of the basic BSR for peak input voltages from 1V to 5V at the light load condition

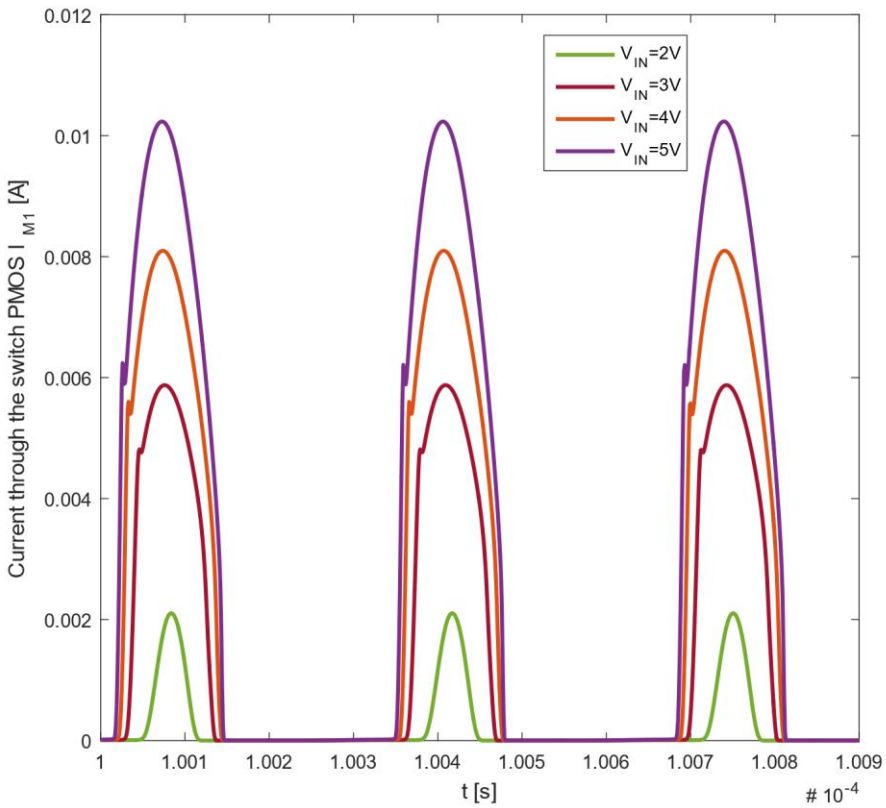

Waveform of current through the switch PMOS M1 of the basic BSR for peak input voltages from 1V to 5V at the heavy load condition

(4) Improved Static BSR

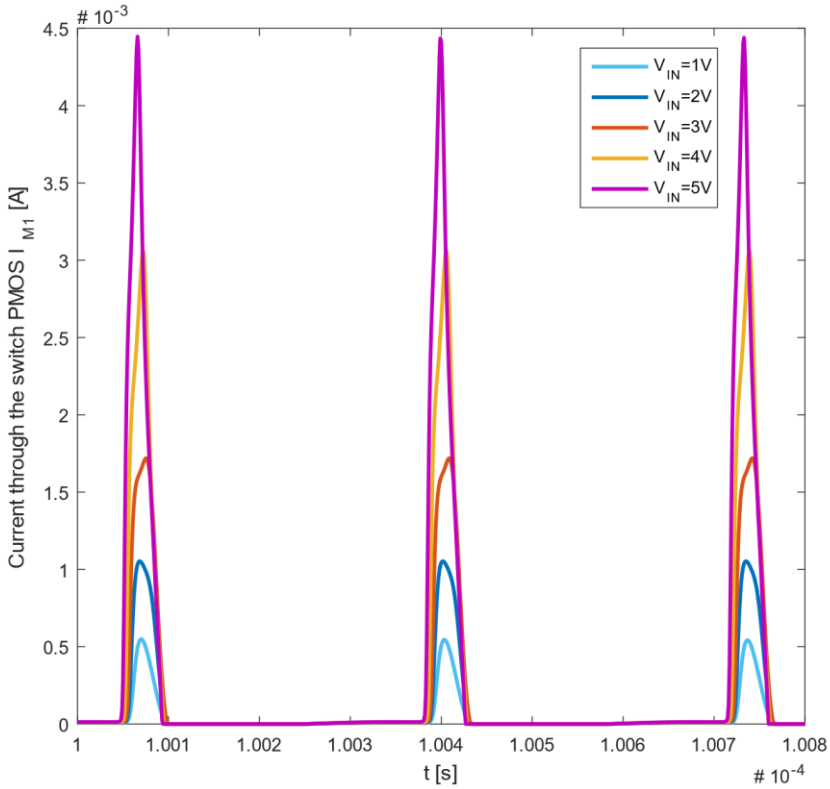

Waveform of current through the switch PMOS M1 of the improved static BSR for peak input voltages from 1V to 5V at the light load condition

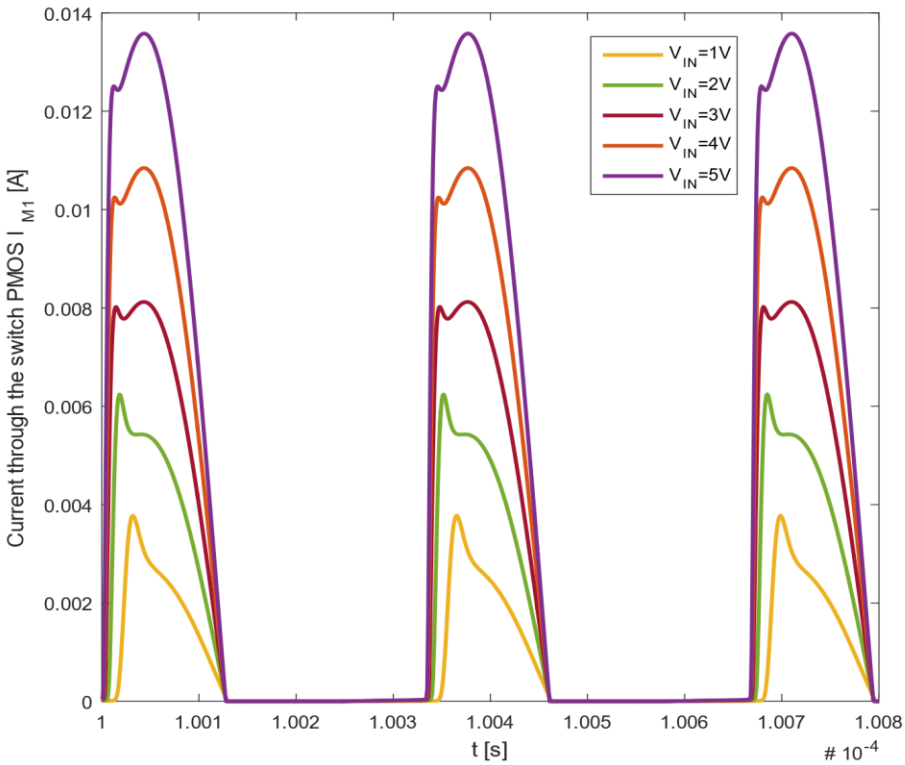

Waveform of current through the switch PMOS M1 of the improved static BSR for peak input voltages from 1V to 5V at the heavy load condition

(5) OCDGC rectifier

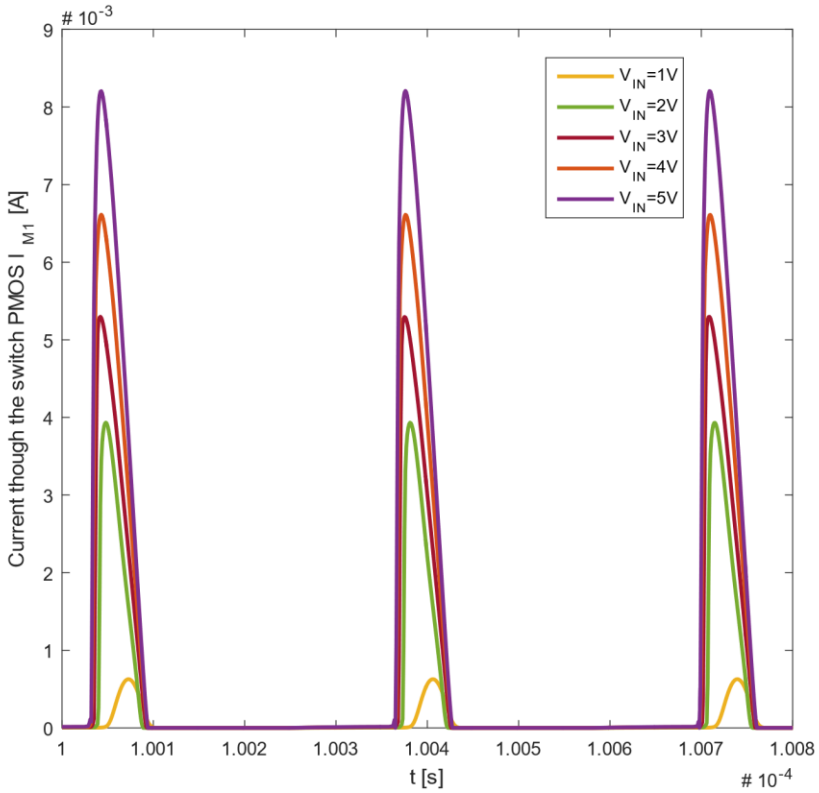

Waveform of the current through the switch PMOS M1 of the OCDGC rectifier for peak input voltages from 1V to 5V at the light load condition. No backward current flows through the PMOS at any time.

A6. Rectifier measurement result

Load line f=8000kHz VIN(p-p)=5V VIN+=2.20V Resistor+X10 probe Load		
VOUT Max (V)	VOUT min (V)	Iout rms (uA)
1.2	0.92	400
1.2	0.94	390
1.22	0.96	380
1.22	0.96	370
1.22	0.98	360
1.24	1	350
1.24	1	340
1.26	1.02	330
1.26	1.04	320
1.28	1.06	310
1.28	1.08	300
1.28	1.08	290
1.3	1.1	280
1.32	1.12	270
1.32	1.12	260
1.34	1.14	250
1.34	1.16	240
1.36	1.18	230
1.38	1.2	220
1.38	1.2	210
1.4	1.24	200
1.4	1.24	190
1.42	1.26	180
1.44	1.28	170
1.44	1.3	160
1.46	1.32	150
1.48	1.32	140
1.48	1.36	130
1.5	1.36	120
1.52	1.4	110
1.52	1.4	100

Load line f=8000kHz VIN(p-p)=5V VIN+=2.3V R+C load C=0.903uF		
VOUT Max (V)	VOUT min (V)	Iout rms (uA)
1.2	0.88	410
1.2	0.9	400
1.2	0.9	390
1.22	0.92	380
1.22	0.94	370
1.24	0.96	360
1.24	0.96	350
1.24	0.98	340
1.24	1	330
1.28	1.02	320
1.28	1.02	310
1.28	1.04	300
1.3	1.06	290
1.3	1.08	280
1.32	1.1	270
1.32	1.1	260
1.34	1.12	250
1.36	1.14	240
1.36	1.16	230
1.38	1.18	220
1.38	1.2	210
1.4	1.2	200
1.4	1.22	190
1.42	1.24	180
1.42	1.26	170
1.44	1.28	160
1.44	1.3	150
1.46	1.32	140
1.48	1.34	130
1.48	1.36	120
1.5	1.38	110
1.52	1.4	100

Load line f=8000kHz VIN(p-p)=6V VIN+=2.85V Resistor+X10 probe Load		
VOUT Max (V)	VOUT min (V)	Iout rms (uA)
1.55	1.2	520
1.55	1.2	510
1.55	1.2	500
1.55	1.2	490
1.55	1.2	480
1.55	1.25	470
1.6	1.25	460
1.6	1.25	450
1.6	1.3	440
1.6	1.3	430
1.6	1.3	420
1.6	1.3	410
1.6	1.3	400
1.65	1.35	390
1.65	1.35	380
1.65	1.35	370
1.65	1.4	360
1.65	1.4	350
1.7	1.4	340
1.7	1.4	330
1.7	1.45	320
1.7	1.45	310
1.7	1.45	300
1.7	1.5	290
1.75	1.5	280
1.75	1.5	270
1.75	1.55	260
1.75	1.55	250
1.8	1.55	240
1.8	1.6	230
1.8	1.6	220
1.8	1.6	210
1.85	1.65	200
1.85	1.65	190
1.85	1.65	180
1.85	1.7	170
1.9	1.7	160
1.9	1.7	150
1.9	1.75	140
1.9	1.75	130

Load line f=8000kHz VIN(p-p)=6V VIN+=2.85V R+C load C=0.903uF					
VOUT Max (V)	VOUT min (V)	Iout rms (uA)	VOUT Max (V)	VOUT min (V)	Iout rms (uA)
1.55	1.15	530	1.7	1.4	320
1.55	1.15	520	1.75	1.45	310
1.55	1.15	510	1.75	1.45	300
1.55	1.15	500	1.75	1.45	290
1.6	1.2	490	1.75	1.5	280
1.6	1.2	480	1.75	1.5	270
1.6	1.2	470	1.75	1.5	260
1.6	1.25	460	1.8	1.55	250
1.6	1.25	450	1.8	1.55	240
1.6	1.25	440	1.8	1.55	230
1.6	1.3	430	1.8	1.6	220
1.65	1.3	420	1.8	1.6	210
1.65	1.3	410	1.85	1.6	200
1.65	1.3	400	1.85	1.65	190
1.65	1.3	390	1.85	1.65	180
1.65	1.35	380	1.85	1.7	170
1.7	1.35	370	1.85	1.7	160
1.7	1.35	360	1.9	1.7	150
1.7	1.4	350	1.9	1.75	140
1.7	1.4	340	1.9	1.75	130
1.7	1.4	330	1.9	1.75	123

Load line f=8000kHz VIN(p-p)=7V VIN+=3.25V Resistor+X10 probe Load					
VOUT Max (V)	VOUT min (V)	Iout rms (uA)	VOUT Max (V)	VOUT min (V)	Iout rms (uA)
1.9	1.45	650	2.1	1.8	390
1.9	1.45	640	2.1	1.8	380
1.9	1.45	630	2.15	1.85	370
1.9	1.5	620	2.15	1.85	360
1.9	1.5	610	2.15	1.85	350
1.9	1.5	600	2.15	1.9	340
1.9	1.5	590	2.2	1.9	330
1.9	1.5	580	2.2	1.9	320
1.9	1.55	570	2.2	1.9	310
1.95	1.55	560	2.2	1.95	300
1.95	1.55	550	2.2	1.95	290
1.95	1.55	540	2.2	2	280
1.95	1.55	530	2.25	2	270
2	1.6	520	2.25	2	260
2	1.65	510	2.25	2	250
2	1.65	500	2.25	2.05	240
2.05	1.65	490	2.3	2.05	230
2.05	1.7	480	2.3	2.05	220
2.05	1.7	470	2.3	2.1	210
2.05	1.7	460	2.3	2.1	200
2.05	1.7	450	2.3	2.1	190
2.05	1.75	440	2.35	2.15	180
2.1	1.75	430	2.35	2.15	170
2.1	1.75	420	2.35	2.2	160
2.1	1.8	410	2.4	2.2	151
2.1	1.8	400			

Load line f=8000kHz VIN(p-p)=7V VIN+=3.25V R+C load C=0.903uF					
VOUT Max (V)	VOUT min (V)	Iout rms (uA)	VOUT Max (V)	VOUT min (V)	Iout rms (uA)
1.9	1.45	660	2.1	1.75	400
1.9	1.45	650	2.15	1.75	390
1.95	1.45	640	2.15	1.75	380
1.95	1.45	630	2.15	1.8	370
1.95	1.5	620	2.15	1.8	360
1.95	1.5	610	2.15	1.8	350
1.95	1.5	600	2.15	1.8	340
1.95	1.5	590	2.2	1.85	330
1.95	1.5	580	2.2	1.85	320
2	1.5	570	2.2	1.85	310
2	1.55	560	2.2	1.9	300
2	1.55	550	2.2	1.9	290
2	1.55	540	2.25	1.9	280
2	1.55	530	2.25	1.95	270
2	1.6	520	2.25	1.95	260
2	1.6	510	2.25	2	250
2.05	1.6	500	2.25	2	240
2.05	1.6	490	2.25	2	230
2.05	1.65	480	2.3	2.05	220
2.05	1.65	470	2.3	2.05	210
2.05	1.65	460	2.3	2.05	200
2.05	1.65	450	2.3	2.1	190
2.1	1.7	440	2.3	2.1	180
2.1	1.7	430	2.35	2.1	170
2.1	1.7	420	2.35	2.15	160
2.1	1.7	410	2.35	2.15	150

A7. Calculation program

1. AC resistance calculation

```
rdc=160; %relative dielectric constant=160
cr=1.72*10^-8; %coil resistivity unit:ohm*m
mr=1/0.625; %media resistivity unit:ohm*m
mrmp=1; %material relative magnetic permeability=1
epsi0=1e-9/(36*pi);%free spae dieletric constant
epsir=160;
miur=1;
miu0=4*pi*1e-7;%free space magnetic permeability
freq=8e6;%operational frequency

%pTX: TX gap interval; NTX: TX turn number; dwireTX: TX wire diame-
ter;
%DTX: TX diameter
dwireTX=1e-3; pTX=2.524e-3; DTX=0.201;  NTX=(1:20)';

%NRX: RX turn number; dwireRX: RX wire diameter; DRX: RX diameter
%pRX: RX gap interval;
dwireRX=1e-4; pRX=1e-4; DRX=2e-3; NRX=(1:250)';

%TX coil resistance

%lTX: length of TX;
lTX=NTX.*dwireTX+(NTX-1).*pTX;
%lwireTX: length of wire of TX; DTX: diameter of TX
lwireTX=((NTX*pi*DTX).^2+(lTX).^2).^0.5;
%AwireTX: area of wire of TX
AwireTX=(pi*dwireTX^2)/4;
%skd: skin depth; freq: operational frequency
skd=(cr/(pi*freq*miu0))^0.5;
%RDCTX: dc resistance of TX
RDCTX=cr*lwireTX/AwireTX;
%skf: skin factor
skf=dwireTX^2/4/(skd*dwireTX-skd^2);
%PrxF: proximity factor
PrxF=1:length(NTX);
%calculation of proximity factor
for i0=1:length(NTX)
for i1=1:9
for i2=1:11
    a=pTX/dwireTX;
    b=lTX(i0)/DTX;
    if a>=prof_pd(i1)&&a<prof_pd(i1+1)&& b>=prof_lD(i2)&&
b<prof_lD(i2+1)
        PrxF(i0)=prof(i2,i1);
    else
        if a>=prof_pd(i1+1)&& b>=prof_lD(i2)&& b<prof_lD(i2+1)
            PrxF(i0)=prof(i2,i1+1);
        else
            if a>=prof_pd(i1)&& a<prof_pd(i1+1)&& b>=prof_lD(i2+1)
               PrxF(i0)=prof(i2+1,i1);
            else
                if a>=prof_pd(i1+1)&& b>=prof_lD(i2+1)
                   PrxF(i0)=prof(i2+1,i1+1);
                end
            end
        end
    end
end
```

```
end
end
% RACTX: ac resistance of TX
RACTX=RDCTX.*(1+(skf-1).*PrxF'.*(NTX-1+1./PrxF')./NTX);

%plot(1:length(NTX),RACTX);
%xlabel('Turn number N');
%ylabel('Rac [?]');

%coupling coil resistane

%Couple coil has 1 turn
lCp=dwireTX;
%lwireCp: length of wire of Couple coil; DTX: diameter of Couple
coil
lwireCp=pi*DTX;
%AwireCp: area of wire of Couple coil
AwireCp=(pi*dwireTX^2)/4;
%RDCTX: dc resistance of Cp
RDCCp=cr*lwireCp/AwireCp;
% RACTX: ac resistance of coupling coil
RACCp=RDCCp.*skf;

%RX coil resistance

%lRX: length of RX;
lRX=NRX.*dwireRX+(NRX-1).*pRX;
%lwireRX: length of wire of RX;
lwireRX=((NRX*pi*DRX).^2+(lRX).^2).^0.5;
%AwireRX: area of wire of RX
AwireRX=(pi*dwireRX^2)/4;
%RDCRX: dc resistance of RX
RDCRX=cr*lwireRX/AwireRX;
%skfRX: skin factor of RX
skfRX=dwireRX^2/4/(skd*dwireRX-skd^2);
%PrxF: proximity factor
PrxFRX=1:length(NRX);
%calculation of proximity factor
for i0=1:length(NRX)
for i1=1:9
for i2=1:11
    a=pRX/dwireRX;
    b=lRX(i0)/DRX;
    if a>=prof_pd(i1)&&a<prof_pd(i1+1)&& b>=prof_lD(i2)&&
b<prof_lD(i2+1)
        PrxFRX(i0)=prof(i2,i1);
    else
        if a>=prof_pd(i1+1)&& b>=prof_lD(i2)&& b<prof_lD(i2+1)
            PrxFRX(i0)=prof(i2,i1+1);
        else
            if a>=prof_pd(i1)&& a<prof_pd(i1+1)&& b>=prof_lD(i2+1)
               PrxFRX(i0)=prof(i2+1,i1);
            else
                if a>=prof_pd(i1+1)&& b>=prof_lD(i2+1)
                   PrxFRX(i0)=prof(i2+1,i1+1);
                end
            end
        end
    end
end
end
end
% RACRX: ac resistance of RX coil
```

```
RACRX=RDCRX.*(1+(skfRX-1).*PrxFRX'.*(NRX-1+1./PrxFRX')./NRX);
```

2. Magnetic field strength calculation

```
%VIN: input voltage; TD: transfer distance
VIN=1; TD=0.2;

%Primary coil current
Ipri=VIN./4./(RACCp.*RACTX).^0.5;

%primary coil magnetic field

c=1:length(NTX);
Hpri=1:length(NTX);
for i3=1:length(NTX)
        Hpri(i3)=0;
for i4=1:NTX(i3)

Hpri(i3)=Hpri(i3)+Ipri(i3).*(DTX/2)^2./2./((DTX/2)^2+(TD+(pTX+dwireT
X).*(i4-1)).^2).^1.5;

c(i3)=Ipri(i3).*(DTX/2)^2./2./((DTX/2)^2+(TD+(pTX+dwireTX)*(i4-
1))^2)^1.5;
end
end

%Attenuation in media
ATT=2*pi*freq*(epsi0*miu0*epsir*miur/2*((1+1/(mr*2*pi*freq*epsi0*ep-
sir)^2)^0.5-1))^0.5;
```

3. Ferrite-core solenoid coil

```
%miufc: relative permeability of ferrite core coil;
%HZ: set magnetic field strength
miufc=80+5i; HZ=1.5;

%ARX: cross-sectional area of RX
ARX=pi*DRX^2/4;

%efc: size factor of ferrite core coil
efc=(1-(DRX./lRX).^2).^0.5;
%Dfe: demagnetising factor of elliptical ferrite core coil
Dfe=DRX^2./2./lRX.^2./efc.^3.*(log((1+efc)./(1-efc))-2.*efc);
%Dfc: demagnetising factor of cylindrical ferrite core coil
Dfc=Dfe.*0.755.*(lRX./DRX).^0.13;
%miuf_RE: real part of ferrite core coil magnetic permeability;
%miuf_IM: imaginary part
miuf_RE=real(miufc./(1+Dfc.*(miufc-1)));
miuf_IM=imag(miufc./(1+Dfc.*(miufc-1)));
%VIND_F: ferrite core coil induced voltage with constant HZ;
VIND_F=2*pi*freq*miu0*miuf_RE.*NRX*HZ*ARX;
%VIND_F1: ferrite core coil induced voltage with transmitter;
Ipri_op=Ipri(6);
NTX_op=6;
c1=1:length(NRX);
VIND_F1=1:length(NRX);
for i3=1:length(NRX)
        Hpri2=0;
        VIND_F1(i3)=0;
for i4=1:NRX(i3)
```

```
    for i5=1:NTX_op
        Hpri2=Hpri2+Ipri_op.*(DTX/2)^2./2./((DTX/2)^2+(TD+(pRX+dwir-
eRX).*(i4-1)+(pTX+dwireTX).*(i5-1)).^2).^1.5;
    end
end
c1(i3)=Hpri2;
VIND_F1(i3)=2*pi*freq*miu0*miuf_RE(i3)*Hpri2*ARX;
end
VIND_F1=VIND_F1';
%LRX0=air core inductance of RX
LRX0=10*pi*miu0.*NRX.^2*(DRX/2)^2./(9*DRX/2+10.*lRX);
%LRXFC=ferrite core inductance of RX
LRXFC=miuf_RE.*LRX0;
%RFC=ferrite coil resistance
RFC=2*pi.*freq*miuf_IM.*LRX0;
%RRXC: total resistance of RX coil
RRXC=RFC+RACRX;
%PRX1: receiver coil output power with set field strength
PRX=VIND_F.^2/4./RRXC;
%PRX2: reeiver coil output power with transmitter coil
PRX1=VIND_F1.^2/4./RRXC;
```

4. Coil capacitance

```
%capacitance of Coupling coil
%epsi_i: internal dielectric constant; epsi_x: external dielectric
%constant;
epsi_i=2.7; epsi_x=1;
%kTX: size factor of TX; ZTX: another size factor of TX
kTX=DTX/lCp;
ZTX=2/pi/kTX;
%kLTX: Nagaoka's coefficient
kLTX=ZTX*(log10(1+1/ZTX)+1/(-10.632+3.347/kTX+1.764/kTX^2-
0.47/(0.755+kTX)^1.44));
%CLCP: capacitance of coupling coil
CLCP=4*epsi0*epsi_x/pi*lCp*(1+(1/kLTX-
1)*(1+epsi_i/epsi_x)/2)+2*epsi0*(epsi_i+epsi_x)*DTX/log(1+pi^2/kTX);
%LCPR: inductance to resonate CLCP
LCPR=1/(2*pi*freq)^2/CLCP;
%LCPS: self-inductance of coupling coil
LCPS=miu0*pi*DTX^2/4*lCp;
ZLCPS=(2*pi*freq)*LCPS;
```

5. Full system performance

```
%Mutual inductance between primary coil and receiver coil
%MTX_RX_air: mutual inductance in air
%MTX_RX_tiss: mutual inductance in tissue
d1=1:length(NRX);
MTX_RX_air=1:length(NRX);
MTX_RX_tiss=1:length(NRX);
for i3=1:length(NRX)
        Hpri3=0;
        MTX_RX_air(i3)=0;
        MTX_RX_tiss(i3)=0;
for i4=1:NRX(i3)
    for i5=1:NTX_op
        Hpri3=Hpri3+(DTX/2)^2./2./((DTX/2)^2+(TD+(pRX+dwireRX).*(i4-
1)+(pTX+dwireTX).*(i5-1)).^2).^1.5;
    end
end
```

```
d1(i3)=Hpri3;
MTX_RX_air(i3)=miu0*miuf_RE(i3)*Hpri3*ARX;
MTX_RX_tiss(i3)=miu0*miuf_RE(i3)*Hpri3*ARX*exp(-ATT*TD);
end
MTX_RX_air=MTX_RX_air';
MTX_RX_tiss=MTX_RX_tiss';

%reflected resistance from RX to primary coil
%RRX_TX_air: air; RRX_TX_tiss: tissue;
%RREC_eq: equivalent resistance of rectifier
RREC_eq=200;
RRX_TX_air=(2*pi*freq.*MTX_RX_air).^2./(RRXC+RREC_eq);
RRX_TX_tiss=(2*pi*freq.*MTX_RX_tiss).^2./(RRXC+RREC_eq);
%reflected resistance from coupling coil to primary coil
RCp_TX_air=1/3.*(RACTX(6)+RRX_TX_air);
RCp_TX_tiss=1/3.*(RACTX(6)+RRX_TX_tiss);
%reflected resistance from TX to RX
RTX_RX_air=(2*pi*freq.*MTX_RX_air).^2./(RACTX(6)+RCp_TX_air);
RTX_RX_tiss=(2*pi*freq.*MTX_RX_tiss).^2./(RACTX(6)+RCp_TX_tiss);

%Full system primary coil current
Ipri_full_air=VIN./4./(RACCp.*(RACTX(6)+RRX_TX_air)).^0.5;
Ipri_full_tiss=VIN./4./(RACCp.*(RACTX(6)+RRX_TX_tiss)).^0.5;
%VIND_F1_full: full system ferrite core coil induced voltage;
Ipri_air_op=Ipri_full_air(6);
Ipri_tiss_op=Ipri_full_tiss(6);
NTX_op=6;
c1_air=1:length(NRX);
VIND_F1_full_air=1:length(NRX);
c1_tiss=1:length(NRX);
VIND_F1_full_tiss=1:length(NRX);
for i3=1:length(NRX)
        Hpri4_air=0;
        VIND_F1_full_air(i3)=0;
        Hpri4_tiss=0;
        VIND_F1_full_tiss(i3)=0;
for i4=1:NRX(i3)
    for i5=1:NTX_op

Hpri4_air=Hpri4_air+Ipri_air_op.*(DTX/2)^2./2./((DTX/2)^2+(TD+(pRX+d
wireRX).*(i4-1)+(pTX+dwireTX).*(i5-1)).^2).^1.5;

Hpri4_tiss=Hpri4_tiss+Ipri_tiss_op.*(DTX/2)^2./2./((DTX/2)^2+(TD+(pR
X+dwireRX).*(i4-1)+(pTX+dwireTX).*(i5-1)).^2).^1.5;
    end
end
c1_air(i3)=Hpri4_air;
VIND_F1_full_air(i3)=2*pi*freq*miu0*miuf_RE(i3)*Hpri4_air*ARX;
c1_tiss(i3)=Hpri4_tiss;
VIND_F1_full_tiss(i3)=2*pi*freq*miu0*miuf_RE(i3)*Hpri4_tiss*ARX*exp(
-ATT*TD);
end
VIND_F1_full_air=VIND_F1_full_air';
VIND_F1_full_tiss=VIND_F1_full_tiss';
%Input power of Rectifier
PREC_air=(VIND_F1_full_air./(RTX_RX_air+RRXC+RREC_eq)).^2*RREC_eq;
PREC_tiss=(VIND_F1_full_tiss./(RTX_RX_tiss+RRXC+RREC_eq)).^2*RREC_eq
;
%Variation of equivalent rectifier resistance with set NRX
RREC_eq_V=(1:1000)';
PREC_air_50=(VIND_F1_full_air(50)./(RTX_RX_air(50)+RRXC(50)+RREC_eq_
V)).^2.*RREC_eq_V;
```

```
PREC_air_100=(VIND_F1_full_air(100)./(RTX_RX_air(100)+RRXC(100)+RREC
_eq_V)).^2.*RREC_eq_V;
PREC_air_150=(VIND_F1_full_air(150)./(RTX_RX_air(150)+RRXC(150)+RREC
_eq_V)).^2.*RREC_eq_V;
PREC_air_200=(VIND_F1_full_air(200)./(RTX_RX_air(200)+RRXC(200)+RREC
_eq_V)).^2.*RREC_eq_V;
PREC_air_250=(VIND_F1_full_air(250)./(RTX_RX_air(250)+RRXC(250)+RREC
_eq_V)).^2.*RREC_eq_V;
PREC_tiss_50=(VIND_F1_full_tiss(50)./(RTX_RX_tiss(50)+RRXC(50)+RREC_
eq_V)).^2.*RREC_eq_V;
PREC_tiss_100=(VIND_F1_full_tiss(100)./(RTX_RX_tiss(100)+RRXC(100)+R
REC_eq_V)).^2.*RREC_eq_V;
PREC_tiss_150=(VIND_F1_full_tiss(150)./(RTX_RX_tiss(150)+RRXC(150)+R
REC_eq_V)).^2.*RREC_eq_V;
PREC_tiss_200=(VIND_F1_full_tiss(200)./(RTX_RX_tiss(200)+RRXC(200)+R
REC_eq_V)).^2.*RREC_eq_V;
PREC_tiss_250=(VIND_F1_full_tiss(250)./(RTX_RX_tiss(250)+RRXC(250)+R
REC_eq_V)).^2.*RREC_eq_V;

%plot(NRX,y1data);
%xlabel('RX turn number NRX');
%ylabel('Induced voltage [V]');
```

6. Impedance matching

```
%T-network
%RZ: virtual impedance of T-network; RS: source impedance;
RZ=100; RS=50;
%MCP: Mutual inductance between coupling coil and primary coil
RACTX_op=RACTX(6);
MCP=(RACCp*RACTX_op)^0.5/(2*pi*freq);
%Reflected impedance from primary coil to coupling coil
RTXrf=(2*pi*freq*MCP)^2/RACTX_op;
%T-network parameters
Q1=(RZ/RS-1)^0.5;
X5=RZ/Q1;
X2=-RS*Q1;
Q2=(RZ/(RACCp+RTXrf))^0.5;
X4=RZ/Q2;
X1=-(RACCp+RTXrf)*Q2;
X3=(X4*X5)/(X4+X5);
VCP=X5/(RS+X2+X5)*X4/(RZ+X4)*VIN*0.5;
C2M=-1/X2/(2*pi*freq);
C1M=-1/X1/(2*pi*freq);
L3M=X3/(2*pi*freq);

%Receiver circuit impedance matching
%RREC:rectifier equivalent resistance
I=1i; RREC=1:5000;
RRXS_air_100=RTX_RX_air(100)+RRXC(100);
RRXS_air_150=RTX_RX_air(150)+RRXC(150);
RRXS_air_200=RTX_RX_air(200)+RRXC(200);
RRXS_air_250=RTX_RX_air(250)+RRXC(250);
Q_100=1:length(RREC);
Q_150=1:length(RREC);
Q_200=1:length(RREC);
Q_250=1:length(RREC);
X1_100=1:length(RREC);
X2_100=1:length(RREC);
X1_150=1:length(RREC);
```

```
X2_150=1:length(RREC);
X1_200=1:length(RREC);
X2_200=1:length(RREC);
X1_250=1:length(RREC);
X2_250=1:length(RREC);
VREC_air_100=1:length(RREC);
VREC_air_150=1:length(RREC);
VREC_air_200=1:length(RREC);
VREC_air_250=1:length(RREC);
for i6=RREC
if RRXS_air_100>RREC(i6)
    Q_100(i6)=(RRXS_air_100/RREC(i6)-1)^0.5;
    X1_100(i6)=RRXS_air_100/Q_100(i6);
    X2_100(i6)=-RREC(i6)*Q_100(i6);

VREC_air_100(i6)=0.5*abs(X1_100(i6)*I/(X1_100(i6)*I+RRXS_air_100))*V
IND_F1_full_air(100);
else if RRXS_air_100<RREC(i6)
        Q_100(i6)=(RREC(i6)/RRXS_air_100-1)^0.5;
        X1_100(i6)=RREC(i6)/Q_100(i6);
        X2_100(i6)=-RRXS_air_100*Q_100(i6);

VREC_air_100(i6)=0.5*abs(X1_100(i6)*I/(X1_100(i6)*I+X2_100(i6)*I+RRX
S_air_100))*VIND_F1_full_air(100);
    %else
       % VREC_air_100(i6)=0.5*VIND_F1_full_air(100);

    end
end
end
VREC_air_100=VREC_air_100';
X1_100=X1_100';
X2_100=X2_100';
L1_100=X1_100/(2*pi*freq);
C2_100=-1/X2_100/(2*pi*freq);

for i6=RREC
if RRXS_air_150>RREC(i6)
    Q_150(i6)=(RRXS_air_150/RREC(i6)-1)^0.5;
    X1_150(i6)=RRXS_air_150/Q_150(i6);
    X2_150(i6)=-RREC(i6)*Q_150(i6);

VREC_air_150(i6)=0.5*abs(X1_150(i6)*I/(X1_150(i6)*I+RRXS_air_150))*V
IND_F1_full_air(150);
else if RRXS_air_150<RREC(i6)
        Q_150(i6)=(RREC(i6)/RRXS_air_150-1)^0.5;
        X1_150(i6)=RREC(i6)/Q_150(i6);
        X2_150(i6)=-RRXS_air_150*Q_150(i6);

VREC_air_150(i6)=0.5*abs(X1_150(i6)*I/(X1_150(i6)*I+X2_150(i6)*I+RRX
S_air_150))*VIND_F1_full_air(150);
    else
        VREC_air_150(i6)=0.5*VIND_F1_full_air(150);
    end
end
end
VREC_air_150=VREC_air_150';
X1_150=X1_150';
X2_150=X2_150';
L1_150=X1_150/(2*pi*freq);
C2_150=-1/X2_150/(2*pi*freq);

for i6=RREC
```

```
if RRXS_air_200>RREC(i6)
    Q_200(i6)=(RRXS_air_200/RREC(i6)-1)^0.5;
    X1_200(i6)=RRXS_air_200/Q_200(i6);
    X2_200(i6)=-RREC(i6)*Q_200(i6);

VREC_air_200(i6)=0.5*abs(X1_200(i6)*I/(X1_200(i6)*I+RRXS_air_200))*V
IND_F1_full_air(200);
else if RRXS_air_200<RREC(i6)
        Q_200(i6)=(RREC(i6)/RRXS_air_200-1)^0.5;
        X1_200(i6)=RREC(i6)/Q_200(i6);
        X2_200(i6)=-RRXS_air_200*Q_200(i6);

VREC_air_200(i6)=0.5*abs(X1_200(i6)*I/(X1_200(i6)*I+X2_200(i6)*I+RRX
S_air_200))*VIND_F1_full_air(200);
    else
        VREC_air_200(i6)=0.5*VIND_F1_full_air(200);
    end
end
end
VREC_air_200=VREC_air_200';
X1_200=X1_200';
X2_200=X2_200';
L1_200=X1_200/(2*pi*freq);
C2_200=-1/X2_200/(2*pi*freq);

for i6=RREC
if RRXS_air_250>RREC(i6)
    Q_250(i6)=(RRXS_air_250/RREC(i6)-1)^0.5;
    X1_250(i6)=RRXS_air_250/Q_250(i6);
    X2_250(i6)=-RREC(i6)*Q_250(i6);

VREC_air_250(i6)=0.5*abs(X1_250(i6)*I/(X1_250(i6)*I+RRXS_air_250))*V
IND_F1_full_air(250);
else if RRXS_air_250<RREC(i6)
        Q_250(i6)=(RREC(i6)/RRXS_air_250-1)^0.5;
        X1_250(i6)=RREC(i6)/Q_250(i6);
        X2_250(i6)=-RRXS_air_250*Q_250(i6);

VREC_air_250(i6)=0.5*abs(X1_250(i6)*I/(X1_250(i6)*I+X2_250(i6)*I+RRX
S_air_250))*VIND_F1_full_air(250);
    else
        VREC_air_250(i6)=0.5*VIND_F1_full_air(250);
    end
end
end
VREC_air_250=VREC_air_250';
X1_250=X1_250';
X2_250=X2_250';
L1_250=X1_250/(2*pi*freq);
C2_250=-1/X2_250/(2*pi*freq);

%tissue
RRXS_tiss_100=RTX_RX_tiss(100)+RRXC(100);
RRXS_tiss_150=RTX_RX_tiss(150)+RRXC(150);
RRXS_tiss_200=RTX_RX_tiss(200)+RRXC(200);
RRXS_tiss_250=RTX_RX_tiss(250)+RRXC(250);
Q_100_tiss=1:length(RREC);
Q_150_tiss=1:length(RREC);
Q_200_tiss=1:length(RREC);
Q_250_tiss=1:length(RREC);
X1_100_tiss=1:length(RREC);
X2_100_tiss=1:length(RREC);
X1_150_tiss=1:length(RREC);
```

```
X2_150_tiss=1:length(RREC);
X1_200_tiss=1:length(RREC);
X2_200_tiss=1:length(RREC);
X1_250_tiss=1:length(RREC);
X2_250_tiss=1:length(RREC);
VREC_tiss_100=1:length(RREC);
VREC_tiss_150=1:length(RREC);
VREC_tiss_200=1:length(RREC);
VREC_tiss_250=1:length(RREC);
for i6=RREC
if RRXS_tiss_100>RREC(i6)
    Q_100_tiss(i6)=(RRXS_tiss_100/RREC(i6)-1)^0.5;
    X1_100_tiss(i6)=RRXS_tiss_100/Q_100_tiss(i6);
    X2_100_tiss(i6)=-RREC(i6)*Q_100_tiss(i6);

VREC_tiss_100(i6)=0.5*abs(X1_100_tiss(i6)*I/(X1_100_tiss(i6)*I+RRXS_
tiss_100))*VIND_F1_full_tiss(100);
else if RRXS_tiss_100<RREC(i6)
        Q_100_tiss(i6)=(RREC(i6)/RRXS_tiss_100-1)^0.5;
        X1_100_tiss(i6)=RREC(i6)/Q_100_tiss(i6);
        X2_100_tiss(i6)=-RRXS_tiss_100*Q_100_tiss(i6);

VREC_tiss_100(i6)=0.5*abs(X1_100_tiss(i6)*I/(X1_100_tiss(i6)*I+X2_10
0_tiss(i6)*I+RRXS_tiss_100))*VIND_F1_full_tiss(100);
    else
        VREC_tiss_100(i6)=0.5*VIND_F1_full_tiss(100);
    end
end
end
VREC_tiss_100=VREC_tiss_100';
X1_100_tiss=X1_100_tiss';
X2_100_tiss=X2_100_tiss';
L1_100_tiss=X1_100_tiss/(2*pi*freq);
C2_100_tiss=-1/X2_100_tiss/(2*pi*freq);

for i6=RREC
if RRXS_tiss_150>RREC(i6)
    Q_150_tiss(i6)=(RRXS_tiss_150/RREC(i6)-1)^0.5;
    X1_150_tiss(i6)=RRXS_tiss_150/Q_150_tiss(i6);
    X2_150_tiss(i6)=-RREC(i6)*Q_150_tiss(i6);

VREC_tiss_150(i6)=0.5*abs(X1_150_tiss(i6)*I/(X1_150_tiss(i6)*I+RRXS_
tiss_150))*VIND_F1_full_tiss(150);
else if RRXS_tiss_150<RREC(i6)
        Q_150_tiss(i6)=(RREC(i6)/RRXS_tiss_150-1)^0.5;
        X1_150_tiss(i6)=RREC(i6)/Q_150_tiss(i6);
        X2_150_tiss(i6)=-RRXS_tiss_150*Q_150_tiss(i6);

VREC_tiss_150(i6)=0.5*abs(X1_150_tiss(i6)*I/(X1_150_tiss(i6)*I+X2_15
0_tiss(i6)*I+RRXS_tiss_150))*VIND_F1_full_tiss(150);
    else
        VREC_tiss_150(i6)=0.5*VIND_F1_full_tiss(150);
    end
end
end
VREC_tiss_150=VREC_tiss_150';
X1_150_tiss=X1_150_tiss';
X2_150_tiss=X2_150_tiss';
L1_150_tiss=X1_150_tiss/(2*pi*freq);
C2_150_tiss=-1/X2_150_tiss/(2*pi*freq);

for i6=RREC
if RRXS_tiss_200>RREC(i6)
```

```
    Q_200_tiss(i6)=(RRXS_tiss_200/RREC(i6)-1)^0.5;
    X1_200_tiss(i6)=RRXS_tiss_200/Q_200_tiss(i6);
    X2_200_tiss(i6)=-RREC(i6)*Q_200_tiss(i6);

VREC_tiss_200(i6)=0.5*abs(X1_200_tiss(i6)*I/(X1_200_tiss(i6)*I+RRXS_
tiss_200))*VIND_F1_full_tiss(200);
else if RRXS_tiss_200<RREC(i6)
        Q_200_tiss(i6)=(RREC(i6)/RRXS_tiss_200-1)^0.5;
        X1_200_tiss(i6)=RREC(i6)/Q_200_tiss(i6);
        X2_200_tiss(i6)=-RRXS_tiss_200*Q_200_tiss(i6);

VREC_tiss_200(i6)=0.5*abs(X1_200_tiss(i6)*I/(X1_200_tiss(i6)*I+X2_20
0_tiss(i6)*I+RRXS_tiss_200))*VIND_F1_full_tiss(200);
    else
        VREC_tiss_200(i6)=0.5*VIND_F1_full_tiss(200);
    end
end
end
VREC_tiss_200=VREC_tiss_200';
X1_200_tiss=X1_200_tiss';
X2_200_tiss=X2_200_tiss';
L1_200_tiss=X1_200_tiss/(2*pi*freq);
C2_200_tiss=-1/X2_200_tiss/(2*pi*freq);

for i6=RREC
if RRXS_tiss_250>RREC(i6)
    Q_250_tiss(i6)=(RRXS_tiss_250/RREC(i6)-1)^0.5;
    X1_250_tiss(i6)=RRXS_tiss_250/Q_250_tiss(i6);
    X2_250_tiss(i6)=-RREC(i6)*Q_250_tiss(i6);

VREC_tiss_250(i6)=0.5*abs(X1_250_tiss(i6)*I/(X1_250_tiss(i6)*I+RRXS_
tiss_250))*VIND_F1_full_tiss(250);
else if RRXS_tiss_250<RREC(i6)
        Q_250_tiss(i6)=(RREC(i6)/RRXS_tiss_250-1)^0.5;
        X1_250_tiss(i6)=RREC(i6)/Q_250_tiss(i6);
        X2_250_tiss(i6)=-RRXS_tiss_250*Q_250_tiss(i6);

VREC_tiss_250(i6)=0.5*abs(X1_250_tiss(i6)*I/(X1_250_tiss(i6)*I+X2_25
0_tiss(i6)*I+RRXS_tiss_250))*VIND_F1_full_tiss(250);
    else
        VREC_tiss_250(i6)=0.5*VIND_F1_full_tiss(250);
    end
end
end
VREC_tiss_250=VREC_tiss_250';
X1_250_tiss=X1_250_tiss';
X2_250_tiss=X2_250_tiss';
L1_250_tiss=X1_250_tiss/(2*pi*freq);
C2_250_tiss=-1/X2_250_tiss/(2*pi*freq);

plot(RREC,y2data);
xlabel('Rectifier input resistance [Ohm]');
ylabel('Rectifier rms input voltage [V]');
```

Reference

[1] F.-G. Zeng, S. Rebscher, W. Harrison, X. Sun, and H. Feng, “Cochlear implants: System design, integration, and evaluation,” IEEE Rev. Biomed. Eng., vol. 1, pp. 115–142, 2008.

[2] I. Hochmair et al., “Med-el cochlear implants: State of the art and a glimpse into the future,” Trends Amplification, vol. 10, no. 4, pp. 201– 219, 2006.

[3] J. F. Patrick, P. A. Busby, and P. J. Gibson, “The development of the nucleus freedom cochlear implant system,” Trends Amplification, vol. 10, no. 4, pp. 175–200, 2006.

[4] J. P. DiMarco, “Implantable cardioverter-defibrillators,” New England J. Med., vol. 349, no. 19, pp. 1836–1847, 2003

[5] J. S. Ho et al., “Wireless power transfer to deep-tissue microimplants,” Proc. Nat. Acad. Sci., vol. 111, no. 22, pp. 7974–7979, 2014.

[6] J. S. Ho, A. J. Yeh, S. Kim, and A. S. Poon, “Wireless powering for miniature implantable systems,” in Neural Computation, Neural Devices and Neural Prosthesis. New York, NY, USA: Springer, 2014, pp. 313–333.

[7] E. Y. Chow, A. L. Chlebowski, S. Chakraborty, W. J. Chappell, and P. P. Irazoqui, “Fully wireless implantable cardiovascular pressure monitor integrated with a medical stent,” IEEE Trans. Biomed. Eng., vol. 57, no. 6, pp. 1487–1496, Jun. 2010

[8] J. Weiland and M. Humayun, “Visual prosthesis,” Proc. IEEE, vol. 96, no. 7, pp. 1076–1084, Jul. 2008

[9] Z. Yang, W. Liu, and E. Basham, “Inductor modeling in wireless links for implantable electronics,” IEEE Trans. Magn., vol. 43, no. 10, pp. 3851– 3860, Oct. 2007.

[10] L. Wu, Z. Yang, E. Basham, and W. Liu, “An efficient wireless power link for high voltage retinal implant,” in Proc. IEEE Biomed. Circuits Syst. Conf., 2008, pp. 101–104.

[11] K. Chen, Z. Yang, L. Hoang, J. Weiland, M. Humayun, and W. Liu, “An integrated 256-channel epiretinal prosthesis,” IEEE J. Solid-State Circuits, vol. 45, no. 9, pp. 1946–1956, Sep. 2010.

[12] D. B. Shire et al., “Development and implantation of a minimally invasive wireless subretinal neurostimulator,” IEEE Trans. Biomed. Eng., vol. 56, no. 10, pp. 2502–2511, Oct. 2009.

[13] S. K. Kelly et al., “Realization of a 15-channel, hermetically-encased wireless subretinal prosthesis for the blind,” in Proc. Annu. Int. Conf. IEEE Eng. Med. Biol. Soc., 2009, pp. 200–203.

[14] J. F. Rizzo III, “Update on retinal prosthetic research: The Boston Retinal Implant Project,” J.Neuro-Ophthalmol., vol. 31, no. 2, pp. 160–168, 2011.

[15] S. K. Kelly et al., “A hermetic wireless subretinal neurostimulator for vision prostheses,” IEEE Trans. Biomed. Eng., vol. 58, no. 11, pp. 3197–3205, Nov. 2011.

[16] L. S. Theogarajan, “A low-power fully implantable 15-channel retinal stimulator chip,” IEEE J. Solid-State Circuits, vol. 43, no. 10, pp. 2322–2337, Oct. 2008.

[17] S. Klauke et al., “Stimulation with a wireless intraocular epiretinal implant elicits visual percepts in blind humans,” Investigative Ophthalmol. Visual Sci., vol. 52, no. 1, pp. 449–455, 2011.

[18] G. Roessler et al., “Implantation and explantation of a wireless epiretinal retina implant device: Observations during the EPIRET3 prospective clinical trial,” Investigative Ophthalmol. Visual Sci., vol. 50, no. 6, pp. 3003–3008, 2009.

[19] E. Zrenner, “Fighting blindness with microelectronics,” Sci. Translational Med., vol. 5, no. 210, 2013, Art. no. 210ps16.

[20] K. Stingl et al., “Artificial vision with wirelessly powered subretinal electronic implant alpha-IMS,” Proc. Roy. Soc. B, Biol. Sci., vol. 280, no. 1757, 2013, Art. no. 20130077.

[21] K. Mathieson et al., “Photovoltaic retinal prosthesis with high pixel density,” Nature Photon., vol. 6, no. 6, pp. 391–397, 2012.
[22] L. Wang et al., “Photovoltaic retinal prosthesis: Implant fabrication and performance,” J. Neural Eng., vol. 9, no. 4, 2012, Art. no. 046014.
[23] E. Zrenner, “Artificial vision: Solar cells for the blind,” Nature Photon., vol. 6, no. 6, pp. 344–345, 2012
[24] R. North, “Neural interface devices: Spinal cord stimulation technology,” Proc. IEEE, vol. 96, no. 7, pp. 1108–1119, Jul. 2008
[25] M. A. Howard et al., “Intradural approach to selective stimulation in the spinal cord for treatment of intractable pain: Design principles and wireless protocol,” J. Appl. Phys., vol. 110, no. 4, 2011, Art. no. 044702
[26] M. A. Lebedev and M. A. Nicolelis, “Brain–machine interfaces: Past, present and future,” Trends Neurosci., vol. 29, no. 9, pp. 536–546, 2006.
[27] D. A. Borton, M. Yin, J. Aceros, and A. Nurmikko, “An implantable wireless neural interface for recording cortical circuit dynamics in moving primates,” J. Neural Eng., vol. 10, no. 2, 2013, Art. no. 026010.
[28] R. R. Harrison et al., “A low-power integrated circuit for a wireless 100-electrode neural recording system,” IEEE J. Solid-State Circuits, vol. 42, no. 1, pp. 123–133, Jan. 2007.
[29] R. R. Harrison et al., “Wireless neural recording with single low-power integrated circuit,” IEEE Trans. Neural Syst. Rehab. Eng., vol. 17, no. 4, pp. 322–329, Aug. 2009.
[30] A. M. Sodagar, G. E. Perlin, Y. Yao, K. Najafi, and K. D. Wise, “An implantable 64-channel wireless microsystem for single-unit neural recording,” IEEE J. Solid-State Circuits, vol. 44, no. 9, pp. 2591–2604, Sep. 2009.
[31] S. B. Lee, H.-M. Lee, M. Kiani, U.-M. Jow, and M. Ghovanloo, “An inductively powered scalable 32-channel wireless neural recording systemon-a-chip for neuroscience applications,” IEEE Trans. Biomed. Circuits Syst., vol. 4, no. 6, pp. 360–371, Dec. 2010.
[32] A. Sharma et al., “Evaluation of the packaging and encapsulation reliability in fully integrated, fully wireless 100 channel utah slant electrode array (usea): Implications for long term functionality,” Sensors Actuators A, Phys., vol. 188, pp. 167–172, 2012.
[33] A. M. Sodagar, K. D. Wise, and K. Najafi, “A wireless implantable microsystem for multichannel neural recording,” IEEE Trans. Microw. Theory Tech., vol. 57, no. 10, pp. 2565–2573, Oct. 2009.
[34] G. Loeb, C. Zamin, J. Schulman, and P. Troyk, “Injectable microstimulator for functional electrical stimulation,” Med. Biol. Eng. Comput., vol. 29, no. 6, pp. NS13–NS19, 1991.
[35] G. E. Loeb, R. A. Peck, W. H. Moore, and K. Hood, “Bion system for distributed neural prosthetic interfaces,” Med. Eng. Phys., vol. 23, no. 1, pp. 9–18, 2001.
[36] R. Jegadeesan, S. Nag, K. Agarwal, N. Thakor, and Y.-X. Guo, “Enabling wireless powering and telemetry for peripheral nerve implants,” IEEE J. Biomed. Health Informat., vol. 19, no. 3, pp. 958–970, May 2015.
[37] M. J. Kane, P. P. Breen, F. Quondamatteo, and G. OLaighin, “Bion ´ microstimulators: A case study in the engineering of an electronic implantable medical device,” Med. Eng. Phys., vol. 33, no. 1, pp. 7–16, 2011.
[38] I. Arcos et al., “Second-generation microstimulator,” Artif. Organs, vol. 26, no. 3, pp. 228–231, 2002.
[39] M. S. George et al., “Vagus nerve stimulation: A new tool for brain research and therapy,” Biol. Psychiatry, vol. 47, no. 4, pp. 287–295, 2000.
[40] K. B. Clark, D. K. Naritoku, D. C. Smith, R. A. Browning, and R. A. Jensen, “Enhanced recognition memory following vagus nerve stimulation in human subjects,” Nature Neurosci., vol. 2, no. 1, pp. 94–98, 1999.

[41] M. J. Sjogren et al., “Cognition-enhancing effect of vagus nerve stimulation in patients with Alzheimer’s disease: A pilot study,” J. Clin. Psychiatry, vol. 63, no. 11, pp. 972–980, 2002.
[42] A. Mauskop, “Vagus nerve stimulation relieves chronic refractory migraine and cluster headaches,” Cephalalgia, vol. 25, no. 2, pp. 82–86, 2005.
[43] B. Barrett, R. K. Reddy, and M. S. Roslin, “Treatment of obesity by bilateral vagus nerve stimulation,” U.S. Patent 6 587 719, Jul. 1, 2003.
[44] J. D. Dobak III, “Wireless electric modulation of sympathetic nervous system,” U.S. Patent 7 236 822, Jun. 26, 2007.
[45] J. A. LeVINe and M. A. Faltys, “Closed-loop vagus nerve stimulation,” U.S. Patent 20,160,067,497, Mar. 10, 2016.
[46] Agarwal, K., Jegadeesan, R., Guo, Y. X. & Thakor, N. V. Wireless power transfer strategies for implantable bioelectronics. IEEE Rev. Biomed. Eng. 10, 136–161 (2017).
[47] Park S, Koo K, Bang S, Park J, Song Y and Cho D 2008 A novel microactuator for microbiopsy in capsular endoscopes J. Micromech. Microeng.
[48] Kong K, Cha J, Jeon D and Cho D D 2005 A rotational micro biopsy device for the capsule endoscope IEEE/RSJ Int. Conf. on Intelligent Robots and Systems (IROS 2005)
pp 1839–43
[49] H. Yu, C.-M. Tang, and R. Bashirullah, “An asymmetric RF tagging IC for ingestible medication compliance capsules,” in Proc. IEEE Radio Frequency Integrated Circuits (RFIC) Symp., June 2009, pp. 101–104.
[50] A. Hoover and K. Howell, “RX for health: Engineers design pill that signals it has been swallowed,” University of Florida News, Mar. 31, 2010.
[51] K. C. Farmer, “Methods for measuring and monitoring medication regimen adherence in clinical trials and clinical practice,” Clin. Ther., vol. 21, no. 6, pp. 1074–1090, June 1999.
[52] Proteus Biomedical [Online]. Available: www.proteusbiomed.com
[53] Z. Xiao, C.-M. Tang, C.-C. Peng, H. Yu, and R. Bashirullah, “A 190uW-915MHz active neural transponder with 4-channel time multiplexed AFE,” in Proc. IEEE VLSI Circuits Symp., June 2009, pp. 58–59
[54] M. Ghovanloo and K. Najafi, “A wide-band frequency-shift keying wireless link for inductively powered biomedical implants,” IEEE Trans. Circuits Syst. I, vol. 51, no. 12, pp. 2374–2383, Dec. 2004.
[55] P. Mohseni and K. Najafi, “Wireless multi-channel biopotential recording using an integrated FM telemetry circuit,” IEEE Trans. Neural. Syst. Rehabil. Eng., vol. 13, pp. 263–271, Sept. 2005.
[56] H. Yu, P. Li, Z. Xiao, C.-C. Peng, and R. Bashirullah, “A multichannel instrumentation system for biosignal recording,” in Proc. IEEE Int. Conf. Engineering in Medicine and Biology Society (EMBS), Aug. 20, 2008, pp. 2020–2023.
[57] R Puers et al 2011 J. Micromech. Microeng. 21 054008
[58] G. Meron, “The development of the swallowable video capsule (M2A),” Gastrointest. Endosc., vol. 52, no. 6, pp. 817–819, Dec. 2000.
[59] A. Moglia1, A. Menciassi, and P. Dario, “Recent patents on wireless capsule endoscopy,” Recent Pat. Biomed. Eng., vol. 1, no. 1, pp. 24–33, Jan. 2008.
[60] F. Carpi, S. Galbiati, and A. Carpi, “Controlled navigation of endoscopic capsules: Concept and preliminary experimental investigations,” IEEE Trans. Biomed. Eng., vol. 54, no. 11, pp. 2028–2036, Nov. 2007.
[61] P. D. Bradley, “An ultra low power, high performance medical implant communication system (MICS) transceiver for implantable devices,” in Proc. IEEE BioCas, Nov. 2006, pp. 158–161.
[62] H. A. Wheeler, “Fundamental limitations of small antennas,” Proc. IRE, vol. 35, no. 12, pp. 1479–1488, Dec. 1947.

[63] R. Bashirullah, “Wireless implants,” in IEEE Microw. Mag.s, Dec. 2010, pp. S14–S23.
[64] T. Akin, K. Najafi, and R. M. Bradley, “A wireless implantable multichannel digital neural recording system for a micromachined sieve electrode,” IEEE J. Solid-State Circuits, vol. 33, no. 1, pp. 109–118, Jan. 1998.
[65] R. R. Harrison, P. T. Watkins, R. J. Kier, R. O. Lovejoy, D. J. Black, B. Greger, and F. Solzbacher, “A low-power integrated circuit for a wireless 100-electrode neural recording system,” IEEE J. Solid-State Circuits, vol. 42, no. 1, pp. 123–133, Jan. 2007.
[66] Marland, J.R.K., Blair, E.O., Flynn, B.W., González-Fernández, E., Huang, L., Kunkler, I. H., Smith, S., Staderini, M., Tsiamis, A., Ward, C., et al., “Implantable microsystems for personalised anticancer therapy,” CMOS Circuits for Biological Sensing and Processing. Springer International Publishing, Cham, pp. 259–286, 2018.
[67] Yue, Hao & Guo, Linke & Li, Ruidong & Asaeda, Hitoshi & Fang, Yuguang. (2014). DataClouds: Enabling Community-Based Data-Centric Services Over the Internet of Things. IEEE Internet of Things Journal. 1. 472-482. 10.1109/JIOT.2014.2353629.
[68] Ericsson,“More than 50 billion connected devices”, Ericsson White Paper 284 23-3149 Uen, Feb. 2011
[69] Boaventura, A.: Efficient wireless power transfer and radio-frequency identification systems. Ph.D. thesis, University of Aveiro (2016)
[70] Marks, R.J.(II): Introduction to Shannon Sampling and Interpolation Theory, Springer-Verlag, 1991.
[71] S. Mandal and R. Sarpeshkar, “Power-efficient impedance-modulation wireless data links for biomedical implants,” IEEE Trans. Biomed. Circuits Syst., vol. 2, no. 4, pp. 301–315, Dec. 2008.
[72] G. Yilmaz, O. Atasoy, and C. Dehollain, “Wireless energy and data transfer for in-vivo epileptic focus localization,” IEEE Sens. J., vol. 13, no. 11, pp. 4172–4179, Nov. 2013.
[73] W. Guoxing, L. Wentai, M. Sivaprakasam, and G. A. Kendir, ‘‘Design and analysis of an adaptive transcutaneous power telemetry for biomedical implants,’’ IEEE Trans. Circuits Syst. I, Reg. Papers, vol. 52, no. 10, pp. 2109–2117, Oct. 2005.
[74] H. M. Lee and M. Ghovanloo, “An integrated power-efficient active rectifier with offset-controlled high speed comparators for inductively powered applications,” IEEE Trans. Circuits Syst. I: Regular Papers, vol. 58, no. 8, pp. 1749–1760, Aug. 2011.
[75] A. Yakovlev, J. H. Jang, and D. Pivonka, “An 11 uW SubpJ/bit Reconfigurable Transceiver for mm-Sized Wireless Implants,” IEEE Trans. Biomed. Circuits Syst., vol. 10, no. 1, pp. 175–185, Feb. 2016.
[76] S. Ha, C. Kim, J. Park, S. Joshi, and G. Cauwenberghs, “Energy recycling telemetry ic with simultaneous 11.5 mW power and 6.78 Mb/s backward data delivery over a single 13.56 MHz inductive link,” IEEE J. Solid-State Circuits, vol. 51, no. 11, pp. 2664–2678, Nov. 2016.
[77] D. Jiang, D. Cirmirakis, M. Schormans, T. A. Perkins, N. Donaldson, and A. Demosthenous, “An integrated passive phase-shift keying modulator for biomedical implants with power telemetry over a single inductive link,” IEEE Trans. Biomed. Circuits Syst., vol. 11, no. 1, pp. 64–77, Feb. 2017.
[78] S. Sonkusale and Z. Luo, “A complete data and power telemetry system utilizing BPSK and LSK signaling for biomedical implants,” in Proc. 30th Annu. Int. Conf. IEEE Eng. Med. Biol. Soc., Vancouver, BC, Canda, Aug. 20–25, 2008, pp. 3216–3219.
[79] Ghovanloo, M.; Najafi, K. “A wideband frequency-shift keying wireless link for inductively powered biomedical implants”. IEEE Transactions on Circuits and Systems I, Volume 51, Issue 12, Dec. 2004.

[80] Y. Hu and M. Sawan, “A fully integrated low-power BPSK demodulator for implantable medical devices,” IEEE Trans. Circuits Syst. I, Fundam. Theory Appl., vol. 52, no. 12, pp. 2552–2562, Dec. 2005.
[81] M. Ghovanloo and S. Atluri, “A wide-band power-efficient inductive wireless link for implantable microelectronic devices using multiple carriers,” IEEE Trans. Circuits Syst. I: Reg. Papers, vol. 54, no. 10, pp. 2211–2221, Oct. 2007.
[82] J. Wu, C. Zhao, Z. Lin, J. Du, Y. Hu, and X. He, ‘‘Wireless power and data transfer via a common inductive link using frequency division multiplexing,’’ IEEE Trans. Ind. Electron., vol. 62, no. 12, pp. 7810–7820, Dec. 2015.
[83] C. Yu, R. Lu, C. Su, and C. Zhu, “Study on wireless energy and data transmission for long-range projectile,” IEEE Trans. Plasma Sci., vol. 41, no. 5, pp. 1370–1375, May 2013
[84] U. K. Madawala, J. Stichbury, and S. Walker, “Contactless power transfer with two-way communication,” in Proc. IEEE Conf. Ind. Electron., Busan, Korea, Nov. 2004, pp. 3071–3075
[85] T. Bieler, M. Perrottet, V. Nguyen, and Y. Perriard, “Contactless power and information transmission,” IEEE Trans. Ind. Appl., vol. 38, no. 5, pp. 1266–1272, Sep./Oct., 2002
[86] K. Gosalia, G. Lazzi, and M. Humayun, ‘‘Investigation of a microwave data telemetry link for a retinal prosthesis,’’ IEEE Trans. Microw. Theory Techn., vol. 52, no. 8, pp. 1925–1933, Aug. 2004
[87] U.-M. Jow and M. Ghovanloo, ‘‘Optimization of data coils in a multiband wireless link for neuroprosthetic implantable devices,’’ IEEE Trans. Biomed. Circuits Syst., vol. 4, no. 5, pp. 301–310, Oct. 2010
[88] L. Wentai et al., “Implantable biomimetic microelectronic systems design,” IEEE Eng. Med. Biol. Mag., vol. 24, no. 5, pp. 66–74, Sep./Oct.2005
[89] S. A. Mirbozorgi, H. Bahrami, M. Sawan, L. A. Rusch, and B. Gosselin, “A single-chip full-duplex high speed transceiver for multi-site stimulating and recording neural implants,” IEEE Trans. Biomed. Circuits Syst., vol. 10, no. 3, pp. 643–653, Jun. 2016
[90] S. Atluri and M. Ghovanloo, “Design of a wideband power-efficient inductive wireless link for implantable biomedical devices using multiple carriers,” in Proc. 2nd Int. IEEE EMBS Conf. Neural Eng., 2005, pp. 533–537.
[91] W. P. Choi, W. C. Ho, X. Liu, and S. Y. R. Hui, “Bidirectional communication techniques for wireless battery charging systems & portable consumer electronics,” in Proc. IEEE Conf. Appl. Power Electron., Palm Springs, CA, USA, 2010, pp. 2251–2257.
[92] R. Bashirullah, W. Liu, Y. Ji, A. Kendir, M. Sivaprakasam, G. Wang, and B. Pundi, “A smart bi-directional telemetry unit for retinal prosthetic device,” in Proc. Int. Symp. Circuits Syst., May 2003, vol. 5, pp. 5–8
[93] G. Wang, W. Liu, M. Sivaprakasam, M. Zhou, J. D. Weiland, and M. S. Humayun, “A dual band wireless power and data telemetry for retinal prosthesis,” in Proc. IEEE 28th EMBS Conf., Sep. 2006, pp. 4292–4295.
[94] W. Liu, M. Sivaprakasam, G. Wang, M. Zhou, J. Granacki, J. LaCoss, and J. Wills, “Implantable biomimetic microelectronic system design,” IEEE Eng. Med. Biol. Mag., vol. 24, pp. 66–74, Sep. 2005
[95] J. H. Schulman et al., ‘‘Battery powered BION FES network,’’ in Proc. Annu. Int. Conf. IEEE 26th Eng. Med. Biol. Soc. (EMBS), Sep. 2004, pp. 4283–4286.
[96] N. M. Neihart and R. R. Harrison, ‘‘Micropower circuits for bidirectional wireless telemetry in neural recording applications,’’ IEEE Trans. Biomed. Eng., vol. 52, no. 11, pp. 1950–1959, Nov. 2005.
[97] H. Yu and K. Najafi, ‘‘Low-power interface circuits for bio-implantable microsystems,’’ in IEEE Int. Solid-State Circuits Conf. (ISSCC) Dig. Tech. Papers, San Francisco, CA, USA, Feb. 2003, pp. 194–487
[98] A 13.56-Mbps Pulse Delay Modulation Based Transceiver for Simultaneous Near-Field Data and Power Transmission

[99] G. Simard, M. Sawan, and D. Massicotte, “High-speed OQPSK and efficient power transfer through inductive link for biomedical implants,” IEEE Trans. Biomed. Circuits Syst., vol. 4, no. 3, pp. 192–200, Jun. 2010
[100] [G. Wang, P. Wang, Y. Tang, and W. Liu, “Analysis of dual band power and data telemetry for biomedical implants,” IEEE Trans. Biomed. Circuits Syst., vol. 6, no. 3, pp. 208–215, Jun. 2012
[101] M. Kiani and M. Ghovanloo, “A 20 Mb/s pulse harmonic modulation transceiver for wideband near-field data transmission,” IEEE Trans. Circuits Syst. II, Exp. Briefs, vol. 60, no. 7, pp. 382–386, 2013.
[102] M. Zhou, M. R. Yuce, and W. Liu, ‘‘A non-coherent DPSK data receiver with interference cancellation for dual-band transcutaneous telemetries,’’ IEEE J. Solid-State Circuits, vol. 43, no. 9, pp. 2003–2012, Sep. 2008.
[103] J. Hirai, K. Tae-Woong, and A. Kawamura, “Study on intelligent battery charging using inductive transmission of power and information,” IEEE Trans. Power Electron., vol. 15, no. 2, pp. 335–345, Mar. 2000.
[104] R. Sarpeshkar, W. Wattanapanitch, B. Rapoport, S. Arfin, M. Baker, S. Mandal, M. Fee, S. Musallam, and R. Andersen, “Low-power circuits for brain-machine interfaces,” in Proc. IEEE Int. Symp. Circ. Sys. (ISCAS’2007), 2007, pp. 2068–2071.
[105] Faraday, M. Experimental researches in electricity. Nineteenth Series. Philos. Trans. R. Soc. Lond. 136, 1–20 (1846).
[106] N. Tesla, The Transmission of Electric Energy Without Wires (The Thirteenth Anniversary Number of the Electrical World and Engineer). New York: McGraw-Hill, Mar. 5, 1904.
[107] N. Tesla, Experiments with Alternate Current of High Potential and High Frequency. New York: McGraw-Hill, 1904.
[108] J.C. Schuder, H.E. Stephenson, Jr., J.F. Townsend, Energy transfer into a closed chest by means of stationary coupling coils and a portable high-power oscillator, Trans Am Soc Artif Intern Organs, 7(1961) 327-31.
[109] J. O. Mur-Miranda, G. Fanti, Y. Feng, K. Omanakuttan, R. Ongie, A. Setjoadi, and N. Sharpe, “Wireless power transfer using weakly coupled magnetostatic resonators,” in Proc. Energy Convers. Congr. Expo., 2010, pp. 4179–4186.
[110] K. Fotopoulou and B. W. Flynn, “Wireless power transfer in loosely coupled links: Coil misalignment model,” IEEE Trans. Magn., vol. 47, no. 2, pp. 416–430, Feb. 2011.
[111] A. K. RamRakhyani, S. Mirabbasi, and M. Chiao, “Design and optimization of resonance-based efficienct wireless power delivery systems for biomedical implants,” IEEE Trans. Biomed. Circuits Syst., vol. 5, no. 1, pp. 48–63, Feb. 2011.
[112] K. Shiba, A. Morimasa, and H. Hirano, “Design and development of lowloss transformer for powering small implantable medical devices,” IEEE Trans. Biomed. Circuits Syst., vol. 4, no. 2, pp. 77–85, Apr. 2010.
[113] C. J. Chen, T. H. Chu, C. L. Lin, and Z. C. Jou, “A study of loosely coupled coils for wireless power transfer,” IEEE Trans. Circuitsand Syst.—Part II: Express Briefs, vol. 57, no. 7, pp. 536–540, Jul. 2010.
[114] T. Sun, X. Xie, and Z. Wang, Wireless Power Transfer for Medical Microsystems. New York, NY, USA: Springer, 2013, doi: 10.1007/978- 1-4614-7702-0.
[115] W. H. Xin, G. Z. Yan, and W. X. Wang, “A stable wireless energy transmission system for gastrointestinal microsystems,” J. Med. Eng. Technol., vol. 34, no. 1, pp. 64–70, Jan. 2010.
[116] U.-M. Jow and M. Ghovanloo, “Modeling and optimization of printed spiral coils in air, saline, and muscle tissue environments,” IEEE Trans. Biomed. Circuits Syst., vol. 3, no. 5, pp. 339–347, Oct. 2009.
[117] S. C. Tang, T. L. T. Lun, Z. Guo, K. W. Kwok, and N. J. McDannold, “Intermediate range wireless power transfer with segmented coil transmitters

for implantable heart pumps," IEEE Trans. Power Electron., vol. 32, no. 5, pp. 3844–3857, May 2017.
[118] R. F. Xue, K.-W. Cheng, and M. Je, "High-efficiency wireless power transfer for biomedical implants by optimal resonant load transformation," IEEE Trans. Circuits Syst. I: Reg. Papers, vol. 60, no. 4, pp. 867–874, Apr. 2013.
[119] J. J. Casanova, Z. N. Low, and J. Lin, "A loosely coupled planar wireless power system for multiple receivers," IEEE Trans. Ind. Electron., vol. 56, no. 8, pp. 3060–3068, Aug. 2009.
[120] U.-M. Jow and M. Ghovanloo, "Design and optimization of printed spiral coils for efficient transcutaneous inductive power transmission," IEEE Trans. Biomed. Circuits Syst., vol. 1, no. 3, pp. 193–202, Sep. 2007.
[121] Y. Zeng, D. Qiu, X. Meng, B. Zhang, and S. C. Tang, "Optimized design of coils for wireless power transfer in implanted medical devices," IEEE Journal of Electromagnetics, RF and Microwaves in Medicine and Biology, vol. 2, no. 4, pp. 277–285, Dec 2018.
[122] S. C. Tang, F. A. Jolesz, and G. T. Clement, "A wireless batteryless deep-seated implantable ultrasonic pulser-receiver powered by magnetic coupling," IEEE Trans. Ultrason., Ferroelectr., Freq. Control, vol. 58, no. 6, pp. 1211–1221, Jun. 2011.
[123] A. K. RamRakhyani and G. Lazzi, "Multicoil telemetry system for compensation of coil misalignment effects in implantable systems," IEEE Antennas Wireless Propag. Lett., vol. 11, pp. 1675–1678, Feb. 2013
[124] M. Kiani, U. M. Jow, and M. Ghovanloo, "Design and optimization of a 3-coil inductive link for efficient wireless power transmission," IEEE Trans. Biomed. Circuits Syst., vol. 5, no. 6, pp. 579–591, Dec. 2011.
[125] M. Zargham and P. G. Gulak, "Maximum achievable efficiency in nearfield coupled power-transfer systems," IEEE Trans. Biomed. Circuits Syst. vol. 6, no. 3, pp. 228–245, Jun. 2012.
[126] K. Na, H. Jang, H. Ma, and F. Bien, "Tracking optimal efficiency of magnetic resonance wireless power transfer system for biomedical capsule endoscopy," IEEE Trans. Microw. Theory Techn., vol. 63, no. 1, pp. 295–304, Jan. 2015
[127] D. C. Ng, C. E. Williams, P. J. Allen, S. Bai, C. S. Boyd, H. Meffin, M. E. Halpern, and E. Skafidas, "Wireless Power Delivery for Retinal Prostheses," in Proc. 33rd Annu. Int. Conf. IEEE Eng. Med. Biol. Soc. (EMBS 2011), Boston, MA, USA, 2011, pp. 8356–8360.
[128] S. A. Mirbozorgi, P. Yeon, and M. Ghovanloo, "Robust wireless power transmission to mm-sized free-floating distributed implants," IEEE Trans. Biomed. Circuits Syst., vol. 11, no. 3, pp. 692–702, Jun. 2017.
[129] T. Mizuno, S. Yachi, A. Kamiya, and D. Yamamoto, "Improvement in efficiency of wireless power transfer of magnetic resonant coupling using magnetoplated wire," IEEE Trans. Magn., vol. 47, no. 10, pp. 4445–4448, Oct. 2011.
[130] A. Khalifa, Y. Karimi, Q. Wang, S. Garikapati, W. Montlouis, M. Stanace-´ vic, N. Thakor, and R. Etienne-Cummings, "The microbead: A highly ´ miniaturized wirelessly powered implantable neural stimulating system," IEEE Transactions on Biomedical Circuits and Systems, vol. 12, no. 3, pp. 521–531, June 2018.
[131] C. Kim et al., "A 3 mm × 3 mm Fully Integrated Wireless Power Receiver and Neural Interface System-on-Chip," in IEEE Transactions on Biomedical Circuits and Systems, vol. 13, no. 6, pp. 1736-1746, Dec. 2019.
[132] F. J. Holler D. A. Skoog and S. R. Crouch, Principles of Instrumental Analysis, Cengage Learning, Boston, 7th edition, 2017, p.9
[133] G. Gautschi, Piezoelectric Sensorics. Berlin, Germany: Springer-Verlag, 2002, p. 76
[134] A. Denisov and E. Yeatman, "Ultrasonic vs. Inductive Power Delivery for Miniature Biomedical Implants," 2010 International Conference on Body Sensor Networks, Singapore, 2010, pp. 84-89. doi: 10.1109/BSN.2010.27

[135] T. Maleki, N. Cao, S. H. Song, C. Kao, S. Ko and B. Ziaie, "An Ultrasonically Powered Implantable Micro-Oxygen Generator (IMOG)," in IEEE Transactions on Biomedical Engineering, vol. 58, no. 11, pp. 3104-3111, Nov. 2011.
[136] P. Theilmann, Wireless power transfer for scaled electronic biomedical implants. Ph.D. dissertation, University of California, San Diego, 2012.
[137] J.E. Kennedy, G.R. Ter Haar, and D. Cranston, “High intensity focused ultrasound: surgery of the future?”, British Journal of Radiology, vol. 76, pp. 590-599, 2003.
[138] S. Suzuki, S. Kimura, T. Katane, H. Saotome, O. Saito and K. Kobayashi, "Power and Interactive Information Transmission to Implanted Medical Device Using Ultrasonic," Japanese Journal of Applied Physics, vol. 41, pp. 3600-3603, 2002.
[139] F. Mazzilli and C. Dehollain, “184 μw ultrasonic on–off keying/ amplitude-shift keying demodulator for downlink communication in deep implanted medical devices,” Electron. Lett., vol. 52, no. 7, pp. 502–504, 2016.
[140] J. Y. Tsai, K.-H. Huang, J.-R. Wang, S.-I. Liu, and P.-C. Li, “Ultrasonic wireless power and data communication for neural stimulation,” in Proc. IEEE Int. Ultrason. Symp., Oct. 2011, pp. 1052–1055.
[141] J. S. Ho and A. S. Y. Poon, ‘‘Energy transfer for implantable electronics in the electromagnetic midfield,’’ Prog. Electromagn. Res., vol. 148, pp. 151–158, Aug. 2014.
[142] A. J. Yeh, J. S. Ho, and A. S. Y. Poon, ‘‘Optical probe for input-impedance measurement of in vivo power-receiving microstructure,’’ in Proc. IEEE Int. Symp. Antennas Propag. (APS), Jul. 2014, pp. 1409–1410.
[143] S. Gabriel, R.W. Lau, and C. Gabriel. “The dielectric properties of biological tissues: III. Parametric models for the dielectric spectrum of tissues,” Phys. Med. Biol., vol. 41, pp. 2271-2293, 1996.
[144] IEEE 2006 IEEE standard for safety levels with respect to human exposure to radio frequency electromagnetic fields, 3 kHz to 300 GHz IEEE Std C95.1-2005 (Revision of IEEE Std C95.1-1991) pp 1–238
[145] A. S. Y. Poon, S. O’Driscoll, and T. H. Meng, ‘‘Optimal operating frequency in wireless power transmission for implantable devices,’’ in Proc. Annu. Int. Conf. IEEE Eng. Med. Biol., Lyon, France, Aug. 2007, pp. 5673–5678.
[146] A. Yakovlev, S. Kim, and A. Poon, ‘‘Implantable biomedical devices: Wireless powering and communication,’’ IEEE Commun. Mag., vol. 50, no. 4, pp. 152–159, Apr. 2012.
[147] J. S. Ho, S. Kim, and A. Poon, “Midfield wireless powering for implantable systems,” Proc. IEEE, vol. 101, no. 6, pp. 1369–1378, Jun. 2013.
[148] S. Kim, J. Ho, and A. Poon, “Wireless power transfer to miniature implants: Transmitter optimization,” IEEE Trans. Antennas Propag., vol. 60, no. 10, pp. 4838–4845, Oct. 2012.
[149] S. Kim, J. S. Ho, and A. S. Y. Poon, ‘‘Midfield wireless powering of subwavelength autonomous devices,’’ Phys. Rev. Lett., vol. 110, p. 203905, May 2013.
[150] L. Huang, A. P. Hu, A. K. Swain, and Y. Su, “Accurate steady-state modelling of capacitive-coupling interface of capacitive power transfer systems with cross-coupling,” Wireless Power Transfer, vol. 3, no. 1, pp. 53-62, Mar. 2016, doi: 10.1017/wpt.2016.2.
[151] Dai, J.; Ludois, D.: A survey of wireless power transfer and a critical comparison of inductive and capacitive coupling for small gap applications. IEEE Trans. Power Electron., 30 (2015), 6017–6029.
[152] Fei, L.; Hua, Z.; Hofmann, H.; Mi, C.: A double-sided LCLC compensated capacitive power transfer system for electric vehicle charging. IEEE Trans. Power Electron., 30 (2015), 6011–6014.
[153] Liu, C.; Hu, A.P.; Nair, N.K.C.: Modelling and analysis of a capacitively coupled contactless power transfer system. IET Power Electron., 4 (2011), 808–815.

[154] Chao, L.; Hu, A.P.; Covic, G.A.; Nair, N.C.: Comparative study of CCPT systems with two different inductor tuning positions. IEEE Trans. Power Electron., 27 (2012), 294–306.
[155] H. Goto, T. Sugiura, Y. Harada, and T. Kazui, “Feasibility of using the automatic generating system for quartz watches as a leadless pacemaker power source,” Med. Biol. Eng. Comput., vol. 37, no. 1, pp. 377–380, Jan. 1999.
[156] R. Elfrink, T. M. Kamel, M. Goedbloed, S. Matova, D. Hohlfeld, Y. van Andel, and R. van Schaijk, “Vibration energy harvesting with aluminum nitride-based piezoelectric devices,” J. Micromechan. Microeng., vol. 19, no. 9, p. 094005, 2009
[157] M. Renaud, K. Karakaya, T. Sterken, P. Fiorini, C. V. Hoof, and R. Puers, “Fabrication, modelling and characterization of MEMS piezoelectric vibration harvesters,” Sensors Actuators A, Phys., vol. 145–146, pp. 380–386, 2008.
[158] J. Olivo, S. Carrara, and G. De Micheli, "Energy Harvesting and Remote Powering for Implantable Biosensors," Sensors Journal, IEEE, vol.11, no.7, pp.1573-1586, July 2011
[159] I. Stark and M. Stordeur, “New micro thermoelectric devices based on bismuth telluride-type thin solid films,” in Proc. 18th Int. Conf. Thermoelectric, pp. 465–472, 1999.
[160] M. Strasser, R. Aigner, C. Lauterbach, T. F. Sturm, M. Franosch, and G. Wachutka, “Micromachined CMOS thermoelectric generators as on-chip power supply,” Sensors Actuators A, Phys., vol. 114, no. 2-3, pp. 362–370, 2004.
[161] R. Drake, B. Kusserow, S. Messinger, and S. Matsuda, “A tissue implantable fuel cell power supply,” ASAIO J., vol. 16, no. 1, pp. 199–205, 1970.
[162] N. Mano, F. Mao, and A. Heller, “Characteristics of a miniature compartment-less glucose- biofuel cell and its operation in a living plant,” J. Amer. Chem. Soc., vol. 125, no. 21, pp. 6588–6594, May 2003
[163] T. Oshita and R. Calderhead, Low Level Laser Therapy: A Practical Introduction. New York: Wiley, 1988.
[164] K. Goto, T. Nakagawa, O. Nakamura, and S. Kawata, “An implantable power supply with an optical rechargeable lithium battery,” IEEE Trans. Biomed. Eng., vol. 48, no. 7, pp. 830–833, Jul. 2001.
[165] S. O’Driscoll, A. Poon, and T. Meng, “A mm-sized implantable power receiver with adaptative link compensation,” in Proc. IEEE Int. SolidState Circuits Conf., Feb. 2009, p. 294.
[166] C. N. Yalung, F. R. G. Cruz, A. C. Paglinawan, J.J.R. Balbin, J. C. Dela Cruz, A. Silverio, J. A. Ngo and W. Y. Chung, “Full-wave AC-DC converter in CMOS 0.18 micron for vibration electromagnetic energy harvest,” 2014 International Conference on HNICEM, pp. 1-4, 2014.
[167] Sun, Y., Jeong, C., Han, S., et al. (2011). A high speed comparator based active rectifier for wireless power transfer systems. MTT-S (pp. 1–2).
[168] H.-K. Cha and M. Je, “A single-input dual-output 13.56 MHz CMOS ac– dc converter with comparator-driven rectifiers for implantable devices,” Microelectron. J., vol. 45, no. 3, pp. 277–281, 2014.
[169] K. Keikhosravy, P. Kamalinejad, S. Mirabbasi, K. Takahata, and V. C. M. Leung, “An ultra-low-power monitoring system for inductively coupled biomedical implants,” in IEEE International Symposium on Circuits and Systems (ISCAS), 2013, pp. 2283–2286.
[170] J. C. Maxwell, “On physical lines of force,” The London, Edinburgh, and Dublin Philos. Mag. J. Sci., p. 161, 1861, and J. C. Maxwell, A Treatise on Electricity and Magnetism, Oxford, U.K.: Clarendon, 1873.
[171] I.S. Grant, W.R. Phillips, “Electromagnetism[M],” John Wiley & Sons, 2013.
[172] S. J. Orfanidis, “Electromagnetic Waves and Antennas [Online],” 2013. Available: http://eceweb1.rutgers.edu/~orfanidi/ewa/

[173] R. Iulian, “Impedance Matching [Online],” 2011. Available: https://www.qsl.net/va3iul/Impedance_Matching/Impedance_Matching.pdf
[174] D. W. Knight, “The self-resonance and self-capacitance of solenoid coils-applicable theory, models and calculation methods [Online],” Private Res., Exeter, U.K., Tech. Rep. 301824613 4, May 2016. Available: https://www.researchgate.net/publication/301824613_The_selfresonance_and_selfcapacitance_of_solenoid_coils_applicable_theory_models_and_calculation_methods doi: 10.13140/RG.2.1.1472.0887.
[175] E. Fraga, C. Prados, and D.-X. Chen, “Practical model and calculation of AC resistance of long solenoids,” IEEE Trans. Magn., vol. 34, no. 1, pp. 205–212, Jan. 1998.
[176] G. L. Johnson, Solid State Tesla Coil. Manhattan, KS: Kansas State Univ., Dec. 2001, Lossy Capacitors, ch. 3. Available: http://ece.k-state.edu/people/faculty/gjohnson/
[177] R. G. Medhurst, “H. F. resistance and self-capacitance of single-layer solenoids,” Wireless Eng., vol. 24, pp. 35–43, Feb. 1947 and pp. 80–92, Mar. 1946.
[178] P. Drude, “Zur construction von Teslatransformatoren. Schwingungsdauer und Selbstinduction von Drahtspulen (On the construction of Tesla transformers: Period of oscillation and self-inductance of the coil),” Ann. Phys. 314 (10) p293-339, 314 (11) p590-610, 1902.
[179] A. J. Palermo, “Distributed Capacity of Single-Layer Coils,” Proc. IRE. Vol. 22, No. 7, pp. 897 – 905, July 1934.
[180] F. Ollendorf, “Die Grunclllugen der Hochfrequeriztechnik,” Springer, Berlin, pp. 79-87, “Das dynamische Feld der mehrwindigen Spule,” 1926.
[181] W. Jackson, "The Self-Capacitance of Single-Layer Coils," Phil. Mag. and Jour. Of Sci., Vol. 19, pp. 823-835, 1935.
[182] L. Hartshorn, “Radio-Frequency Measurements by Bridge and Resonance Methods,” Chapman & Hall, Vol. X of "Monographs on Electrical Engineering," ed. H P Young, 3rd imp, Ch VI, “section 3: Calculation of capacitance,” p104, 1942.
[183] Hayt, William Hart, “Engineering Electromagnetics (7th ed.),” McGraw Hill, New York, p63, 2006.
[184] F. E. Terman, “Radio Engineering Handbook,” McGraw-Hill, New York, “details electromagnetic proximity and skin effects,” 1943.
[185] D. W. Knight, “Solenoid Inductance Calculation [Online],” 2013, Available: http://g3ynh.info/zdocs/magnetics/Solenoids.pdf.
[186] J. D. Kraus, Antennas. McGraw-Hill, Inc., second edition ed., 1988.
[187] C. Gabriel, S. Gabriel, and E. Corthout, “The dielectric properties of biological tissues: I. Literature survey,” Phys. Med. Biol., vol. 41, pp. 2231-2249, 1996
[188] C. Johnson and A. Guy, "Nonionizing electromagnetic wave effects in biological materials and systems," Proc. IEEE, vol. 60, no. 6, pp. 692-718, 1972.
[189] D. Ahn and M. Ghovanloo, “Optimal design of wireless power transmission links for millimeter-sized biomedical implants,” IEEE Trans. Biomed. Circuits Syst., vol. 10, no. 1, pp. 125–137, Feb. 2016.
[190] International Commission on Non-Ionizing Radiation Protection, “ICNIRP guidelines for limiting exposure to time-varying electric, magnetic and electromagnetic fields (up to 300GHz),” Health Phys., vol. 74, no. 4, pp. 494–522, 1998.
[191] S. Michaelson, “Health implications of exposure to radiofrequency/microwave energies,” British J. Ind. Med., vol. 39, pp. 105–119, 1982.
[192] D. Hermann and K. Hossmann, “Neurological effects of microwave exposure related to mobile communication,” J. Neurolog. Sci., vol. 152, no. 1, pp. 1–14, 1997.

[193] L. Sandrolini, U. Reggiani, G. Puccetti, and Y. Neau, “Equivalent circuit characterization of resonant magnetic coupling for wireless transmission of electrical energy,” Int. J. Circ. Theor. Appl., 2013.
[194] L. Xun, W. M. Ng, C. K. Lee, and S. Y. Hui, “Optimal operation of contactless transformers with resonance in secondary circuits,” in Proc. 23rd Annu. IEEE Appl. Power Electron. Conf. Exposition, 2008. Austin, TX, pp. 645–650.
[195] K. Fotopoulou, “Inductive wireless power transfer for RFID and embedded devices: Coils misalignment analysis and design,” Ph.D. dissertion, School of Eng. and Electron., Univ. of Edinburgh, Edinburgh, U.K., 2008.
[196] E. C. Snelling, “Soft ferrites: properties and applications. Second edition.,” Butterworth & Co. (Publishers) Ltd, London, 1988
[197] R. M. Bozorth and D. M. Chapin, “Demagnetizing factors of rods,” J. Appl. Phys., vol. 13, pp. 320-326, May 1942.
[198] W. J. Polydoroff, High-Frequency Magnetic Materials: Their characteristics and principle applications, New York: John Wiley, 1960.
[199] J. A. Stratton, Electromagnetic Theory, New York: McGraw-Hill, 1941, pp. 212-214, 258.
[200] D.-X. Chen, J. A. Brug, and R. B. Goldfarb, “Demagnetizing factors for cylinders,” IEEE Trans. Magn., vol. 27, no. 4, pp. 3601–3619, Jul. 1991.
[201] Bartoli, M. , A. Reatti , and M. K. Kazimierczuk . "High-frequency models of ferrite core inductors." Proceedings of IECON'94 - 20th Annual Conference of IEEE Industrial Electronics IEEE, 1994.
[202] H. A. Wheeler, “Simple inductance formulas for radio coils,” Proc. IRE., vol. 16, no. 10, pp. 1398-1400, Oct. 1928.
[203] “Ferrites and accessories - SIFERRIT material K1 [Online],” TDK Electronics, May 2017. Available: www.tdk-electronics.tdk.com › download › pdf-k1
[204] T. Dai, B. Zhang, X. N. Kang, K. Bao, W. Z. Zhao, D. S. Xu, G. Y. Zhang, and Z. Z. Gan, “Light extraction improvement from GaN-based lightemitting diodes with nano-patterned surface using anodic aluminum oxide template,” IEEE Photon. Tech. Lett., vol. 20, no. 23, pp. 1974–1976, Dec. 2008.
[205] R. Wang, H. P. T. Nguyen, A. T. Connie, J. Lee, I. Shih, and Z. Mi, “Color-tunable, phosphor-free InGaN nanowire light-emitting diode arrays monolithically integrated on silicon,” Opt. Express, vol. 22, no. S7, pp. A1768–A1775, 2014.
[206] “Photodiodes and Phototransistors [Online],” Neur. Robot. Lab, Cen. Robot. Bios., Northwestern University, Feb. 2011. Available: http://hades.mech.northwestern.edu/index.php/Photodiodes_and_Phototransistors
[207] “EG & G ELECTRO-OPTICS,” 35 CONGRESS STREET, SALEM, MASSACHUSETTS 01970, USA, October 1979
[208] “Chapter 11 Inductance and Magnetic Energy [Online],” Massachusetts Institute of Technology, 2014. Available: http://web.mit.edu/viz/EM/visualizations/notes/modules/guide11.pdf
[209] Lander, W. Cyril, "2. Rectifying Circuits," Power electronics (3rd ed.), London: McGraw-Hill, 1993. ISBN 978-0-07-707714-3.
[210] “Rectifier circuits [Online]”, Wikipedia. Available: https://en.wikipedia.org/wiki/Rectifier#cite_note-Lander93-2
[211] Neamen. D, “Electronic Circuit Analysis and Design,” McGraw-Hill, 2nd Edition, 2001. ISBN 0072451947